

Technische Universität Dresden

DESIGN OF AN ULTRA-WIDEBAND RADIO  
FREQUENCY IDENTIFICATION SYSTEM WITH  
CHIPLESS TRANSPONDERS

Marvin Renan Barahona Medina

von der Fakultät Elektrotechnik und Informationstechnik  
der Technische Universität Dresden  
zur Erlangung des akademischen Grades

Doktoringenieur  
(Dr.-Ing)

genehmigte Dissertation

Promotionskommission:

Vorsitzender	Prof. Dr.-Ing. habil. Wolf-Joachim Fischer Technische Universität Dresden
1. Gutachter	Prof. Dr. sc. techn. Frank Ellinger Technische Universität Dresden
2. Gutachter	Prof. Dr.-Ing. Arved Carl Hübler Technische Universität Chemnitz
Weiteres Mitglied	Prof. Dr. rer. nat. Stefan Mannsfeld Technische Universität Dresden

Tag der Einreichung: 08.12.2018

Tag der Verteidigung: 04.07.2019



## Acknowledgments

I would like to express my deepest gratitude to Prof. Dr. sc. techn. Frank Ellinger for giving me the opportunity to pursue my doctoral studies at the chair for circuit design and network theory, his kindness, patience and valuable guidance throughout my time at Technische Universität Dresden. I'm also grateful to Prof. Dr.-Ing. Arved Carl Hübler for the second revision of this work, as well as the remaining members of the promotion's committee Prof. Dr.-Ing. habil. Wolf-Joachim Fischer and Prof. Dr. rer. nat. Stefan Mannsfeld. I will always associate Prof. Mannsfeld with the working principle of one specific device and the way he remembered some figures and tables of my thesis, thank you very much!

A special thanks to my parents Alejandrina and Evelio, and their efforts to provide me with the best education they could, as well as to all my family members, above all, those who have felt my absence the most. I know I have missed a lot of important events in your lives and I can only hope I will be able to make it up to all of you someday. Time can be such a precious thing while living abroad and away from the dear ones.

I also would like to thank Michael, Rana and Vera for their support and motivational words throughout the writing of this dissertation. Moreover, to those who have always believed in me, and encouraged me to never give up despite how difficult or unfair the circumstances might have been: César, Fany, and Victor. Karin, Michael, thank you very much for your support during the defense, it meant the world to me.

It is thanks to all of you, that after evaluating my life's chessboard once more, at this specific point in time, I can say with great amazement and satisfaction: checkmate! A person who believes in his own ideals shall never fear to follow his own path, doing what one believes is right will provide us enough strength to overcome any difficulties lying ahead and the consequences of our actions, every blow life gives to us will only be forging our character, and I certainly forged mine one these past years.

“Talent develops in solitude, character develops in the stream of life”

Johann Wolfgang von Goethe





## Abstract

The state-of-the-art commercially available radio-frequency identification (RFID) transponders are usually composed of an antenna and an application specific integrated circuit chip, which still makes them very costly compared to the well-established barcode technology. Therefore, a novel low-cost RFID system solution based on passive chipless RFID transponders manufactured using conductive strips on flexible substrates is proposed in this work. The chipless RFID transponders follow a specific structure design, which aim is to modify the shape of the impinging electromagnetic wave to embed an identification code in it and then backscatter the encoded signal to the reader.

This dissertation comprises a multidisciplinary research encompassing the design of low-cost chipless RFID transponders with a novel frequency coding technique, unlike usually disregarded in literature, this approach considers the communication channel effects and assigns a unique frequency response to each transponder. Hence, the identification codes are different enough, to reduce the detection error and improve their automatic recognition by the reader while working under normal conditions. The chipless RFID transponders are manufactured using different materials and state-of-the-art mass production fabrication processes, like printed electronics. Moreover, two different reader front-ends working in the ultra-wideband (UWB) frequency range are used to interrogate the chipless RFID transponders. The first one is built using high-performance off-the-shelf components following the stepped frequency modulation (SFM) radar principle, and the second one is a commercially available impulse radio (IR) radar.

Finally, the two readers are programmed with algorithms based on the conventional minimum distance and maximum likelihood detection techniques, considering the whole transponder radio frequency (RF) response, instead of following the commonly used approach of focusing on specific parts of the spectrum to detect dips or peaks. The programmed readers automatically identify when a chipless RFID transponder is placed within their interrogation zones and proceed to the successful recognition of its embedded identification code. Accomplishing in this way, two novel fully automatic SFM- and IR-RFID readers for chipless transponders. The SFM-RFID system is capable to successfully decode up to eight different chipless RFID transponders placed sequentially at a maximum reading range of 36 cm. The IR-RFID system up to four sequentially and two simultaneously placed different chipless RFID transponders within a 50 cm range.



## Kurzfassung

Die handelsübliche Technologie der Identifizierung mit Hilfe elektromagnetischer Wellen (RFID, englisch: radio-frequency identification) Transponder bestehen nach dem Stand der Technik üblicherweise aus einer Antenne und einem anwendungsspezifischen integrierten Schaltungschip, weshalb sie im Vergleich zur bekannten Barcode-Technologie noch sehr kostenintensiv sind. Um die Herstellungskosten weiter zu senken, wird daher eine neuartige, kostengünstige RFID-Systemlösung basierend auf passiven chiplosen RFID-Transponder vorgeschlagen, die unter Verwendung von leitfähigen Streifen auf flexiblen Substraten hergestellt werden. Die chiplosen RFID-Transponder folgen einem speziellen Strukturdesign, welches darauf abzielt, die Form der auftreffenden elektromagnetischen Welle zu modifizieren, um einen Identifikationscode in diese einzubetten und dann das codierte Signal zum Lesegerät zurück zu streuen.

Die vorliegende Dissertation umfasst multidisziplinäre Forschungsarbeit, die das Design von kostengünstigen, chiplosen RFID-Transponder mit einer neuartigen Frequenzkodierungstechnik umfasst. Im Gegensatz zum aktuellen Stand von Literatur und Technik, berücksichtigt dieser Ansatz die Auswirkungen des Kommunikationskanals und weist jedem Transponder eine eindeutige Frequenzantwort zu. Daher sind die Identifikationscodes unterschiedlich genug, um den Erkennungsfehler zu reduzieren und ihre automatische Erkennung durch das Lesegerät während des Arbeitens unter normalen Bedingungen zu verbessern. Die chiplosen RFID-Transponder werden unter Verwendung verschiedener Materialien und modernster Massenproduktionsfertungsverfahren, wie gedruckter Elektronik, hergestellt. Darüber hinaus werden zwei unterschiedliche Lesegerät-Frontends, die im Ultrabreitband-Frequenzbereich (UWB) arbeiten, zur Abfrage der chiplosen-RFID-Transponder eingesetzt. Der erste ist mit High-Performance-Standardkomponenten nach dem Prinzip des gestuften Frequenzmodulations-Radars (SFM-Radar) gebaut, und der zweite ist ein kommerziell verfügbarer Impulsradio-Radar (IR-Radar).

Schließlich werden die beiden Lesegeräte mit Algorithmen programmiert, die auf den herkömmlichen Techniken der minimalen Entfernung und die maximale Wahrscheinlichkeit-Methode basieren, wobei die gesamte Antwort der Transponder-Radiofrequenz (HF) berücksichtigt wird, statt dem üblichen Ansatz der Fokussierung auf bestimmte Teile des Spektrums (Frequenzspitzen oder abfall) zu folgen. Die

programmierten Lesegeräte identifizieren automatisch einen in ihrer Abfragezone platzierten, chiplosen RFID und führen selbstständig die Erkennung des eingebetteten Identifikationscodes durch. Auf diese Weise wurden die neuartigen beiden vollautomatischen SFM- und IR-RFID-Lesegeräte für chiplose Transponder realisiert. Das SFM-RFID-System ist in der Lage bis zu acht verschiedene chiplose RFID Transponder in einem maximalen Lesebereich von 36 cm sequenziell zu decodieren und das IR-RFID-System ermöglicht die Erkennung von vier sequentiell und zwei gleichzeitig platzierten, verschiedenen chiplosen RFID-Transponder innerhalb eines Bereichs von 50 cm.

## Table of Contents

Acknowledgments.....	I
Abstract.....	III
Kurzfassung .....	V
Table of Contents .....	VII
Index of Figures .....	XI
Index of Tables .....	XVII
Index of Abbreviations .....	XX
Index of Symbols .....	XXIV
<b>1 Introduction.....</b>	<b>1</b>
1.1 Motivation.....	1
1.2 Scope of Application .....	3
1.3 Objectives and Structure.....	8
<b>2 Fundamentals of the RFID Technology.....</b>	<b>10</b>
2.1 Automatic Identification Systems Background .....	10
2.1.1 Barcode Technology.....	11
2.1.2 Optical Character Recognition.....	11
2.1.3 Biometric Procedures .....	12
2.1.4 Smart Cards.....	12
2.1.5 RFID Systems .....	13
2.2 RFID System Principle .....	13
2.2.1 RFID Features .....	14
2.3 RFID with Chipless Transponders .....	16
2.3.1 Time Domain Encoding.....	17
2.3.2 Frequency Domain Encoding .....	24
2.4 Summary .....	31

<b>3</b>	<b>Manufacturing Technologies .....</b>	<b>33</b>
3.1	Organic and Printed Electronics.....	33
3.1.1	Substrates.....	34
3.1.2	Organic Inks.....	35
3.1.3	Screen Printing.....	37
3.1.4	Flexography .....	38
3.2	The Printing Process.....	39
3.3	A Fabrication Alternative with Aluminum or Copper Strips.....	40
3.4	Fabrication Technologies for Chipless RFID Transponders .....	41
3.5	Summary.....	42
<b>4</b>	<b>UWB Chipless RFID Transponder Design.....</b>	<b>43</b>
4.1	Scattering Theory .....	43
4.1.1	Radar Cross-Section Definition .....	44
4.1.2	Radar Absorbing Material's Principle.....	45
4.1.3	Dielectric Multilayers Wave Matrix Analysis .....	47
4.1.4	Frequency Selective Surfaces .....	50
4.2	Double-Dipoles UWB Chipless RFID Transponder .....	52
4.2.1	An Infinite Double-Dipole Array.....	52
4.2.2	Double-Dipoles UWB Chipless Transponder Design.....	55
4.2.3	Prototype Fabrication .....	58
4.3	UWB Chipless RFID Transponder with Concentric Circles .....	60
4.3.1	Concentric Circles UWB Chipless Transponder .....	61
4.3.2	Concentric Rings UWB Chipless RFID Transponder.....	84
4.4	Concentric Octagons UWB Chipless Transponders .....	92
4.4.1	Concentric Octagons UWB Chipless Transponder Design 1 .....	92
4.4.2	Concentric Octagons UWB Chipless Transponder Design 2 .....	98

4.5 Summary .....	101
<b>5 RFID Readers for Chipless Transponders .....</b>	<b>104</b>
5.1 Background .....	104
5.1.1 The Radar Range Equation .....	104
5.1.2 Range Resolution .....	106
5.1.3 Frequency Band Selection .....	107
5.2 Frequency Domain Reader Test System.....	108
5.2.1 Stepped Frequency Waveforms .....	109
5.2.2 Reader Architecture.....	112
5.2.3 Test System Results.....	114
5.3 Time Domain Reader.....	116
5.3.1 Novelda Radar.....	117
5.3.2 Test System Results.....	118
5.4 Summary .....	119
<b>6 Detection of UWB Chipless RFID Transponders .....</b>	<b>120</b>
6.1 Background .....	120
6.2 The Communication Channel .....	122
6.2.1 AWGN Channel Modeling and Detection.....	123
6.2.2 Free-Space Path Loss Modeling and Normalization.....	124
6.3 Detection and Decoding of Chipless RFID Transponders .....	126
6.3.1 Minimum Distance Detector.....	127
6.3.2 Maximum Likelihood Detector.....	128
6.3.3 Correlator Detector.....	128
6.3.4 Test Results.....	129
6.4 Simultaneous Detection of Multiple UWB Chipless Transponders.....	137
6.5 Summary .....	140

<b>7 System Implementation.....</b>	<b>142</b>
7.1 SFM-UWB RFID System with CR-Chipless Transponders.....	143
7.2 IR-UWB RFID System with COD1-Chipless Transponders.....	149
7.3 Summary .....	153
<b>8 Conclusion and Outlook.....</b>	<b>157</b>
<b>References .....</b>	<b>161</b>
<b>Publications .....</b>	<b>170</b>
<b>Appendix A .....</b>	<b>172</b>
RCS Calculation.....	172
Measurement Setups .....	175
<b>Appendix B.....</b>	<b>178</b>
Resistance and Skin Depth Calculation.....	178
<b>Appendix C .....</b>	<b>181</b>
List of Videos.....	181
Test Videos.....	181
Consortium Videos .....	181
<b>Curriculum Vitae.....</b>	<b>182</b>



## Index of Figures

Fig. 1.1: eVACUATE framework overview .....	4
Fig. 1.2: UWB RFID with chipless transponders system overview .....	7
Fig. 2.1: RFID system working principle [11] .....	14
Fig. 2.2: SAW RFID transponder schematic working principle [19] .....	18
Fig. 2.3: Chipless RFID transponder based on high speed time domain delay lines: a) transmission line equivalent circuit and reflection principle, b) photograph of the prototype with size 8.3 cm × 3.1 cm and its measurement setup, taken from [20] .....	20
Fig. 2.4: Geometry of the chipless RFID transponder based on a uniplanar monopole antenna and CPW [21] .....	21
Fig. 2.5: Chipless RFID transponders' backscattered waveform for matched, open and short circuit terminations and CPW length: a) 37.6 mm, b) 41.6 mm, after [21] .....	21
Fig. 2.6: Proposed receiver architecture for CPW chipless RFID transponders [21] .....	22
Fig. 2.7: Chipless RFID transponder based on C-section transmission line: a) geometry, b) coding principle [23] .....	23
Fig. 2.8: Proposed RFID transmitter architecture to read chipless RFID transponders based on C-section transmission line, three pulses with carrier frequencies of $f_1 = 3$ GHz, $f_2 = 4$ GHz and $f_3 = 5$ GHz are generated [23] .....	23
Fig. 2.9: Chipless RFID transponder based on spiral resonators: a) geometry, b) principle of encoding [25] .....	25
Fig. 2.10: Proposed UWB reader architecture to read chipless RFID transponders based on spiral resonators [27] .....	26
Fig. 2.11: Chipless RFID transponder based on open stub resonators: a) geometry, b) measured response, modified from [28] .....	27
Fig. 2.12: Chipless RFID transponder based on RF barcode principle: a) geometry, b) measurement results for codes 11111 and 11010, modified from [29] .....	28
Fig. 2.13: Chipless RFID transponder based on C-section like scatters a) geometry and coding principle, b) simulated  RCS  for codes 11111111111111111111 and 1011111110111111101, modified from [31] .....	29

Fig. 2.14: Chipless RFID transponder based on open conical resonators: a) geometry, b) calculated $ RCS $ from measured scattering parameters [32].....	30
Fig. 2.15: Classification of chipless RFID transponders according to their coding technique and structures.....	31
Fig. 3.1: Screen printing principle .....	37
Fig. 3.2: Flexography principle .....	39
Fig. 4.1: Radar cross-section definition .....	45
Fig. 4.2: One-layer shunt equivalent circuit [50] .....	48
Fig. 4.3: Multilayer shunt circuit [50].....	49
Fig. 4.4: Two-layer power reflection for $T_1 = T_2 = \lambda_0/4$ , $f_0 = 5$ GHz, calculated according to Eq. (4.18).....	50
Fig. 4.5: Typical FSS element geometries [50] [52] .....	51
Fig. 4.6: Geometry of an infinite double-dipole array with different terminal loads composed of two interlaced dipoles [53] .....	53
Fig. 4.7: Calculated power reflection of an infinite double-dipole array with: a) different terminal loads according to Eq. (4.20) and b) equal terminal loads with irregular array spacing according to Eq. (4.21). $R_M = 45 \Omega$ , $X_M = -70 \Omega$ , $f_0 = 5$ GHz, $X = 50 \Omega$ , $R_A = 55 \Omega$ , and $X_A = 1000f/f_0 - 1000 \Omega$ [53] .....	54
Fig. 4.8: Geometry of the dipole-based UWB chipless RFID transponder .....	55
Fig. 4.9: Simulated $ RCS $ of a dipole-based UWB chipless RFID transponder, $l_1 = 35$ mm, $l_2 = 25$ mm, $w = 1$ mm, $d = 5$ mm, $T = 35 \mu m$ , $SubT = 100 \mu m$ .....	57
Fig. 4.10: Simulated $ RCS $ of different dipole-based UWB chipless RFID transponder for the different lengths configurations specified in Table 4.2 [58] .....	58
Fig. 4.11: Photograph of a) an UWB chipless RFID transponder prototype with two aluminum dipoles on bond paper substrate, $w = 1$ mm, $l_1 = 35$ mm, $l_2 = 25$ mm, and $d = 5$ mm b) all four UWB chipless RFID transponders defined in Table 4.2 [58].....	59
Fig. 4.12: Calculated $ RCS $ from measured scattering parameters for the different DD-UWB chipless RFID transponders [58] .....	60
Fig. 4.13: CC-UWB chipless RFID transponder: a) geometry based on three concentric rings and one disk, b) $ RCS $ simulation results for $r = 14$ mm, $g = w = 1$ mm [60].	62

Fig. 4.14: CC-UWB chipless RFID transponders fabricated using: a) screen printing technology on PET, glossy paper and Fasson, b) flexography printing on PET and glossy paper.....	63
Fig. 4.15: Calculated $ RCS $ from measured scattering parameters for a transponders fabricated with: a) screen printing technology on glossy and Fasson papers, as well as PET, and b) flexography printing on glossy paper and PET.....	64
Fig. 4.16: Flexography printed CC-UWB chipless RFID transponders on: a) glossy paper with conductive thin film thicknesses $SG - T_1 = 2.8 \mu m$ , $SG - T_2 = 3.2 \mu m$ and $SG - T_3 = 3.7 \mu m$ , b) PET with conductive thin film thicknesses $SP - T_1 = 3.9 \mu m$ , $SP - T_2 = 4.2 \mu m$ , $SP - T_3 = 6.2 \mu m$ , $SP - T_4 = 6.4 \mu m$ , and $SP - T_5 = 7.5 \mu m$ ...	68
Fig. 4.17: Laser-scanning microscope pictures of two conductive thin film with thickness $T_1$ and $T_5$ printed on PET substrate (Photo by Dr. Georg Schmidt, TUC) .....	68
Fig. 4.18: Calculated $ RCS $ from measured scattering parameters for a CC-UWB chipless RFID transponder fabricated printing silver-ink with different thin film thicknesses on: a) glossy paper $SG - T_1 = 2.8 \mu m$ , $SG - T_2 = 3.2 \mu m$ and $SG - T_3 = 3.7 \mu m$ , b) PET $SP - T_1 = 3.9 \mu m$ , $SP - T_2 = 4.2 \mu m$ , $SP - T_3 = 6.2 \mu m$ , $SP - T_4 = 6.4 \mu m$ , and $SP - T_5 = 7.5 \mu m$ .....	71
Fig. 4.19: Copper-based ink flexography printed CC-UWB chipless RFID transponders on: a) glossy paper with conductive thin film thicknesses $CG - T_1 = 5.4 \mu m$ , $CG - T_2 = 7.7 \mu m$ and $CG - T_3 = 12.2 \mu m$ b) PET with conductive thin film thicknesses $CP - T_1 = 7.5 \mu m$ , $CP - T_2 = 9.7 \mu m$ , $CP - T_3 = 11.7 \mu m$ .....	74
Fig. 4.20: Calculated $ RCS $ from measured scattering parameters for a copper ink-based CC-UWB chipless RFID transponder fabricated with different thin film thicknesses on: a) glossy paper with conductive thin film thicknesses $CG - T_1 = 5.4 \mu m$ , $CG - T_2 = 7.7 \mu m$ and $CG - T_3 = 12.2 \mu m$ b) PET with conductive thin film thicknesses $CP - T_1 = 7.5 \mu m$ , $CP - T_2 = 9.7 \mu m$ , $CP - T_3 = 11.7 \mu m$ .....	76
Fig. 4.21: CC-UWB chipless RFID transponders fabricated using copper and aluminum thin films on: a) bond paper, b) PET [47] .....	78
Fig. 4.22: Calculated $ RCS $ from measured scattering parameters for CC-UWB chipless RFID transponder fabricated with either aluminum or copper thin films on: a) bond paper, b) PET [47].....	79

Fig. 4.23: Multiple sets of CC-UWB chipless RFID transponders: a) placement schematic and sequence, b) simulated $ RCS $ response for different constellations [60] .....	81
Fig. 4.24: CC-UWB chipless RFID transponders fabricated using copper strips on bond paper: a) picture of all five transponders, b) calculated $ RCS $ from measured scattering parameters for different sets [60].....	82
Fig. 4.25: CR-UWB chipless RFID transponder's geometry of a) one array element based on five concentric rings, b) all four arrays of elements .....	84
Fig. 4.26: CR-UWB chipless RFID transponder $ RCS $ simulation results for the different geometries configurations .....	85
Fig. 4.27: Picture of one array element of each eight CC-UWB chipless RFID transponders fabricated using silver ink on PET .....	88
Fig. 4.28: CR-UWB chipless RFID transponders calculated $ RCS $ from measured scattering parameters .....	90
Fig. 4.29: COD1-UWB chipless RFID transponder's a) geometry of one array element with $l_1 = 22.4$ mm, $l_2 = 18.8$ mm, $l_3 = 15.3$ mm, $l_4 = 12.4$ mm, $l_5 = 10.5$ mm, $l_6 = 9.0$ mm, $l_7 = 6.6$ mm, $w_1 = w_2 = w_3 = 22.4$ mm, $w_4 = 0.7$ mm and $w_5 = w_6 = 0.6$ mm, b) $ RCS $ simulation results .....	93
Fig. 4.30: Picture of each eight COD1-UWB chipless RFID transponders identification codes fabricated using a) silver ink on PET b) venues substrates.....	95
Fig. 4.31: COD1-UWB chipless RFID transponder fabricated on the different venues substrates calculated $ RCS $ for identification codes a) 00 b) 01 c) 10 d) 11.....	96
Fig. 4.32: COD2-UWB chipless RFID transponder: a) geometries, b) $ RCS $ simulation results for the two geometries and the combination of two .....	99
Fig. 4.33: COD2- UWB chipless RFID transponder: a) picture, b) calculated $ RCS $ ..	100
Fig. 5.1: Radar system basic principle, Tx: transmit waveform, Rx: receive waveform.....	105
Fig. 5.2: Range resolution: a) concept, b) resolved signals, c) unresolved signals, d) limit.....	106
Fig. 5.3: Obtaining UWB chipless RFID transponder frequency profile from stepped frequency measurements.....	108
Fig. 5.4: UWB RFID reader for chipless transponders: a) basic architecture, b) SF transmit and receive waveforms.....	110

Fig. 5.5: Discrete UWB RFID reader for chipless transponders system architecture..	113
Fig. 5.6: Photograph of the discrete UWB SFM RFID reader for chipless transponders.....	113
Fig. 5.7: UWB SFM reader front-end measurements of chipless RFID transponders based on concentric rings.....	115
Fig. 5.8: UWB chipless RFID transponder with identification code 100: a) five different frequency response measurements with the UWB SFM reader, b) calculated standard deviation.....	116
Fig. 5.9: Time domain reader working principle.....	117
Fig. 5.10: Novelda radar: a) basic architecture [88], b) Gaussian pulse shape .....	118
Fig. 5.11: COD2-UWB chipless RFID transponder calculated $ RCS $ .....	119
Fig. 6.1: CR-UWB chipless RFID identification code 00 measured at different distances of 80 cm, 120 cm, and 180 cm a) received $ S_{21} $ , b) normalized $ S_{21} $ according to Eq. (6.5).....	125
Fig. 6.2: Minimum distance detector architecture.....	127
Fig. 6.3: Maximum likelihood detector architecture .....	128
Fig. 6.4: Correlator detector architecture .....	129
Fig. 6.5: UWB chipless RFID transponder measurements results: a) received $S_{21}$ b) calculated $s_{tx}^m$ .....	130
Fig. 6.6: Calculated time domain received $S_{21}$ for the COD1-UWB chipless RFID transponder on PET substrate.....	135
Fig. 6.7: UWB chipless RFID transponder with same identification code a) multi-detection scenario, b) multi-path channel scenario c) received signal .....	137
Fig. 6.8: Chipless RFID transponders simultaneous multi-detection scenarios: a) A – A, two type A located at 10 and 30 cm from the antennas, b) B – B, two type B located at 10 and 30 cm from the antennas, c) A – B, A located at 10 cm and B at 30 cm from the antennas, d) B – A, B located at 10 cm and A at the 30 cm from the antennas, e) A – A + B, A located at 10 cm and A + B at 30 cm from the antennas, f) A + B – A, A + B located at 10 cm and B at 30 cm from the antennas, (g) A – 2B, A located at 10 cm and 2 B at 30 cm from the antennas, and (h) 2B – A, 2 B located at 10 cm and A at 30 cm from the antennas [76]. .....	138
Fig. 7.1: UWB SFM-RFID reader detection algorithm .....	144

Fig. 7.2: FD RFID system sequence of detection: a) No. 2 – child, b) No. 8 – first responder, c) No. 5 – handicap, d) No. 4 – pregnant woman, e) No. 6 – crew f) No. 1 – adult, g) No. 7 – official, h) No. 3 baby.....	146
Fig. 7.3: UWB IR-RFID reader detection algorithm .....	149
Fig. 7.4: IR-UWB RFID system sequence of detection: a) ONE b) TWO c) THREE, d) FOUR and e) ONE and THREE.....	151
Fig. 7.5: IR-UWB chipless RFID system pilot demonstrations at: a) Anoeta soccer stadium [10], b) Athens international airport (photo courtesy of Vicente Serrulla), c) MSC Meraviglia cruise ship [10], d) Bilbao San Mamés metro station [10] .....	153
Fig. A.1: VNA 37397D with Chengdu antennas measurement setup .....	175
Fig. A.2: VNA MS46122A with Rohde & Schwarz antennas measurement setup .....	176
Fig. A.3: VNA 37397D with Rohde & Schwarz antennas measurement setup.....	176
Fig. A.4: IR radar measurement setup: a) top view, b) rear view .....	177
Fig. B.1: UWB chipless RFID transponder two-point resistance: a) measurement schematic, and equivalent circuit b) straightened strip ring, equivalent circuit.....	179

## Index of Tables

Table 2.1: Comparison of technical features between barcode and RFID technologies [6] [12] [16] .....	16
Table 3.1: Physical properties of substrate materials for chipless RFID transponders [9].....	35
Table 3.2: EKRA X1 SL technical data [43] .....	38
Table 4.1: Free-space wavelength to substrate/dipole thickness relation .....	56
Table 4.2: Double-dipole UWB chipless RFID transponder strips lengths [58].....	57
Table 4.3: Calculated frequency peak magnitudes and dips depths for the different DD-UWB chipless RFID transponders.....	60
Table 4.4: Measured frequency peak and dips positions .....	65
Table 4.5: Calculated frequency peak magnitudes and dips depths for the CC-UWB chipless RFID transponders fabricated on different substrates and printing technologies.....	66
Table 4.6: CC-UWB chipless RFID transponder printed with different silver-ink thin film thicknesses electric parameters (thin film thicknesses provided by Mrs. Katherina Haase, TUC) .....	70
Table 4.7: Calculated frequency peak magnitudes and dips depths for the CC-UWB chipless RFID transponders fabricated on different substrates and thin film thicknesses.....	72
Table 4.8: Copper-ink printed CC-UWB chipless RFID transponder electric parameters (thin film thicknesses provided by Mrs. Katherina Haase, TUC) .....	75
Table 4.9: Calculated frequency peak magnitudes and dips depths for the CC-UWB chipless RFID transponders fabricated on different substrates printing copper-based conductive thin film with different thicknesses .....	77
Table 4.10: Calculated frequency peak magnitudes and dips depths for the CC-UWB chipless RFID transponders fabricated with aluminum or copper thin films on different substrates .....	80
Table 4.11: Calculated frequency peak magnitudes and dips depths for the CC-UWB chipless RFID transponders constellations .....	83

Table 4.12: CR-UWB chipless RFID transponders frequency response characteristics .....	86
Table 4.13: CC-UWB chipless RFID transponders different physical dimensions .....	87
Table 4.14: Silver-ink printed CR-UWB chipless RFID transponder electric parameters (thin film thicknesses and resistance values provided by Mrs. Katherina Haase and Dr. Georg Schmidt, TUC).....	89
Table 4.15: Calculated frequency peak magnitudes and dip depths for the CR-UWB chipless RFID transponders .....	91
Table 4.16: Calculated frequency peak magnitudes and dips depths for the COD1-UWB chipless RFID transponders fabricated on the different venues' substrates .....	97
Table 4.17: Calculated frequency peak magnitudes and dips depths for the two COD2-UWB chipless RFID transponders .....	101
Table 4.18: Calculated frequency peak magnitudes and dips depths for the different UWB chipless RFID transponders .....	102
Table 5.1: Amplitude and phase response of the UWB chipless RFID transponder, obtained at each frequency step.....	109
Table 6.1: Minimum distance detector results for different UWB chipless RFID transponders based on double-dipoles, according to Eq. (6.12).....	131
Table 6.2: Minimum distance detector results for different UWB chipless RFID transponders based on double-dipoles and different measurement parameters, according to Eq. (6.12).....	132
Table 6.3: Minimum distance detector results for different UWB chipless RFID transponders based on concentric rings, according to Eq. (6.12).....	133
Table 6.4: Minimum distance detector results for UWB chipless RFID transponders based on concentric rings and different measurement parameters, according to Eq. (6.12) ..	134
Table 6.5: Minimum distance detector results for UWB chipless RFID transponders based on concentric rings and different measurement parameters, according to Eq. (6.12) ..	134
Table 6.6: Maximum likelihood detector results for UWB chipless RFID transponders based on COD1 on different substrates, according to (6.14) .....	136
Table 6.7: Correlation detector results for different scenarios, *partial results of scenarios A – AB and AB + A, according to Eq. (6.15) [76].....	139
Table 6.8: Calculated received pulse energy, according to Eq. (6.16) [76].....	140



Table 7.1: Identification codes assigned numbers and images .....	145
Table 7.2: SFM-UWB system detector results.....	147
Table 7.3: Identification codes assigned numbers and images .....	150
Table 7.4: IR-Reader detector results [82].....	152
Table 7.5: RFID systems with chipless transponders comparison.....	154

## Index of Abbreviations

1D	One dimensional
2D	Two dimensional
3D	Three dimensional
ADC	Analog-to-digital converter
ASK	Amplitude-shift keying
ASIC	Application Specified Integrated Circuit
AWGN	Additive white Gaussian noise
CA	Circuit analog
CC	Concentric-circles
CG	Copper-ink on Glossy paper
CMOS	Complementary metal-oxide-semiconductor
CP	Copper-ink on PET
CPW	Co-planar waveguide
CR	Concentric-rings
CST	Computer systems technology
DAC	Digital-to-analog converter
DC	Direct-current
DD	Double-dipoles
EEPROM	Electrically erasable programmable read-only memory
FDX	Full duplex
FPGA	Field programmable gate array
FSS	Frequency selective surface
HDX	Half duplex
HF	High frequency
IC	Integrated circuit
IR	Impulse radio
ISM	Industrial, scientific, and medical
LAN	Local area network
LF	Low-frequency
LNA	Low-noise amplifier

LO	Local oscillator
LOS	Line-of-sight
LPF	Low-pass filter
ML	Maximum likelihood
MW	Microwave
OCR	Optical character recognition
OOK	On-off keying
PC	Personal computer
PCB	Printed circuit board
PET	Polyethylene terephthalate
PNA	Programmable network analyzer
PPM	Pulse-position modulation
PSK	Phase-shift keying
QR	Quick response
RADAR	Radio detection and ranging
RAM	Radar absorbing material
RCS	Radar cross-section
RCSR	Radar cross-section reduction
RF	Radio frequency
RFID	Radio frequency identification
RAM	Random access memory
ROM	Read-only memory
RS-232	Recommended standard 232
SAW	Surface acoustic wave
SEQ	Sequential
SG	Silver-ink on Glossy paper
SOFIA	Smart objects for intelligent applications
SP	Silver-ink on PET
SFM	Stepped frequency modulation
ToA	Time-of-arrival
UHF	Ultra-high frequency
USB	Universal serial bus

UWB	Ultra-wideband
VNA	Vector network analyzer
VCO	Voltage-controlled oscillator
WLAN	Wireless local area network



## Index of Symbols

$d$	Distance between two resonators
$D$	Distance between two-unit arrays of chipless RFID transponders
$\delta$	Skin depth
$E$	Electric Field
$\varepsilon$	Permittivity
$\varepsilon_r$	Relative permittivity
$\varepsilon_0$	Free space permittivity
$\varepsilon_{eff}$	Effective dielectric constant
$\zeta_{rx}$	Signal received energy
$f$	Frequency
$g$	Gap
$\kappa$	Conductivity
$k$	Waveform number
$k_0$	Free space waveform number
$l$	Length
$\lambda$	Wavelength
$\lambda_0$	Free space wavelength
$\eta$	Normalized impedance
$n$	Refraction index
$r$	Radius
$R$	Resistance
$\Gamma$	Reflection coefficient
$s_{rx}$	Received signal
$s_{tx}$	Transmitted signal
$S$	Scattering parameter
$t$	Time
$T$	Thickness
$\tau$	Pulse duration

$\tau_d$	Time delay
$\mu$	Permeability
$\mu_r$	Relative permeability
$\mu_0$	Free space permeability
$\bar{\mu}$	Mean
$\sigma$	Standard deviation
$\emptyset$	Angle between incident and scattered field
$\theta$	Angle
$w$	Width
$\omega$	Angular frequency
$x$	Separation distance
$X$	Reactance
$Y$	Admittance
$Z$	Intrinsic impedance
$Z_0$	Free space impedance







# 1 Introduction

## 1.1 Motivation

The progress of the fundamental understanding of the electromagnetic theory during the XIX century performed mainly by Michael Faraday and James Clerk Maxwell, as well as the first transmission and reception of radio waves, credited to Heinrich Rudolph Hertz in 1887 [1]. Marked the evolution of wireless communication systems, opening a gate for a wide range of applications including but not limited to radio, television, personal communications, radar, and identification systems. Especially the radar technology contributed to the modern identification systems by means of electromagnetic waves. The radar was developed mainly for military purposes during World War II, aiming the detection and location of an object using the reflected radio waves, it also first included a transponder to distinguish between friends or foes.

In 1948, Harry Stockman published his work on “Communication by Means of Reflected Power”, where he proposed the used of radio, light, or sound waves for the transmission and mentioned variable damping modulation, position modulation, and polarization modulation between others, as ways the reflector may perform the modulation [2]. Nevertheless, the development of the electronic components like the integrated circuits (IC), microprocessors, and especially the personal computer (PC) were still needed to make feasible a realization of the identification systems on a commercial level. And it was not until the 1980s with the help of all these developments that the radio frequency identification (RFID) system starts its technological breakthrough with implementations in areas like public transportation, personnel access, animal tagging, industrial and business [1].

Nowadays, RFID systems have become an integral part of our daily lives, increasing productivity by reducing waiting times in a wide variety of applications: tracking of products from the supplier premises to the point of sale throughout the logistics and supply chain process, buildings access control to prevent unauthorized access for security purposes, or the monitoring and tracking of patients information and history in the healthcare branch between others [1], [3], [4]. IDTechEx Research has

analyzed the RFID market for the last 18 years and reported a total RFID market's worth of US\$ 11.2 billion in 2017, for both hardware and software, and expecting it to growth to US\$ 14.9 billion by 2022. Nevertheless, it also mentions that in the specific case of apparel tagging in retails, where RFID has the greatest market penetration above other applications by volume, it still barely reached only 20% of the addressable market in 2017, which means there are still huge market opportunities for the RFID technology [5].

The fabrication cost of the RFID transponder is often referred as the main impediment to overtake this growing market of item-level tagging and compete against other widespread automatic identification technologies such as barcodes or smart cards [6] [7]. Currently, searching through authorized distributors of electronic components' websites, a standard ultra-high frequency (UHF) RFID transponder can be found for no less than approximately US \$0.10 (for example [8]). Therefore, a further price reduction to achieve a transponder price below US \$0.01 is desired in order to gain additional market penetration [6] [9].

In the past decades, developments on the solid-state electronics manufacturing procedures have led toward miniaturization, concentration of functionalities and price reduction of the ICs, which are used to fabricate the RFID transponders. However, the ICs require an external energy source and it is not possible to connect all of them to the power grid or attach them batteries that last for a lifetime to guarantee their proper and interrupted functionality. Moreover, the production of billions of such enduring devices that last beyond their host object, represents a considerable environmental impact and the development of an ecofriendly solution and energetically autonomous becomes evident. For that reason, in the last decades research has been focused on the development of new technologies beyond conventional semiconductors, introducing new concepts and materials like organic printed electronics, where low cost, easily producible in large areas and ecofriendly materials are being investigated e.g. paper, bioplastics, Polyethylene terephthalate (PET) to produce electronic devices [9].

Organic printed electronics on flexible substrates, is a promising technology to mass produce RFID transponders without ICs and reduce furthermore the manufacturing costs. The RFID transponders are environmental friendlier than ICs and fabricated by printing metallic inks on flexible substrates like paper or PET.

This thesis presents for the first time, two ultra-wideband (UWB) RFID systems with chipless transponders for low-cost short-range tagging applications ( $< 50$  cm). The two systems are composed by two different sets of UWB chipless RFID transponders manufactured with organic materials on flexible substrates by printed electronics. And two different and fully automatic UWB RFID readers used to interrogate each set in either the time- or frequency-domain respectively. The UWB chipless RFID transponders are encoded using a novel differential frequency coding technique that together with the implementation of conventional detection techniques, the UWB chipless RFID transponders identification codes can be successfully recognized, after being placed in the system's interrogation zone.

Despite the act of determining the identification of people without or against their own will is a complicated ethical problem and must be discussed on a social scale. Engineers must perceive their responsibility in this discussion. I hereby express my wish that this work shall not be used in systems aiming at localizing and identifying people without their explicit consent.

## 1.2 Scope of Application

This research was conducted in the scope of the European integration project with title "*A holistic, scenario-independent, situation-awareness and guidance system for sustaining the Active Evacuation Route for large crowds*", with acronym eVACUATE. The goal of the eVACUATE project is the development of an evacuation assistance tool for mass gathering venues (e.g. soccer stadiums, metro stations, airports, cruise ships, etc.), that fuses the information coming from different sensor technologies, and in case of an emergency, provides to the crisis managers and first responders with a total situation-awareness of the crowds' behavior. If The crisis managers deem necessary to trigger the evacuation procedure, the evacuation tool provides the crowd by mean of its different sensors with the optimal evacuation routes to leave the premises in a timely and safely manner [10].

The eVACUATE framework overview diagram can be seen in Fig. 1.1, it is mainly composed of four key elements: smart spaces, crowd models, simulation tools, and the decision center. The Smart spaces are implemented including different types of sensors and cameras, they feed the system with enough information to assess the venue's

infrastructure condition and analyze the crowd behavior using the crowd models. If a triggering event is detected, like an abnormal crowd behavior or a physical event that compromises the venue's or people's integrity, the system sends an alarm to the crisis managers located at the decision center. The crisis managers evaluate the situation and decide whether an evacuation procedure must be triggered or not, if they decide to do so, the system assess with the help of the simulation tool, the most optimal evacuation routes to timely guide the crowd safely out of danger, avoiding possible crowd congestion scenarios [10].

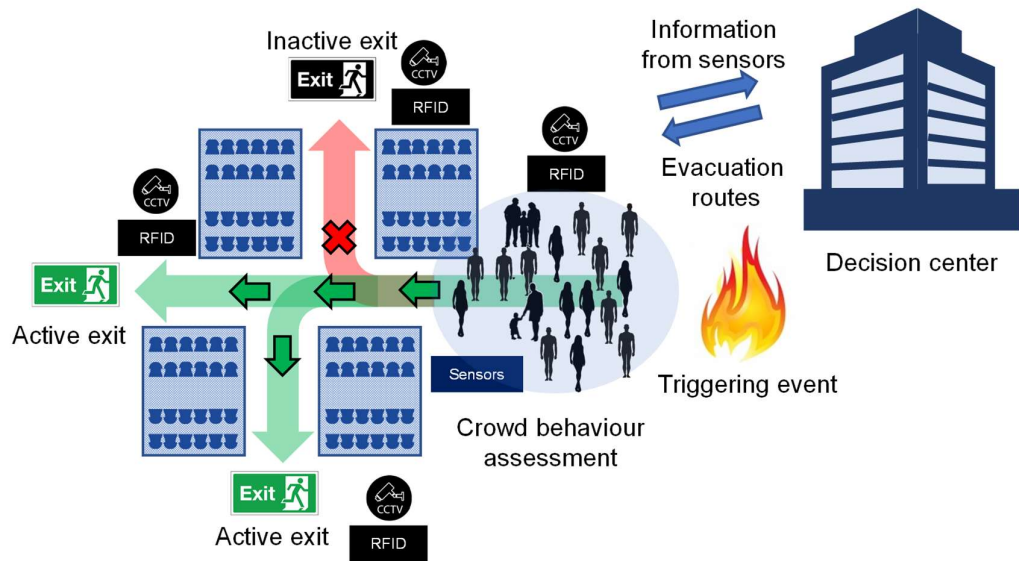


Fig. 1.1: eVACUATE framework overview

For the realization of the project, several partners were involved in the development of different technologies and tasks. The tasks and technologies per project partner are briefly described in the following list [10]:

- *EXODUS S.A., Greece*, overall project management
- *University of Southampton, IT Innovation Centre, Great Britain*, lead the crowd behavior detection and recognition in crisis situations models, study of crowd psychology and typology of behaviors, develop and implement crowd behavior recognition tools
- *Institute of Communications and Computer Systems, Greece*, lead the communication and adaptive interfaces implementation, carry out the system communications and network architectures deployment

- *HKV, The Netherlands*, lead the definitions of evacuation scenarios and user/system requirements, as well as the evaluation of the system demonstrations
- *Telesto Technologies, Greece*, develop and implement the wireless sensor networks, mobile application, and positioning system for people location assessments
- *TEKNIKER-Ik4, Spain*, lead the smart spaces implementation, process the data to generate comprehensive information, and develop the exit signs
- *Athens International Airport, Greece*, provide expertise regarding the security and evacuation issues at airport facilities, and the use of its premises for the project system validation
- *Vitrociset, Italy*, lead the decision making and optimal evacuation strategy, as well as the dissemination and exploitation activities. Set the decision rules according to the specific scenarios at the different venues and the information coming from the smart devices
- *Crowd Dynamics International, Great Britain*, model and simulate the crowd behavior, determine the optimum evacuation routes for the different venues and evacuation scenarios
- *INDRA, Spain*, lead the framework design and system integration, adapt the smart objects for intelligent applications (SOFIA) interoperability platform to eVACUATE and manage the database
- *Katholieke Universiteit Leuven, Belgium*, formulate the legal requirements for eVACUATE
- *DIGINEXT, France*, develop the three dimensional (3D) interactive common operational picture system and iterative simulation of evacuation scenarios
- *Politecnico Di Torino – Department of Mathematics, Italy*, identify real-time crowd modelling techniques of crowd behavior
- *STX France S.A., France*, provide expertise regarding the security and evacuation issues at cruise ship facilities, and the use of cruise ships for the project system validation
- *Technische Universität Dresden, Germany*, designs the chipless RFID transponder's architecture. Conducts performance tests, reader

development/programming and overall RFID system integration to the framework

- *Technische Universität Chemnitz, Germany*, manufacturing of the printed RFID transponders and development of roll-to-roll printing technology
- *Real Sociedad de Fútbol S.A.D., Spain*, provide expertise regarding the security and evacuation issues at professional sport arenas, and the use of Anoeta soccer stadium for the project system validation
- *Metro Bilbao S.A., Spain*, provide expertise regarding the security and evacuation issues at underground transportation facilities, and the use case of the Metro Bilbao stations for the project system validation
- *Telecom Italia, Italy*, provide the necessary expertise/support for the implementation of the resilient communications and adaptive interfaces, system demonstrations, ethics, and mobile positioning

In the case an evacuation procedure is started, it becomes imperative to guarantee that all the endangered persons leave safely the facilities. To do so, the system must keep track and count of all the people located inside the premises by all available technological means. Moreover, it shall be able to subtract the number of persons leaving through the evacuation routes from the total count and calculate whether people are still left behind or not. Thus, an RFID system becomes a feasible solution to perform this specific task. However, the venues where the system shall be implemented, are mass gathering places, most of them with high traffic and continuous dynamic movement of people, entering and leaving confined rooms, staying only for a short period of time. Therefore, the implementation of a conventional RFID system could become very costly, infrastructure and logistic demanding, and the need to exploit the deployment of a low-cost RFID system with chipless transponders becomes evident, with the capability to be integrated, at no major cost, in the already existing venue's respective access tickets or cards systems [10].

The proposed RFID system with chipless transponders, foresees the use of roll-to-roll printing technology to fully integrate the chipless RFID transponders on paper or foil, allowing its implementation on the already existing venue's ticketing system, and the counting of people passing through predefined checkpoints (emergency exits), as shown in Fig. 1.1.

Fig. 1.2 shows the RFID system with chipless transponders overview, it consists of three major components:

1. Chipless RFID transponders, which are printed on the venue's tickets to be identified.
2. RFID reader, that sends the RF signal to interrogate the chipless RFID transponder and retrieve its stored identifying information.
3. Data processing subsystem associates the chipless RFID transponder stored data with arbitrary records, namely the name or picture of object to be identified and keeps count of the amount of tickets passing through the checkpoints.

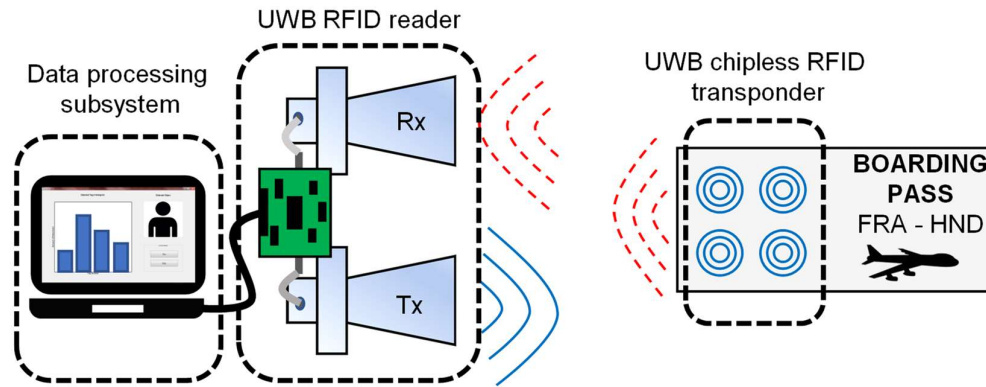


Fig. 1.2: UWB RFID with chipless transponders system overview

The RFID system with chipless transponders can be integrated to the eVACUATE framework either by means of a local area network (LAN) or a wireless local area network (WLAN).

A set of specifications has been defined for the operation of the RFID system with chipless transponders:

1. *Number of bits*: represents the quantity of items that can be distinguished, the aim is to be able to code at least 3 bits, which means a minimum of 8 different objects can be recognized.
2. *Coverage range*: determines the maximum distance at which the UWB chipless RFID transponders can be detected, a value of at least 1-meter range is specified as a target.
3. *Power consumption*: the necessary electrical energy over time to operate the chipless RFID transponder is set to zero.



4. *Lifetime*: the duration of the chipless RFID transponder before its complete degradation has to be greater than 3 months.
5. *Cost*: the chipless RFID transponder fabrication cost with roll-to-roll printing technology should round the 1 Eurocent per 30 cm<sup>2</sup>.
6. *Simultaneous detection*: the RFID system should be capable to simultaneous detect at least two chipless transponders.
7. *License free operation*: to allow the implementation in any part of the world, the RFID system must operate in an international reserved frequency band.

### 1.3 Objectives and Structure

This work presents a structured approach for the design of an UWB RFID system with chipless transponders. The UWB chipless RFID transponders are designed to perform the coding by means of their frequency response. Two types of reader architectures based on the stepped frequency modulation (SFM) and impulse radio (IR) radar principles, are studied to perform the chipless RFID transponders detection. This dissertation is organized as follows:

Chapter 2 discusses the fundamentals of RFID systems. A brief overview of several automatic identification system with special emphasis on the barcode technology and RFID is presented. Followed by the introduction to the RFID working principles, features and development challenges that has led to current research focusing on the low-cost approach with chipless RFID transponders. A classification of chipless RFID transponders according to their coding techniques and type of structures is provided along with some typical geometries.

Chapter 3 introduces the manufacturing technologies used to fabricate the chipless RFID transponders presented in this work. The working principle of the different printing electronics with metallic inks technologies are explained, to understand the influence of the fabrication process in the frequency response performance of the chipless RFID transponders, and the major challenges the printing technology still faces. Additionally, an alternative fabrication process is described, for fast prototyping with metals that cannot currently be synthesized into metallic inks.

Chapter 4 describes the design of chipless RFID transponders based on different scattering geometries placed on flexible substrates, and their novel differential frequency

coding technique. It also presents the results of the investigations concerning the influence of main manufacturing parameters like type of substrate, metallic-ink, and fabrication process on the chipless RFID transponder radio frequency (RF) performance. Five different transponders based on three different patterns (double-dipoles, concentric-circles or octagons) are designed and fabricated using different technologies to obtain distinct frequency responses and conduct several studies on detection techniques.

Chapter 5 illustrates the two RFID readers front-ends architectures used to retrieve the responses of the chipless RFID transponders designed in chapter 4, and their working principles based on SFM and IR are explained. The first one is fabricated using high performance off-the-shelf components and the second one, an already commercially available pulse radar front-end, they are used to interrogate the chipless RFID transponders in the frequency and time domain respectively.

Chapter 6 presents the three different detection rules used to retrieve the identification codes of four chipless RFID transponders designs presented in chapter 4. The detection rules are based on the implementation of minimum distance, maximum likelihood or simple correlation detectors. The chipless RFID transponders are placed at different distances and measured with different parameters to analyze the performance of the detectors. Additionally, the importance of a robust coding technique capable to be detected by a computing system is highlighted.

In chapter 7, the results of the detection algorithms implementation on the RFID readers front-ends to interrogate the chipless RFID transponders and build fully automatic systems are presented. Including the deployment of the IR based system to perform real case-test scenario evacuation procedures on each of the different venues described previously. This investigative work is concluded in chapter 8, highlighting the main achievements and findings, as well as outlining further areas of research to improve the current system.

## **2 Fundamentals of the RFID Technology**

This chapter provides an overview of different automatic identification systems with special emphasis on the barcode and RFID technologies. The classical RFID working principle and features based on the interaction between transponder and reader are described. The novel concept of RFID with chipless transponders is introduced as a low-cost alternative to compete against the well-established barcode technology. RFID systems with chipless transponders are based on metallic structures placed on a substrate and have the capability to modify the received signal and retransmit or backscatter it to the reader.

Chipless RFID transponders follow the basic principles of conventional microwave circuits and antennas design and are built on these foundations to achieve the coding in the time or frequency domains. A brief overview of some typical structures employed is given, their basic working and encoding principles, as well as their implementation are discussed.

### **2.1 Automatic Identification Systems Background**

Automatic identification systems (Auto-ID) have become an attractive solution in a wide range of customer-oriented industries, logistics and supply chain management, fabrication and processing of products from raw materials. The Auto-ID aim is to provide information about people, animals, assets and products being processed [11].

The widely used barcode labels started the revolution in automatic identification systems in the 1980s, however nowadays are being found insufficient for an increasing number of applications. Barcodes are very cheap, but they reading distance is limited to a few centimeters, require direct line-of-sight (LOS) to be read and they can't be reprogrammed [11].

The use of ICs to store the data would be the technical optimal solution to overcome the barcode disadvantages. The smart card is the most used type of electronic data-carrying appliance (bank cards, library cards, personal identification cards, etc.), it is based on a contact field that requires mechanical contact with the reader, which also

makes it often quite impractical. Therefore, the need to implement a contactless system to transfer data between the data-carrying device and its reader becomes obvious, and in an ideal case, the power needed to operate the electronic data-carrying device should also be transferred from the reader using contactless technology. The Auto-ID system that uses radio waves to contactless transfer power and data is the RFID system [11].

The following subsections provide a brief introduction to different Auto-ID systems.

### 2.1.1 Barcode Technology

The barcode is a binary representation of data and is the most used technology for identification of products, with billions of daily scans all over the world. There are two main types of barcodes currently being used: one-dimensional (1D) and the two-dimensional (2D) barcode. The 1D barcode is the most popular and it consists of a set of bars and gaps arranged in a parallel configuration. The data representation takes place by varying the widths and spacing between bars according to a predeterminate pattern. The barcode is read by optical laser scanning, e.g. by calculating the difference in the reflection of a laser beam from black bars and white gaps, the European article number EAN-13, which is the most used standard, encodes 13 digits. The 2D barcode on the other hand, such as the quick response (QR) codes, encodes the data in both horizontal and vertical dimensions increasing the capacity, the model 2 with  $177 \times 177$  modules can store up to 7,089 digits, it has recently been gaining more market, especially due to the advancement of the smartphone technology, where the barcodes can be capture by the device's integrated camera and the message extracted using a mobile application [11] [12] [13] [14].

### 2.1.2 Optical Character Recognition

The optical character recognition system (OCR) was first used by companies in the 1960s. Its aim was to convert printed text to machine-encoded text, therefore, special fonts with stylized characters were developed in a way that they could be read both by

the human eye as well as automatically by the OCR reader. Allowing to have high density information and in case of an emergency, be able to read the data visually [11].

Although OCR system failed to become universally applicable due to the development of its complicated reader, which at the time increased its price when compare to other Auto-ID products [11]. Nowadays, as the processing capabilities of mobile/wearable devices increases and are being equipped with high resolution cameras and microprocessors, the OCR has become feasible, attractive and ubiquitously available using sources like scanned documents, digital photographs, business cards, etc. to obtain information [15].

### **2.1.3 Biometric Procedures**

The biometric procedures involve measuring of physical characteristics of living beings, that is, identifying people by comparing unmistakable its individual characteristics like fingerprints, voice, retina or iris [11].

### **2.1.4 Smart Cards**

A smart card is a system where the data is stored electronically, in some cases with additional processing capacity like a microprocessor card. It comes in a plastic card of the same size as a credit card (85.60 mm × 53.98 mm). The smart card is read by placing it in the reader, where the card's contact springs make a galvanic connection with the respective set in the reader. The data transfer takes place using a bi-directional serial interface. Two different type of cards could be found: the memory card and the microprocessor one [11].

The information in the memory card is accessed using a state machine, they can be cost effective for some type of applications and that is why they are predominantly used in price sensitive, large-scale applications [11].

The microprocessor cards contain a microprocessor connected to a segmented memory: read-only memory (ROM), random access memory (RAM) and electrically erasable programmable read-only memory (EEPROM). The ROM and its content are inserted during the manufacturing of the integrated circuit. The EEPROM contains the

application data, the operation system allows the reading or writing of data to this memory [11], and the RAM is the microprocessors temporary working memory. The data stored in the RAM is lost after the smart card is disconnected from its supply voltage [11].

Microprocessor cards are mainly being used in security sensitive applications like banking e.g. EC-cards (electronic cash) [11].

### 2.1.5 RFID Systems

The RFID systems stored the data in an electronic data-carrying device, namely the transponder. The power supply as well as the data transfer between transponder and reader is achieved by means of electromagnetic fields. Due to the advantages of the RFID systems compared to other Auto-ID systems, RFID Systems are currently being developed to overcome new mass markets like item level tagging. The working principle taken from the fields of radio and radar engineering, will be explained further in the next section [11].

## 2.2 RFID System Principle

The RFID system is composed of three major elements [11], as shown in Fig. 2.1:

1. RFID transponder, which is placed on the object to be identified.
2. The interrogator or reader, which, depending upon the design or the technology used, may be a read/write device.
3. Data processing subsystem associates the transponder stored data with arbitrary records of object to be identified.

The reader typically consists of a radio front-end to generate and receive radio signals, a control unit and an antenna. Additionally, the reader is equipped with other standard interfaces to send and receive data to another system like a PC, e.g. universal serial bus (USB), recommended standard 232 (RS-232), etc. [11].

The RFID transponder, which is the actual data-carrying device of an RFID system, normally consists of a coupling element and an electronic application specified integrated circuit (ASIC). The RFID transponder is usually a passive device and is only activated whenever it is placed within the reader's interrogation zone. The energy necessary to operate the transponder is supplied through the antenna unit, in the same way, the timing

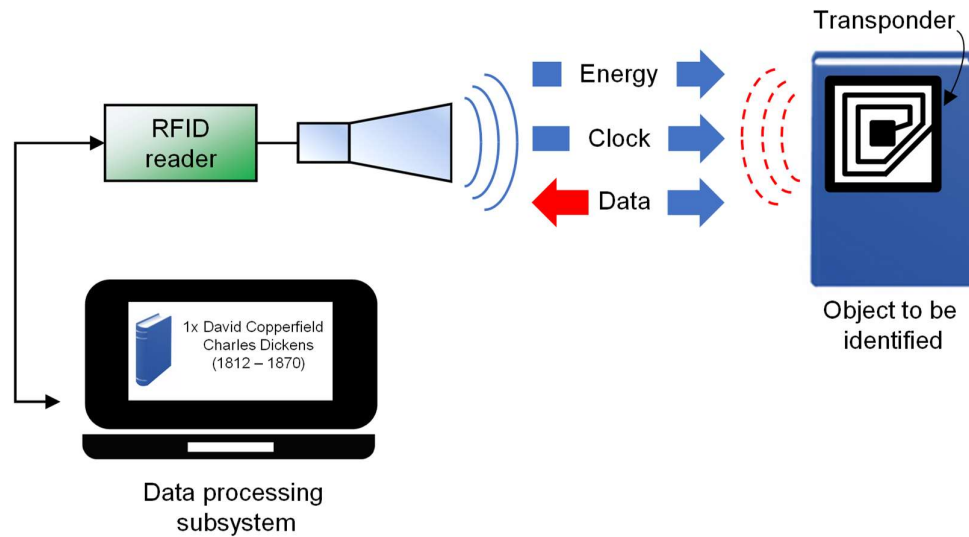


Fig. 2.1: RFID system working principle [11]

pulse (if necessary) as well as the data is transferred through this mean [11]. To transfer the data, the transponder sends or backscatters an electromagnetic EM wave to the reader.

### 2.2.1 RFID Features

RFID system are available in different variants and fabricated by probably equal number of manufacturers. A technical comparison between two different RFID systems may include features like [11]:

1. Operating frequency range, it's an important feature and is the frequency at which the reader and transponder transmit, which also has an influence on the reading distance of the system. Commercially available RFID systems can be found operating at a wide range of frequencies, ranging from 135 kHz longwave to 5.8 GHz in the microwave range.
2. Reader-transponder's communication type is the way transponder and reader communicate to each other, the signal received at the reader from the transponder could be very weak compared to the signal sent by the reader, therefore, an appropriate communication procedure must be employed to be able to differentiate one signal from the other. Two different transmission procedures can be implemented:

- a. Full duplex (FDX)/ half duplex (HDX) systems, is a point to point communication procedure, in an FDX system, both devices communicate with each other simultaneously, and in a HDX system, both devices communicate with each other in one direction at a time.
  - b. Sequential (SEQ) systems, in this procedure, the power of the reader is switched off at specific intervals of time, which are recognized by the transponder and used to send its data to the reader.
3. Frequency response is the frequency range used by the RFID transponder to send its response, it could be the same as the reader, a frequency ratio of 1:1, or the use of subharmonics with a frequency ratio of 1: n-fold.
4. RFID transponder's power supply is one important feature of RFID systems. Active RFID transponders incorporate a battery, that supplies all of part of the power needed for the operation of the microchip. Passive RFID transponders on the other hand, acquire its power for operation from the transmitted signal energy of the reader.
5. The operation principle of the data carrier: with IC or not
6. The type of processing used: state machine or microprocessor
7. Programmable RFID transponder is the possibility for the reader to write data to the RFID transponder.
8. RFID transponder storage capacity is the measure of the amount of data an RFID transponder may contain, it could range from one bit to several kilobytes.
9. Data transmission from the RFID transponder to the reader, is the procedure how the RFID transponder sends data to the reader:
  - a. The RFID transponder sends a reflection or backscatter signal to the reader.
  - b. The RFID transponder modulates the received signal from the reader with a load modulator.
  - c. The RFID transponder sends its information using radio waves of a different frequency range that the one used by the reader.

RFID international standards are used to facilitate the different manufactures to fabricate interoperable products with same characteristics, and therefore the RFID transponder design is driven by these specifications defined according to the frequency



of operation. Passive RFID transponders operating in the low-frequency (LF) of 125, 134 – 135 kHz or high-frequency (HF) of 13.56 MHz bands, are powered by the magnetic field of the reader, include an IC which could also be programmed, and are used for applications with typical distances no greater than 15 cm or 1.5 m respectively. The LF and HF wavelengths are much larger than the reader or RFID transponder antennas (greater than 2200 m and 22 m respectively), therefore the data transfer must take place by magnetic coupling between the reader and transponders coils. RFID transponders operating in the ultra-high (UHF) and microwave (MW) can be either passive or active, their wavelengths are shorter than 35 cm and for that reason, they are based on electric field coupling. Passive RFID transponders could reach a reading range of up to 10 m and active ones even larger distances [6] [16].

Now that the main features of the barcode and RFID technologies have been introduced, a comparison between their main technical capabilities can be done and it is shown in Table 2.1 [6] [12] [16].

Feature	Barcode	RFID
LOS required	Yes	No
Simultaneous reading	No	Yes
Requires human operation	Yes	No
Rewritable	No	Yes
Storage capacity	EAN-13: 13 digits QR: up to 7,089 digits	Typically, 2 KB
Power consumption	Reader	Reader and transponder
Environmentally friendly	Yes	No
Durability	Low	High

Table 2.1: Comparison of technical features between barcode and RFID technologies [6] [12] [16]

### 2.3 RFID with Chipless Transponders

In the previous sections, the technical aspects of different Auto-ID systems have been discussed, with special emphasis on the barcode and RFID technologies. Although both systems provide advantages and disadvantages, as explained before, efforts are being made to develop an RFID system for barcode replacement on an item-level tagging [7].

The main limitation to achieve this goal is the RFID transponder price, most of up to date RFID systems typically required a complementary metal-oxide-semiconductor (CMOS) chip in addition to an antenna, which significantly increases their price compared to the barcode. Therefore, further works are being conducted to achieve a meaningful reduction in the RFID transponder fabrication cost, one of them investigates the implementation of a solution in which the RFID transponder does not require an IC chip, or in other terms, an RFID system with chipless transponders [9].

The RFID system with chipless transponders offers a promising solution for price reduction, conserving important features from the classical RFID (e.g. multi-reading, no direct LOS, no human operation, etc.) while adopting others from the barcode technology (e.g. environmental friendlier, cost). The chipless RFID transponders are passive devices based on electric circuits that when placed in their reader interrogation zone, re-transmit or backscatters a modulated version of the received electromagnetic wave. Therefore, in RFID Systems with chipless transponders, one of the main challenges is to generate a modulation technique or coding principle based on the chipless transponder frequency signature, that allows to send the information and be unequivocally decoded by the reader [7] [9].

Several coding techniques mostly developed from the chipless transponder's perspective have been proposed in literature with different types of structures and ways in which the information is transmitted. Two main classifications can be found: time and frequency domain encoding, and they will be discussed briefly in the following subsection. Other coding techniques, which are a combination of these two can also be found in literature [17].

### **2.3.1 Time Domain Encoding**

The time domain encoding basically consist in assigning specific re-transmission delays to each different chipless RFID transponder's received signal, which theoretically allows the reader to determinate which code has been sent by performing a pulse time-of-arrival (ToA) analysis. Two main types of structures working principle can be found: surface-acoustic-waves (SAW), and delay lines.

### 2.3.1.1 Surface Acoustic Waves Chipless RFID Transponders

White and Voltmer first described the principle of surface-acoustic-wave (SAW) transduction by means of direct piezoelectric coupling in 1965. They fabricated their sample by depositing aluminum on a quartz substrate and then pattern it by means of photolithography [18]. Since then, there has been continuous development on the fabrication processes for mass production and on the applications of SAW devices, being RFID with chipless transponders one of those. Nowadays, commercially available SAW RFID transponders can be found working on the industrial scientific medical (ISM) frequency band at 2.4 GHz [19].

The principle of operation of a SAW RFID transponder is shown schematically in Fig. 2.2, it is based on piezoelectricity, the electromechanical interaction between the electrical and mechanical state in a material. In certain dielectric crystals, the application of a mechanical force generates an electrical charge, and the opposite, a mechanical strain due to the application of an electric field [19].

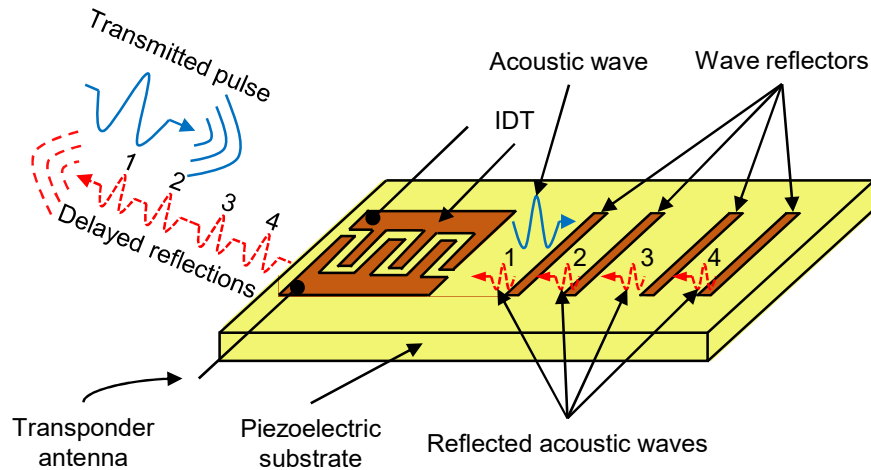


Fig. 2.2: SAW RFID transponder schematic working principle [19]

In Fig. 2.2, the RFID transponder antenna receives the pulse transmitted by the reader, the interdigital transducer (IDT) performs the transduction between the electrical signal and the acoustic mechanical wave, which then propagates across the surface of the substrate. The generated SAW is then partially reflected and transmitted by each of the reflectors placed at specific distances on the substrate. Each of the reflectors reflected SAW returns to the IDT with a delay proportional to its distance to the IDT, are

transduced to radio waves and send back through the antenna to the reader to perform the recognition of the transmitted identification code [19].

The SAW encoding method is achieved considering the time delays of the reflected SAW pulses, an amplitude-shift keying (ASK) is implemented by dividing the time into specific slots, a binary 1 is represented by a pulse being received in the given timeslot and a binary 0 otherwise. A phase-shift keying (PSK) coding technique could also be realized by designing the reflectors as phase shifters, more coding techniques could also be achieved by analyzing any other suitable distinctive characteristic for the received pulses like pulse-position modulation (PPM), etc. [19].

One disadvantage of the SAW RFID transponders is that its capacity is limited by its size, to make it competitive against other Auto-ID technologies, it must be small and cheap. However, achieving delays of 2 to 4  $\mu$ s requires propagation distances around 8 and 16 mm respectively. Therefore, the number of achievable codes is still rather limited, and efforts are being conducted to increase the SAW transponder capacity [19].

Another type of passive time-domain encoded chipless RFID transponders with similar functionalities as the SAW are described in the next section.

### 2.3.1.2 Chipless RFID Transponder Based on Delay Lines

One approach to realize a system with delayed reflected signals is proposed by Zhang et. al. [20], and is based on the transmission lines matching principle. A transmission line is terminated with a load that is equal to its characteristic impedance to prevent undesired reflections, on the other hand, a mismatched termination will generate signals reflections. Therefore, the authors propose to design a transmission line with different impedance mismatches along it and connect it to an external antenna. One single chipless transponder transmission line is designed placing 4 different capacitive discontinuities at regular intervals, its equivalent circuit and basic reflection principle are shown Fig. 2.3a, a resistance is placed at the end of the line to dissipate the forward pulse. The coding is based on the PPM technique and up to 16 different codes are claimed. A photograph of the chipless transponder prototype fabricated using Rogers 4350 as a substrate is shown in Fig. 2.3b, a UWB pulse generator is used to send a train of Gaussian pulses with a width of 2 ns and a period of 20 ns as an interrogation signal, and the period

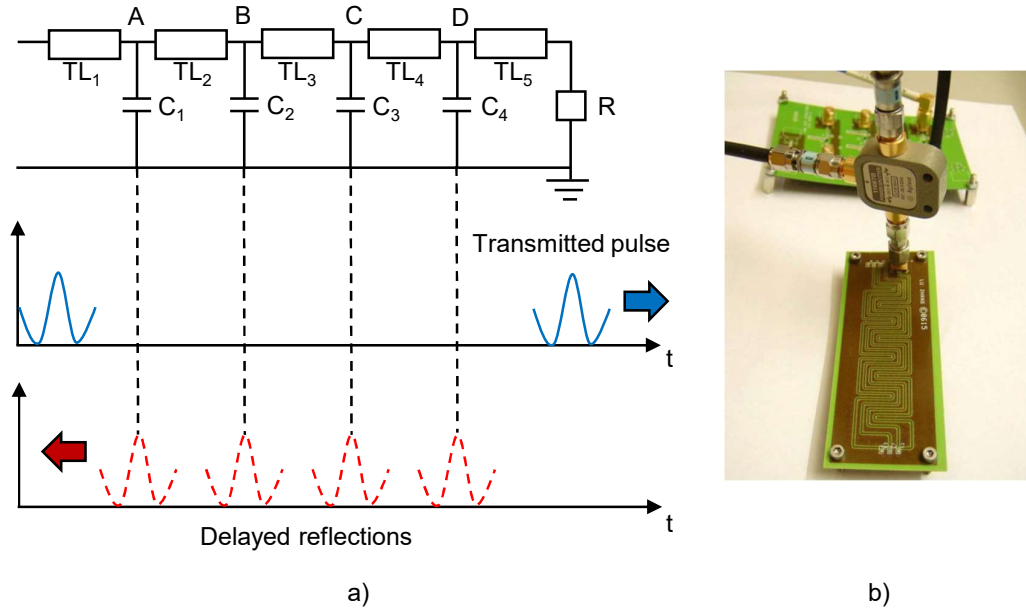


Fig. 2.3: Chipless RFID transponder based on high speed time domain delay lines: a) transmission line equivalent circuit and reflection principle, b) photograph of the prototype with size 8.3 cm  $\times$  3.1 cm and its measurement setup, taken from [20]

is set long enough to avoid undesired collisions. The total length of the transmission line is determined by the amount of desired identification codes and the pulse duration. Thus, it suffers from the same size limitations as the SAW transponder.

Later works like the ones proposed by Hu et. al. in [21] and [22], involves the design of a uniplanar monopole antenna. The geometry of the chipless RFID transponder is shown in Fig. 2.4, it consists of trimmed elliptical ring patch antenna and by a meandered coplanar waveguide (CPW). The coding is done by varying the CPW length and terminating it with different kind of loads: matched, short and open circuit.

Six different chipless RFID transponder are fabricated on Rogers 4003C substrate, three with CPW length of 37.6 mm and three with 41.6 mm. The chipless RFID transponders are measured using a fifth order Gaussian pulse, and the results are shown in Fig. 2.5. The first received pulse is the reflection generated once the waveform reaches the RFID transponder, it is the same for all chipless RFID transponders and it could serve to calculate their location. The delay between the first and the second received pulses is due to the time it takes for the Gaussian pulse to travel along the meandered CPW, these delays with respect to the first pulse, along the different shapes obtained due to the CPW termination type should serve to generate the different codes.

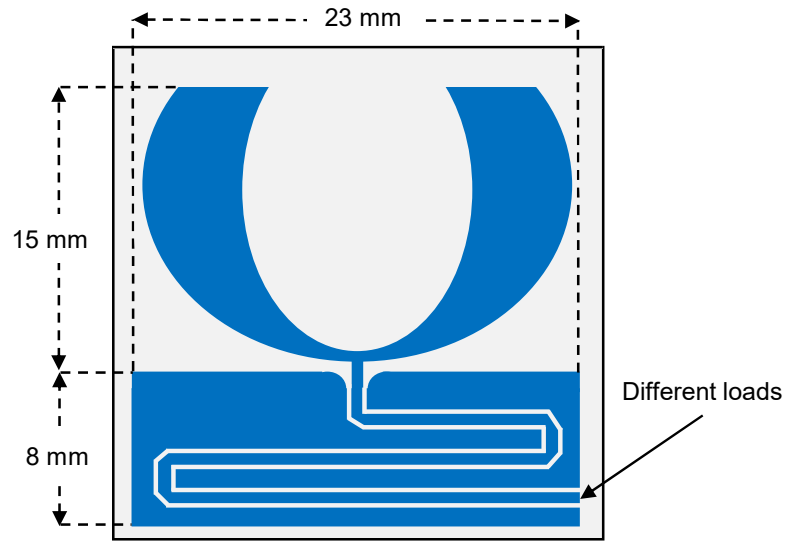


Fig. 2.4: Geometry of the chipless RFID transponder based on a uniplanar monopole antenna and CPW [21]

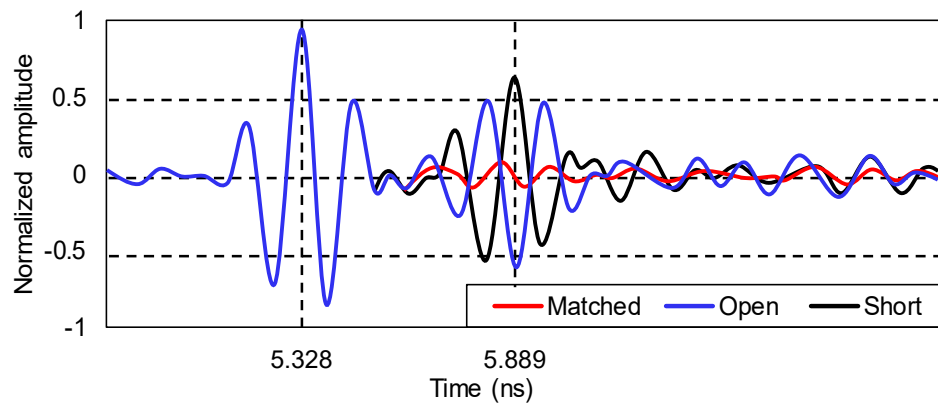
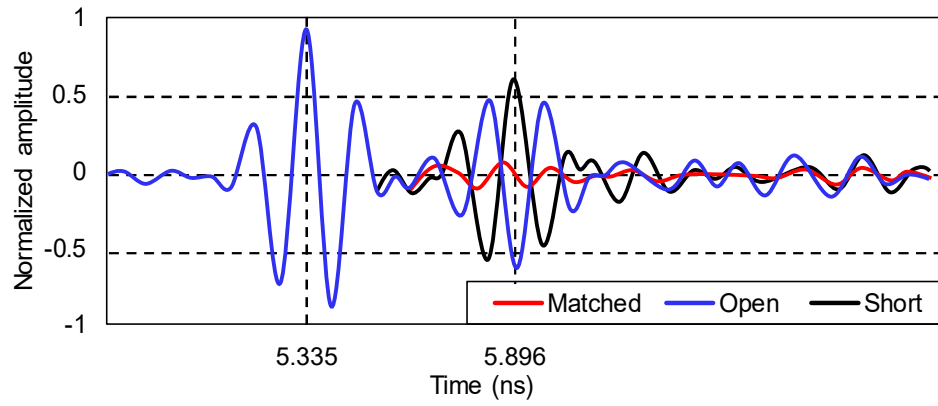


Fig. 2.5: Chipless RFID transponders' backscattered waveform for matched, open and short circuit terminations and CPW length: a) 37.6 mm, b) 41.6 mm, after [21]

To decode the CPW chipless RFID transponders, the authors proposed theoretically the architecture of the receiver illustrated in Fig. 2.6. The received signal is split  $M$  different paths, then it is multiplied with a delayed version of itself. Each path has a unique delay  $\tau_{d_M}$  that corresponds to a specific time difference between the first and second pulse of the  $M^{\text{th}}$ -chipless RFID transponder. The low-pass-filters (LPF) serves as envelope detector for the signal coming out of the mixers. To perform the detection, the authors suggest the selection of the signal with the largest amplitude and correct polarity, additionally, the chipless RFID transponder position can also be calculated using the ToA and positioning algorithms. Nevertheless, no practical experimental data to evaluate the functionality of the receiver and the effectivity of detection algorithm is provided [21].

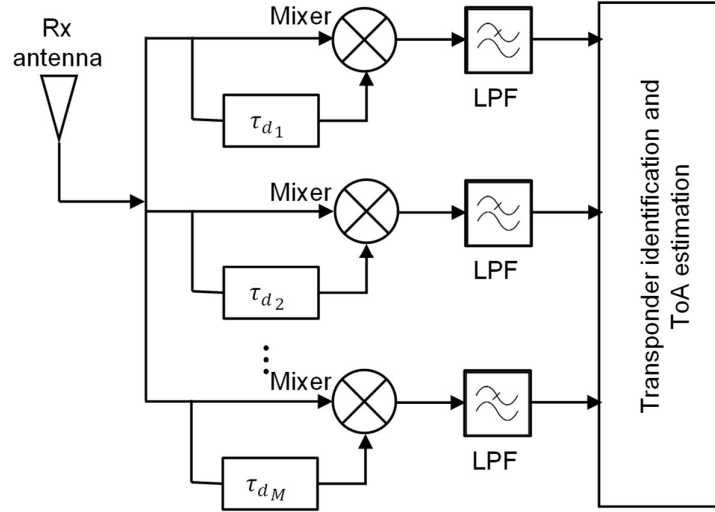


Fig. 2.6: Proposed receiver architecture for CPW chipless RFID transponders [21]

Another way to codify a chipless transponder, which should also serve as a transition between time and frequency domain coding principles, is a PPM technique using the group delay characteristics of meandered transmission lines, as proposed by Gupta et. al. in [23], Fig. 2.7a illustrates the design schematic of the chipless RFID transponder, consisting of microwave C-section dispersive delay structures, and Fig. 2.7b the coding principle. The non-commensurate coupled-lines realized by cascading several C-sections with different lengths and coupling levels are particularly suitable to generate a group delay with dispersive characteristics. A variation in the inter-coupled lengths, produces a quasi-arbitrary group-delay response, which is the superposition of all the group delays provided by each C-section with their peak  $\tau_{d_n}$  centered at  $\omega_n$  [23].

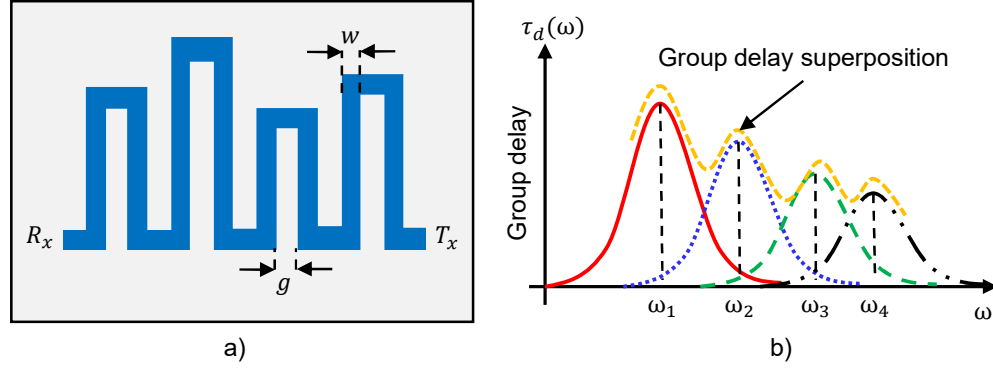


Fig. 2.7: Chipless RFID transponder based on C-section transmission line: a) geometry, b) coding principle [23]

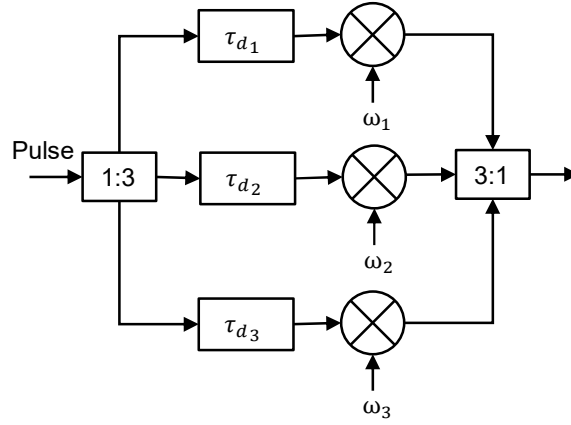


Fig. 2.8: Proposed RFID transmitter architecture to read chipless RFID transponders based on C-section transmission line, three pulses with carrier frequencies of  $f_1 = 3$  GHz,  $f_2 = 4$  GHz and  $f_3 = 5$  GHz are generated [23]

Three chipless RFID transponders are fabricated on Rogers 4003C substrate, the schematic of proposed transmitter is shown in Fig. 2.8, 1-ns long pulse with rise and fall times of 65-ps is generated, it is divided and send through three different paths with different delays and modulation frequencies of 3, 4, and 5 GHz, to be finally combined and transmitted through a horn antenna to interrogate the chipless RFID transponder, and the coded response is measured in the frequency domain with the help of an oscilloscope connected to another horn antenna [23].

In general, the coding capacity of time domain chipless transponders based on the delay lines/group delay principles is directly proportional to the chipless RFID transponder size, which could make its placement on an object impractical. Furthermore, a greater size translates into an increase of its fabrication cost, that is also a disadvantage, especially when compared to the barcode technology. Although efforts are being



conducted to reduce the chipless transponder occupied area, like the one proposed by Rodrigues et. al. in [24], where a methodology of folded multi-layer chipless RFID transponders is evaluated. Nevertheless, the printed area continues to be the same, and although the occupation area is reduced, more complexity to its fabrication process is added to overcome the effects of folding, which could also affect the cost of the chipless RFID transponder. For that reason, researchers are also focusing their attention in development of the frequency domain coding methodology, which is mostly based on the spectral signature of the chipless RFID transponder as will be described in the next subsection.

### 2.3.2 Frequency Domain Encoding

The frequency domain coding resides on modifying the chipless RFID transponder frequency response for a given bandwidth, allocating specific signatures to every individual chipless RFID transponder that the reader should be able to analyze and successfully identify. As per the time domain case, two different types of structures can be found in literature: frequency resonating circuits with antennas or scatters.

#### 2.3.2.1 Chipless RFID Transponders Based on Resonating Circuits

Preradovic et. al. presented in [25] a concept considering the amplitude and phase of the spectral signature of a multi-resonator circuit, assigning a 1:1 correspondence between resonators and data bits. The geometry of the chipless RFID transponder is shown in Fig. 2.9a, it theoretically encodes a total of 6 bits, and is composed of six microstrip spiral resonators, and two microstrip UWB disc loaded monopole antennas for cross-polarized transmission and reception. By varying each spiral resonator dimensions, a new different stopband is generated, and therefore, six different frequency dips within the 2 – 2.5 GHz frequency band are achieved, which are separated around 100 MHz from each other, starting from 2 GHz.

The coding technique consist of an on-off-keying (OOK) and is illustrated in Fig. 2.9b, if a resonance is generated, it is considered as a digital 0, if the resonance is removed, then it becomes a digital 1. The resonance removal is achieved by

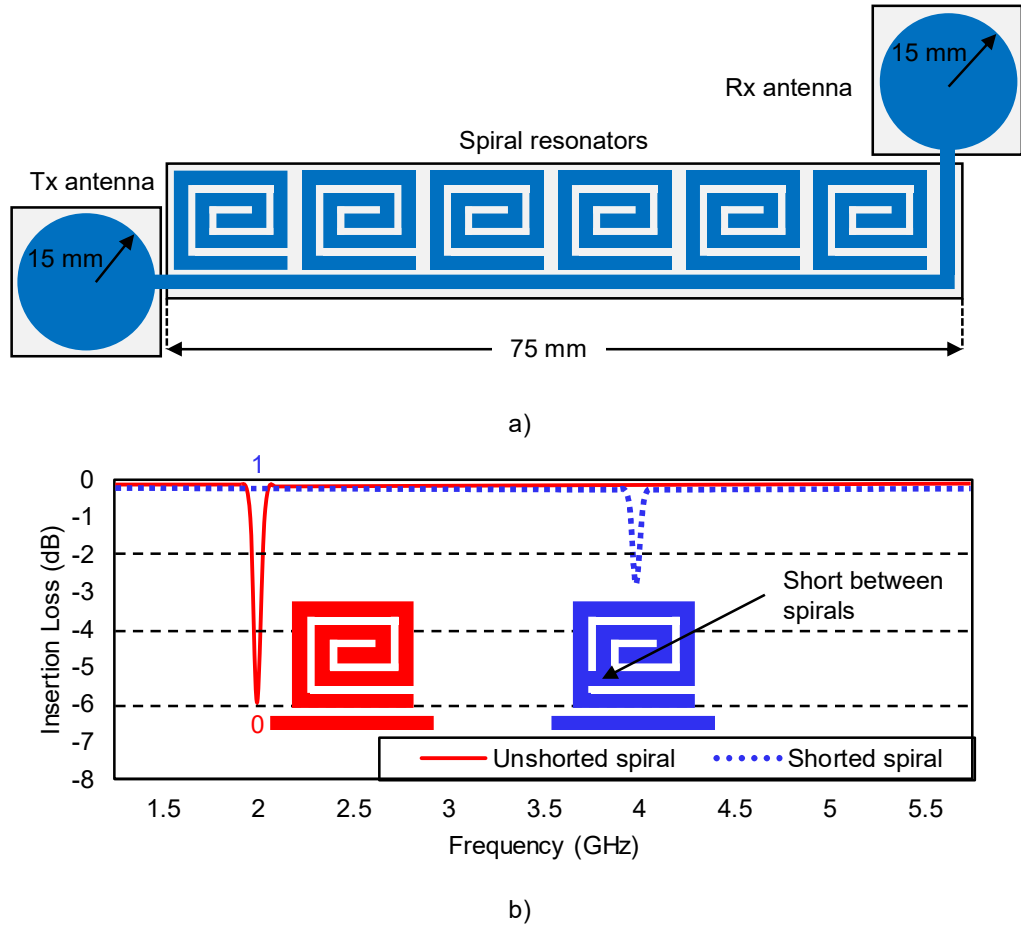


Fig. 2.9: Chipless RFID transponder based on spiral resonators: a) geometry, b) principle of encoding [25]

short-circuiting the spiral resonators, a short circuit will generate a shift in the frequency dip locating it outside the designed chipless RFID transponder operational range, forming a digital 1, where the original resonance should have taken place [25].

The multi-resonators circuits and the antennas are fabricated on Taconic TLX-0 substrate and the chipless transponder frequency response is measured using a vector network analyzer (VNA). Another 35-bits chipless RFID transponder composed of a 35 spiral resonators circuit is also fabricated in [25], working under the same coding principle. Later in [26] and [27], the same author proposed the reader architecture illustrated in Fig. 2.10, is fabricated and used to detect two 23-bit chipless transponders based on the same spiral resonators principle. For transmission, the micro-controller generates a sequence of bits that are converted to voltages by the analog-to-digital converter (ADC) and fed to a *Teledyne* YIG oscillator, which generates a frequency

sweeping signal (7 and 10.7 GHz) with 15 dBm constant power that is sent through the 10-dB coupler to the antenna to interrogate the chipless RFID transponder. The received signal through the antenna is down-converted by the mixer and sent to the gain/phase detector to be compared with the down-converted version of the transmitted one. The comparison voltages are converted to bits by the digital-to-analog converter (DAC) and sent to the microprocessor. The detection is performed using a simple peaks detector algorithm, and variations on the amplitude and phase of one single chipless transponder were detected up to 15 cm away from the horn antennas in a noise free environment.

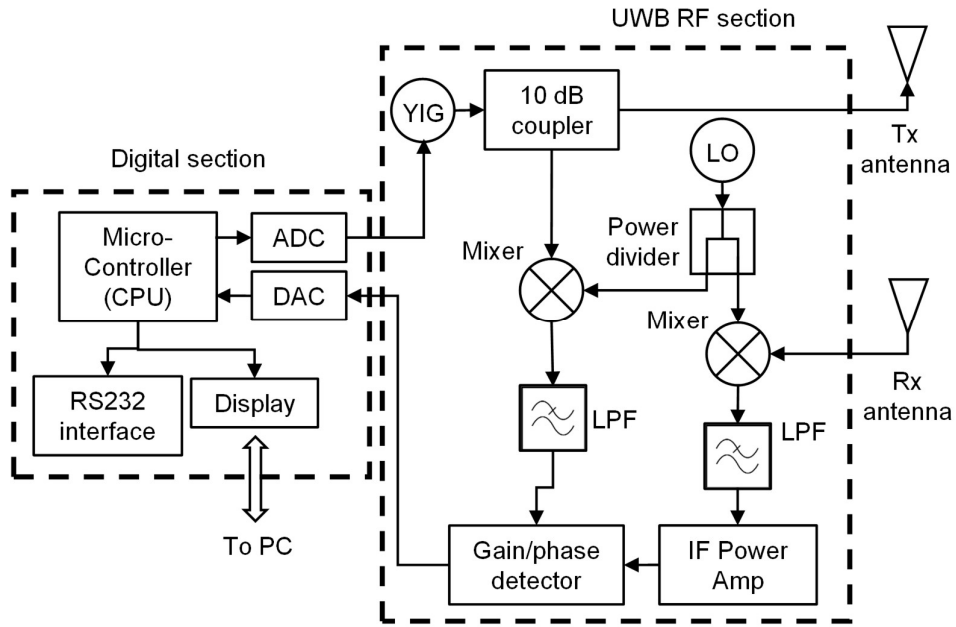


Fig. 2.10: Proposed UWB reader architecture to read chipless RFID transponders based on spiral resonators [27]

A more compact structure based on open stubs in a microstrip transmission line and two cross-polarized transmitting and receiving disc monopole antennas is proposed in [28] and its geometry shown in Fig. 2.11a, eight different resonators are designed to produce equal number of resonating dips and bits. It is based on the OOK coding principle or a further analysis of the group delays. The chipless transponder was measured in an anechoic chamber with a programmable network analyzer (PNA) and the results are shown in Fig. 2.11b, a measurement considering only the transmission line directly connected to the PNA (no antennas) is also illustrated.

The chipless RFID transponders based on resonating circuits have the disadvantage, that they additionally required the fabrication and design of antennas, which increases

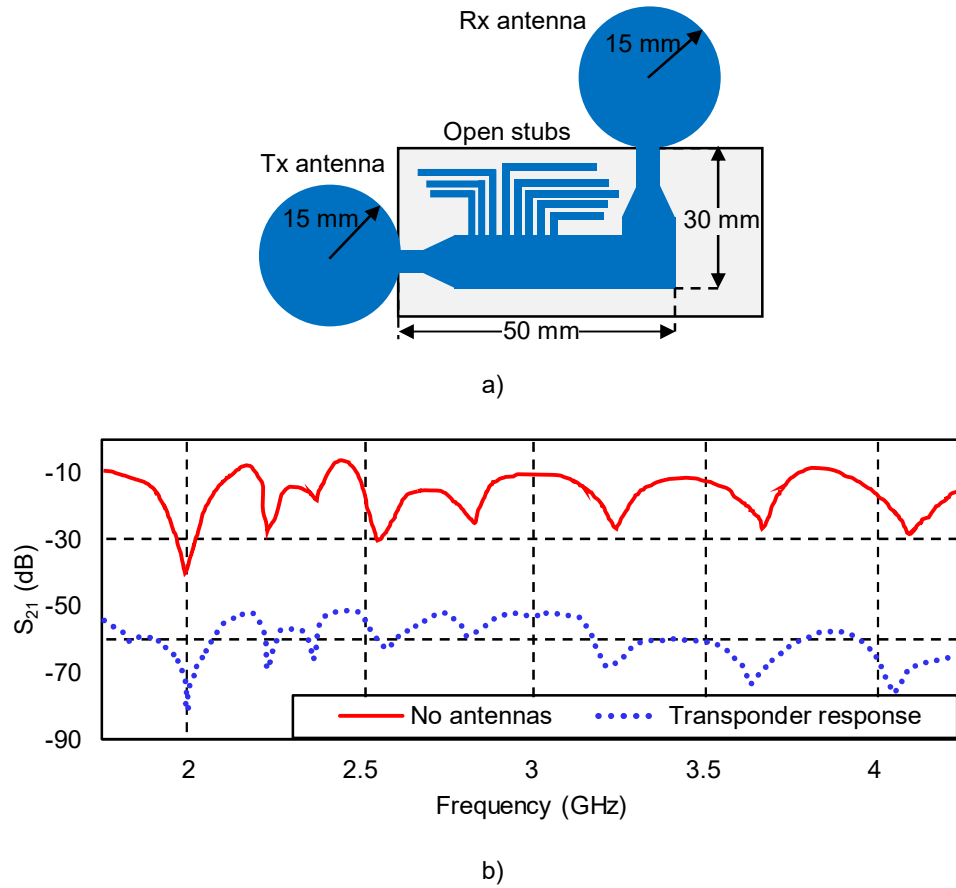


Fig. 2.11: Chipless RFID transponder based on open stub resonators: a) geometry, b) measured response, modified from [28]

their size and fabrication cost. Therefore, another type of structures based on scatters are also being investigated and are presented below.

### 2.3.2.2 Chipless RFID Transponders Based on Scattering Structures

In 2005, Jalaly and Robertson presented two works on RF barcodes using multiple frequency bands inspired by frequency selective surfaces (FSS) and the barcode technology: one approach considering between others, a chipless RFID transponder consisting of an arrays of five opaque metallic microstrip dipoles with different lengths and widths [29]. And the second one, considering an array of eleven identical split dipoles [30], both in the 5.8 GHz frequency band, fabricated on Taconic's TLY-5 substrate, and using the same coding principle: OOK. The geometry of the work presented in [29] is

illustrated in Fig. 2.12a, the dipole-like structures behave in a similar ways as the previous discussed structures, generating a resonant band pass or band stops frequency response. However, the author does not explain clearly how the coding is implemented physically on the UWB chipless RFID transponder (short-circuit or complete removal of a specific dipole). The network analyzer measurement results for two transponders with codes 11111 and 11010 are shown in Fig. 2.12b. The presence of a resonance dip represents a one, and its absence a zero.

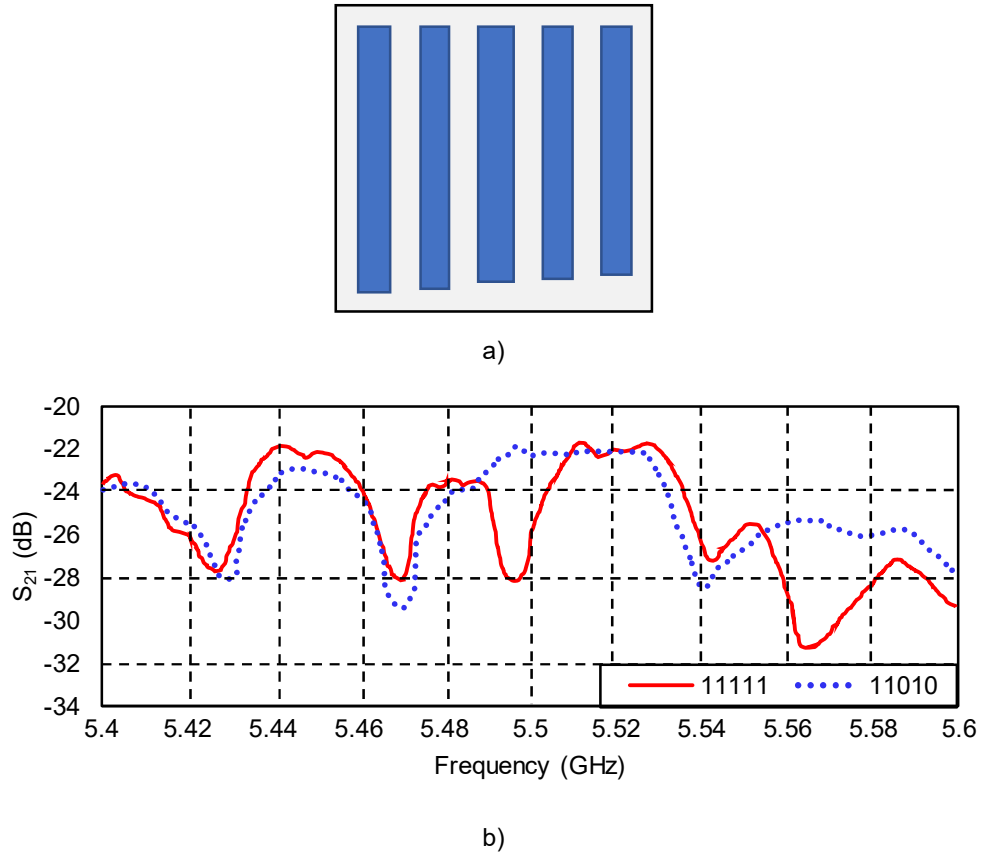


Fig. 2.12: Chipless RFID transponder based on RF barcode principle: a) geometry, b) measurement results for codes 11111 and 11010, modified from [29]

The geometry of another scattering structure proposed by Vena et. al [31] is shown in Fig. 2.13a, it is based on 20 C-sections without antennas or ground plane and fabricated on FR-4 substrate. The author explores the OOK and the group delays as coding principle. To configure the chipless RFID transponders, each resonator is replaced by a conductive strip of the same dimensions. As illustrated in Fig. 2.13b, the chipless transponder produces 20 resonance peaks between the 2 – 4 GHz frequency band, which should

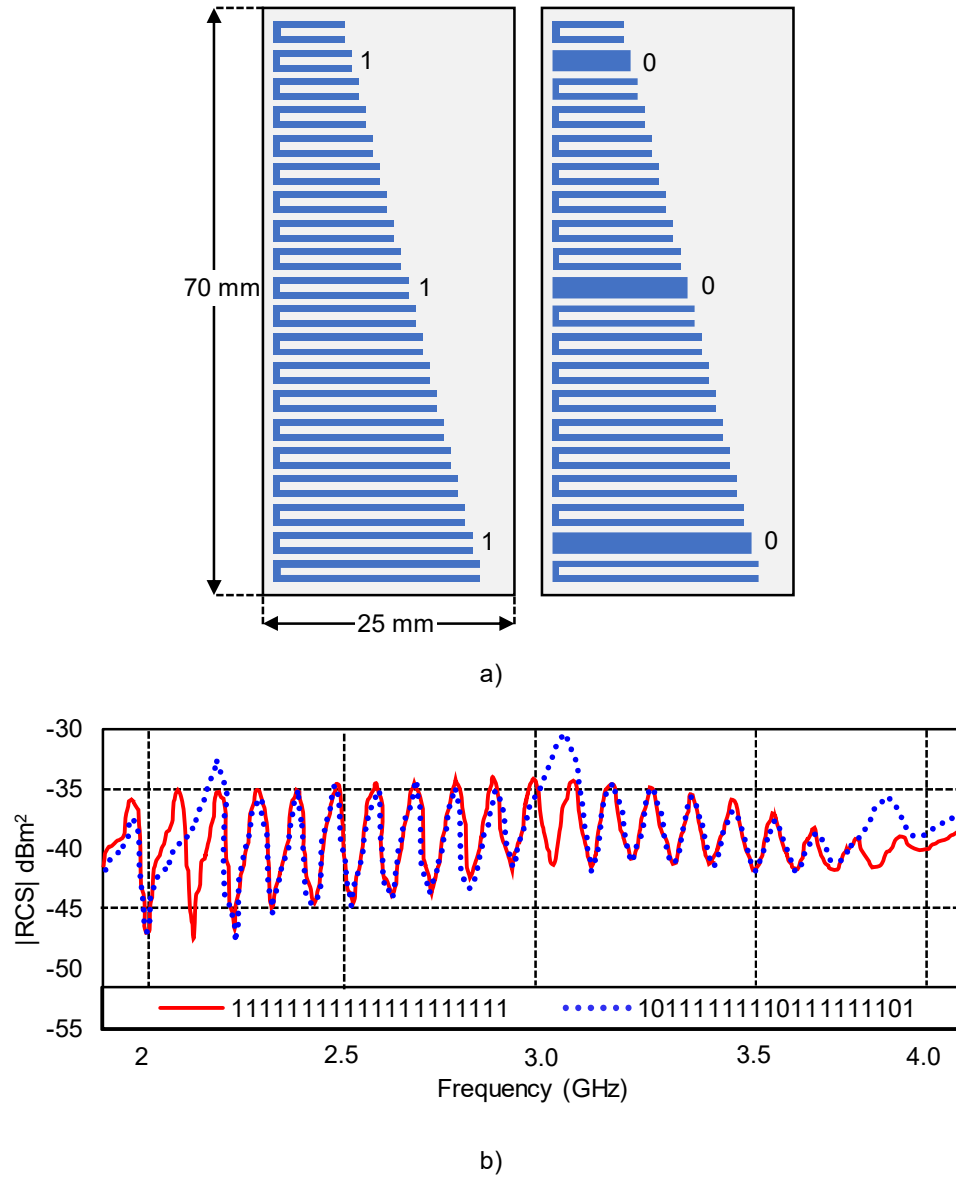


Fig. 2.13: Chipless RFID transponder based on C-section like scatters a) geometry and coding principle, b) simulated  $|RCS|$  for codes 11111111111111111111 and 10111111111011111101, modified from [31]

correspond to 20 bits. Finally, the chipless transponder are measured with the help of a VNA and radar cross-section (RCS) response, which is a measure of the detectability of an object, is calculated from the measured scattering parameters and a calibration method. The RCS concept will be further explained in subsection 4.1.1.

Another similar structure based on open conical resonators is proposed by Nair et. al. in [32], a picture of the prototype is shown in Fig. 2.14a. The chipless transponder is fabricated printing silver ink on PET, it produces 12 peaks in the 2.5 – 9.5 GHz frequency

band, its calculated  $|RCS|$  from the VNA measured scattering parameters and a calibration method, as well as the coding principle based on PPM is shown in Fig. 2.14b. A peak placed at a specific frequency represents a digital zero and if placed in another frequency represents a digital one. The chipless RFID transponder physical coding is achieved by the changing the length of the resonators.

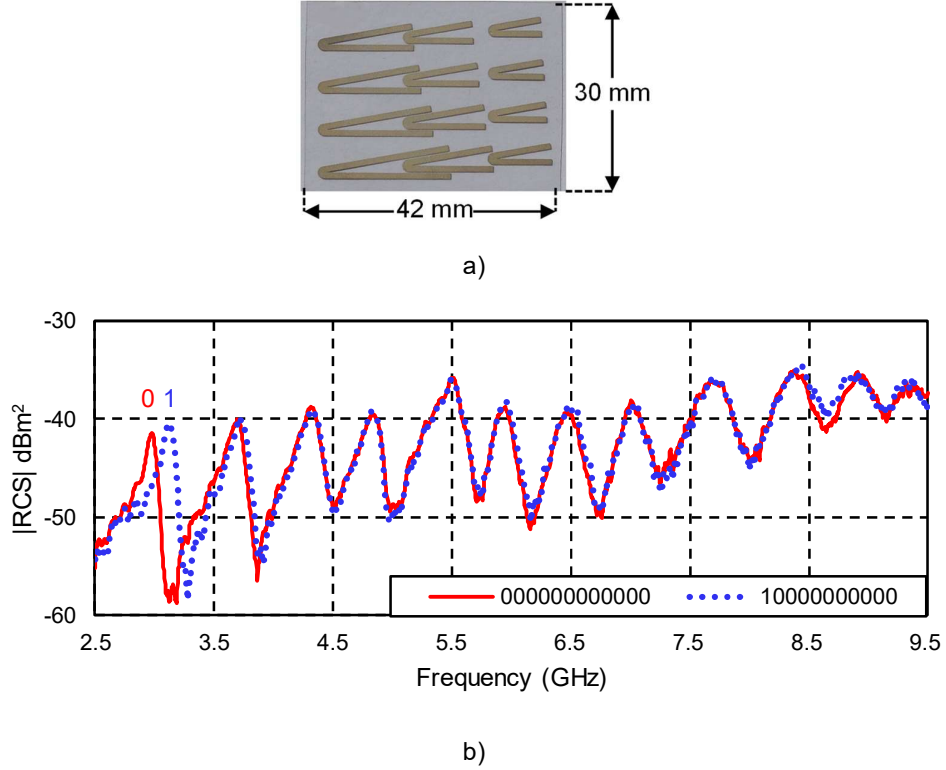


Fig. 2.14: Chipless RFID transponder based on open conical resonators: a) geometry, b) calculated  $|RCS|$  from measured scattering parameters [32]

Thus, different geometries consisting of squares [33], rings [34], and a very interesting approach using genetic algorithms to generate a change in the frequency response [35], are being investigated to encode the chipless transponders using any desirable characteristics: amplitude, phase, group delay, etc. The maximum coding capacity claimed for frequency domain transponders are: 35 bits for transponders based on resonating circuits plus antennas [25], and of 42 bits for scattering structures [34]. However, these capacity claims are mostly based solely on the visual inspection of the chipless transponders generated peaks or dips, obtained through a front-end or measurement equipment without the proper implementation of a computer-based detection algorithm under normal working conditions or taking the influence of the

communication channel into consideration. Furthermore, under normal working conditions, the chipless RFID transponder may experience frequency response degradations due to its handling while being placed in the interrogation zone, which compromises a detection technique based solely on the position of the peaks or the dips, and the need for a more robust coding and detection techniques becomes evident [33].

Finally, a block diagram containing the classification of chipless RFID transponders according to their coding technique and structures is illustrated in Fig. 2.15.

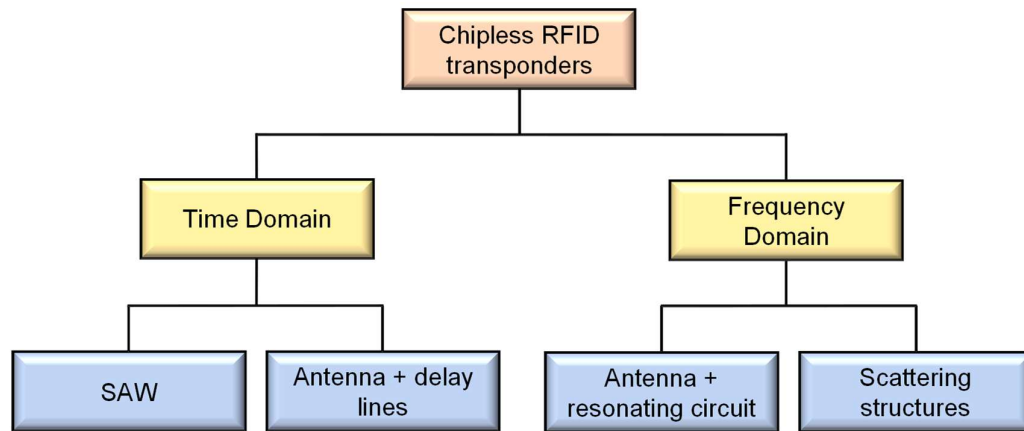


Fig. 2.15: Classification of chipless RFID transponders according to their coding technique and structures

## 2.4 Summary

This chapter provided an overview of different automatic identification systems, their working principles, technical features, major advantages and implementation challenges. The RFID technology has been specially emphasized as it continues gaining market penetration in a wide range of applications. Furthermore, due to price-constraints, a novel system based on chipless RFID transponders is presented as a feasible solution for barcode replacement on a in item-level tagging. The RFID system with chipless transponders aims to implement additional features like simultaneous detection, no human operation required, etc. to the ones that are currently being offered by the barcode technology, like environmentally friendly, cost, etc.

Different types of chipless RFID transponders structures and coding techniques have been discussed, ranging from the already commercially available time domain SAW



RFID transponders to the frequency domain scattering structures currently being investigated and which are the structures used to conduct this investigation. The importance to implement a proper coding and detection techniques for their implementation in a real case scenario has been highlighted, and their different manufacturing processes will be discussed in the next chapter.

### **3 Manufacturing Technologies**

The two-main printed electronics techniques used to produce UWB chipless RFID transponders, and the overall manufacturing processes are discussed in this chapter. The key physical parameters of the substrate materials and the challenges to produce metallic inks are explained, to provide a general understanding of the technology and its limitations, which need to be considered at the time to design a printable UWB chipless RFID transponder on flexible substrates. Finally, an alternative procedure to manufacture low-cost prototypes in an expedite way with other available organic materials is introduced.

#### **3.1 Organic and Printed Electronics**

Conventional semiconductor devices used today, are being manufactured in a series of steps involving bulky expensive equipment to perform the deposition of inorganic materials from the gas phase. Processes that are realized at vacuum with relative high temperatures. Between steps, the deposited material is patterned via photolithography with a precise mask containing the desired design. In photolithography, a light sensitive chemical called photo resist is used to cover the substrate, after the mask is placed, light is used to harden the photo resist and transfer the desired mask design to the substrate. The light exposed photoresist is then developed with chemical treatments, an exact mask representation made of photoresist is obtained. An etching process removes the unwanted areas using a plasma that reacts with the inorganic material not covered by the photoresist. The process is repeated until all the desired layers have been successfully developed. Thus, the manufacturing of semiconductor electronics generates an increasing significant quantity of inorganic material and chemicals waste, causing not only economic liability due to increasing disposal cost but also environmental [36].

Organic and printed electronics is a field of material science and an emerging technology in terms of mass production techniques. Organic molecules or polymers with desired electronic properties like conductivity can be formulated in functional inks, which can then be implemented in mass production printers. Technique that could significantly reduce the production cost, especially compared to the inorganic electronics, and with

additional added values like being light weighted, flexible, environmental friendlier and easier to dispose [37]. Although some concepts are taken from the classic device theory, fabrication materials including the substrates, inks, and the development process are quite different from the ones used in the conventional semiconductor industry [38].

#### 3.1.1 Substrates

The substrate is the underlying layer on which the flexible electronic devices will be developed. Its main function is to serve as device carrier. Therefore, large area sheets or rolls can be easily used to implement batch or roll-to-roll fabrication processes. All organic printed electronics substrates are being used in other markets segments where mass production capabilities have been implemented, which allows the application of these mature process in the fabrication of flexible electronics [38].

One of the main advantages of organic printed electronics is that flexible low-cost substrates of different sizes can be employed for fabrication. Nowadays polymer films like the PET are mostly used, nevertheless there's an important focus on the utilization of paper. However, the material to be chosen depends on its mechanical properties (surface roughness, thermal expansion, etc.) and the device development process required for a specific application [38].

Each substrate material has its advantages and disadvantages, glass substrates present a higher barrier while paper is more flexible and cheaper. Plastic materials like PET can be modified to fulfill certain physical and surface requirements and employed for different applications. Other materials are high temperature resistance allowing the implementation of more complex development processes. According to its specific properties, the right material can be found to fulfill the requirements of a specific application [38].

As it will be further explained in chapter 4, the impedance of microstrip lines depends on the relative dielectric constant  $\epsilon_r$ , as well as the physical dimensions of the substrate such as thickness. Therefore, the final dimensions of the microstrip line (width, gap) are determinate by the selected substrate. To reduce the size of a device, a high relative dielectric constant  $\epsilon_r$  is desired, given that it increases the capacitance of the components, reducing the size and radiation losses. On the other hand, a low relative

dielectric constant material  $\epsilon_r$  can serve as a good substrate for RFIDs [9]. The substrate thickness has a direct influence on the effective dielectric constant  $\epsilon_{eff}$ , therefore it also determines the resonance frequency, and the sizes of the components on the substrate, as well as the substrate losses and overall system flexibility [9].

In the specific case of RFID with chipless transponders, a low-cost substrate with capabilities for large volume item tagging needs to be used. In the best-case scenario, the chipless RFID transponder will be directly printed on the product package without the need of an extra label or special substrate [38]. Given the high price pressure, PET and paper are mostly selected for their low-cost availability. Thus, their main parameters are of great interest, Table 3.1 presents some key mechanical/electrical properties for PET and paper [9].

Parameter	PET	Paper
Relative permittivity ( $\epsilon_r$ )	3.4	2.8~3
Loss tangent ( $\tan \delta$ )	$2.0 \times 10^{-3}$	0.05~0.06
Coefficient of thermal expansion ( $tppm/^\circ C$ )	6	-
Young's modulus ( $psi$ )	$4.0\sim 4.5 \times 10^5$	144~838
Water absorption (% <i>after 24 hrs</i> )	0.16	2
Compound	PET	Cellulose

Table 3.1: Physical properties of substrate materials for chipless RFID transponders [9]

The influence of the permittivity and the loss tangent will be further explained in subsection 4.1.2. However, PET has a higher permittivity than paper which has a direct influence on the position of the UWB chipless RFID transponder's frequency dip, and it also has a higher physical resistance to mechanical tension or compression. Paper, on the other hand, presents higher losses than PET.

### 3.1.2 Organic Inks

The ink is the organic material that needs to be transferred to surface of the substrate. For that reason, functional materials need to be transformed to a physical state in which they can be easily transported, namely the liquid state. Furthermore, this liquid

state needs to fulfill the respective printing technology specifications. Two parameters are mainly considered: viscosity, which is the ability to transfer mechanical stress and hydrodynamic pressure to the substrate, and surface tension, which are the capillary forces between the fluid-substrate and fluid-air interfaces. The printing ink needs to be set sensitively in viscosity and surface tension for the given substrate, printing process, and drying conditions [37].

In printed electronics, the conductive inks are based on conductive metal nanoparticles. However, to stabilize the ink against aggregation and precipitation, and provide reproducible performance, an agent which is usually a polymer is required. This polymer is especially important to prevent dispersions of inks with high metal content, which are required to produce high conductivity printed patterns. Therefore, the best metal candidates to produce the inks are the ones with high conductivity as silver Ag ( $6.3 \times 10^7$ ), copper Cu ( $5.96 \times 10^7$ ), gold Au ( $4.42 \times 10^7$ ), and aluminum Al ( $3.78 \times 10^7$ ). Nowadays, silver-based ink, is the most reported and studied worldwide conductive film material in printed electronics [39] [40]. Silver is a novel metal well known for its privilege position in terms of electrical conductivity, lower affinity to oxygen if compare to copper or aluminum. It can be found in a rate of 25 to 1 with respect to gold on the earth crust, and therefore is cheaper. Additionally, it possesses interesting physical properties, that enables the silver-based inks to have a good adhesion to the substrate, reducing the coffee-ring effect and particles aggregation. It also provides a suitable viscosity and surface tension helping to determine the drop size improving its placement accuracy [40] [41] [42].

Nevertheless, silver is still quite costly and a major challenge in this field is to replace it with cheaper ones like copper or aluminum, but this depends on finding the proper fabrication process to avoid their oxidation at ambient conditions, for example aluminum gets a dense thin amorphous aluminum oxide layer ( $Al_2O_3$ ) of around 2 – 6 nm within approximately 100 picoseconds, losing electrical conductivity and making it inapplicable for conductive inks formulations. In the case of copper, it undergoes a slower oxidation process, which allows to coat it with a capping agent or with another air stable metal and this way, prevent penetration of air in the surface of the nanoparticles [39].

Now that the main materials used in printed electronics has been described, an introduction to the different printing technologies and process is given in the following subsections.

### 3.1.3 Screen Printing

The screen-printing principle is shown in Fig. 3.1. A screen-printing machine usually is composed by a screen (a mesh generally made of natural silk, plastic, and metal mounted on a frame), a squeegee, a flooding blade, and a substrate holder or base plate. The metallic based ink is applied to the screen by the syringe, the flooding blade is used to distribute homogenously the ink all over the screen without pressure and without bending it. The mesh is designed with different textures for printing and non-printing areas. An impermeable layer called stencil covers the mesh for non-printing areas preventing the ink from passing through the mesh to the substrate. The ink is pressed through the mesh to the substrate on the printing areas by the squeegee, which puts the mesh under local stress and bends it. The squeezed ink then adheres to the substrate surface [37].

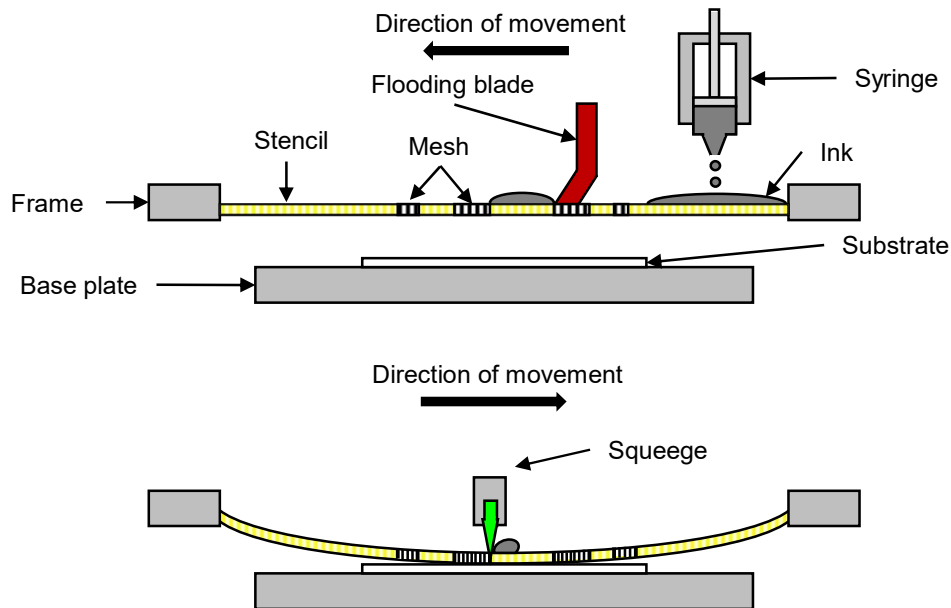


Fig. 3.1: Screen printing principle

The UWB chipless RFID transponders presented in this thesis are fabricated by the Technische Universität Chemnitz's personnel, using the semi-automatic screen and

stencil printing machine X1 SL with manual positioning system from EKRA – ASYS Group and its printing characteristics are presented in Table 3.2[43]. The conductive layers are printed using silver-based ink Dupont 5028 [44].

Parameter	Value
Print speed	10 - 200 mm/s
Print pressure	10 - 250 N
Print format	460 x 460 mm
Print material thickness	max. 30 mm
Repeat accuracy	$\pm 10 \mu\text{m}$

Table 3.2: EKRA X1 SL technical data [43]

The first printing technology used for the fabrication of electronic components was the screen printing [37]. Nowadays, due to the technological advancements, screen printing has expanded its range of applications and is currently being used to print chipless RFID transponders on conventional flexible substrates [7]. Nevertheless, another printing technique based on flexography can also be used and its working principle is explained in the next subsection.

#### 3.1.4 Flexography

The principle of flexography is shown in Fig. 3.2. The ink is stored in the ink feed chamber and covers the anilox roller as it rotates removing the excess of ink. The anilox roller is usually composed of a steel core and a ceramic or metallic surface with engraved cells that allow the storage of enough ink. The ink is then transferred from the anilox roller to the printing plate, that is mounted on the plate cylinder by means of a double face adhesive tape and contains the printing pattern. The ink is then transfer to the substrate as it is pressed against the printing plate by the impression cylinder [37].

Nowadays, flexography is also being used in printing electronics for the fabrication of electronic devices, given the facilities to produce printing plates with higher printing resolutions. These advancements in the fabrication of printing plates has enable the use of this technology in fields like chipless RFID [37] [45].

The UWB chipless RFID transponders presented in this thesis are printed by the Technische Universität Chemnitz's personnel, using the Flexography test machine

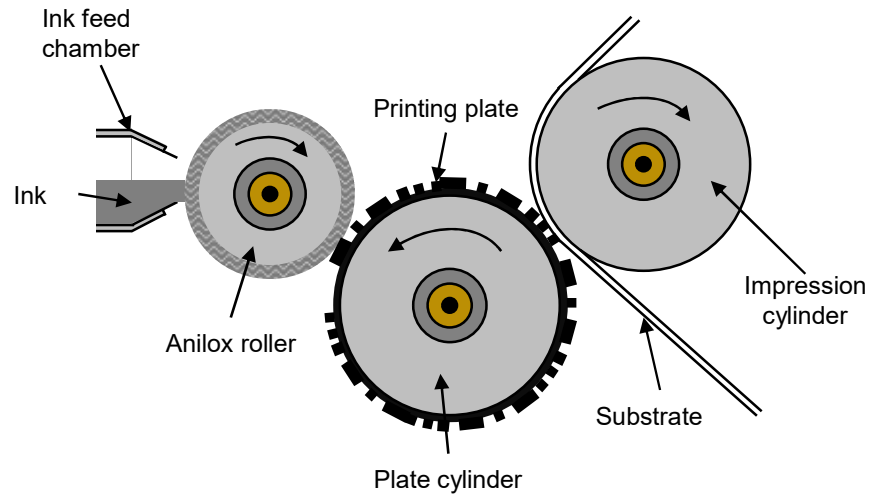


Fig. 3.2: Flexography principle

Flexiproof 100 model 630 from ERICHSEN [46]. The transponders are printed with a conductive thin film based on silver-based ink Dupont 5028 [44].

### 3.2 The Printing Process

The process of transferring the ink to the substrates involves a series of sub-steps that need to be considered depending on the properties of the ink, the substrate and the electronic device to be printed [37]:

*Conditioning*, the surface of the substrates must be prepared for the deposition of the ink: sheets must be separated or unrolled individually, external contaminations need to be removed. In some cases, a pretreatment of the substrate using an electrical discharge or ionized gas is required if the printing fluid has an unsatisfactory wetting behavior.

*Fluid acquisition* is the step in which a specific amount of ink is placed in the respective machine ink chamber.

*Pre-dosing* is the distribution of the ink in a way it can be uniformly applied to the printing mask. For example, in Flexography printing this action is performed by the anilox roller.

*Dosing* is the specific task of the printing mask, at this point, each point of the mask surface acquires a specific amount of ink that is going to be used to reproduce the desired pattern.



*Transfer*, after the dosing of the ink has taken place, the ink is transferred to the desired point on the substrate, in screen and flexography printing, this is achieved by means of mechanical pressure.

*Relaxation* is the surface-leveling process as an effect to the wetting of the substrate by the creation of a free, highly mobile ink surface.

*Drying, curing or sintering*, the use of conductive inks for printed electronics must produce a high electrical conductivity of the printed pattern, preferable close the bulk metal, under relatively mild conditions, at which the properties of the substrate material are not affected (this is especially important for flexible electronics), which can be quite challenging. A main effect that needs to be overcome after the relaxation process has occurred, is the formation of numerous percolation paths between metal particles caused by the presence of stabilizing agents and components that prevents direct electrical contacts between nanoparticles. Therefore, the nanoparticles-based ink is sintered by heating to produce a continuous metallic path. However, this process is limited by the substrate heat-sensitivity, in the case of flexible substrates like paper or PET, they could not resist temperatures above 120 – 150°C [39].

### 3.3 A Fabrication Alternative with Aluminum or Copper Strips

To evaluate the performance of chipless RFID transponders fabricated using other metallic materials like aluminum or copper, that as explained previously cannot be easily synthesized to produce metallic inks suitable for flexible substrates like bond paper. An alternative manual fabrication process was developed to produce chipless RFID transponders prototypes using commercial copper or aluminum tape for the conductive strips, and commercial bond paper or PET for the substrate.

The fabrication process of the chipless RFID transponders consists on printing two full scaled pattern masks with the desired design original dimensions on a sheet of bond paper using a commercial inkjet printer. The first mask pattern should serve to shape the metal strips and the second one to be used as a template where the finalized strips are glued.

One of the printed masks is fixed with an adhesive agent from the non-printed side to the non-metal side of the respective tape, to prevent the reduction of conductivity due to influence of additives on the metallic surface. Then using a cutting tool, the metal tape

is shaped in the desired pattern. Finally, the protective paper of the patterned tape strips is removed, and they are pasted on the surface of the second mask following its printed design. This way, a very cheap and fast design prototype can be fabricated, to verify the chipless RFID transponder frequency response and later, to compare performance to its organic electronics printed version [47].

### 3.4 Fabrication Technologies for Chipless RFID Transponders

As discussed in section 2.3, different types of fabrication technologies and substrates can be used to manufacture chipless RFID transponders, being the printed circuit boards (PCB) the most commonly used. The term printed comes from the fact that the conductive strips are usually generated by means of a screen-printing or photo-engraving process. The main components of a PCB are [48]:

*The base*, it is a thin board made of an insulating material that provides mechanical support for all conductive strips and components and it also influences the electrical properties of the complete circuit.

*The conductors*, which are normally made copper strips of high purity, which are firmly attached to the base material.

To keep the manufacturing cost as low as possible, the chipless RFID transponders can be easily fabricated on a single-sided PCB, which means that the conductive strips are found on one side of the insulating substrate. The fabrication process is mostly performed by means of a “print and etch” technique or by a “die-cut” method, where a die carries an image of the chipless RFID transponder shape and then it is photo-engraved, or machine engraved [48].

Although PCB fabrications are commonly found in literature for the fabrication of chipless RFID transponders [20] - [31]. Their fabrication cost rounds the several dollars range, depending on their size and substrate selection, which is still way above the US \$0.10 of a standard ultra-high frequency (UHF) RFID transponder already commercially found [8], and the barcode replacement target of below US \$0.01, as discussed in section 1.1. Therefore, the implementation of manufacturing technologies like printed electronics on flexible substrates capable to mass produce UWB chipless RFID transponders becomes evident, not only to the fact of the used cheaper materials but also the waste

reduction. Chipless RFID transponders fabricated by means of printed electronics can already be found in [7], [32], [33], [35], [45], [47] and [49].

## 3.5 Summary

In this chapter, the two main printing technologies based on screen and flexography were discussed, as well as the manufacturing process used to fabricate the UWB chipless RFID transponders presented in this investigation work. The main substrate parameters, as well as the conductive ink synthesis and deposition challenges were explained to provide an initial baseline to understand the design of the chipless RFID transponders and the RF performance results presented in the next chapter.

## 4 UWB Chipless RFID Transponder Design

In this chapter, the fundamentals of the UWB chipless RFID transponder design based on waveform scattering structures are introduced. They have their foundations on the radar scattering with absorbing materials and frequency selective surfaces (FSS) theory, to produce band selective frequency responses.

To develop one single multi-purpose structure to fulfill all the required features of the RFID technology is quite challenging, and out of the scope of this work. Therefore, five UWB chipless RFID transponders based on three different geometries with distinct characteristics are designed and manufactured, using either printed electronics or the alternative fabrication technique discussed in the previous chapter, and employing different materials to investigate their influence in the frequency response. Furthermore, the structures are developed within different frequency bands, and implementing different coding techniques to study their influence in the successful detection and recognition of the identification codes. A novel differential frequency coding technique is introduced, that will be used in later chapters to realize a real system application scenario, with a computer developed detection algorithm to automatic detect and successfully recognize the different UWB chipless RFID transponders identification codes.

### 4.1 Scattering Theory

The UWB chipless RFID transponder working principle is founded in the scattering radar theory, which describes the collision and scattering of a waveform with some material or object. The radar is a device designed to transmit an electromagnetic signal and receive the object's echo, usually to determine its location and in some cases its characteristics. Nevertheless, with the evolution of the radar technology and the increasing development of sophisticated detection systems, a new threat to reduce mission effectiveness of many weapons and platforms in the military field was identified. Therefore, attention was driven to study new methods to reduce radar detectability, one of them is the RCS reduction (RCSR), which focuses on how the radar signature can be shaped to prevent an object from being easily identified [50]. To be able to understand

this concept, a general understanding of RCS is required and therefore its definition is explained in detail in the next subsection.

#### 4.1.1 Radar Cross-Section Definition

The IEEE standard radar definitions describe the RCS as “the measure of reflective strength of a target, usually represented by the symbol  $\sigma$  and measured in square meters”. It can be mathematically expressed as “ $4\pi$  times the ratio of power per unit solid angle scattered in a specific direction to the power per unit area solid angle scattered from a specified direction. More precisely, it is the limit of that ratio as the distance from the scatterer to the point where the scattered power is measured approaches infinity” [50]:

$$\sigma = \lim_{r \rightarrow \infty} 4\pi r^2 \frac{|E^{scat}|^2}{|E^{inc}|^2} \quad (4.1)$$

where  $E^{scat}$  and  $E^{inc}$  are the scattered and incident electric field of the target respectively. Three different cases or types of RCS that can be distinguished and as depicted in Fig. 4.1 [51]:

- a) Monostatic or backscatter RCS: there's a reflected scattering wave that travels in the opposite direction of the incident wave:

$$E^{scat} \cdot E^{inc} = -|E^{scat}||E^{inc}| \quad (4.2)$$

- b) Forward-scatter RCS: the energy scattered travels in the same direction as the incident wave:

$$E^{scat} \cdot E^{inc} = |E^{scat}||E^{inc}| \quad (4.3)$$

- c) Bistatic RCS: the energy reflected or scattered travels in any direction other than the incident or opposite incident direction.

$$E^{scat} \cdot E^{inc} = |E^{scat}||E^{inc}| \cos \emptyset \quad (4.4)$$

where  $\emptyset$  is a measure of the angle between  $E^{scat}$  and  $E^{inc}$ .

For this research work, the monostatic or backscatter RCS definition, is the case of interest. Thus, from now on, every time the term RCS is used, it will mean the backscatter RCS taken from this definition and measured in terms of decibel relative to one square meter dBm<sup>2</sup>.

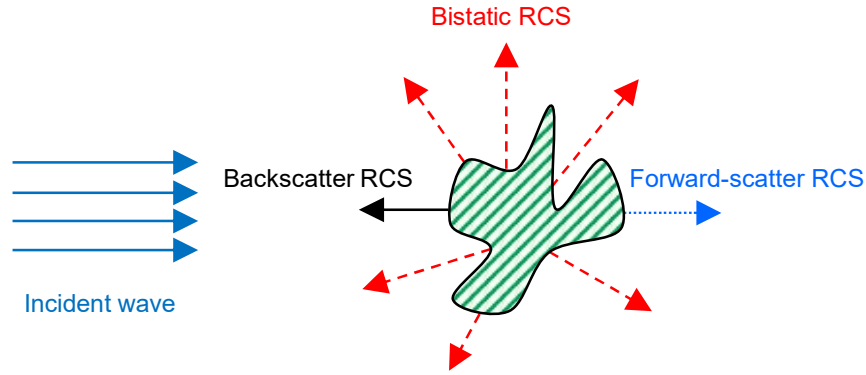


Fig. 4.1: Radar cross-section definition

In radar technology, complex targets like ships and aircraft can be represented as a collection of different basic geometric elements. The dominant echo sources of the target are isolated, and detection is then performed focusing to a limited number of elements rather than the whole composite target. Four different techniques were developed for RCSR: shaping, radar absorbing materials, passive and active cancellation. The first two, are the most practical and applied RCSR techniques. Being shaping the first one to be employed to create a design with low RCS, and the radar absorber materials (RAM) are used in areas where the shape could not be optimized or to reduce the effects of the traveling wave forms on the radar signature [50].

In the specific case of UWB chipless RFID transponders, the application requirements and fabrication technology limitations, prevent the shaping of its surfaces and edges to deflect the scattered energy in directions away from the RFID reader for specific frequencies. Nevertheless, the knowledge of the electromagnetic aspects of RAM design, can be of great advantage since it focuses on the synthesis and arrangement of materials to provide a specific radar signature to a distinct incident waveform. Understanding this theory can be helpful at the time to design an UWB chipless RFID transponder and manipulate its respective radar signature [50].

#### 4.1.2 Radar Absorbing Material's Principle

The principle of radar absorbing materials is based on the fact, that the electromagnetic energy of fields passing through a determinate substance can be absorbed. Furthermore, the refraction index is an intrinsic property of materials and

describes how a waveform propagates through it, includes the magnetic as well as the electric fields effects, it is represented by complex numbers, and the imaginary component represents the loss. The effects of the loss mechanisms can be grouped into the material's permittivity  $\epsilon$  and permeability  $\mu$ , in general, the complex relative permittivity and permeability concepts are used, which are normalizations by their free space values  $\epsilon_0$  and  $\mu_0$  respectively, and can be expressed as [50]:

$$\begin{aligned}\epsilon_r &= \epsilon_r' + j\epsilon_r'' \\ \mu_r &= \mu_r' + j\mu_r''\end{aligned}\tag{4.1}$$

where the real part of each parameter representing the stored energy is denoted by a prime and the imaginary part of each representing the loss is denoted by a double prime. Since the loss depends on the material conductivity  $\kappa$ , the effect of the conductivity can be related to  $\epsilon_r''$  by [50]:

$$\epsilon_r'' = \frac{\kappa}{\omega\epsilon_0}\tag{4.2}$$

It can be seen, that the losses also depend of the angular frequency  $\omega$ . The electric and magnetic loss tangents are given by [50]

$$\begin{aligned}\tan \delta_e &= \frac{\epsilon_r''}{\epsilon_r'} \\ \tan \delta_m &= \frac{\mu_r''}{\mu_r'}\end{aligned}\tag{4.3}$$

The refraction index  $n$  is given by the ratio between the waveform number inside the material  $k$  and the waveform number in free-space  $k_0$  [50]

$$n = \frac{k}{k_0} = \frac{\omega\sqrt{\epsilon\mu}}{\omega\sqrt{\epsilon_0\mu_0}} = \sqrt{\epsilon_r\mu_r}\tag{4.4}$$

The intrinsic impedance  $Z$  of the material is the value seen by an incident wave normal to the surface on a semi-infinite plate of material, represented by [50]

$$Z = Z_0 \sqrt{\frac{\mu_r}{\epsilon_r}}\tag{4.5}$$

where  $Z_0$  is the free-space impedance,  $120\pi$ , that is approximately  $377 \Omega$ . In the case of the UWB chipless RFID transponder design, a conductive layer is placed on the material.

Therefore, a transmission line analysis can be conducted to calculate the effective input impedance at the front of the layer.

Considering a flat metallic surface placed on a layer of dielectric material, the normalized input impedance  $\eta$  for an incident wave normal to the front surface is described by [50]

$$\eta = \sqrt{\frac{\mu_r}{\epsilon_r}} \tanh(-jk_0 T \sqrt{\mu_r \epsilon_r}) \quad (4.6)$$

where  $T$  represents the dielectric layer thickness, the normalized impedance can be used to calculate the reflection coefficient  $\Gamma$  [50]

$$\Gamma = \frac{\eta - 1}{\eta + 1} \quad (4.7)$$

The reflected power in decibels can be expressed as

$$|\Gamma|(dB) = 20 \log_{10} |\Gamma| \quad (4.8)$$

In radar technology, the RAM is designed to produce a material for which  $|\Gamma|$  remains as small as possible over a wide frequency range as possible. In the UWB RFID with chipless transponders technology, the objective is to achieve an  $|\Gamma|$  that remains as small as possible for a desired section of the frequency band, while remaining as high as possible for another portion of the same spectrum and fit the desired frequency signature requirements [50].

In UWB chipless RFID transponders design, two main objectives need to be achieved: To deliver the electromagnetic energy into the material, Eq. (4.7) shows that the impedance mismatch seen by the incident waveform as it enters the UWB chipless RFID transponder is the key factor to achieve this goal. The second objective is, the UWB chipless RFID transponder should absorb/reflect energy for given frequency bands, and for that, the mechanisms available for attenuating waveforms within materials need to be understood. Thus, to achieve this, the problem is approached in the next section from a wave matrix perspective to easily comprehend the physics behind it [50].

#### 4.1.3 Dielectric Multilayers Wave Matrix Analysis

A wave matrix approach can be used to calculate the scattering from a flat multilayer dielectrics structure, based on cascade matrix, by simply relating the output side of a



two-port network to its input side, that is, the relation between the incident and reflection scattering coefficients. The equivalent transmission line shunt element circuit is depicted in Fig. 4.2.

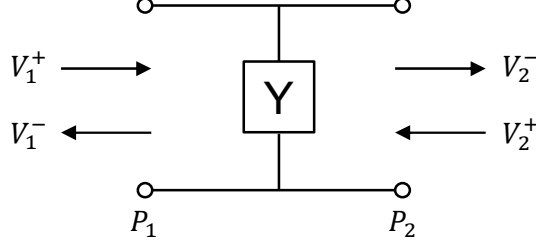


Fig. 4.2: One-layer shunt equivalent circuit [50]

The reflective waves represented by  $V_1^-$  and  $V_2^-$  are related to the incident waves  $V_1^+$  and  $V_2^+$  by a scattering matrix  $\mathbf{S}$  given by [50]

$$\begin{bmatrix} V_1^- \\ V_2^- \end{bmatrix} = \begin{bmatrix} S_{11} & S_{12} \\ S_{21} & S_{22} \end{bmatrix} \begin{bmatrix} V_1^+ \\ V_2^+ \end{bmatrix} = [\mathbf{S}] \begin{bmatrix} V_1^+ \\ V_2^+ \end{bmatrix} \quad (4.9)$$

$S_{11}$  and  $S_{22}$  represent the reflection coefficient by a waveform incident at ports  $P_1$  and  $P_2$  respectively,  $S_{12}$  and  $S_{21}$  are the transmission coefficients from ports  $P_2$  to  $P_1$  and  $P_1$  to  $P_2$  respectively. The scattering matrix for the shunt circuit of Fig. 4.2 is [50]

$$[\mathbf{S}] = \frac{1}{2 + Y} \begin{bmatrix} -Y & 2 \\ 2 & -Y \end{bmatrix} \quad (4.10)$$

The scattering matrix described in Eq. (4.11) represents the interface between dielectric layers,  $Y^-$  and  $Y^+$  are the admittances on the left and right respectively [50]

$$[\mathbf{S}] = \frac{1}{Y^- + Y^+} \begin{bmatrix} Y^- - Y^+ & 2Y^+ \\ 2Y^- & Y^+ - Y^- \end{bmatrix} \quad (4.11)$$

The admittances depend on the wave polarization and angle of incidence, for an electric field parallel to the interface is represented by [50]

$$\frac{Y_{TM}}{Y_0} = \frac{\epsilon_r}{\sqrt{\mu_r \epsilon_r - \sin^2 \theta_0}} \quad (4.12)$$

where  $\theta_0$  is the angle of incidence, an electric field also parallel to the interface is described by [50]

$$\frac{Y_{TE}}{Y_0} = \frac{\sqrt{\mu_r \epsilon_r - \sin^2 \theta_0}}{\mu_r} \quad (4.13)$$

The scattering matrix to represent the phase shift and the loss of wave traveling through a dielectric plane of thickness  $T$  can be expressed as [50]

$$[\mathbf{S}] = \begin{bmatrix} 0 & e^{-jkT} \\ e^{jkT} & 0 \end{bmatrix} \quad (4.14)$$

where

$$k = k_0 \sqrt{\mu_r \varepsilon_r - \sin^2 \theta_0} \quad (4.15)$$

As pointed out previously, each circuit analog (CA) sheet can be represented as an admittance shunted across the transmission line. A multilayer design implies that the reflection coefficient at each shunt element will be small, which should also translate in that all admittances are small, and the total reflection coefficient is simply given by the sum of each individual reflection coefficient, plus the influence of the phase shift due to the transmission line length. Fig. 4.3 illustrates the multilayer shunt circuit model for this analysis [50].

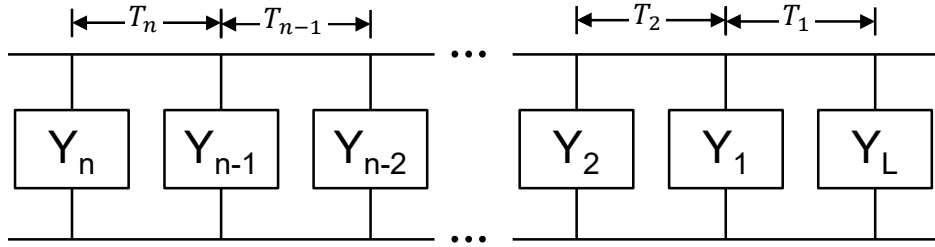


Fig. 4.3: Multilayer shunt circuit [50]

The reflection coefficient of the multilayer shunt circuit without considering multiple reflection is approximately expressed by [50]

$$\Gamma \approx \Gamma_n + \Gamma_{n-1} e^{j2kT_n} + \dots + \Gamma_1 e^{j2k(T_n + T_{n-1} + \dots + T_2)} + \Gamma_L e^{j2k(T_n + T_{n-1} + \dots + T_2 + T_1)} \quad (4.16)$$

The reflected power is the square of the absolute value of Eq. (4.16), and considering the simple cases of one or two shunt elements with equal length lines ( $\theta = kT$ ), a load reflection coefficient of -1 (i.e. a short circuit), and all reflection coefficients to be real and small, the reflected power can be described as [50]

$$|\Gamma|^2 = \begin{cases} 1 - 2\Gamma_1 \cos 2\theta, & n = 1 \\ 1 - 2\Gamma_1 \cos 2\theta - 2\Gamma_2 \cos 4\theta, & n = 2 \end{cases} \quad (4.17)$$

Using trigonometric identities, Eq. (4.17) can also be expressed in a polynomial form as [50]

$$|\Gamma|^2 = \begin{cases} 1 + 2\Gamma_1 - 4\Gamma_1 \cos^2 \theta, & n = 1 \\ 1 + 2\Gamma_1 - 2\Gamma_2 + (-4\Gamma_1 + 16\Gamma_2) \cos^2 \theta - 16\Gamma_2 \cos^4 \theta, & n = 2 \end{cases} \quad (4.18)$$

One design solution is to set all the polynomial coefficients to zero, except for the higher power terms [50]:

$$\begin{aligned} \Gamma_1 &= -\frac{1}{2}, & n &= 1 \\ \Gamma_1 &= -\frac{2}{3}, \Gamma_2 = -\frac{1}{6} & n &= 2 \end{aligned} \quad (4.19)$$

The power reflection for two-layers with  $T_1 = T_2 = \frac{\lambda_0}{4}$ , and  $f_0 = 5$  GHz is shown in Fig. 4.4. The graph shows how a frequency dip can be generated, modifying this way the radar signature of the system by just selecting the appropriate layer thickness.

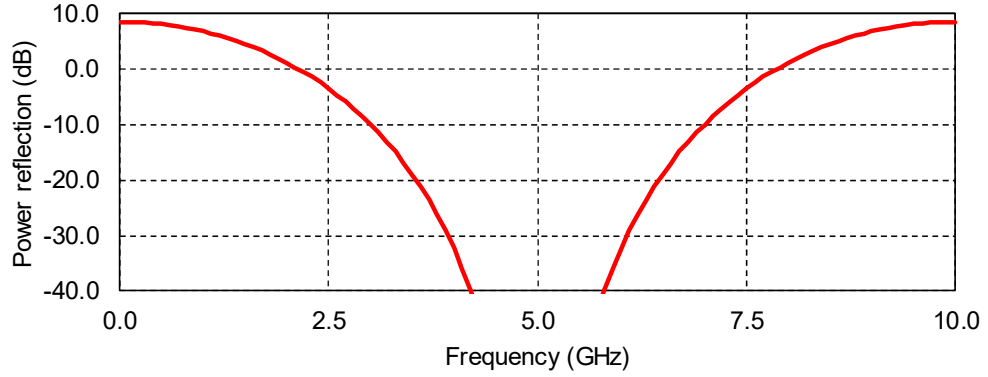


Fig. 4.4: Two-layer power reflection for  $T_1 = T_2 = \lambda_0/4$ ,  $f_0 = 5$  GHz, calculated according to Eq. (4.18)

Therefore, as previously discussed in section 2.3, the design of an UWB chipless RFID transponder is equivalent to the matching problem of a transmission line, where the main objective is to prevent reflections seen at the input cause by a short-circuit termination for a given frequency range. A case of a pure resistive sheets was studied, considering only the real part of the admittance as matching element. However, the design process gains more flexibility if the sheets can have a susceptance. An admittance imaginary part can be achieved if the continuous resistive sheets are replaced by ones with conductive material that has been deposited in a given geometrical form (e.g. dipoles, rings, octagons), namely frequency selective surfaces, which are discussed in the next section [50].

#### 4.1.4 Frequency Selective Surfaces

Frequency selective surfaces (FSS) are periodic structures, that provide a specific reflection characteristic for incident electromagnetic waves [52]. The FSS resonate at a

designed frequency and present a design problem closely related to the CA one, they are used as frequency filters which design relies on changes in reactance to achieve the desired bandpass or band stop characteristics. Typically, FSS designs consist of elements, such as dipoles, that are in the order of half-wavelength long. Fig. 4.5 depicts FSS typical geometries implemented for bandpass applications, some of them already being used as elementary elements for the design of chipless RFID transponders, as discussed in subsection 2.3.2.2 [50] [52].

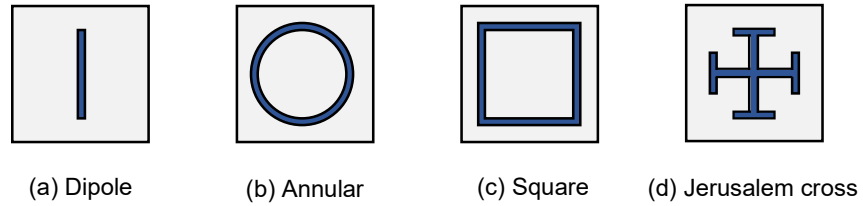


Fig. 4.5: Typical FSS element geometries [50] [52]

The design of FSS relies practically on quite sophisticated, and usually time-consuming computer programs. However, this does not prevent us from understanding the design techniques implemented, which also serve as a baseline to the design of UWB chipless RFID transponders. Considering that the layer thickness is already given, and the desired frequency performance has been established. Four main steps can be identified to complete the design process of the FSS and UWB chipless RFID transponders [50]:

1. The first step is to reach the admittance characteristics as a function of the frequency for each CA layer. The number of CA sheets depends on the RCSR required and the desired bandwidth. In the case of UWB chipless RFID transponders, they are typically designed using one single substrate layer.
2. Find a realizable geometry and conductance combinations that match closely the desired admittance characteristics.
3. Compute the design performance with the simulation tool.
4. Optimize the design performing iterations until an acceptable and doable combination is found.

The fundamentals introduced in this section, as well as the previous design steps are followed as guideline throughout this work, to design the different UWB chipless RFID transponders presented in the following sections.

## 4.2 Double-Dipoles UWB Chipless RFID Transponder

In this section, an UWB chipless RFID transponder designed based on double-dipoles (DD) is introduced. Its purpose is to conduct different detection and code identification studies using its frequency response, measured employing a VNA, and to set a baseline for the comparison to other designs and coding techniques. Its working principle and main design parameters are explained below and should serve to understand further the design basics of a multiband UWB chipless RFID transponder.

### 4.2.1 An Infinite Double-Dipole Array

It is widely known that an infinite array of dipoles can be used as a single-layer FSS and will produce a  $\Gamma$  equal to one for a resonant length of approximately half wavelength [53]. Different authors have demonstrated theoretically and practically this characteristic of FSS in the simple case of a single band-stop response [53], [54], [55]. Nevertheless, for UWB chipless RFID transponders different band-stop responses might be required to modify its radar signature in a desired form. Therefore, the single-band single-layer design illustrated in Fig. 4.5a must be modified in such a way that two or more resonant structures are placed within the same surface.

An array of elements with different resonant frequencies will produce a multi-band response but the unit reflection coefficient is no longer achieved due to the frequency dependencies between the fundamental and the harmonics frequency resonances [53]. Although a multi-band response may also be obtained by placing multiple dielectric layers of single-band FSS, as reported in [56], this solution might become quite impractical in the case of UWB chipless RFID transponders since it increases the fabrication process complexity. For that reason, only the single-layer multiband design is considered here.

To achieve the multi-band design, two types of perturbation could be applied to the single-band one: element and spacing. Element perturbation means that additional elements with different resonance frequencies are included, and space perturbation means that the same array of elements have an irregular periodicity. For the infinite double-dipole array shown in Fig. 4.6, the periodicity is regular if  $D_x = 2d$  [53]. Munk et al.

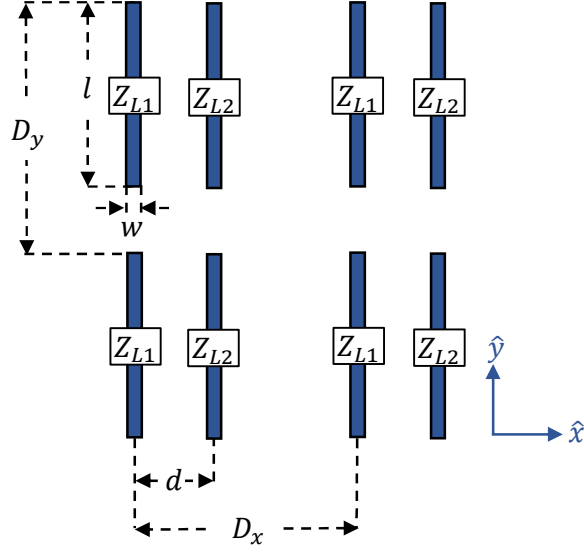


Fig. 4.6: Geometry of an infinite double-dipole array with different terminal loads composed of two interlaced dipoles [53]

developed a method to analyze these perturbations between dipole arrays using a mutual impedance approach in [54] [57]. The work was extended to include the case of two elements having different resonance frequencies by changing their terminal loads in [53], where an array of dipoles of same length and different terminal loads is assumed to simplify calculations. Then, the terminal load between the elements of an array are obtained, as well as the mutual impedance between different arrays. Afterwards,  $\Gamma$  can be found according to Eq. (4.20), for two subarrays of terminal loads  $X_{L1} = -X$  and  $X_{L2} = X$  and regular periodicity [53].

$$\Gamma = \frac{1}{1 + j \frac{X_A^2 - X^2 - X_M^2}{2R_A[X_A - X_M]}} \quad (4.20)$$

where

$X_A$  is the array reactance

$X_M$  is the array mutual reactance

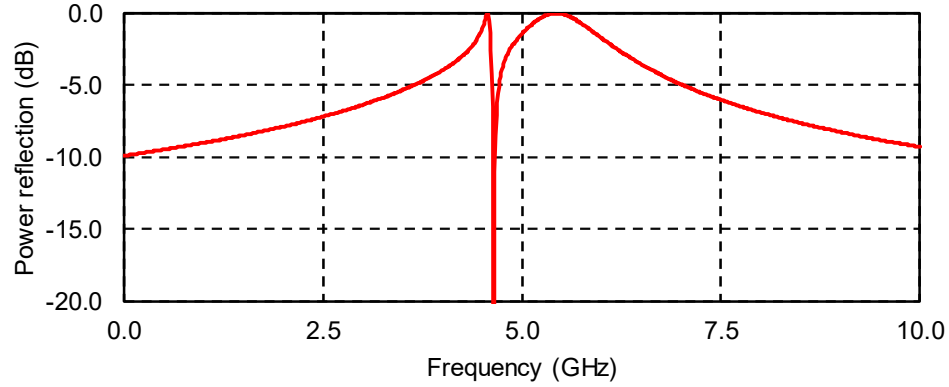
$R_A$  is the array resistance

From Eq. (4.20), it can be noted that the zero reflection is achieved when  $X_A = X_M$ , and two-unit reflections occur for  $X_A = \pm\sqrt{X^2 + X_M^2}$ . The power reflection results of the array are depicted in Fig. 4.7a for typical values for the impedance [53]. If the loads of

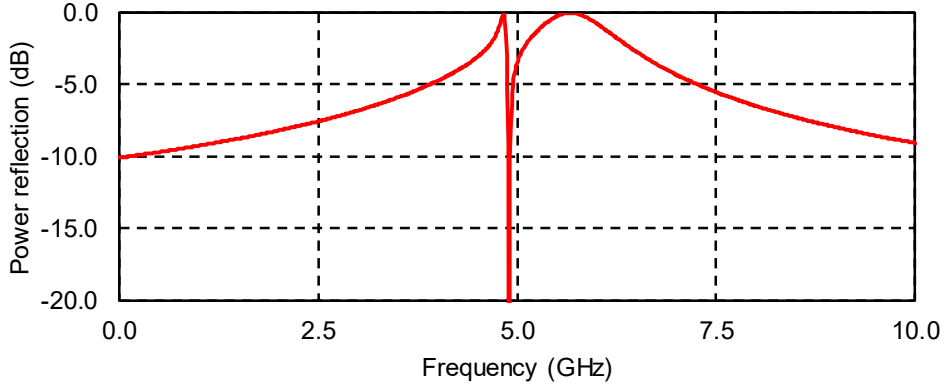
the two subarrays are equal  $X_{L1} = X_{L2} = X$  but the spacing is irregular  $D_x \neq 2d$ , the array mutual impedance obtains an additional real component  $R_M$  and  $\Gamma$  becomes [53]:

$$\Gamma = \frac{1}{1 + j \frac{(X_A - X)^2 - R_M^2 - X_M^2}{2R_A[X_A - X - X_M]}} \quad (4.21)$$

with a null when  $X_A = X + X_M$  and two unitary reflections at  $X_A = \pm \sqrt{R_M^2 + X_M^2} + X$ . The power reflection obtained is depicted in Fig. 4.7b. It can be clearly understood, that adding an element resonating at a different frequency or placing an array at irregular distances can generate a null in the final frequency response. Therefore, these effects need to be considered when designing an UWB chipless RFID transponder.



a)



b)

Fig. 4.7: Calculated power reflection of an infinite double-dipole array with: a) different terminal loads according to Eq. (4.20) and b) equal terminal loads with irregular array spacing according to Eq. (4.21).  $R_M = 45 \Omega$ ,  $X_M = -70 \Omega$ ,  $f_0 = 5 \text{ GHz}$ ,  $X = 50 \Omega$ ,  $R_A = 55 \Omega$ , and  $X_A = 1000f/f_0 - 1000 \Omega$  [53]

#### 4.2.2 Double-Dipoles UWB Chipless Transponder Design

As demonstrated in the previous section, an infinite array of two dipoles having different terminal loads, and therefore different individual resonant frequency transmission characteristics, can produce a frequency null in a determinate position in the spectrum. Although to simplify the calculations, dipoles of equal length are considered, the terminal loads can be varied by modifying the length of each dipole, thus, a finite array of two dipoles having different lengths can be used as a single-layer UWB chipless RFID transponder.

The geometry of the proposed DD-UWB chipless transponder is shown in Fig. 4.8. It consists two dipoles of lengths  $l_1$  and  $l_2$ , width  $w$ , thickness  $T$ , and separated a distance  $d$  from each other. The dipoles are placed on a dielectric substrate of relative permittivity  $\epsilon_r$  and thickness  $SubT$  [58].

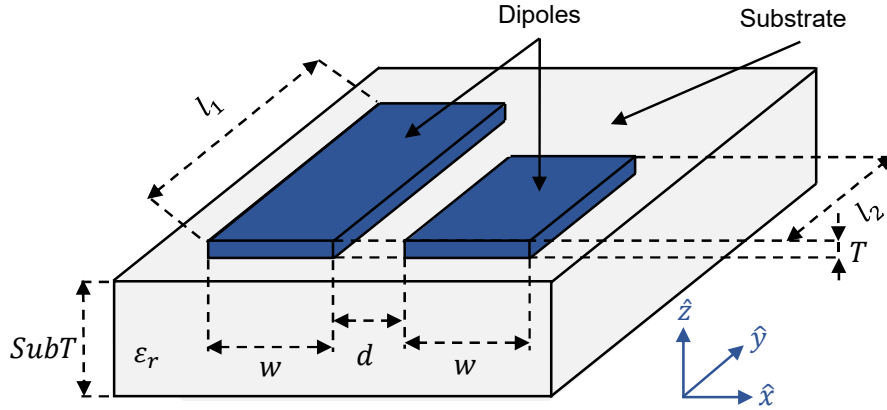


Fig. 4.8: Geometry of the dipole-based UWB chipless RFID transponder

The DD-UWB chipless transponder is designed to work between the 3 – 9 GHz frequency band and be fabricated using available low-cost organic materials or flexible electronics. Aluminum with a thin film thickness of  $35 \mu m$  is considered for the conductive dipoles, commercial bond paper with  $100 \mu m$  thickness for the substrate and are fabricated according to the procedure described in section 3.3. To assess the influence of the substrate, the ratio between the free-space wavelength  $\lambda_0$  to the lower and upper limit of the UWB frequency band is calculated and presented in Table 4.1. The substrate thickness is at least 283 times greater than  $\lambda_0$ . Therefore no resonances due to the



interaction of these two materials should be expected within this frequency range and the final frequency signature is influenced by the dipoles geometry and the materials electrical properties, like conductivity and losses, as explained in chapter 3 and section 4.1.

Frequency (GHz)	Free-space wavelength $\lambda_0$ (cm)	$\lambda_0/SubT$ $SubT = 100 \mu m$	$\lambda_0/T$ $T = 35 \mu m$
3.1	10	968	2,785
10.6	3	283	809

Table 4.1: Free-space wavelength to substrate/dipole thickness relation

Designing an UWB chipless RFID transponder with just one metallic DD array of different strip lengths and thin film thickness, as well as a substrate with different layer thickness and properties, increases considerably the problem complexity presented in previous subsection. Thus, a computer simulation software is required to perform the calculations and modeling of the UWB chipless RFID transponder frequency response. For the UWB chipless RFID transponders presented in this investigation work, Computer Simulation Technology (CST) Microwave Studio is used to obtain the RCS calculations. CST is also capable to model more complex structures, as the ones that will be presented in the following sections.

An UWB chipless RFID transponder based on a single double-dipole array with lengths  $l_1 = 35 \text{ mm}$ ,  $l_2 = 25 \text{ mm}$ , width  $w = 1 \text{ mm}$ , separation distance  $d = 5 \text{ mm}$ , and the previous mentioned materials, is modeled and simulated using CST Microwave Studio. The calculated  $|RCS|$  results for a frequency band between 3 and 9 GHz are shown in Fig. 4.9. The default material properties for aluminum and bond paper provided by CST Microwave Studio are used to run the simulation. The obtained simulation results show a similar behavior generating a frequency dip at around 5 GHz, as the theoretical calculate ones for the infinite double-dipole arrays of Fig. 4.7 in section 4.2.1. However, unlike its theoretical calculation, no zero or unitary reflections are achieved since the array is no longer infinite.

The peak magnitude and frequency dip depth terms are introduced, to evaluate the performance and be able to compare between different UWB chipless RFID transponders frequency responses. The first one, as a measured of the reflectivity and the second one

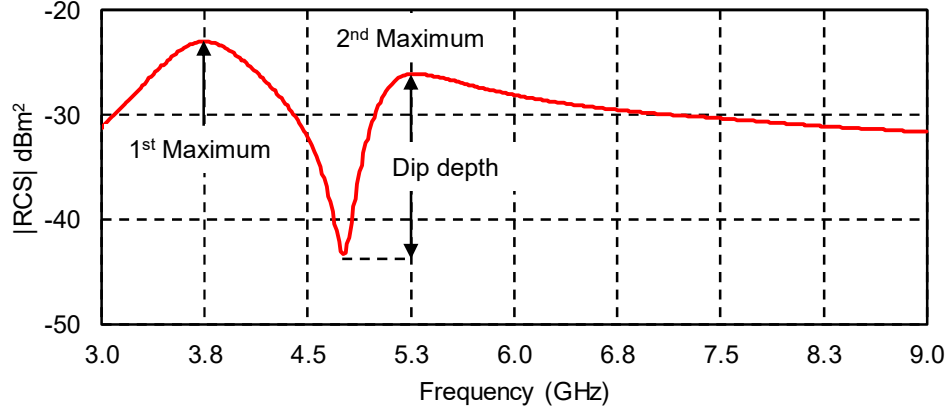


Fig. 4.9: Simulated  $|RCS|$  of a dipole-based UWB chipless RFID transponder,  $l_1 = 35 \text{ mm}$ ,  $l_2 = 25 \text{ mm}$ ,  $w = 1 \text{ mm}$ ,  $d = 5 \text{ mm}$ ,  $T = 35 \text{ }\mu\text{m}$ ,  $SubT = 100 \text{ }\mu\text{m}$

of the resonance capabilities. The peak magnitude is given by the maximum value of the RCS at each specific peak. The dip frequency depth is the difference between the dip center frequency and the closest peak magnitudes. Both terms are also illustrated in Fig. 4.9. In general, peaks and dips are numbered in increasing order starting from the one located at the lower frequency. As can be seen, the first peak magnitude is located at 3.8 GHz and has a value of -23 dBm<sup>2</sup> and the dip depth measured from the dip center frequency located at 4.8 GHz and the second peak magnitude at 5.3 GHz is 16.5 dB.

Additional frequency resonances can be generated varying the dipoles lengths. Table 4.2 presents four different length configurations to produce equal number of DD-UWB chipless RFID transponders, and their respective  $|RCS|$  simulation results are shown in Fig. 4.10. It can be noticed by simple visual inspection, that as the dipoles' lengths are reduced, the observed frequency dip is shifted to the higher frequencies, and

Transponder number	Microstrip line 1 length (mm)	Microstrip line 2 length (mm)	Assigned binary code
1	35	25	00
2	32	22	01
3	28	18	10
4	23	13	11

Table 4.2: Double-dipole UWB chipless RFID transponder strips lengths [58]

its stop band becomes wider. Furthermore, under this context, each UWB chipless RFID transponder can be considered as having its own unique frequency response, which is determinate by its whole spectrum characteristic, and with special emphasis on the different frequency dips generated at specific frequency ranges.

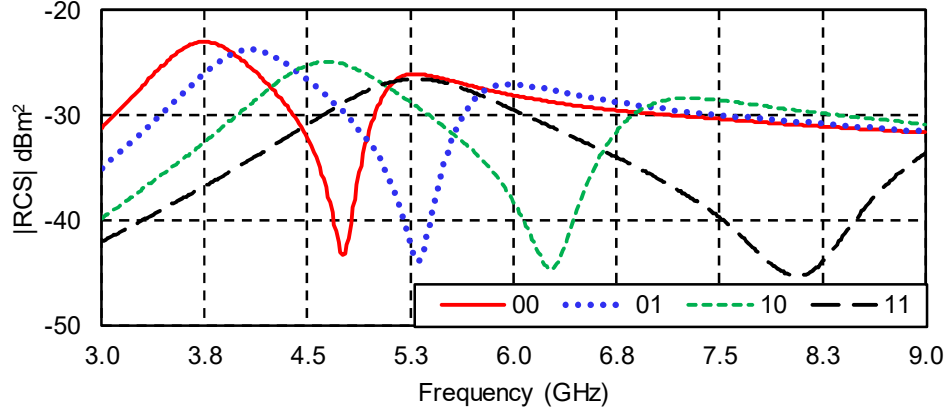


Fig. 4.10: Simulated  $|RCS|$  of different dipole-based UWB chipless RFID transponder for the different lengths configurations specified in Table 4.2 [58]

The UWB chipless RFID transponders coding principle is based on these frequency signatures, however, as explained in section 2.3, every author chooses a distinct characteristic to encode the information e.g. frequency dip/peak, phase, group delay, etc. In this work, a computer system and not the human eye must perform the detection. Thus, the coding technique must be developed not only from the transponders perspective but also considering the detector limitations. Therefore an arbitrary identification code will be assigned to each transponder having a unique frequency response, as done in Table 4.2, and further details regarding the coding techniques and detection capabilities will be discussed in detail in chapter 6.

### 4.2.3 Prototype Fabrication

A photograph of a DD-UWB chipless RFID transponder prototype with dipoles lengths  $l_1 = 35$  mm and  $l_2 = 25$  mm is shown in Fig. 4.11a. All four previously modeled and simulated different combinations of UWB chipless RFID transponders are fabricated and shown in Fig. 4.11b with their respective assigned identification codes.

The scattering parameters of all the fabricated DD-UWB chipless RFID transponders are obtained using the bi-static measurement setup depicted in Fig. A.1. The

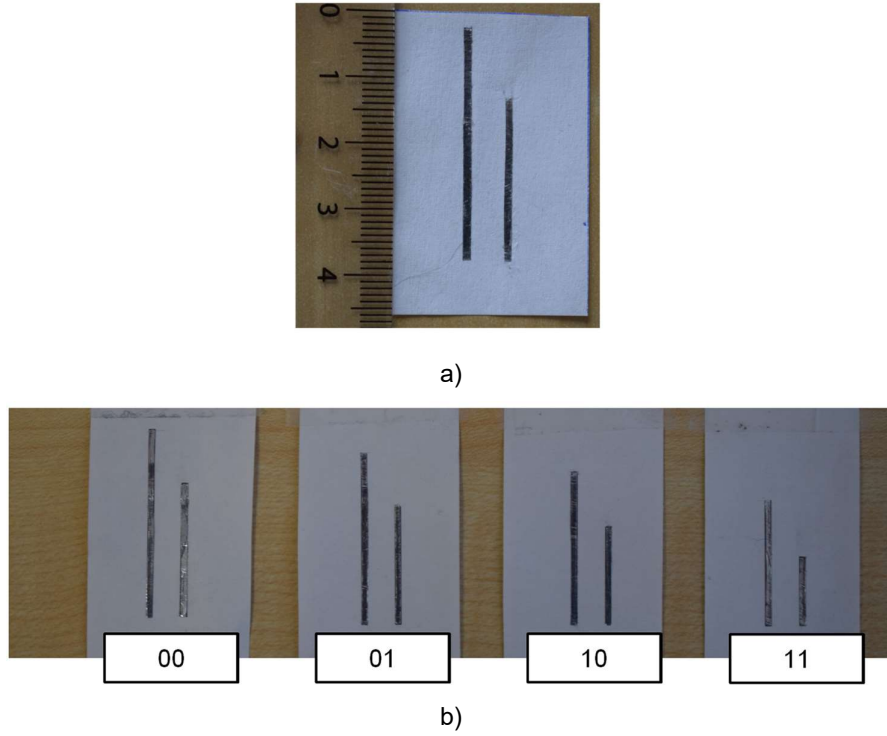


Fig. 4.11: Photograph of a) an UWB chipless RFID transponder prototype with two aluminum dipoles on bond paper substrate,  $w = 1$  mm,  $l_1 = 35$  mm,  $l_2 = 25$  mm, and  $d = 5$  mm b) all four UWB chipless RFID transponders defined in Table 4.2 [58]

VNA has been configured to measure the 3.5 – 9 GHz frequency spectrum, with a power control of 3 dB, and an averaging factor of 20 sweeps per measurement, a total of 201 frequency samples are taken. The separation distance between the horn antennas and the DD-UWB chipless RFID transponders is 30 cm.

The  $|RCS|$  values of each DD-UWB chipless RFID transponder are calculated using Eq. (A.10) and the procedure described in Appendix A. The calculated  $|RCS|$  results are shown in Fig. 4.12. As can be seen, all UWB chipless RFID transponders frequency responses can be easily identified by visual inspection, differentiated between them and are in accordance with the simulated ones presented in Fig. 4.10.

Table 4.3 resumes the  $|RCS|$  performance values for all fabricated DD-UWB chipless RFID transponders. The frequency peaks magnitudes and the frequency dip depths differ slightly among identification codes. The measurements show a 300 MHz shift to a lower frequency, an average peak magnitude and peak depth variation of around  $\pm 1$  dB with respect to the simulated values.

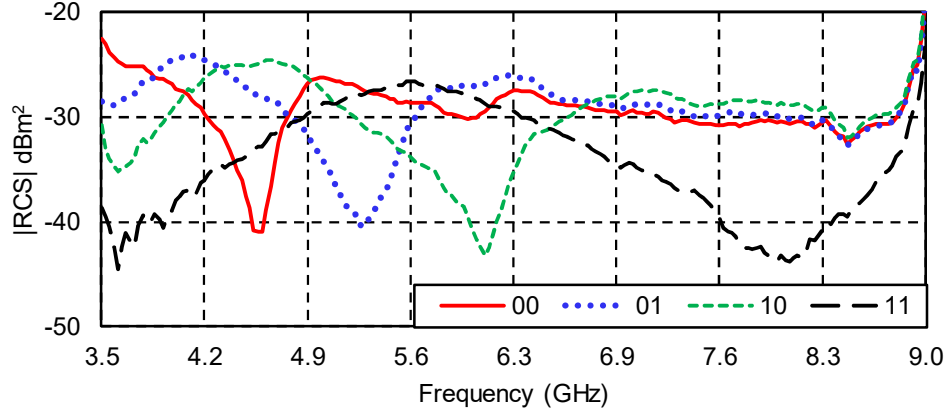


Fig. 4.12: Calculated  $|RCS|$  from measured scattering parameters for the different DD-UWB chipless RFID transponders [58]

Tranponder code	Peak magnitude (dBm <sup>2</sup> )		Frequency dip depth (dB)
	1 <sup>st</sup>	2 <sup>nd</sup>	
00	-25.8	-26.9	13.9
01	-24.2	-27.8	12.5
10	-24.9	-27.6	14.9
11	-26.7	-29.3	14.4
Average	-25.4	-26.9	13.9

Table 4.3: Calculated frequency peak magnitudes and dips depths for the different DD-UWB chipless RFID transponders

### 4.3 UWB Chipless RFID Transponder with Concentric Circles

An array of concentric circles can also be used to design an UWB chipless RFID transponder, as previously proposed by Vena et. al. in [34] and Islam et. al. in [59], adding features like polarization and orientation independency. In this section, two different structures based on the concentric circles' geometries are presented and designed to work in different frequency bands.

The concentric circles (CC) UWB chipless RFID transponder is designed to study the influence of the fabrication technologies, substrate materials and metallic thin film

conductivity on the frequency response. As well as to explore potential characteristics that could be useful in the simultaneous detection of multiple nearly placed UWB chipless RFID transponders having the same identification code or to improve the  $|RCS|$  response [60]. The concentric rings (CR) UWB chipless RFID transponder on the other hand, is designed to implement a novel coding technique based on frequency response differentiation and is meant to be interrogated by the SFM-reader developed in chapter 5.

#### 4.3.1 Concentric Circles UWB Chipless Transponder

The geometry of the proposed CC-UWB chipless transponder is shown in Fig. 4.13a, it is based on three concentric rings and one disk. The previous basically due to its orientation independent backscattered response, reduced size and easiness to fabricate employing different manufacturing processes. It consists of three concentric rings and one disk. The concentric rings are placed on a dielectric substrate of relative permittivity  $\epsilon_r$  and thickness  $SubT$  [60].

The concentric circles UWB chipless RFID transponder is modeled using commercial bond paper with  $100\ \mu m$  thickness for the substrate, copper with a thin film thickness of  $35\ \mu m$  for the conductive strips, an outer radius  $r = 14\ mm$ , and equal strip widths  $w$  and gaps  $g$  of  $1\ mm$ . The  $|RCS|$  is simulated between the  $0 - 8\ GHz$  frequency band using CST Microwave Studio and the results are shown in Fig. 4.13b. The CC-UWB chipless RFID transponder is designed to obtain three frequency reflection peaks and dips within a  $3.2\ GHz$  bandwidth ( $3.1 - 6.3\ GHz$ ), the simulated peaks are located at  $3.4, 4.0$  and  $5\ GHz$ , and three frequency dips at  $3.6, 4.5$  and  $6.3\ GHz$ , as can be clearly seen [60].

As previously mentioned, the CC-UWB chipless RFID transponder's purpose, is to investigate the influence on the frequency signature of the selection of different types of substrates and conductive thin films materials, as well as the fabrication processes. Furthermore, the impact of placing several CC-UWB chipless RFID transponders side by side and close to each other on the  $|RCS|$  is also studied, to help in the development of proper approaches to achieve the multi-detection of chipless RFID transponders having the same identification code. Thus, for this specific UWB chipless RFID transponder, no coding technique or additional transponders with different identification codes are designed nor fabricated [60].

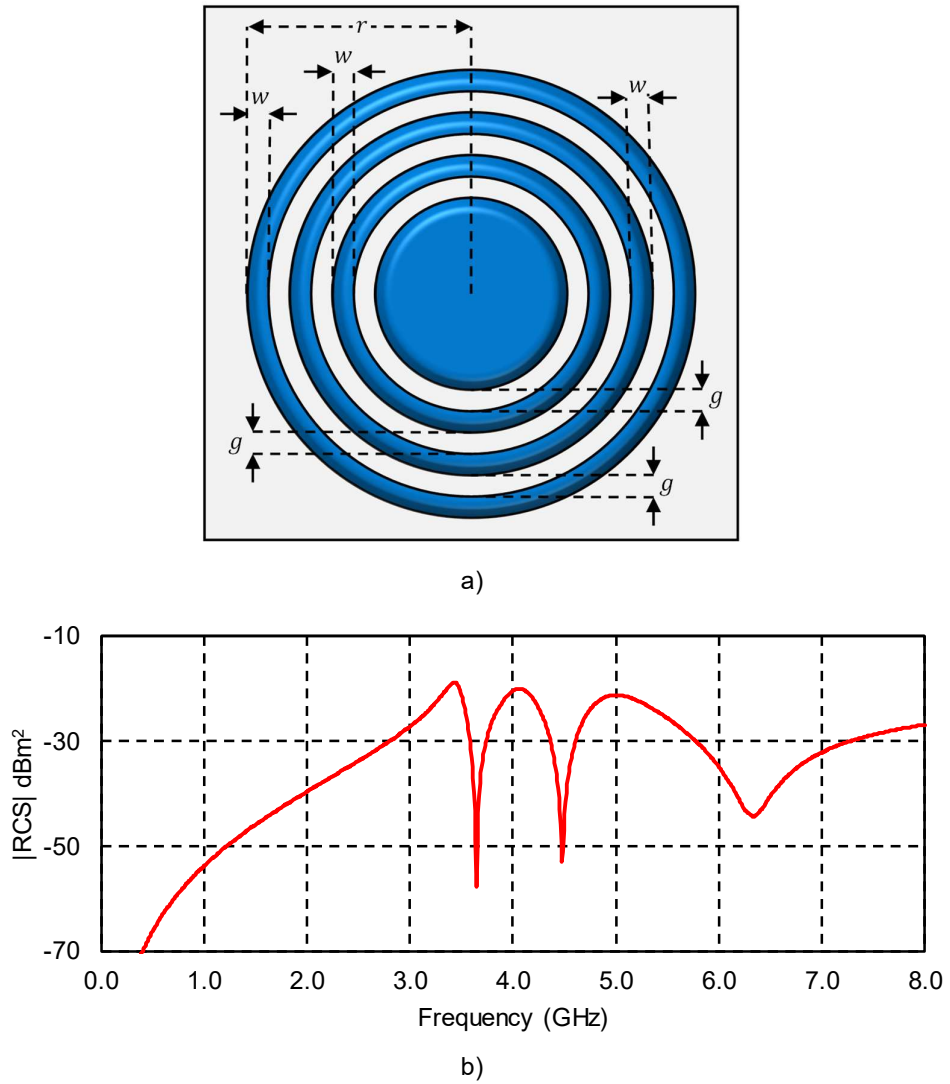


Fig. 4.13: CC-UWB chipless RFID transponder: a) geometry based on three concentric rings and one disk, b)  $|RCS|$  simulation results for  $r = 14 \text{ mm}$ ,  $g = w = 1 \text{ mm}$  [60]

#### 4.3.1.1 Substrate Influence

The influence of the substrate selection on the frequency response of the proposed CC-UWB chipless RFID transponder is experimentally investigated in this section. As no information regarding the electrical parameters for these substrates is available, and the simulation tool does not provide the option to simulate metallic inks, no simulations can be ran and the experiments are conducted merely empirically.

The CC-UWB chipless RFID transponders are manufactured on three different substrates employing both the screen and flexography printing technologies described in Chapter 3. A picture of the different prototypes can be seen in Fig. 4.14, five prototypes of the proposed structure are fabricated, three using screen printing on either PET, glossy paper or Fasson are shown in in Fig. 4.14a, and two using flexography printing on PET or glossy paper are illustrated in Fig. 4.14b.

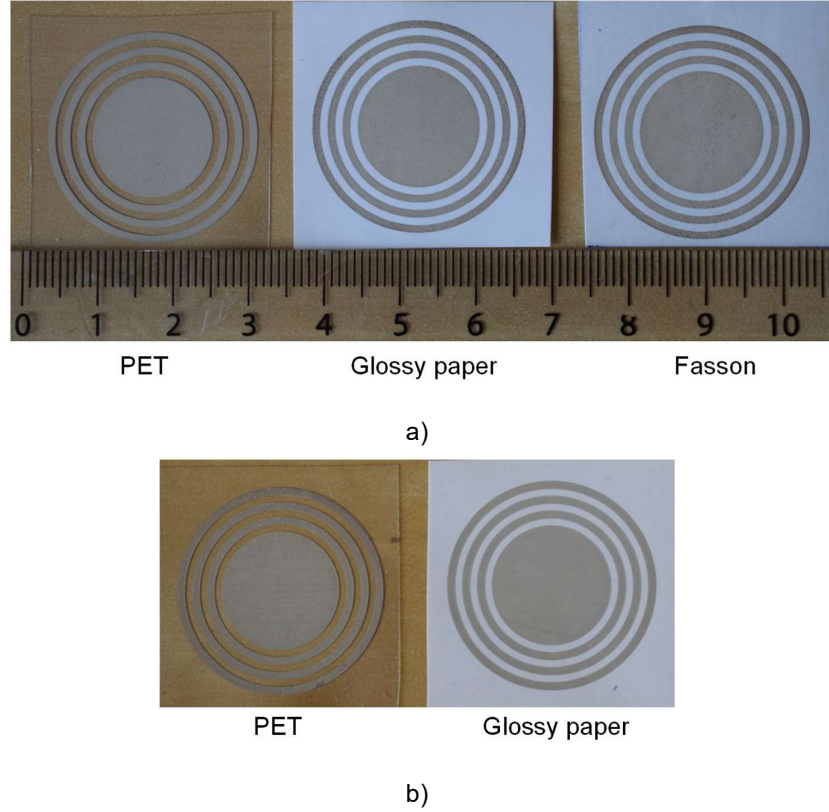
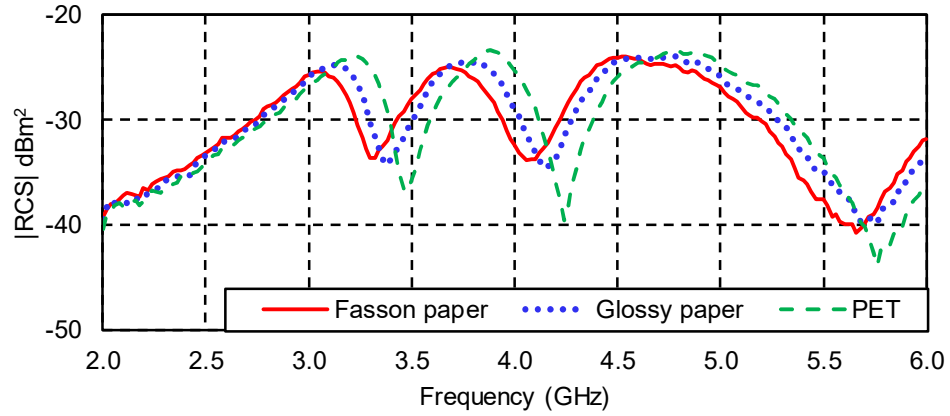


Fig. 4.14: CC-UWB chipless RFID transponders fabricated using: a) screen printing technology on PET, glossy paper and Fasson, b) flexography printing on PET and glossy paper

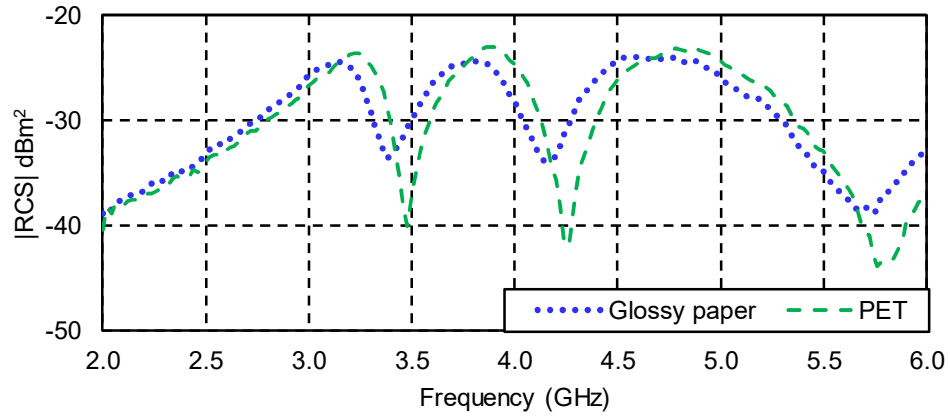
The scattering parameters of the different prototypes are measured using the measurement setup of Fig. A.1 in Appendix A, the VNA is configured to sweep the frequency band of interest (2 – 6 GHz), with a power control of 3 dB, an averaging factor of 90 sweeps per measurement and a total of 201 frequency samples. The separation distance between the horn antennas and the CC-UWB chipless RFID transponders is of 30 cm. The  $|RCS|$  is calculated using the methodology and procedure described in Appendix A, and the results are shown in Fig. 4.15, as can be seen, changing the type of



substrate has a direct influence on the frequency signature of the UWB chipless RFID transponder, as explained in sections 4.1.2 and 3.1.1. Two main frequency effects can be clearly identified: a frequency shift due to the different material permittivities, and a change in the  $|RCS|$  magnitude values due to the material losses.



a)



b)

Fig. 4.15: Calculated  $|RCS|$  from measured scattering parameters for a transponders fabricated with: a) screen printing technology on glossy and Fasson papers, as well as PET, and b) flexography printing on glossy paper and PET

Table 4.4 resumes the position of the measured frequency peaks and dips for each substrate fabrication and printing technology. In the case of the screen-printed technology, a change from Fasson substrate to glossy paper represents in average a shift to a higher frequency of about 100 MHz, in the same way, but for both printed technologies, changing from glossy paper to PET represents another shift to a higher frequency of about 100 MHz, and no major frequency shift difference is experienced due to the use of a specific printed technology for prototypes fabricated on the same substrate.

Furthermore, comparing the PET samples against the copper thin film on bond paper simulated results of Fig. 4.13b, a frequency shift to a lower frequency of 100 MHz is observed for the first frequency dip, one of 200 MHz for the second one, and around 500 MHz for the third one, this due to the higher permittivity values of the PET over the bond paper, as explained in subsection 3.1.1.

Frequency	Position (GHz)				
	Screen			Flexography	
	Fasson paper	Glossy paper	PET	Glossy paper	PET
1 <sup>st</sup> peak	3.1	3.2	3.3	3.2	3.3
2 <sup>nd</sup> peak	3.7	3.8	3.9	3.8	3.9
3 <sup>rd</sup> peak	4.5	4.6	4.7	4.6	4.9
1 <sup>st</sup> dip	3.3	3.4	3.5	3.4	3.5
2 <sup>nd</sup> dip	4.1	4.2	4.3	4.2	4.3
3 <sup>rd</sup> dip	5.7	5.8	5.9	5.7	5.8

Table 4.4: Measured frequency peak and dips positions

Depending on the type of implemented coding technique and the UWB chipless RFID transponder frequency signature, a frequency shift due to a change of substrate might represent a significant degradation that could lead to incorrectly recognize the intended identification code. Researches are specially focused on investigating coding techniques, where the frequency peaks/dips have sharper characteristics, and in this way, produce more peaks/dips within the same bandwidth, in an effort to use the UWB frequency spectrum more efficiently, e.g. the UWB chipless RFID transponder based on open conical resonators presented in section 2.3.2.2 uses a frequency peak-position coding technique, where the difference between a peak representing a 1 and one representing a 0 is of only 100 MHz. Therefore, replacing the substrate for this type of structure, represents a shift to a new bit leading to detecting the wrong identification code. Thus, the UWB chipless RFID transponder designer will have to either re-design the transponder according to the desired substrate or implement another coding technique robust enough to overcome the effects of a substrate change.

Table 4.5 resumes the CC-UWB chipless RFID transponders  $|RCS|$  performance values for all manufactured prototypes. The frequency peaks magnitudes and the frequency dip depths differ among different substrate and printing technology fabrications. The screen printed on glossy paper prototypes seen in Fig. 4.15a have slightly better performance than their Fasson counterparts, and a major improvement is achieved from Fasson to PET, where especially the resonance capabilities measured by the dip depth is improved considerably by an average value of 5.4 dB. Comparing the PET samples against the copper thin film on bond paper simulated results of Fig. 4.13b, degradations of around 4 dB in the peak magnitude and around 12 dB in the dip depth are observed with respect to the simulated ones.

Printing technology	Frequency peak/dip	Peak magnitude (dBm <sup>2</sup> )			Dip depth (dB)		
		Fasson	Glossy	PET	Fasson	Glossy	PET
Screen	1 <sup>st</sup>	-25.5	-24.8	-24.2	8.5	9.1	13.0
	2 <sup>nd</sup>	-25.1	-24.5	-23.6	8.7	9.6	16.0
	3 <sup>rd</sup>	-24.4	-24.3	-23.7	15.8	14.9	20.2
Average		-25.0	-24.5	-23.8	11.0	11.2	16.4
Flexography	1 <sup>st</sup>		-24.9	-23.7		9.3	16.95
	2 <sup>nd</sup>		-23.9	-23.2		10.4	18.85
	3 <sup>rd</sup>		-24.2	-23.3		14.1	20.6
Average			-24.3	-23.4		11.3	18.8

Table 4.5: Calculated frequency peak magnitudes and dips depths for the CC-UWB chipless RFID transponders fabricated on different substrates and printing technologies

The flexography printed prototypes shown in Fig. 4.15b, experience a similar trend as their screen printed counterparts, where an improvement in the peaks magnitude can be appreciated from glossy paper to PET, but the major change is produced in the dip depth with an average improvement value of 7.5 dB. Moreover, the flexography printed prototypes also show in general better performance than the screen-printed ones, due to the influence of conductive thin film thickness that will be explained in the next section.

#### 4.3.1.2 Conductive Thin Film Thickness Influence

The conductive film thickness is one key parameter that has a direct impact on the final manufacturing cost of UWB chipless RFID transponders in printed electronics on flexible substrates, as well on its RF performance. As explained in section 3.1.2, nowadays, silver-based ink, is the most reported conductive film material in printed electronics. Nevertheless, its cost is still high, and additionally, production parameters like thin film thickness need to be optimized to fabricate the best cost-efficient UWB chipless RFID transponder, while fulfilling at the same time the target performance requirements of the design.

In this section, the CC-UWB chipless RFID transponders prototypes depicted in Fig. 4.16 are fabricated to assess the influence of the conductive thin film thickness on the frequency signature performance. For this purpose, the transponders are printed by flexography with different conductive thin film thicknesses on glossy paper or PET substrates. Eight prototypes with different conductive thin film thicknesses of the proposed structure are fabricated, three on glossy paper shown in Fig. 4.16a and five on PET illustrated in Fig. 4.16b.

The thin film thicknesses variations are achieved by changing the silver-ink density, that is, the proportion between silver particles and polymers. The pictures of two different CC-UWB chipless RFID transponder conductive thin films, printed with different thicknesses on PET substrate are shown in Fig. 4.17. The pictures were taken using the Technische Universität Chemnitz's Keyence laser-scanning microscope VK-9700. The silver ink on PET (SP) samples with the thinner  $T_1$  and thicker  $T_5$  thin films are chosen to contrast the silver particles deposition differences. As explained in section 3.1.2 and illustrated in the pictures, the formation of numerous percolation paths between metal particles is experienced in the case of the thinner film  $SP - T_1$  prototype, which should reduce the conductive thin film conductivity, while the thicker thin film, on the other hand, shows a more homogeneous appearance.

To evaluate the influence of the thin film thickness on the performance of the CC-UWB chipless RFID transponder, the achieved thin film conductivity  $\kappa$  values need to be correlated with the  $|RCS|$  calculated ones. Therefore, the value of the conductivity is required for each prototype under test. A procedure was established to estimate the

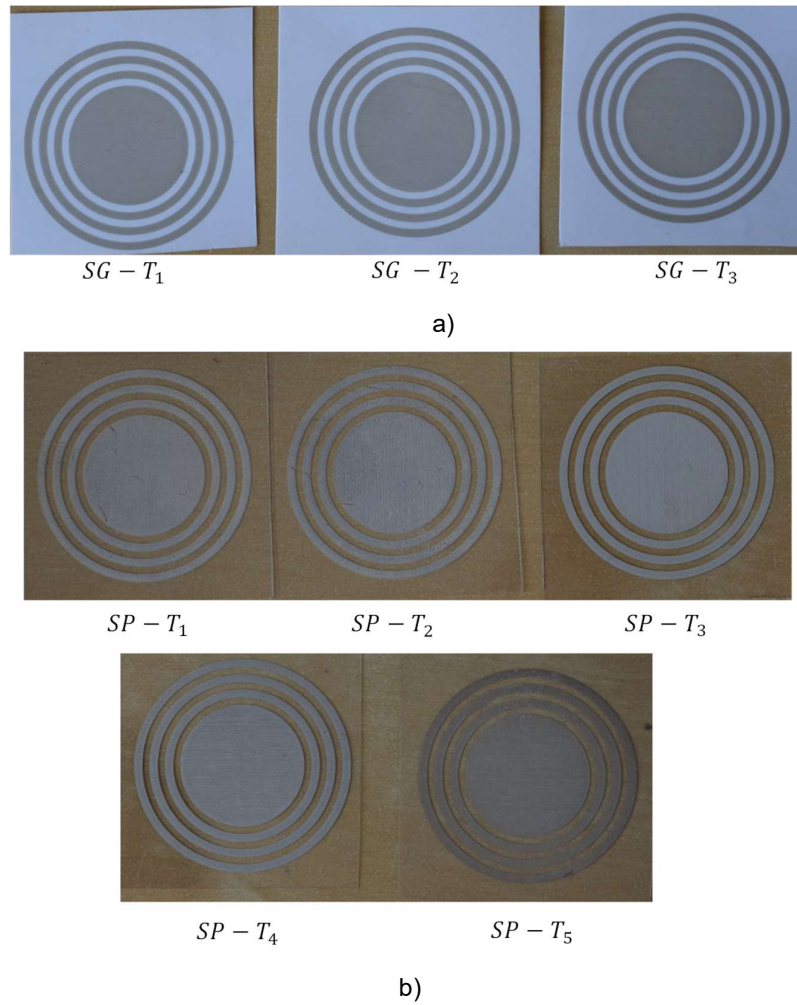


Fig. 4.16: Flexography printed CC-UWB chipless RFID transponders on: a) glossy paper with conductive thin film thicknesses  $SG - T_1 = 2.8 \mu m$ ,  $SG - T_2 = 3.2 \mu m$  and  $SG - T_3 = 3.7 \mu m$ , b) PET with conductive thin film thicknesses  $SP - T_1 = 3.9 \mu m$ ,  $SP - T_2 = 4.2 \mu m$ ,  $SP - T_3 = 6.2 \mu m$ ,  $SP - T_4 = 6.4 \mu m$ , and  $SP - T_5 = 7.5 \mu m$

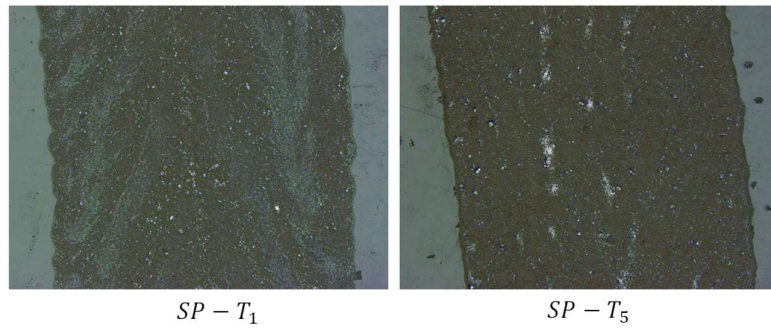


Fig. 4.17: Laser-scanning microscope pictures of two conductive thin film with thickness  $T_1$  and  $T_5$  printed on PET substrate (Photo by Dr. Georg Schmidt, TUC)

conductivity values, considering the thin film thickness, as well as the two-points direct current (DC) resistance measurements, and is described in detail in Appendix B. Table 4.6 presents the results of the average measured thin film thickness for each prototype taken by the laser-scanning microscope at the Technische Universität Chemnitz premises. The DC resistance values of each individual ring resonator, starting from the outer ring  $R_1$  to the inner one  $R_3$ , are measured using the digital multimeter Voltcraft model VC830 and the conductivity values are calculated using the measured resistances and the ring resonators physical dimensions, as explained in Appendix B. As can be seen, as the layer thickness increases, the measured resistance decreases, not only as a product of the its dependency of the thin film thickness  $R \sim 1/T$ , but also because of the improvement in the resultant thin film conductivity  $R \sim 1/\kappa$ , which has also increased with the thickness. The previous due to an enhancement in the connections between the silver particles and the reduction of the percolation paths. For the specific case of the concentric rings printed on PET, a thin film thickness change from 3.9 to 7.5  $\mu\text{m}$ , that is, an increase of roughly two times its initial value, represents an estimated average conductivity increase from  $0.02 \times 10^6$  to  $1.85 \times 10^6$  S/m, which means an average increase of almost 92 times. The concentric rings printed on glossy paper, on the other hand, a change 1.32 times in the thin film thickness, represents an average increase of 2.4 times in the resultant estimated conductivity.

Another parameter shown the Table 4.6, is the skin depth  $\delta$ , and is meant to show the minimum thickness required for the conductive thin film to dissipate  $1/e$  of the current density. The skin depth is calculated considering the respective conductivity values at the specific frequency. As can be seen, for the ring resonators of  $SP - T_1$ , which have the highest DC resistance and the lowest conductive thin film thickness values, a thickness of at least 62.10  $\mu\text{m}$  at 3.1 GHz is required, that is 16 times more than the 3.90  $\mu\text{m}$  it has. Therefore, the thin film doesn't provide enough thickness to keep the current density, and this last one will pass through to the substrate and be lost in material losses rather than generating the desired frequency resonance. The thicker ring resonators  $SP - T_5$ , on the other hand, which are the ones with the lowest DC resistance values, required a thin film thickness is 6.65  $\mu\text{m}$  at 3.1 GHz, which represents 0.90 of the 7.50  $\mu\text{m}$  it has.

The scattering parameters of the different prototypes are measured with the measurement setup described in Fig. A.2 of Appendix A. The VNA has been configured

Substrate	Prototype	Thickness $T$ ( $\mu\text{m}$ )	Resistance $R$ ( $\Omega$ )			Conductivity $\kappa$ (S/m) ( $10^6$ )			Skin depth $\delta$ ( $\mu\text{m}$ )	
			$R_1$	$R_2$	$R_3$	$\kappa_1$	$\kappa_3$	$\kappa_3$	@3.1 GHz	@6 GHz
Glossy paper	$SG - T_1$	2.8	6.0	5.0	4.2	1.26	1.29	1.27	8.01	5.76
	$SG - T_2$	3.2	2.5	2.1	1.7	2.65	2.69	2.74	5.51	3.96
	$SG - T_3$	3.7	1.9	1.6	1.3	3.02	3.05	3.10	5.17	3.72
PET	$SP - T_1$	3.9	322.4	240.0	139.5	0.02	0.02	0.03	62.1	44.6
	$SP - T_2$	4.2	34.5	38.3	28.5	0.15	0.11	0.13	25.30	18.20
	$SP - T_3$	6.2	3.5	3.1	2.5	0.90	0.88	0.83	9.69	6.97
	$SP - T_4$	6.4	3.7	3.2	2.8	0.98	0.94	0.96	9.23	6.63
	$SP - T_5$	7.5	1.5	1.3	1.1	1.88	1.85	1.81	6.65	4.78

Table 4.6: CC-UWB chipless RFID transponder printed with different silver-ink thin film thicknesses electric parameters (thin film thicknesses provided by Mrs. Katherina Haase, TUC)

to measure the frequency spectrum located between 2 and 7 GHz, with a maximum power output, an averaging factor of 200 sweeps per measurement, and the sample point's number is set to 201. The  $|RCS|$  is calculated following the procedure described in Appendix A, the results for both type of substrates, glossy paper and PET, are shown in Fig. 4.18, as illustrated, changing the conductive thin film thickness has a direct impact on frequency signature of the UWB chipless RFID transponder. As the thin film thickness increases and therefore its conductivity, enhancing the resonance capabilities and obtaining sharper dips with greater depths, improving the shape of the frequency response

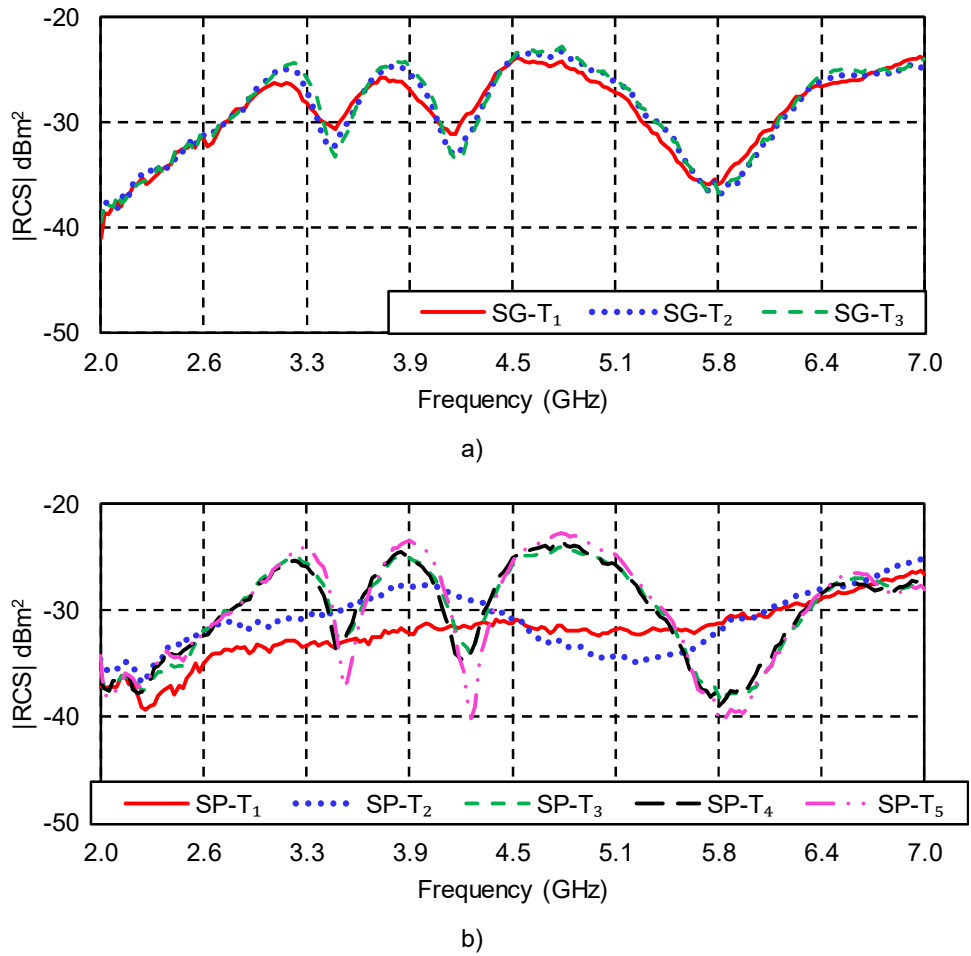


Fig. 4.18: Calculated  $|RCS|$  from measured scattering parameters for a CC-UWB chipless RFID transponder fabricated printing silver-ink with different thin film thicknesses on: a) glossy paper  $SG - T_1 = 2.8 \mu m$ ,  $SG - T_2 = 3.2 \mu m$  and  $SG - T_3 = 3.7 \mu m$ , b) PET  $SP - T_1 = 3.9 \mu m$ ,  $SP - T_2 = 4.2 \mu m$ ,  $SP - T_3 = 6.2 \mu m$ ,  $SP - T_4 = 6.4 \mu m$ , and  $SP - T_5 = 7.5 \mu m$



and approaching it to the simulated shape of the copper thin film on bond paper in Fig. 4.13b.

Table 4.7 presents the silver-ink based CC-UWB chipless RFID transponders [RCS] performance values for all manufactured prototypes. For the prototypes fabricated with silver-ink on glossy paper (SG), approximately an average of 1 dB peak magnitude improvement is achieved from  $SG - T_1$  to  $SG - T_2$ , and no significant changes (around 0.5 dB) are experienced from  $SG - T_2$  to  $SG - T_3$ . The resonance capabilities given by the dip depth are improved in 2.4 dB average from  $SG - T_1$  to  $SG - T_2$  and no meaningful changes are observed from  $SG - T_2$  to  $SG - T_3$  (0.9 dB). In the case of the prototypes fabricated on PET substrate, the  $SP - T_1$  and  $SP - T_2$  samples, have the poorest conductivity, and thin film thickness way below the required minimum skin depth. Thus, they are not able to produce a frequency response according to the expected shape shown in Fig. 4.18b. Nevertheless, a major enhancement is experienced from  $SP - T_2$  to  $SP - T_3$ , obtaining a well-defined frequency response in accordance to the simulated one. The peak magnitude calculations also show no significant changes from  $SP - T_3$  to  $SP - T_4$ , and from  $SP - T_4$  to  $SP - T_5$  up to 1.5 dB. However, a considerable change in the resonance capabilities of the frequency dips is obtained from  $SP - T_4$  to  $SP - T_5$ , where an average dip depth of 4.8 dB achieved. In general, for the  $SP - T_3$  and  $SP - T_5$  samples, degradations can be observed of around 3 dB in the peak magnitude with respect

Parameter	Frequency peak/dip	Glossy paper			PET		
		SG- $T_1$	SG- $T_2$	SG- $T_3$	SP- $T_3$	SP- $T_4$	SP- $T_5$
Peak magnitude (dBm <sup>2</sup> )	1 <sup>st</sup>	-26.4	-24.9	-24.4	-25.1	-25.3	-24.2
	2 <sup>nd</sup>	-25.8	-24.9	-24.2	-25.1	-24.5	-23.5
	3 <sup>rd</sup>	-23.8	-23.5	-23.3	-24.4	-24.2	-22.9
Average		-25.3	-24.4	-23.9	-24.9	-24.7	-23.5
Dip depth (dB)	1 <sup>st</sup>	4.0	7.2	8.5	7.6	7.7	12.6
	2 <sup>nd</sup>	5.2	9.3	10.3	9.9	9.9	16.6
	3 <sup>rd</sup>	12.0	12.0	12.3	11.0	10.7	13.4
Average		7.1	9.5	10.4	9.5	9.4	14.2

Table 4.7: Calculated frequency peak magnitudes and dips depths for the CC-UWB chipless RFID transponders fabricated on different substrates and thin film thicknesses

to the copper thin film on bond paper simulation of Fig. 4.18b, and around 18 dB and 14 dB in their dip depth respectively.

Now that the printed conductive thin film thickness/conductivity influence on the RF performance of the UWB chipless RFID transponders fabricated has been assessed, and the baseline for their characterization has been established. Further studies involving other metallic inks based on copper can be carried out and are explained in the next section.

### 4.3.1.3 Copper-Inks based Prototypes

As discussed in subsection 3.1.2, although copper is cheaper than silver and therefore a suitable candidate for the fabrication of UWB chipless RFID transponders, copper-based inks are more challenging to fabricate than silver ones due to the oxidation process. Additionally, the previous section has taught us the importance of the conductive thin film thickness to achieve higher values of conductivity. Therefore, in this section, the frequency response of the CC-UWB chipless RFID transponder fabricated using a copper-based ink is investigated. For that reason, a water-based ink formulation is synthesized using copper flakes and 40% of silver-coating at the Technische Universität Chemnitz premises by its personnel. Thicker conductive thin films as the ones studied in the previous section are printed, to improve the final conductivity values and compensate the expected degradations. The manufactured prototypes are depicted in Fig. 4.19 and are flexography printed on either glossy paper or PET.

Table 4.8 presents the results of the average measured conductive thin film thickness taken with the laser-scanning microscope at Technische Universität Chemnitz. The DC resistance values of each individual ring resonator are measured using digital multimeter Voltcraft model VC830. The conductivity values are estimated using the measured conductive thin film thickness, the DC resistances, and the ring resonators physical dimensions, as explained in Appendix B. As can be seen, once again, as the layer thickness increases, the measured resistance decreases, and the obtained resistance values are in general higher than the ones presented in Table 4.6 for the working silver-ink based prototypes but lower than the ones that didn't produce a satisfactory frequency response. Thus, an enhancement with respect to these last ones can be expected but with performances below the ones with lower DC resistance values.

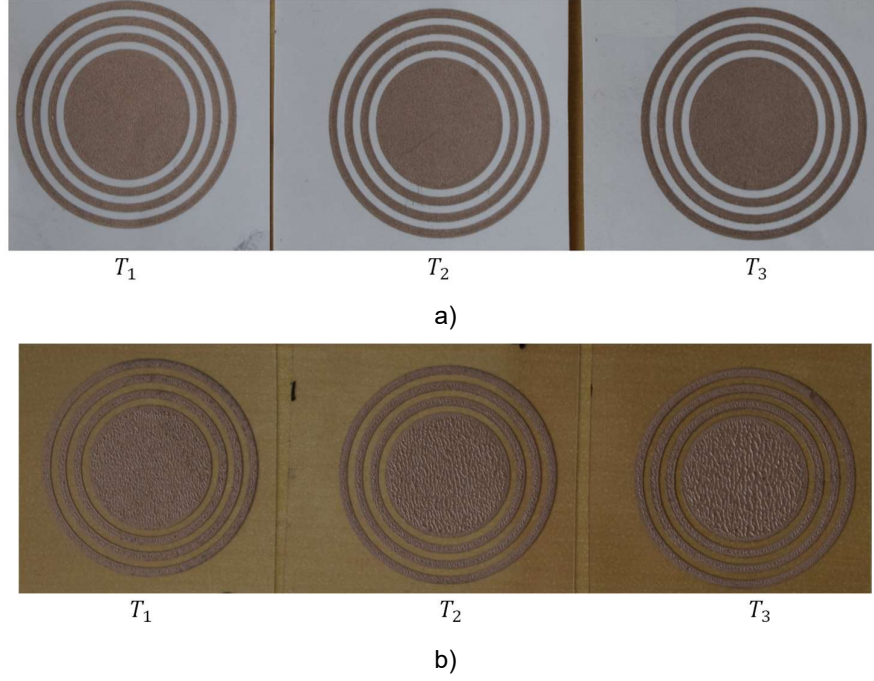


Fig. 4.19: Copper-based ink flexography printed CC-UWB chipless RFID transponders on: a) glossy paper with conductive thin film thicknesses  $CG - T_1 = 5.4 \mu m$ ,  $CG - T_2 = 7.7 \mu m$  and  $CG - T_3 = 12.2 \mu m$  b) PET with conductive thin film thicknesses  $CP - T_1 = 7.5 \mu m$ ,  $CP - T_2 = 9.7 \mu m$ ,  $CP - T_3 = 11.7 \mu m$

The scattering parameters of the different prototypes are measured with the measurement setup described in Fig. A.2 of Appendix A, The VNA has been configured to measure the 2 – 6.5 GHz frequency spectrum, with a maximum power output, an averaging factor of 200 sweeps per measurement, and the sample point's number is set to 201. Fig. 4.20a and Fig. 4.20b shows the  $|RCS|$  results for both type of substrates, glossy paper and PET respectively, calculated following the procedure described Appendix A. As per the silver-ink based prototypes, increasing the conductive thin film thickness enhances the frequency signature.

In general, the copper-ink based UWB chipless RFID transponders performance is poorer than their silver-ink counterparts, as expected by the DC resistance measurements. However, comparing the results against the silver-ink printed prototype  $SP - T_2$ , where no satisfactory response is obtained, but an average conductivity of  $1.28 \times 10^5$  S/m is achieved. The copper-ink based UWB chipless RFID transponders present better results with comparable conductivity values, this due to their thicker thicknesses and their lower

Substrate	Prototype	Thickness	Resistance $R$ ( $\Omega$ )			Conductivity $\kappa$ $10^6$ (S/m)			Skin depth $\delta$ ( $\mu\text{m}$ )	
		$T$ ( $\mu\text{m}$ )	$R_1$	$R_2$	$R_3$	$\kappa_1$	$\kappa_2$	$\kappa_3$	@3.1 GHz	@6 GHz
Glossy paper	$CG - T_1$	5.37	26.7	21.2	17.2	0.11	0.11	0.12	27.0	19.4
	$CG - T_2$	7.66	18.0	14.4	11.1	0.14	0.15	0.16	23.7	17.1
	$CG - T_3$	10.64	12.2	10.1	8.4	0.15	0.15	0.15	23.3	16.7
PET	$CP - T_1$	7.50	25.5	19.9	14.7	0.16	0.17	0.19	21.9	15.7
	$CP - T_2$	9.68	19.2	13.5	10.6	0.14	0.18	0.19	22.1	16.9
	$CP - T_3$	11.70	13.0	10.7	8.9	0.15	0.16	0.16	22.8	16.4

Table 4.8: Copper-ink printed CC-UWB chipless RFID transponder electric parameters (thin film thicknesses provided by Mrs. Katharina Haase, TUC)

relations to the minimum required skin depth, which means that more power is kept in the conductive strips enabling the resonance.

Table 4.9 presents the copper-ink based CC-UWB chipless RFID transponders  $|RCS|$  calculated performance values for all manufactured prototypes. Once again, a consistent improvement in the peak magnitude and dip depth is experienced for both, the copper-ink on glossy paper (CG) and the copper-ink on PET (CP) samples. Although, the achieved values are still below their silver-based counterparts, it is interesting to point out, that the values of the last dip depth, which is mainly produced by the resonance

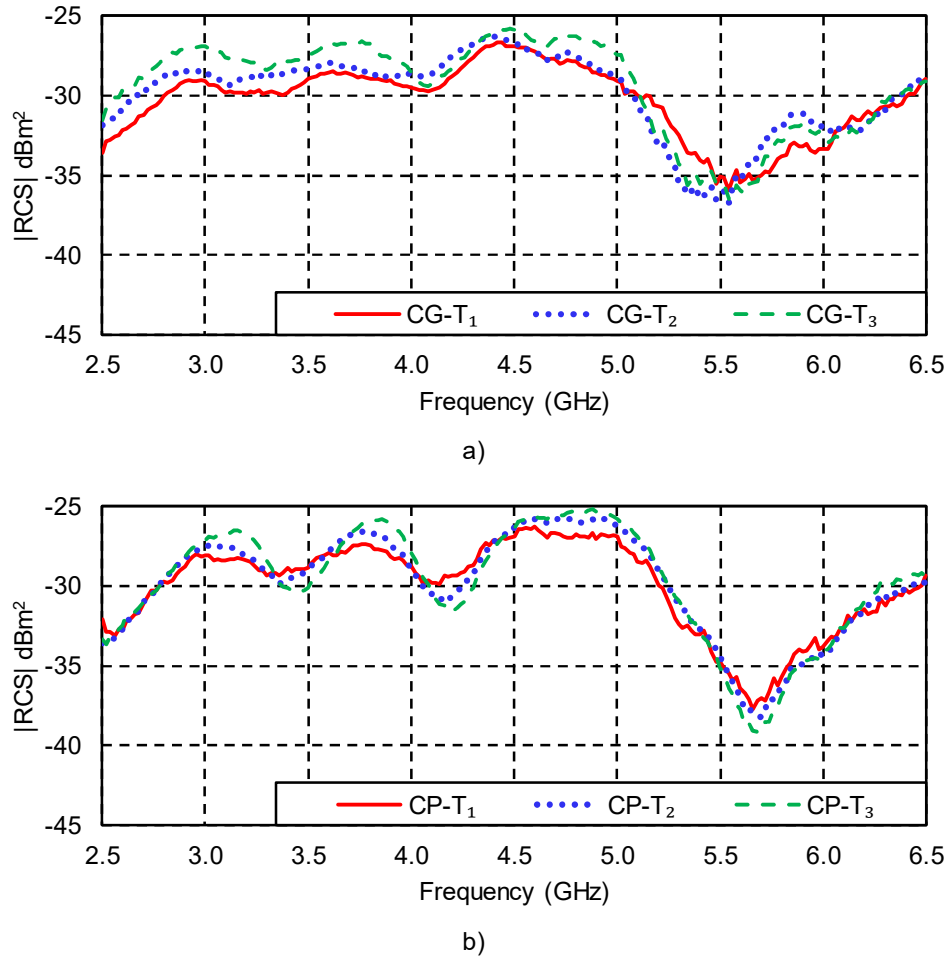


Fig. 4.20: Calculated  $|RCS|$  from measured scattering parameters for a copper ink-based CC-UWB chipless RFID transponder fabricated with different thin film thicknesses on: a) glossy paper with conductive thin film thicknesses  $CG - T_1 = 5.4 \mu m$ ,  $CG - T_2 = 7.7 \mu m$  and  $CG - T_3 = 12.2 \mu m$  b) PET with conductive thin film thicknesses  $CP - T_1 = 7.5 \mu m$ ,  $CP - T_2 = 9.7 \mu m$ ,  $CP - T_3 = 11.7 \mu m$

between the disk and the third resonator, are comparable to the ones obtained in Table 4.7, especially for the thicker conductive thin films with values around 7 dB and 9 dB for the glossy paper and PET substrates respectively.

Parameter	Frequency peak/dip	Glossy paper			PET		
		CG-T <sub>1</sub>	CG-T <sub>2</sub>	CG-T <sub>3</sub>	CP-T <sub>1</sub>	CP-T <sub>2</sub>	CP-T <sub>3</sub>
Peak maximum (dBm <sup>2</sup> )	1 <sup>st</sup>	-29.1	-28.5	-26.9	-28.2	-27.5	-26.6
	2 <sup>nd</sup>	-28.6	-28.0	-26.7	-27.4	-26.6	-25.8
	3 <sup>rd</sup>	-26.9	-26.5	-25.8	-26.4	-25.8	-25.3
Average		-28.2	-27.7	-26.5	-27.3	-26.6	-25.9
Dip depth (dB)	1 <sup>st</sup>	0.6	0.8	1.4	0.9	2.1	3.6
	2 <sup>nd</sup>	1.0	0.8	2.6	2.2	4.3	5.8
	3 <sup>rd</sup>	6.2	7.1	6.8	7.8	8.3	9.9
Average		2.6	2.9	3.6	3.6	4.9	6.4

Table 4.9: Calculated frequency peak magnitudes and dips depths for the CC-UWB chipless RFID transponders fabricated on different substrates printing copper-based conductive thin film with different thicknesses

In general, for the  $CG - T_3$  and  $CP - T_3$  samples, degradations can be observed of around 5 dB in the peak magnitude with respect to the copper thin film on bond paper simulation of Fig. 4.18b, and around 25 dB and 22 dB in their dip depth respectively.

There's still room for research on printed electronics regarding the synthesis of conductive inks based on copper particles, and even more challenges are faced with respect to the aluminum ones. Nevertheless, with respect to the RFID with chipless transponders technology, it is still of great interest, due to their price advantage, to evaluate the performance of chipless RFID transponders, fabricated using copper or aluminum conductive thin films and in this way, set the baselines for future works comparisons in this area. Therefore, in the next subsection the RF performance of aluminum or copper conductive thin films based UWB chipless RFID transponders, fabricated using the alternative manufacturing process described in section 3.3 is evaluated.

#### 4.3.1.4 Aluminum or Copper Strips based Fabrications

Regardless of the mass production technique used to manufacture the UWB chipless RFID transponder to the lowest cost possible, initial research on the types of raw materials that can be used for fabrication needs to be conducted. To evaluate their impact on the UWB chipless RFID transponder's RF response and establish a comparison baseline for future developments with other technologies. Hence, is deemed necessary to exploit other alternatives to fabricate prototypes using metals like aluminum or copper and conduct these studies [47]. For that reason, the CC-UWB chipless RFID transponders are realized with the alternative manufacturing process described section 3.3 using copper or aluminum tape, for the conductive thin films, on either commercial bond paper or PET as a substrate. The fabricated prototypes are depicted in Fig. 4.21 [47].

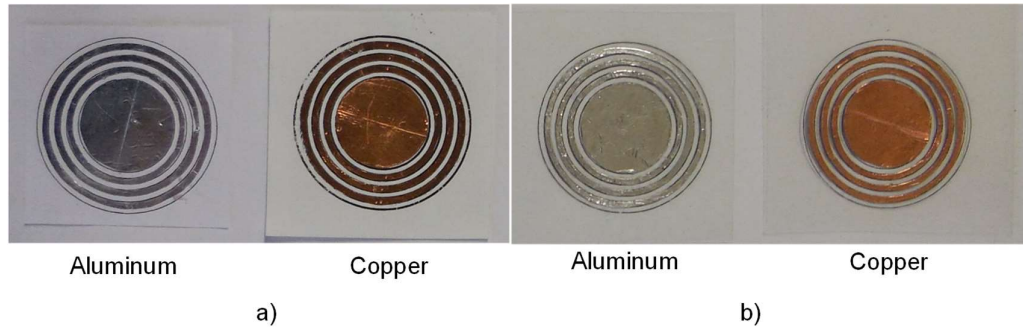
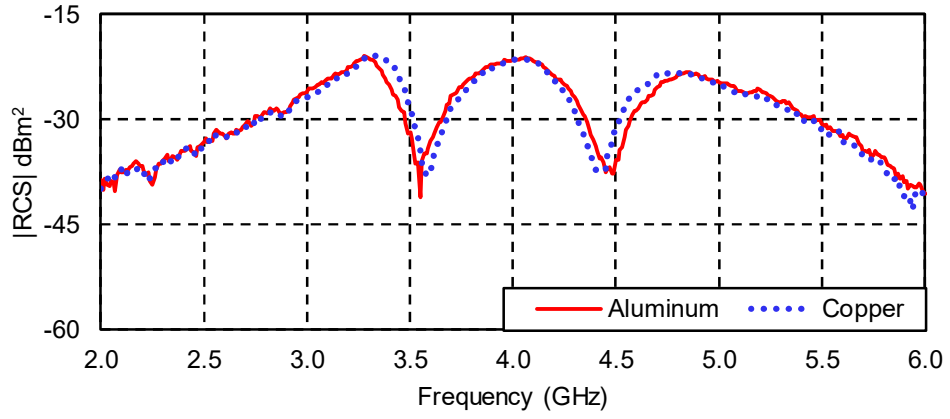
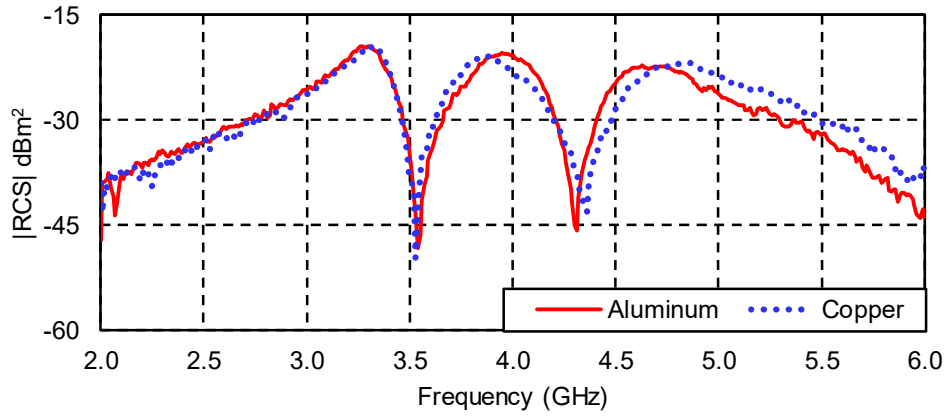


Fig. 4.21: CC-UWB chipless RFID transponders fabricated using copper and aluminum thin films on: a) bond paper, b) PET [47]

The scattering parameters of the different prototypes are measured with the measurement setup described in Fig. A.3 of Appendix A, The VNA has been configured to measure the frequency spectrum located between 2 and 6 GHz, with a power control of 3 dB, an averaging factor of 20 sweeps per measurement and a total of 401. The  $|RCS|$  is calculated following the procedure described in Appendix A. The results for both type of substrates, bond paper and PET, are shown in Fig. 4.22, and Table 4.10 presents the correspondent  $|RCS|$  calculated performance values for all manufactured prototypes. The obtained results show well defined frequency responses in accordance to the simulation values obtained in Fig. 4.13b for bond paper substrate, the measurements show a degradation of 1.5 dB average for the peak magnitude and around 11.3 dB for the dip depth with respect to the simulated values, no frequency shift is experienced.



a)



b)

Fig. 4.22: Calculated  $|RCS|$  from measured scattering parameters for CC-UWB chipless RFID transponder fabricated with either aluminum or copper thin films on: a) bond paper, b) PET [47]

Furthermore, a better performance in terms of peak magnitude and frequency depth can be observed for the aluminum and copper prototypes than the metallic-ink ones depicted in Fig. 4.18 and Fig. 4.20, based on silver and copper inks respectively, and which performance values are resumed in Table 4.7. The results presented in Table 4.9 confirm once more, that better resonance depths are obtained for UWB chipless RFID transponders fabricated on PET. Both aluminum and copper produce similar frequency responses despite their different conductivity values, with the additional advantage for aluminum that its cost is at least 65% less than copper [47].

The measurements results obtained confirmed that by fabricating the UWB chipless transponders with materials like copper or aluminum on bond paper or PET, a cheaper



Parameter	Frequency peak/dip	Bond paper		PET	
		Aluminum	Copper	Aluminum	Copper
Peak magnitude (dBm <sup>2</sup> )	1 <sup>st</sup>	-21.3	-20.9	-19.4	-19.6
	2 <sup>nd</sup>	-21.7	-21.5	-20.6	-21.0
	3 <sup>rd</sup>	-23.3	-23.3	-22.2	-22.0
Average		-22.1	-21.9	-20.7	-20.9
Dip depth (dB)	1 <sup>st</sup>	19.4	16.1	27.7	28.8
	2 <sup>nd</sup>	16.1	15.9	23.5	19.6
	3 <sup>rd</sup>	16.1	19.5	21.4	16.2
Average		17.2	17.2	24.2	21.5

Table 4.10: Calculated frequency peak magnitudes and dips depths for the CC-UWB chipless RFID transponders fabricated with aluminum or copper thin films on different substrates

UWB chipless transponders can be realized. Adding a potential further reduction to its production cost with respect to their silver-ink printed counterparts in case a mass production technique like printed electronics is also applied. Therefore, these materials are suitable and a promising solution to manufacture low-cost UWB chipless RFID transponders on flexible substrates like bond paper or PET. Furthermore, the alternative manufacturing process can be used to produce low-cost prototypes in an expedite way, to conduct experimental test on the designed geometries or set the grounds for further RF performance comparisons with their printed counterparts [47]. The next subsection presents a clear example, on how the copper strip CC-UWB chipless RFID transponder can be used to evaluate the influence of multiple arrays placed together.

#### 4.3.1.5 Space Perturbation of Multiple Chipless RFID Transponders

As explained in subsection 4.2.1, placing two or more arrays at irregular periodicity causes a space perturbation that can also produce a multi-band design. Subsection 4.2.2 discussed the difference in the reflectivity between one single and a periodic infinite array of DD, the later reaching the maximum theoretical calculated value of 1. The previous intuitively supposed that adding more periods to the UWB chipless RFID transponder could create an incremental effect on the  $|RCS|$ .

In this subsection the influence of a space perturbation for  $D \gg d$  is investigated. For that reason, five CC-UWB chipless RFID transponder are modelled, and sequentially placed as illustrated in the schematic of Fig. 4.23a, to form constellations with different amounts/sets of UWB chipless RFID transponders. Simulations are conducted using CST Microwave Studio to analyze the  $|RCS|$  individual contribution that each UWB chipless RFID transponder adds to the whole constellation. The simulations results are shown in Fig. 4.23b and, as can be seen, as a new UWB chipless transponder is added to the previous constellation, the  $|RCS|$  values consequently increase, which means more power can be backscattered towards the receiver, and different received power values are obtained for different sets located at the same distance.

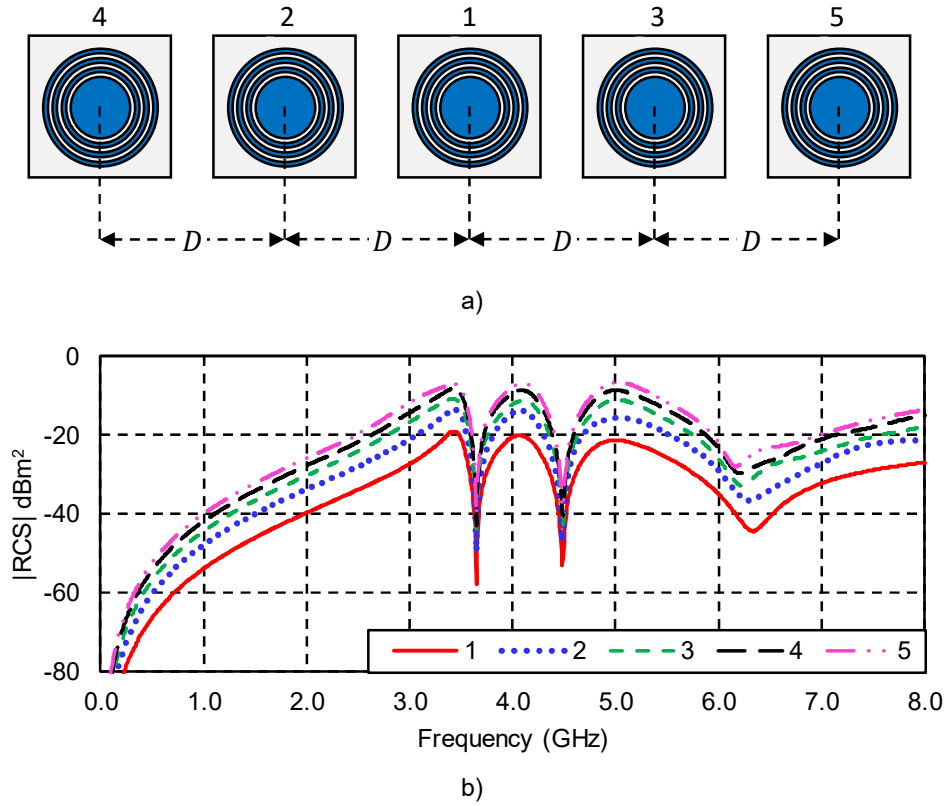


Fig. 4.23: Multiple sets of CC-UWB chipless RFID transponders: a) placement schematic and sequence, b) simulated  $|RCS|$  response for different constellations [60]

The five CC-UWB chipless transponders shown in Fig. 4.24a, are fabricated with the alternative manufacturing process described in section 3.3, using copper for the conductive strips, and bond paper as a substrate. The  $|RCS|$  results are shown Fig. 4.24b, they are calculated following the procedure described in Appendix A, and the

measured scattering parameters of the different prototypes constellations placed sequentially as depicted. They are measured with the measurement setup described in Fig. A.3 of Appendix A. The VNA has been configured to measure the frequency spectrum located between 2 and 6 GHz, with a power control of 0 dB, an averaging factor of 30 sweeps per measurement and a total of 401 frequency samples [60].

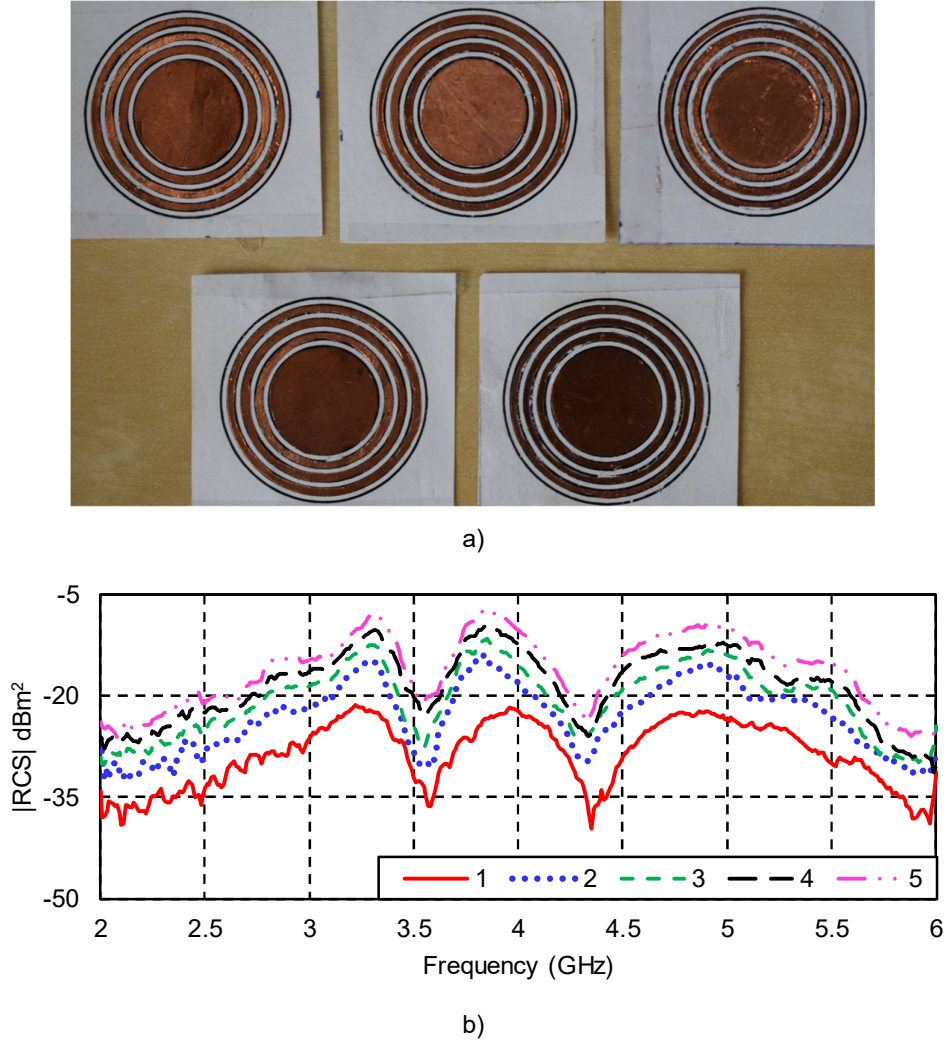


Fig. 4.24: CC-UWB chipless RFID transponders fabricated using copper strips on bond paper: a) picture of all five transponders, b) calculated  $|RCS|$  from measured scattering parameters for different sets [60]

The measurement results obtained are in accordance to the expected simulated ones, and a progressive increase in the  $|RCS|$  is observed, as the number of CC-UWB chipless RFID transponders in the constellation is incremented. The performance values are calculated for all constellations and are resumed in Table 4.11. A significance peak magnitude

enhancement in the order 7.2 dB average is experience from one transponder to a set of two, and progressively increases to reach a 13.7 dB average to the set of five constellation. The dip depths on the other hand, are slightly reduced as the more CC-UWB chipless RFID transponders are added to each new constellation.

Parameter	Frequency peak/dip	Constellation				
		1	2	3	4	5
Peak magnitude (dBm <sup>2</sup> )	1 <sup>st</sup>	-21.5	-15.1	-12.5	-10.3	-7.9
	2 <sup>nd</sup>	-22.1	-14	-11.8	-9.9	-7.2
	3 <sup>rd</sup>	-22.4	-15.3	-13.4	-12.2	-9.7
	Average	-22.0	-14.8	-12.6	-10.8	-8.3
Dip depth (dB)	1 <sup>st</sup>	14.3	15.0	15.4	12.8	12.5
	2 <sup>nd</sup>	17.2	14.3	12.6	13.0	14.3
	3 <sup>rd</sup>	15.5	17.2	16.2	17.1	15.8
	Average	15.7	15.5	14.7	14.3	14.2

Table 4.11: Calculated frequency peak magnitudes and dips depths for the CC-UWB chipless RFID transponders constellations

The previous results could serve as a basis to use the received  $|RCS|$  to simultaneously detect and identify multiple UWB chipless RFID transponders. This feature can be advantageously to determine the amount of UWB chipless RFID transponders placed close and side by side in the interrogation zone. Calculating the received  $|RCS|$  or received power values and setting proper values for power thresholds, further studies results in this regard will be presented in chapter 6 [60].

Another application for this feature, is looking at Table 4.11 as the result of five different UWB chipless RFID transponders, where each has its own peak magnitude and dip depth, increasing considerable its  $|RCS|$  and therefore its reader detection capabilities, but having as a trade-off, making the simultaneous detection more difficult to achieve. This increased  $|RCS|$  capability is exploited in the next sections.

### 4.3.2 Concentric Rings UWB Chipless RFID Transponder

In the previous subsection, it has been shown that an elements array of three rings and one disk generates a frequency response that can be used in the design of UWB chipless RFID transponders. Different investigations were conducted to characterize the reflection properties of this type structure and the importance of a robust coding technique to overcome small frequency variations due to the substrate or ink has been highlighted. In this subsection, the concentric rings (CR) UWB chipless RFID transponder is proposed with a novel coding technique based on frequency response distinction, that together with the SFM reader developed in chapter 5, constitutes an automatic UWB RFID system capable to detect the embedded identification codes. The CR-UWB chipless RFID transponder element geometry shown in Fig. 4.25a and is designed to produce three frequency peaks and four dips within a 1.9 GHz bandwidth between the 4.0 – 5.9 GHz. The core of the model is focused on the single array element geometry shown in Fig. 4.25a and is slight variation of its predecessor, it consists of five metallic concentric rings placed on a substrate. The model is achieved by first considering just one array element and then repeat it to form a  $2 \times 2$  grids by placing a new one at a distance  $D$  from

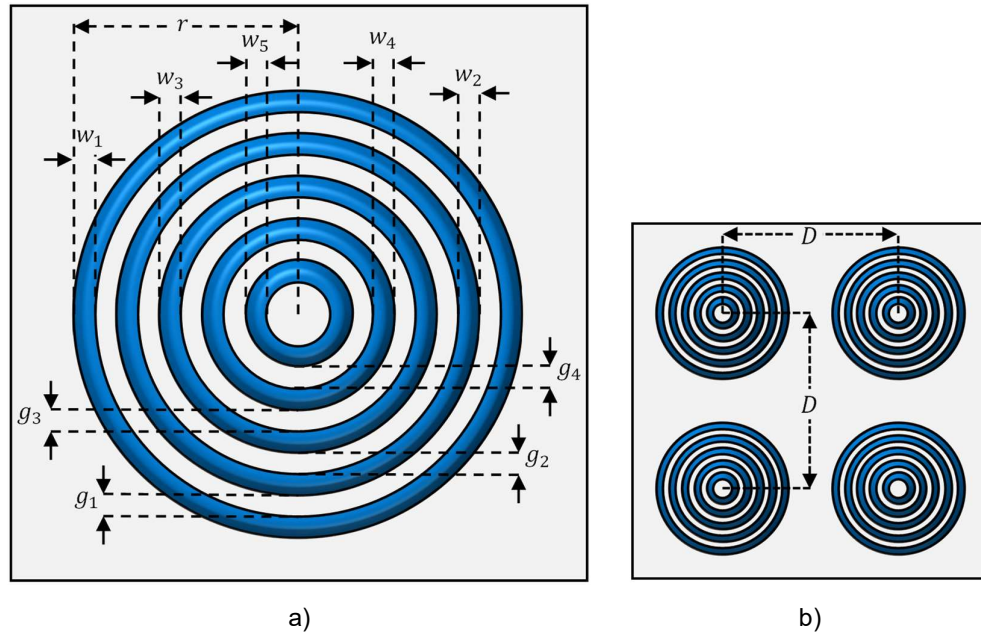


Fig. 4.25: CR-UWB chipless RFID transponder's geometry of a) one array element based on five concentric rings, b) all four arrays of elements

the closest neighbor, the final four arrays geometry composing one single transponder is shown Fig. 4.25b.

Fig. 4.26 shows the  $|RCS|$  simulation results for eight different transponders, the simulations were conducted considering a silver thin film on bond paper and a separation distance  $D$  of 2.8 mm. To illustrate the coding technique, a pulse position encoding is schematized to differentiate in a simple way between two different identification codes. Nevertheless, the whole shape of the frequency response of the transponder should be considered as one unique code, as the main goal is to allocate eight different identification within one quarter of the UWB frequency bandwidth and serve as templates that can be reproduced all through the remaining three sections of UWB spectrum. To generate the different frequency responses, a simple rule of thumb based on frequency peak position

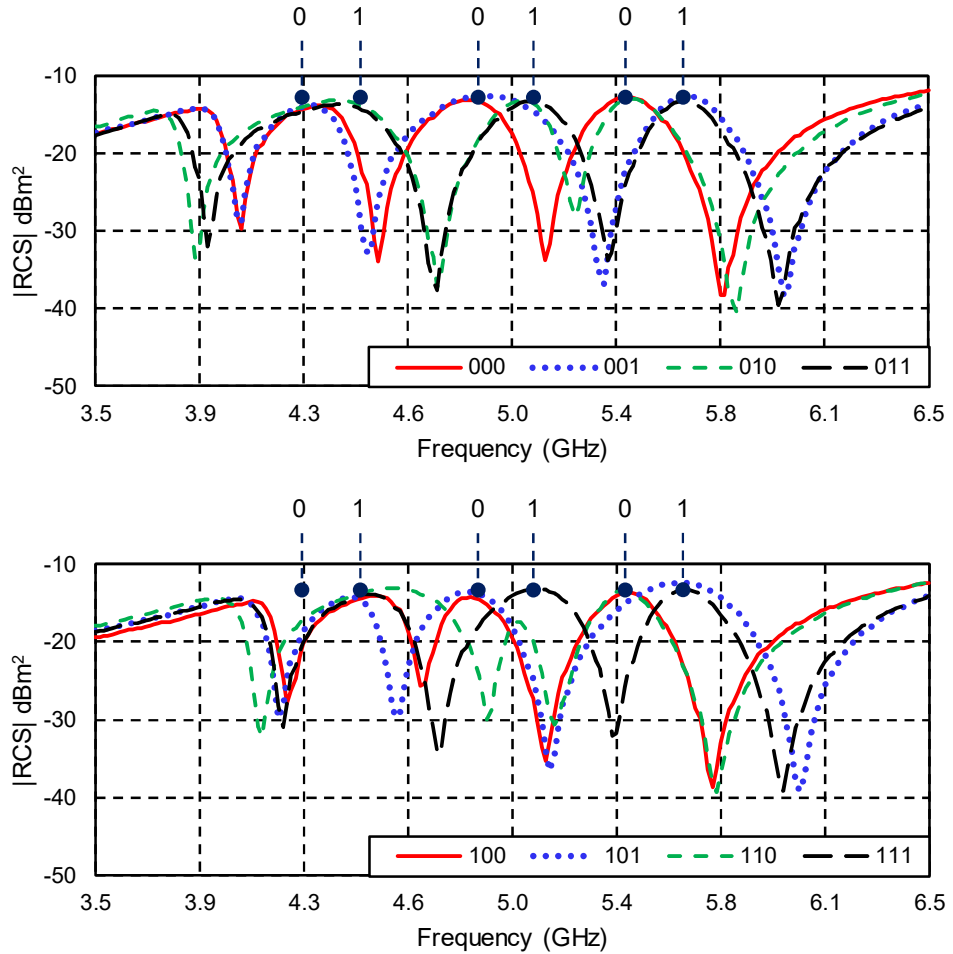


Fig. 4.26: CR-UWB chipless RFID transponder  $|RCS|$  simulation results for the different geometries configurations

was used, six different target center frequencies are set, and the resonators dimensions are changed considering fabrication dimension restrictions to produce the peaks near of those frequencies. The frequency responses are generated changing the dimensions of all resonators for each single UWB chipless RFID transponder to achieved the desired peaks and dips configurations rather than modifying just the one resonator corresponding to a specific peak as conventionally proposed [34] [59]. Furthermore, due to the coupling characteristics between resonating rings for this type of structure, it can be noticed by simple visual inspection, that all eight transponders generate frequency responses that differ not only on the position of the peak but on also on its width, magnitude and dip depth, characteristic that will be exploited during detection in chapter 6.

The frequency position and peak bandwidth differences are summarized in Table 4.12. Analyzing the specific case of code 000 and 010, a difference of 300 MHz bandwidth and 100 MHz position shift can be observed for the first peak, up to a 100 MHz bandwidth and 100 MHz position difference for the second peak and third peaks, as well as a 100 MHz bandwidth and no position difference for the third peak. All these distinct characteristics provide rich information that can be used to recognize the UWB chipless RFID transponders, if a proper encoding methodology based on these differences together with a proper computer detection technique are implemented.

Code	Peak bandwidth			Peak center		
	(GHz)			frequency (GHz)		
	1 <sup>st</sup>	2 <sup>nd</sup>	3 <sup>rd</sup>	1 <sup>st</sup>	2 <sup>nd</sup>	3 <sup>rd</sup>
000	0.5	0.6	0.7	4.3	4.9	5.4
001	0.5	0.8	0.7	4.3	4.9	5.6
010	0.8	0.5	0.6	4.4	5.0	5.4
011	0.8	0.6	0.7	4.4	5.0	5.6
100	0.5	0.5	0.5	4.5	4.9	5.4
101	0.4	0.5	0.9	4.4	4.9	5.6
110	0.8	0.3	0.5	4.6	5.0	5.4
111	0.5	0.7	0.6	4.5	5.1	5.6

Table 4.12: CR-UWB chipless RFID transponders frequency response characteristics

The eight-different physical configurations realized are presented in Table 4.13, as can be noticed, due to the frequency band and fabrication restrictions, a minimum ring width  $w$  of 0.3 mm and maximum of 1.1 mm, as well as a minimum separation gap  $g$  of 0.5 mm and a maximum of 1.7 mm are considered as physical design restrictions to prevent major performance degradations due to the printing technology. These dimensions are used to realize the eight prototypes that should serve as a proof of concept of an UWB chipless RFID transponder, with a novel encoding based on whole frequency signature differences and a capacity of three bits within a 1.9 GHz bandwidth.

Code	Physical dimension (mm)									
	$r$	$w_1$	$w_2$	$w_3$	$w_4$	$w_5$	$g_1$	$g_2$	$g_3$	$g_4$
000	12.2	1.0	0.4	0.4	0.4	0.3	1.7	1.1	1.1	0.9
001	12.2	1.0	0.4	0.3	0.5	0.3	1.7	1.1	1.3	1.0
010	12.2	0.6	0.5	0.4	0.3	0.3	1.3	1.9	1.1	0.6
011	12.0	1.0	0.4	0.5	0.3	0.3	1.7	1.7	0.8	0.5
100	11.6	1.1	0.3	0.3	0.4	0.3	1.7	1.1	0.6	0.8
101	11.8	1.0	0.4	0.3	0.4	0.3	1.7	1.0	0.8	1.2
110	11.9	0.5	0.4	0.4	0.4	0.3	1.2	1.7	1.1	0.8
111	11.8	1.0	0.4	0.4	0.4	0.3	1.7	1.1	1.1	0.8

Table 4.13: CC-UWB chipless RFID transponders different physical dimensions

#### 4.3.2.1 Fabricated Prototypes

The different identification codes combinations of the UWB chipless RFID transponder based on the periodic concentric rings' structures are fabricated at the Technische Universität Chemnitz premises, using silver-ink based screen printing technology on PET, to guarantee the best performance possible, for the given design dimensions requirements. Fig. 4.27 shows a picture of one single array element of each of the eight-different UWB chipless RFID transponders fabrications. As can be seen, each prototype has its unique shape with different resonators radius, widths and gaps.



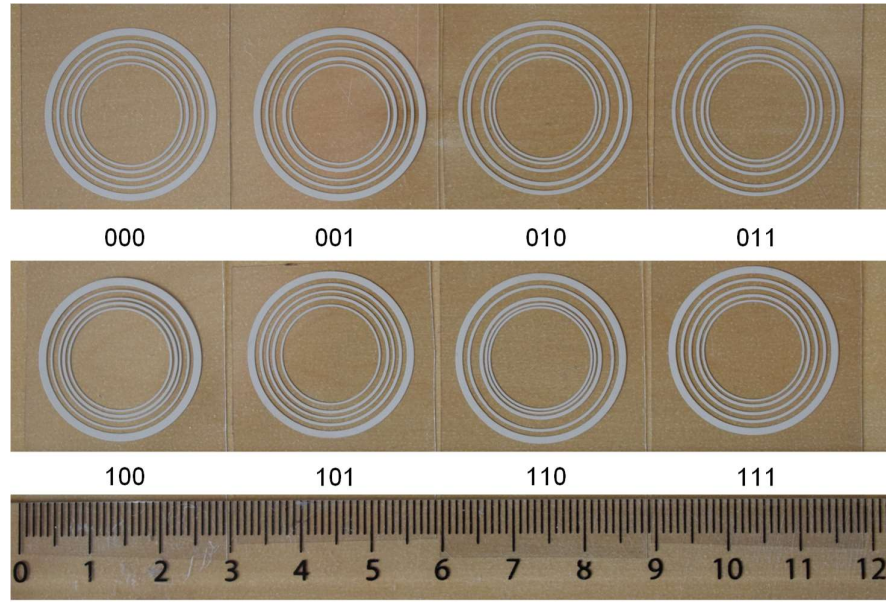


Fig. 4.27: Picture of one array element of each eight CC-UWB chipless RFID transponders fabricated using silver ink on PET

The electrical parameters of CR-UWB chipless RFID transponders are resumed in Table 4.14. The layer thicknesses of each single resonator are measured with the Technische Universität Chemnitz's Keyence laser-scanning microscope VK-9700, following the procedure described in detail in Appendix B. The two-points DC resistance values of each individual ring resonator, starting from the outer  $R_1$  to the inner one  $R_5$ , are measured using digital multimeter Voltcraft model VC830. The conductivity and skin depth are calculated considering the conductive thin film thickness, the DC resistances, and the ring resonators physical dimensions.

The resistance values above  $2 \Omega$  have been highlighted in Table 4.14, as part of a quick quality check control to evaluate the performance of the respective measured CR-UWB chipless RFID transponders response. The third ring resonator of identification code 001 has the highest measured resistance value of  $2.77 \Omega$ , which corresponds to the lowest conductive thin film thickness of  $4.74 \mu\text{m}$  and the smallest ring width of  $0.3 \text{ mm}$ , despite it has an acceptable estimated conductivity value of  $3.05 \times 10^6 \text{ S/m}$ . It is important to notice that the identification codes 010 and 101 have the highest number of rings with resistance values above  $2 \Omega$ , all 5 and 4 respectively. Therefore, frequency response degradations are expected with respect to other identification codes. In general, all ring

Code	Thickness ( $\mu\text{m}$ )					Resistance $R$ ( $\Omega$ )					Conductivity $\kappa$ (S/m) $10^6$					Skin depth $\delta$ ( $\mu\text{m}$ )		
	$T_1$	$T_2$	$T_3$	$T_3$	$T_5$	$R_1$	$R_2$	$R_3$	$R_4$	$R_5$	$\kappa_1$	$\kappa_2$	$\kappa_3$	$\kappa_4$	$\kappa_5$	3.1 GHz	6 GHz	6 GHz
000	5.47	6.02	5.85	6.26	5.55	1.17	1.76	1.64	1.52	1.67	2.86	3.82	3.77	3.34	4.09	4.78	3.44	3.44
001	5.08	5.10	4.74	5.04	5.01	1.65	<b>2.40</b>	<b>2.77</b>	1.88	<b>2.27</b>	2.20	3.30	3.69	2.61	3.20	5.22	3.75	3.75
010	5.24	5.55	5.13	4.89	4.77	<b>2.12</b>	<b>2.17</b>	<b>2.20</b>	<b>2.43</b>	<b>2.28</b>	2.81	2.78	3.05	3.42	3.44	5.13	3.69	3.69
011	6.21	6.88	6.17	6.04	6.84	1.24	1.89	1.46	1.84	1.83	4.80	3.17	3.82	2.71	2.90	4.84	3.48	3.48
100	5.84	5.33	5.85	6.40	5.77	1.51	<b>2.68</b>	<b>2.43</b>	1.97	<b>2.20</b>	1.79	3.57	3.19	2.50	3.00	5.40	3.88	3.88
101	5.78	5.26	4.97	5.45	5.14	1.57	<b>2.28</b>	<b>2.55</b>	<b>2.05</b>	<b>2.27</b>	1.95	3.25	3.70	2.84	3.12	5.24	3.77	3.77
110	5.95	6.12	5.87	5.91	6.28	1.84	<b>2.00</b>	1.78	1.60	1.84	1.64	3.24	2.52	4.22	3.23	5.24	3.77	3.77
111	5.48	5.63	5.83	5.95	5.87	1.47	<b>2.11</b>	1.96	1.83	<b>2.08</b>	2.21	3.28	3.02	2.77	2.98	5.35	3.85	3.85

Table 4.14: Silver-ink printed CR-UWB chipless RFID transponder electric parameters (thin film thicknesses and resistance values provided by Mrs. Katherina Haase and Dr. Georg Schmidt, TUC)

resonators have thin film thickness than are around or above their respective minimum required skin depth thickness, which shall guarantee that at least  $1/e$  of the current density remains within it.

The scattering parameters of the CR-UWB chipless RFID transponders are measured with the measurement setup described in Fig. A.3 of Appendix A. The VNA has been configured to measure the frequency spectrum located between 2 and 6 GHz, with a power control of 0 dB, an averaging factor of 20 sweeps per measurement and a total of 201 frequency samples. The  $|RCS|$  is calculated following the procedure described in Appendix A. The results are shown Fig. 4.28, and the performance values as well as the measured frequency signature characteristics are resumed in Table 4.15. In general, all transponders follow the simulated response shape, a shift of 100 MHz to a lower

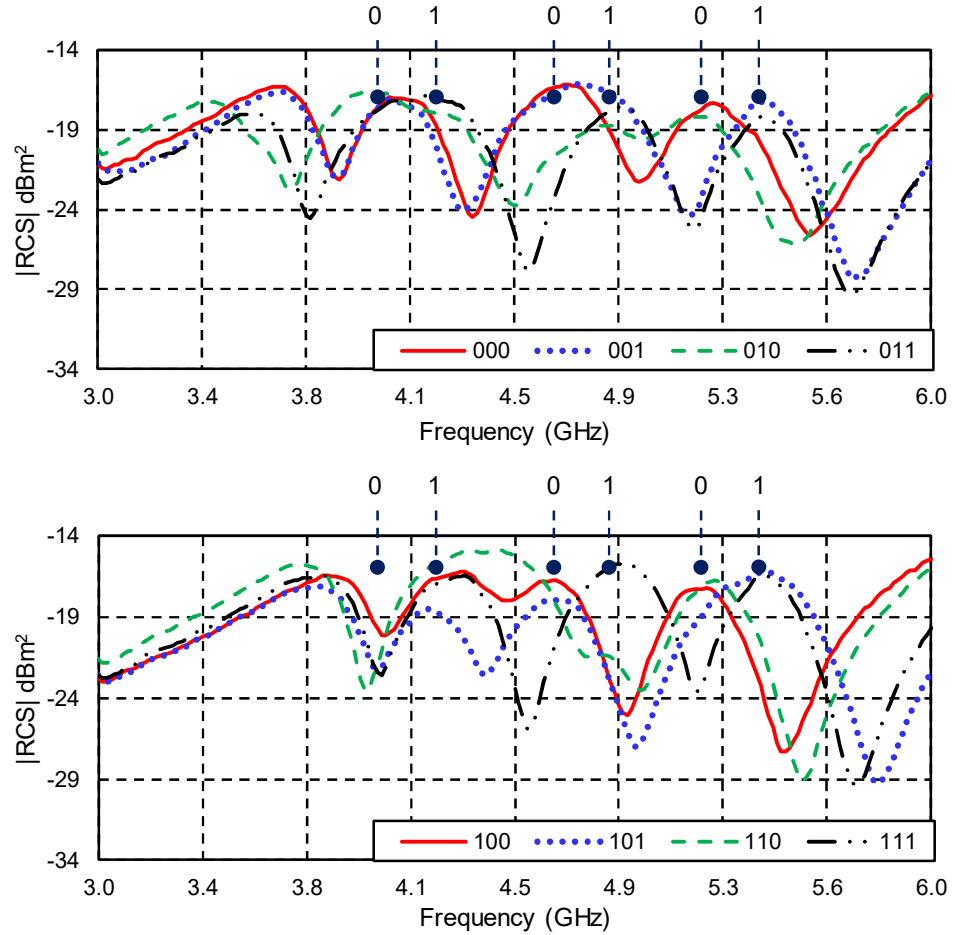


Fig. 4.28: CR-UWB chipless RFID transponders calculated  $|RCS|$  from measured scattering parameters

frequency is experienced with respect to the simulation due to the PET substrate, degradations can be observed in the peak magnitudes ranging between 3 and 4 dB, and dip depths of up to 10 dB with respect to the simulated values. However, as expected per the resistance measurements, the identification codes 010 shows a performance degradation with respect to the other identification codes, its third resonance dip is not properly generated, and its third and fourth peak amplitudes are below the average.

Parameter	Frequency peak/dip	Identification code							
		000	001	010	011	100	101	110	111
Peak magnitude (dBm <sup>2</sup> )	1 <sup>st</sup>	-17.0	-17.3	-16.7	-16.9	-16.3	-18.6	-15.0	-16.8
	2 <sup>nd</sup>	-16.2	-16.1	-18.7	-17.6	-16.7	-17.9	-21.3	-15.7
	3 <sup>rd</sup>	-17.4	-17.2	-18.2	-18.2	-17.2	-16.3	-16.7	-16.5
	Average	-16.9	-16.9	-17.9	-17.6	-16.7	-17.6	-17.7	-16.3
Dip depth (dB)	1 <sup>st</sup>	5.1	4.6	5.5	6.6	3.7	3.6	7.8	5.8
	2 <sup>nd</sup>	8.0	6.8	5.1	10.2	1.3	3.8	0.1	8.9
	3 <sup>rd</sup>	4.7	7.1	0.9	7.0	7.5	9.0	2.2	6.7
	4 <sup>th</sup>	8	11.03	8.0	11.0	10.1	13.0	12.4	12.7
	Average	6.5	7.4	4.9	8.7	5.7	7.4	5.6	8.5
Peak bandwidth (GHz)	1 <sup>st</sup>	0.5	0.4	0.8	0.7	0.5	0.4	0.8	0.5
	2 <sup>nd</sup>	0.5	0.8	0.5	0.6	0.4	0.5	0.2	0.7
	3 <sup>rd</sup>	0.6	0.6	0.5	0.6	0.6	0.9	0.7	0.5
Center frequency (GHz)	1 <sup>st</sup>	4.1	4.1	4.0	4.2	4.3	4.2	4.5	4.3
	2 <sup>nd</sup>	4.7	4.7	4.8	4.9	4.7	4.7	4.9	4.9
	3 <sup>rd</sup>	5.3	5.4	5.2	5.4	5.2	5.4	5.2	5.4

Table 4.15: Calculated frequency peak magnitudes and dip depths for the CR-UWB chipless RFID transponders

Similar analysis can be conducted for identification codes 011, 100 and 101, correlating the  $|RCS|$  with the electric parameters of Table 4.14. Identification code 110 second peak is not generated properly either, which could compromise its functionality in a peak detection-based system. However, its unique frequency response characteristic is kept when compared to all identification codes, which means it still fulfills the main objective of this coding technique that focuses on the whole frequency response, and

explores the differences between each identification code rather than concentrating in one specific frequency peak or dip, which can be easily influenced by the substrate, conductive thin film, handling, or other fabrication process deviations. Therefore, the next section explores the implementation of the same coding principle using an already published UWB chipless RFID transponder based on octagons.

### 4.4 Concentric Octagons UWB Chipless Transponders

In this section, another two UWB chipless RFID transponder are presented, both structures are based on concentric octagons (CO) and designed to be interrogated by the time-domain UWB RFID reader of chapter 5, to perform signal detection and decoding studies. Furthermore, the CO-UWB chipless RFID transponder design 1 (D1) composes together with the time-domain RFID reader a fully automatic and operational UWB RFID system to be implemented in real test-case scenarios in the different venues mentioned in chapter 1. The CO-UWB chipless RFID transponder design 2 (D2), is meant to conduct experiments on simultaneous detection of multiple UWB chipless RFID transponders containing different identification codes.

#### 4.4.1 Concentric Octagons UWB Chipless Transponder Design 1

The concentric octagons chipless RFID transponder is the one proposed by Betancourt et. al. in [49] and its geometry is depicted in Fig. 4.29a. It consists of six concentric octagons rings and one concentric octagon patch, designed to generate five frequency dips in the 2 – 10 GHz frequency range. Nevertheless, for this investigation, only the 3.8 – 8.8 GHz frequency response is of interest, to work with the IR-reader presented in chapter 5, and be fabricated using the different venues substrates for the real test-case scenarios. The original proposed coding is physically achieved placing shorts between resonators to produce a sort of dip OOK modulation technique like the ones reviewed in subsection 2.3.2 for the spiral and C-like resonators [25] [31]. However, as explained, this type of coding approach is realized by shifting the unwanted dip to a higher frequency, which implies the designed higher frequency dips might be affected in an UWB design. Moreover, it also generates shifts in the remaining frequency dip original designed position, which makes it difficult to apply a simple rule to perform its detection,

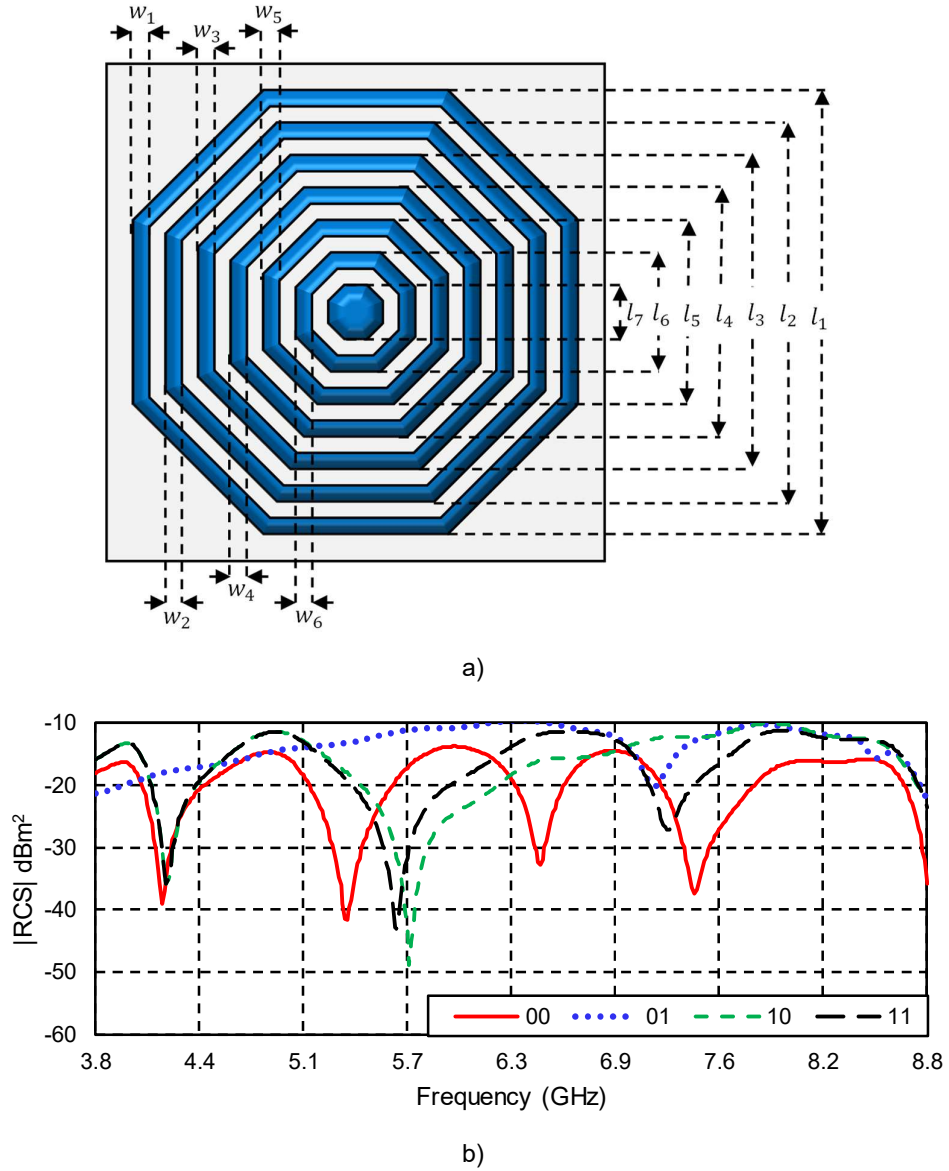


Fig. 4.29: COD1-UWB chipless RFID transponder's a) geometry of one array element with  $l_1 = 22.4$  mm,  $l_2 = 18.8$  mm,  $l_3 = 15.3$  mm,  $l_4 = 12.4$  mm,  $l_5 = 10.5$  mm,  $l_6 = 9.0$  mm,  $l_7 = 6.6$  mm,  $w_1 = w_2 = w_3 = 22.4$  mm,  $w_4 = 0.7$  mm and  $w_5 = w_6 = 0.6$  mm, b)  $|RCS|$  simulation results

and rather these frequency shifts need to be considered for every new identification code, completely losing the essence of applying a simple OOK as coding technique. Therefore, here again a coding technique based on the differences in the frequency response is proposed, using the original developed mechanical shorts-based physical coding principle, and selecting only specific frequency responses, which differ significantly

between codes, and produce variations in the received frequency pulse from the time-domain reader described in chapter 5.

Four different chipless UWB transponders with a periodicity of four array elements each are simulated considering a silver thin film, and the results are shown in Fig. 4.29b. As can be noticed, the dips depth and position vary from one identification code to another, product of employing the shorts-based coding technique. Furthermore, the identification codes according to the proposed original coding technique would be 1111, 0001, 1100, and 1101 respectively, where 1 corresponds to the presence of a dip and a 0 to its absence, as explained previously, the frequency dip shifts are evident for all UWB chipless RFID transponders, which could lead to a wrong identification if an OOK detector is employed, as they are completely shifted from its meant position. Therefore, a new identification code is assigned to each chipless RFID transponder, as shown in the figure  $1111 \rightarrow 00$ ,  $0001 \rightarrow 01$ ,  $1100 \rightarrow 10$  and  $1101 \rightarrow 11$ . Thus, four different identification codes with a completely different frequency response are generated. Nevertheless, as the whole frequency bandwidth has been already used to produce this UWB chipless RFID transponders, the frequency responses cannot be reproduced in other sections like in the case of the CR-UWB chipless RFID transponder.

#### 4.4.1.1 Prototypes Fabrication

A picture of all four different identification codes prototypes, fabricated printing silver-ink on PET is shown in Fig. 4.30a, the physical configuration is performed with the help of a silver ink pen for codes 01, 10 and 11. As explain previously, the COD1-UWB chipless RFID transponders, are meant to be used in real test-case scenarios, using the respective venues tickets. Thus, Fig. 4.30b shows a picture of a few prototypes fabricated printing silver ink on the different venues' substrates: cruise ship and metro station plastic cards, soccer stadium and airport paper tickets. In this case, only the soccer stadium prototypes are coded after printing with the silver pen as explained in [49], and the rest were printed at once adding shorts to the required resonators during the printing process.

The scattering parameters of the COD1-UWB chipless RFID transponders, fabricated on the different venues substrates, are measured with the measurement setup

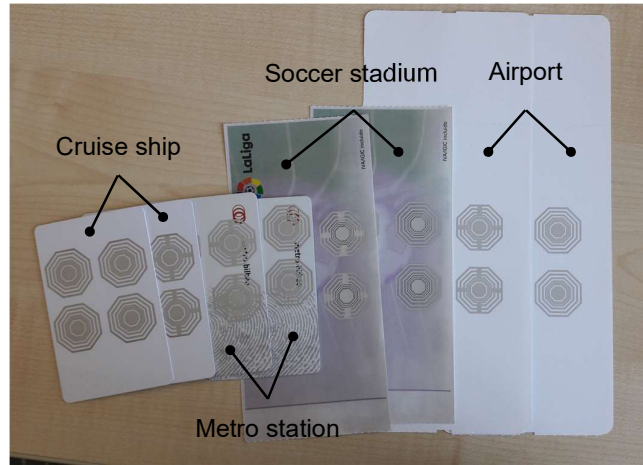
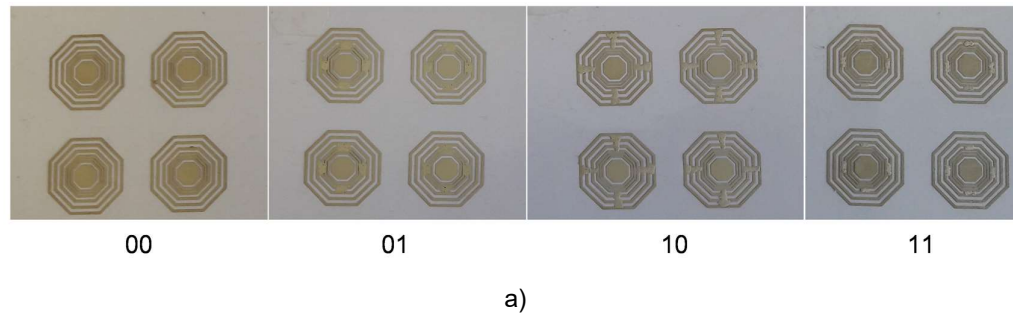


Fig. 4.30: Picture of each eight COD1-UWB chipless RFID transponders identification codes fabricated using a) silver ink on PET b) venues substrates

described in Fig. A.2 of Appendix A. The VNA has been configured to measure the frequency spectrum located between 3.8 and 8.8 GHz, maximum output power, an averaging factor of 200 sweeps per measurement and a total of 401 frequency samples. The  $|RCS|$  is calculated following the procedure described in Appendix A, the results are shown in Fig. 4.31 and the performance values as well as the measured dip frequency position are resumed in Table 4.16.

In general, the prototypes fabricated on PET present results consistent with the expected simulated ones, and the differences between identification codes can be clearly seen by simple human inspection. The fourth dip depth of identification codes 00 and 01 goes from 11.0 dBm<sup>2</sup> to 4.2 dBm<sup>2</sup> respectively, which represents a degradation of 7 dB due to this short-based coding technique.

Taking the identification code 00 on PET substrate graph as a reference, the frequency dips have been enumerated to illustrate the influence of the change in substrate in their position. The shift to a lower frequency due to the paper-based airplane ticket is



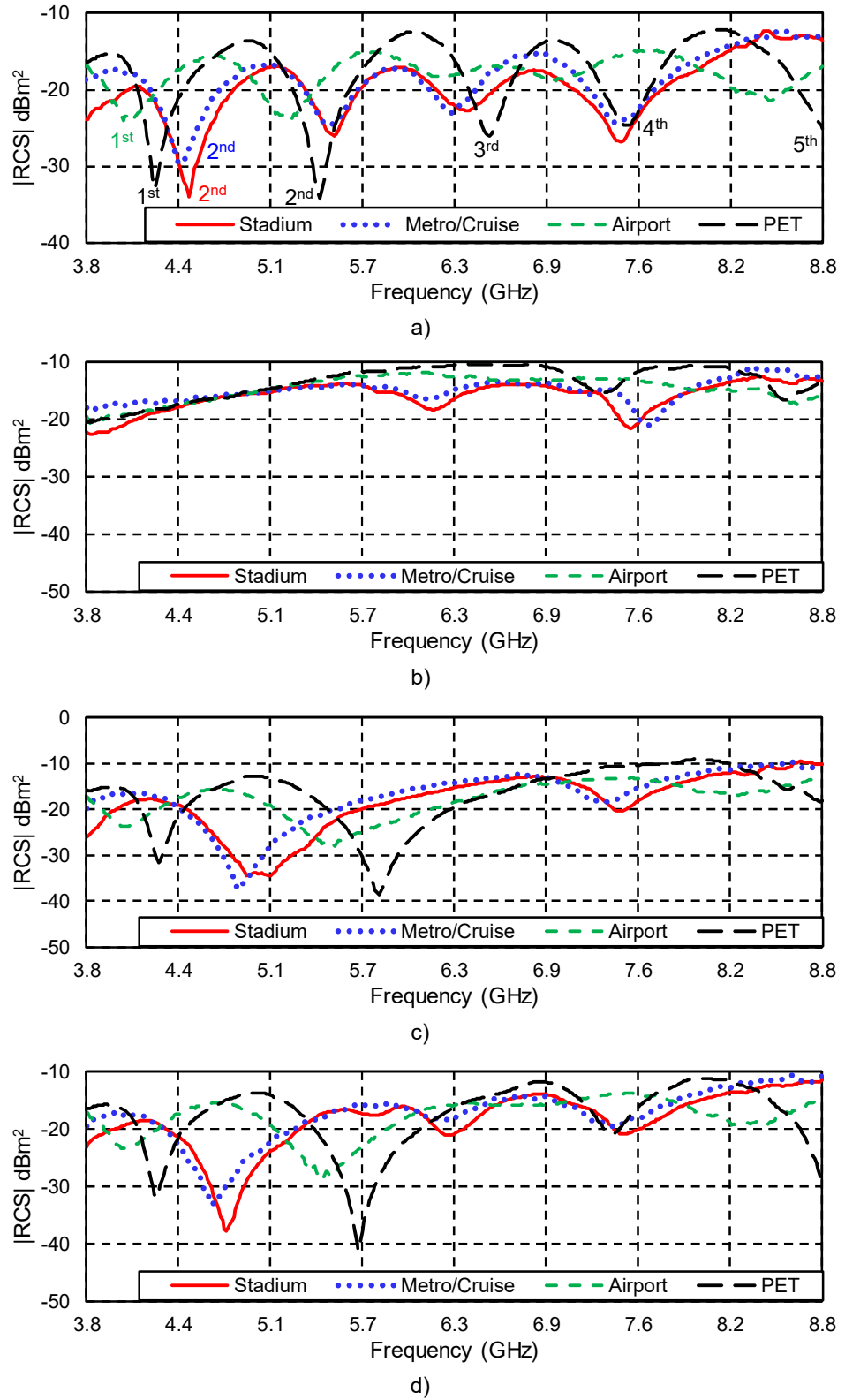


Fig. 4.31: COD1-UWB chipless RFID transponder fabricated on the different venues substrates calculated  $|RCS|$  for identification codes a) 00 b) 01 c) 10 d) 11

Table 1: Comparison of the peak magnitude of the received signal at different venues' substrates													
00				01				10				11	
Peak magnitude (dBm <sup>2</sup> )	Peak/Dip	Stadium	Metro/Cruise	Airport	PET	Stadium	Metro/Cruise	Airport	PET	Stadium	Metro/Cruise	Airport	PET
	1 <sup>st</sup>	-19.8	-17.4	-15.4	-13.6					-17.3	-16.7	-15.9	-15.2
	2 <sup>nd</sup>	-17.0	-16.7	-15.0	-12.4								
	3 <sup>rd</sup>	-17.1	-17.3	-17.0	-13.6	-13.9	-13.9	-11.7	-10.4	-12.4	-12.2	-13.2	-10.4
	4 <sup>th</sup>	-17.5	-15.3	-14.9	-12.2	-13.8	-13.6	-12.9	-10.8	-13.9	-14.7	-13.7	-11.2
	Average	-17.9	-16.7	-15.6	-13.0	-13.9	-13.8	-12.3	-10.6	-14.9	-14.5	-14.6	-12.8
Dip depth (dB)	1 <sup>st</sup>			8.2	17.6			8.6				7.9	16.1
	2 <sup>nd</sup>	14.2	12.1	8.4	20.6			21.8				14.6	25.8
	3 <sup>rd</sup>	8.8	7.3	1.6	12.2					19.3	20.7		
	4 <sup>th</sup>	5.2	5.8	3.7	11.0	4.4	2.5	0.2	4.2				
	5 <sup>th</sup>	9.2	8.9	6.6	11.4	7.5	7.2	4.4	7.5	7.9	6.2	3.8	8.0
	Average	9.4	8.5	5.1	13.8	6.0	4.8	2.3	5.9	14.9	13.5	9.2	16.9
Center frequency (GHz)	1 <sup>st</sup>			4.1	4.3					3.8		4.1	4.3
	2 <sup>nd</sup>	4.5	4.4	5.2	5.4			5.0			4.9	5.5	5.8
	3 <sup>rd</sup>	5.5	5.5	6.3	6.6					4.8			
	4 <sup>th</sup>	6.4	6.3	7.0	7.5	6.2	6.1	6.7	7.4				
	5 <sup>th</sup>	7.4	7.4	8.5	8.8	7.3	7.6	8.6	8.5	7.4	7.3	8.2	8.8

Table 4.16: Calculated frequency peak magnitudes and dips depths for the COD1-UWB chipless RFID transponders fabricated on the different venues' substrates

around 300 MHz in average, while the paper-based soccer stadium and cruise ship/metro station plastic card substrates both produce 1.1 GHz shift in average, which locates the originally designed first dip outside the frequency bandwidth of interest. The  $|RCS|$  presents a general degradation going from an average maximum peak magnitude of  $-13.0 \text{ dBm}^2$  for the PET prototype to  $-15.6 \text{ dBm}^2$  for the airplane ticket,  $-16.7 \text{ dBm}^2$  for the cruise ship/metro station plastic card and  $-17.9 \text{ dBm}^2$  soccer stadium ticket. Furthermore, the different dip depths are also degraded, for example, the depth of the 3<sup>rd</sup> dip of the prototype on PET goes from 12.2 dB to 1.6 dB for the airplane ticket, 7.3 dB for cruise ship/metro station plastic card and 8.8 dB for the soccer stadium ticket. Therefore, all UWB chipless RFID transponders experience performance variations due to the change of substrates. Moreover, the fourth frequency dip of identification code 01 practically disappears for the airplane ticket substrate, going from 4.2 dB on PET to 0.2 dB on the airplane ticket, which in an OOK detector implementation, it will be most probably recognized as a dip absence, leading to its wrong recognition.

Although the COD1-UWB chipless RFID presents a unique frequency response for the selected configurations, its coding procedure and effects on the corresponding spectrum signature, limits the use of this technique to generate more identification codes in a structured manner. For that reason, one last design also based on octagons is proposed in the next subsection, with the objective to generate better resonance dips and modify the time-domain RFID reader sent signal, to investigate the simultaneous detection of multiple UWB chipless RFID transponders with different identification codes.

#### 4.4.2 Concentric Octagons UWB Chipless Transponder Design 2

The COD2-UWB chipless RFID transponders are a modified version of the ones described in the previous subsection, they have been designed to work in the frequency range from 4 to 8 GHz and conduct studies on the simultaneous detection of two UWB chipless RFID transponders having the same or different identification codes. Fig. 4.32a illustrates the geometry of chipless RFID transponders to generate two frequency responses. They are named A and B and consist of one single element with one ring and one patch octagonal resonators each.

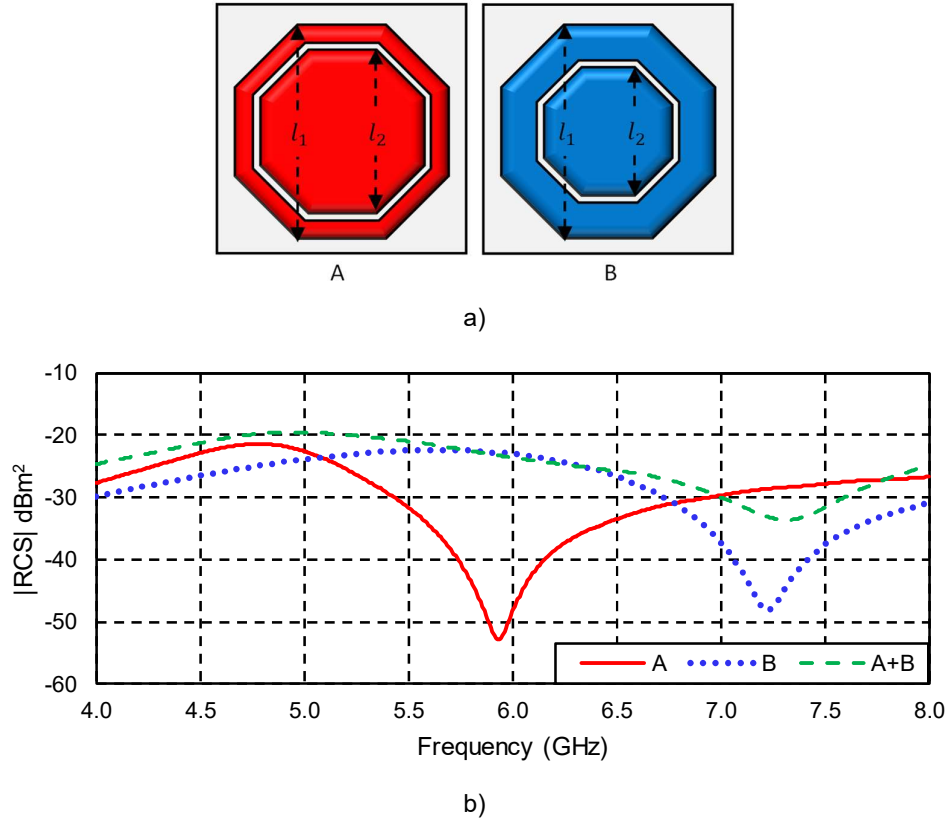


Fig. 4.32: COD2-UWB chipless RFID transponder: a) geometries, b)  $|RCS|$  simulation results for the two geometries and the combination of two

The COD2-UWB chipless transponders coding technique also differs from the original proposed technique in [49] and the adaptation presented in the previous subsection. Here, the codification used for these two transponders is the dip's frequency shift generated by changing the dimensions of the resonators' width, as per the DD-UWB chipless RFID transponders presented in section 4.2. Fig. 4.32b shows their simulated  $|RCS|$  using CST Microwave Studio considering an aluminum thin film on bond paper substrate. Considering the results obtained in section 4.3.1.5, where same identification codes were studied product of a constructive interference effect that increased the overall  $|RCS|$ . The expected effect for the frequency response of two different identification codes placed side by side, is a destructive interference. Therefore, the frequency shift coding for these two transponders is chosen to generate frequency responses different enough, to guarantee its successful individual detection, and the generated response of the combination of the two identification codes (i.e. A + B) produce a third frequency response which is also different from the first two identification codes which originally

generated it, as shown in Fig. 4.32b. This difference allows that the generated frequency response of the combined UWB chipless RFID transponder can be processed as an extra identification code.

#### 4.4.2.1 Prototype

A photograph of the UWB chipless RFID transponders is shown on Fig. 4.33, they are fabricated with the alternative manufacturing process described section 3.3, using aluminum tape for the conductive strips on a PET substrate. The scattering parameters of the different prototypes are measured with the measurement setup described in Fig. A.3 of Appendix A. The VNA has been configured to measure the frequency spectrum located between 3 and 8 GHz, with a power control of 3 dB, an averaging factor of 20 sweeps per measurement and a total of 401 frequency points. The  $|RCS|$  is calculated following the procedure described in Appendix A. The results shown in Fig. 4.33b, are in accordance with the simulated values, a shift to a lower frequency of around 200 MHz can be

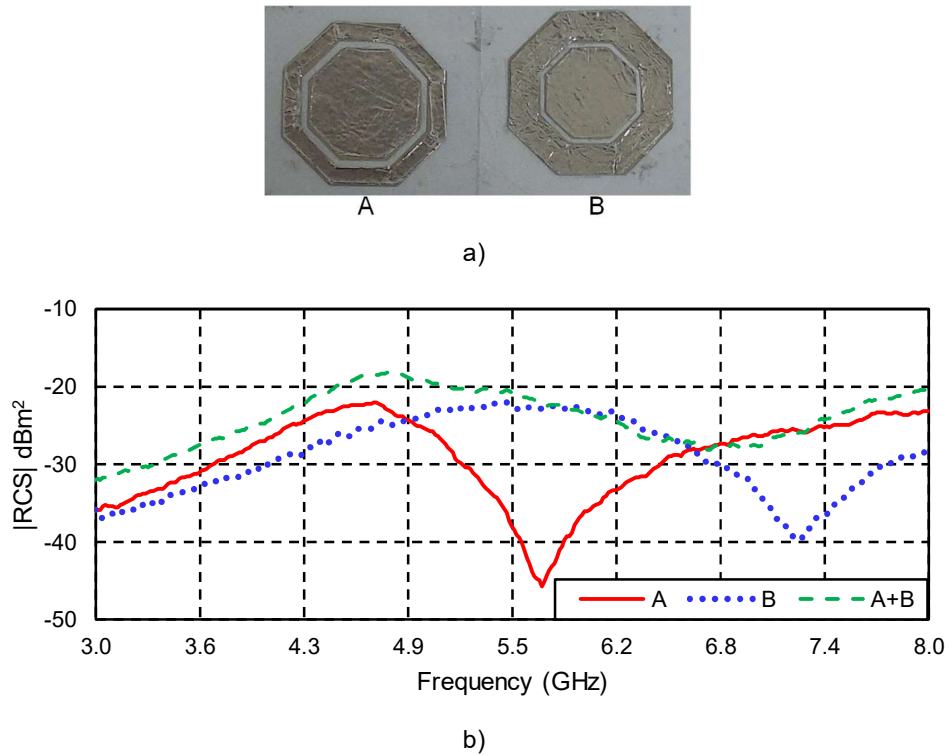


Fig. 4.33: COD2- UWB chipless RFID transponder: a) picture, b) calculated  $|RCS|$

observed for the prototype A, and unlike its predecessor, with this coding technique, no major dip degradations are experienced in the higher frequencies.

Finally, Table 4.18 resumes the performance results for this specific UWB chipless RFID transponder. An average degradation of around 1 dB is observed peak magnitude with respect to the simulated values, and around 7 dB for the dip depth.

Tranponder code	Peak magnitude (dBm <sup>2</sup> )		Frequency dip depth (dB)
	1 <sup>st</sup>	2 <sup>nd</sup>	
A	-22.1	-23.2	22.5
B	-22.5	-28.4	11.3
Average	-22.3.	-25.8	16.9
A + B	-22.3.	-25.8	7.5

Table 4.17: Calculated frequency peak magnitudes and dips depths for the two COD2-UWB chipless RFID transponders

## 4.5 Summary

In this chapter, we have discussed the most important parameters to design UWB chipless RFID transponders, several prototypes based on five different simple structures were fabricated using two different manufacturing techniques, fabrication specifications and their frequency response measured, analyzed and characterized.

Novel prototypes fabricated using low-cost materials like aluminum or copper conductive strips on either PET or bond paper substrates were presented. These UWB chipless RFID transponders are suitable to be produced with alternative mass-production techniques and are a promising solution to further reduce the manufacturing cost of chipless RFID technologies.

The peak magnitude and frequency dip depth terms are introduced in the chipless RFID technology, to evaluate the performance of the UWB chipless RFID transponders frequency responses and be able to compare between different designs.

To conduct a final evaluation among all fabricated structures, one specific prototype of each geometry and type of fabrication has been chosen, and their main parameters are resumed in Table 4.18. The peak magnitude and dip depth values are calculated averaging the different peaks and dip depths results, to obtain one single comparison parameter per UWB chipless RFID transponder.

Parameter	UWB chipless RFID transponder				
	DD	CC	CR	COD1	COD2
Amount of codes	4	1	8	4	2
Conductive strip	Aluminum	Copper	Silver-ink	Silver-ink	Aluminum
Substrate	Bond paper	PET	PET	PET	PET
Periods	1	1	4	4	1
Frequency band (GHz)	3 - 9	3 - 6	4 - 6	4 - 9	4 - 8
Peak magnitude (dBm <sup>2</sup> )	-26.2	-20.9	-17.2	-12.2	-24.05
Peak std (dB)	1.5	1.0	1.2	1.5	2.5
Dip depth (dB)	13.9	21.5	6.8	13.7	16.9
Dip depth std (dB)	0.9	5.3	3.3	6.7	5.6

Table 4.18: Calculated frequency peak magnitudes and dips depths for the different UWB chipless RFID transponders

The results show, that the highest  $|RCS|$  peak magnitudes are obtained for the silver-ink printed periodic structures CR and COD1, which should mean that they have the higher detectability among all, in terms of received power at the reader. COD1 has around 5 dB more  $|RCS|$  than CR with similar peak standard deviations of 1.5 dB and 1.2 dB respectively. However, its dip depth has a higher deviation of 6.7 dB than the 3.3 dB of CR due to the employed dip absence/presence shorts-technique to achieve the coding. The highest resonance dip depths, on the other hand, are the ones obtained for the prototypes fabricated with alternative processes and lower bulk-conductivity than silver metals: copper and aluminum.

Although, these UWB chipless RFID transponders are not designed to improve the theoretical state-of-the-art in terms of coding capacity, based solely on structures design to achieve more peaks in less frequency band like being done conventionally. Their uniqueness relies on the novel coding technique implemented and are designed to be

detected in a real-case application scenario. Therefore, their main purpose is to be part of a real system, where their identification codes will be successfully recognized in a fully automatic way, by the UWB RFID readers used to interrogate these UWB chipless RFID transponders and obtain their frequency signature. The reader architectures used to obtain the frequency response will be discussed in the next chapter.



## 5 RFID Readers for Chipless Transponders

The main objective of this chapter is to introduce the fundamentals of the UWB RFID reader for chipless transponders and describe two main design architectures based on frequency and time domains, which are founded on the conventional radar principles. UWB RFID readers are meant to detect when an UWB chipless transponder is placed within its coverage area, determine its identification code, and, in some cases, its location and track its movements. They may include a wide variety of platforms for different application scenarios, depending on the chipless transponder and how the information needs to be retrieved and analyzed. A general understanding on how the current radar technology can also be applied to the UWB chipless RFID reader is discussed [61].

UWB RFID readers for chipless transponders follow the basic principles of conventional radar design and are built on these foundations to interrogate the UWB chipless RFID transponder and retrieve its signature. The main functional components employed, the basic principles of radars and their implementation to detect UWB chipless RFID transponders are discussed.

### 5.1 Background

#### 5.1.1 The Radar Range Equation

Radar stands for radio detection and ranging, is meant to detect objects and determine their range, angle or velocity. The basic concept of a radar system using the electromagnetic spectrum to transmit a waveform and receive a backscatter from the target is depicted in Fig. 5.1.

The transmitter generates a waveform of power  $P_{tx}$ , which is sent through the transmit antenna of gain  $G_{tx}$  into free space, where it propagates at the speed of light  $c$ . The main objective of the antenna is to concentrate the waveform energy in a specific direction, namely the area of interest, where a target should be detected. The waveform beam broadens as it propagates through free space from the radar, and loses strength with

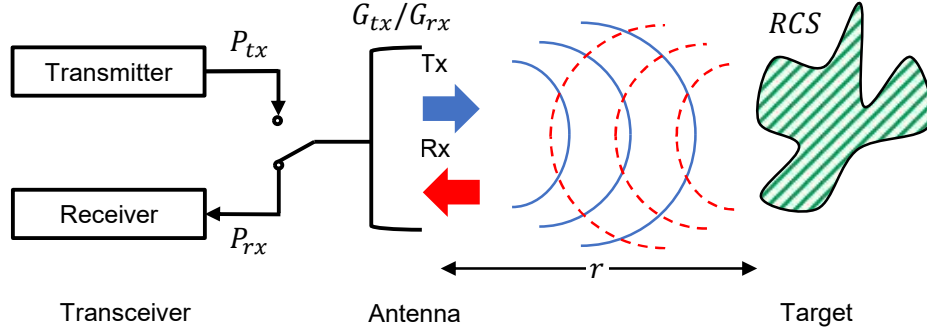


Fig. 5.1: Radar system basic principle, Tx: transmit waveform, Rx: receive waveform

increasing distance (path loss), the power density  $p$  at a specific distance  $r$  from the antenna is given by [61]

$$p = \frac{P_{tx} G_{tx}}{4\pi r^2} \quad (5.1)$$

Once the waveform reaches the target, some of the incident energy is absorbed and another amount is backscattered according to the target specific RCS. The backscattered waveform attenuates again as it propagates through free space toward the direction of the transceiver and is incident upon the receiving antenna of effective aperture  $a_{rx}$ , then the power received can be expressed by [61]

$$P_{rx} = \frac{P_{tx} G_{tx} a_{rx}}{(4\pi r^2)^2} RCS \quad (5.2)$$

the effective aperture of any antenna can also be written as [61]

$$a = \frac{\lambda^2 G}{4\pi} \quad (5.3)$$

and the received power becomes [61]

$$P_{rx} = \frac{P_{tx} G_{tx} G_{rx} \lambda^2}{(4\pi)^3 r^4} RCS \quad (5.4)$$

Equation (5.4) is known as the radar equation. It provides the relation between the free space losses, antenna gains, wavelength, received and transmit power of a radar system.

As shown in Fig. 5.1, the radar waveform must make a two-way journey to the target and back, the distance or range to the target is given by  $r$ , so the waveform travels a total distance of  $2r$  at a speed of  $c$ . If time  $t$  that it takes the waveform to travel from the radar to the target and back is known, then the range can also be calculated as [61]

$$r = \frac{ct}{2} \quad (5.5)$$

### 5.1.2 Range Resolution

The resolution is the UWB readers' ability, like in a radar system, to distinguish between two or more UWB chipless RFID transponders that are closely spaced, whether in angle or space. Fig. 5.2a illustrates the concept. The UWB reader transmits a single pulse of duration  $\tau$ , which is backscattered by two UWB chipless RFID transponders located at  $r_1$  and  $r_2$  distances from the RFID reader antennas, separated a distance  $\Delta r$  from each other. In the case  $\Delta r$  is large enough, the RFID reader should receive two distinctive signals as shown in Fig. 5.2b, and the chipless RFID transponders are resolved in range. In Fig. 5.2c, the chipless RFID transponders are located so close together that the received signals overlap, producing a composite signal, which means that the chipless RFID transponders are not resolved in range, and since they both carry embedded

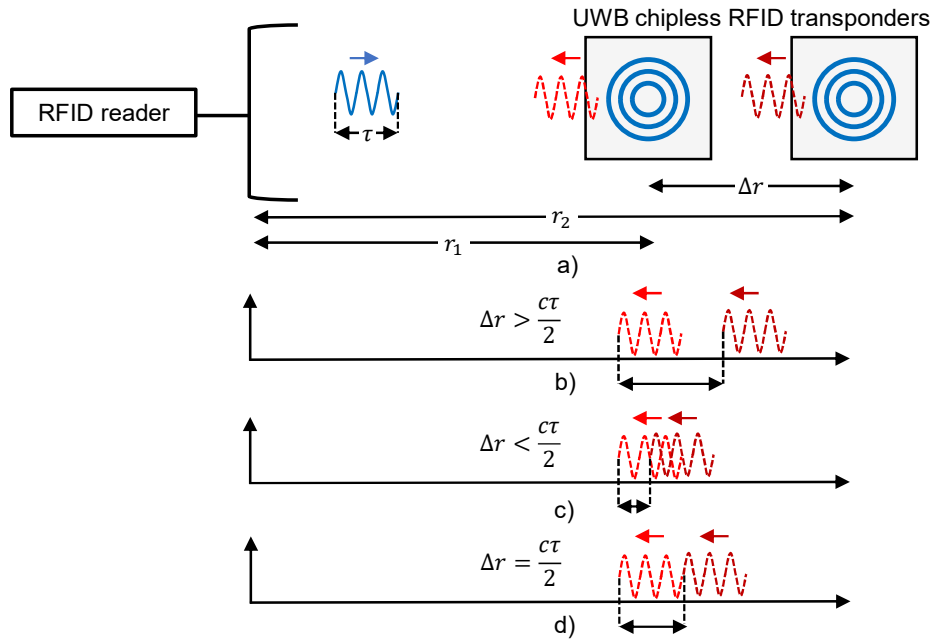


Fig. 5.2: Range resolution: a) concept, b) resolved signals, c) unresolved signals, d) limit

information, they combine destructively, which means, no identification code could be retrieved from neither of them [62].

Fig. 5.2d shows the limit, when the pulses arrive exactly one after the other, and this specific distance value can be found replacing  $t$  by  $\tau$  and  $r$  by  $\Delta r$  in equation (5.5)

$$\Delta r = \frac{c\tau}{2} \quad (5.6)$$

where  $\Delta r$  is named the range resolution, two UWB chipless RFID transponders spaced a distance greater than  $\Delta r$  will be resolved in range (Fig. 5.2b), while transponders spaced by less than  $\Delta r$  will not (Fig. 5.2c) for a pulse of duration  $\tau$  [62]. A pulse duration of 1 ns result in a range resolution of 15 cm, which could make the simultaneous detection of multiple chipless RFID transponders quite difficult, when separated at distances smaller than that. Furthermore, to achieve finer resolutions, shorter pulses are required, nevertheless, they will have less energy and therefore make the detection more challenging [62].

### 5.1.3 Frequency Band Selection

The selection of the frequency band of the RFID system with chipless transponders is based on several requirements. As discussed in chapter 4, the design of chipless RFID transponders based on scattering structures require larger bandwidths, as well as, to implement additional features like the simultaneous detection of multiple chipless RFID transponders, a high range resolution is needed, as discussed in section 5.1.2.

The UWB technology spreads the signal over a very wide frequency range allowing the transmission of information at very low power levels. Because the targeted RFID system with chipless transponders range is low, it may be classified as a short-range device (SRD), having low capability to interfere with other radio equipment. The European Telecommunications Standard Institute (ETSI) has issued a standardization allocating the unlicensed UWB frequencies between 3.1 GHz and 10.6 GHz with a signal width no less than 500 MHz and with a radiated power density of -41 dBm/MHz for the frequency bands: 3.1 to 4.8 GHz and 6 to 9 GHz, -70 dBm from 4.8 to 6 GHz and -65 dBm from 9 to 10.6 GHz [63], [64].

The previous UWB spectrum specifications should serve as a baseline for the design and implementation of the RFID Systems with chipless transponders. Provided that the transponder is merely a passive device and can't generate power by itself, the supply of the required power relies completely in the reader part and need to be optimized to guarantee the achievement of the target reading range. Moreover, the influence of the path loss increases with the frequency, thereby limiting the chipless RFID transponder reading range for its higher frequency components due to a decrease in the received signal-to-noise ratio (SNR). Therefore, two different sections of the UWB frequency band are chosen to guarantee maximum reading capabilities: 3.8 – 5.7 GHz, and 4 – 9 GHz for the frequency domain and time domain readers respectively.

## 5.2 Frequency Domain Reader Test System

The working principle of the frequency domain reader to detect UWB chipless RFID transponders is depicted in Fig. 5.3. As discussed in chapter 4, the strength of the backscattered waveform from the UWB chipless RFID transponder is frequency dependent. Therefore, the UWB reader transmits an increasing sequence of stepped frequency waveforms to fully scan the desired frequency band, each waveform is shifted by a constant frequency offset  $\Delta f$ , and they impinge in the UWB chipless RFID

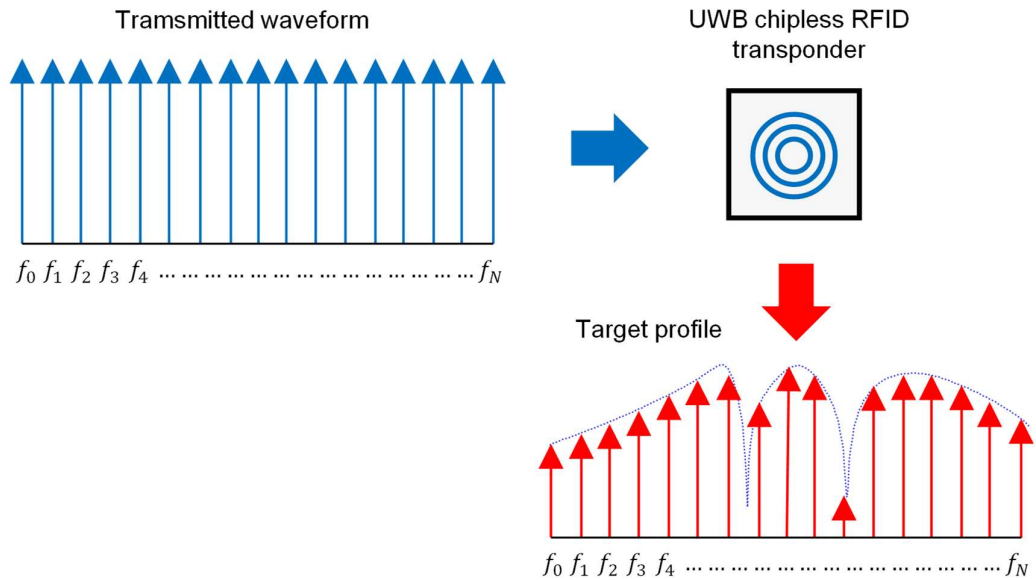


Fig. 5.3: Obtaining UWB chipless RFID transponder frequency profile from stepped frequency measurements

transponder to obtain its signature at each specific frequency. The UWB chipless RFID transponder backscatters the waveforms including changes in amplitude strength and phase shift. Then, the waveforms are measured at the receiver and recorded for further analysis, as illustrated in Table 5.1.

Sequence of pulses	Backscattered amplitude and phase
$f_0$	$A(f_0), \theta(f_0)$
$f_1 = f_0 + \Delta f$	$A(f_1), \theta(f_1)$
$f_2 = f_0 + 2\Delta f$	$A(f_2), \theta(f_2)$
$f_3 = f_0 + 3\Delta f$	$A(f_3), \theta(f_3)$
$\vdots$	$\vdots$
$f_N = f_0 + (N - 1)\Delta f$	$A(f_N), \theta(f_N)$

Table 5.1: Amplitude and phase response of the UWB chipless RFID transponder, obtained at each frequency step

The conventional approach to decode the UWB chipless RFID transponder frequency response is to initially detect it, record its frequency signature and determinate its identification code, which depends on the coding technique and decoding algorithm being employed. Operations such as determine the embedded code of the signature data, thresholding or averaging for noise reduction would be performed. As well as normalization to enable UWB chipless RFID transponders measured at different distances to be compared with a consistent basis. The frequency signature data is then correlated with a stored database and the best code match or best codes matches could be assigned with various ranking levels of confidence as further explained in chapter 6.

### 5.2.1 Stepped Frequency Waveforms

The frequency domain UWB RFID reader is indeed based on the reflective radar front-end model shown in Fig. 5.4a. The simple frequency domain UWB reader for chipless RFID transponder consist of a stepped frequency generator, transmit and receive antennas, mixer to down convert the received signal and a processing section to perform further signal operations.

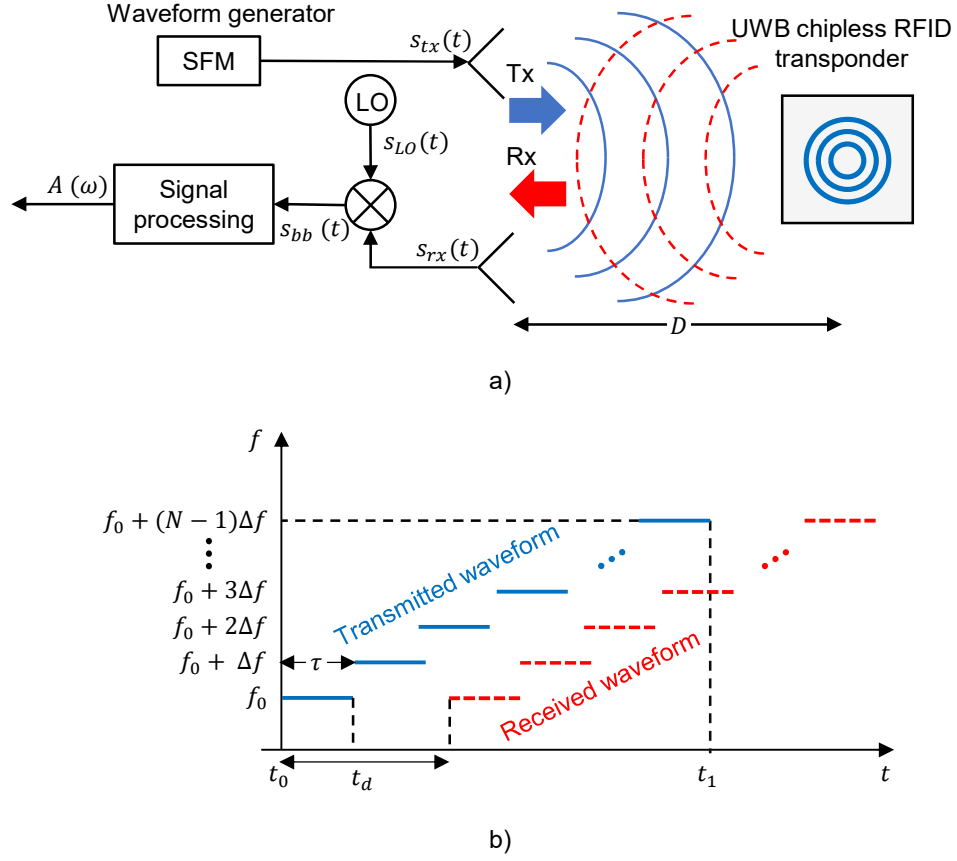


Fig. 5.4: UWB RFID reader for chipless transponders: a) basic architecture, b) SF transmit and receive waveforms

Fig. 5.4b shows the transmitted waveform shape, which consist of a wideband, stepped frequency modulated waveform with a sweeping bandwidth  $\beta = N\Delta f$ , and transmission time  $\Delta t = t_1 - t_0$ . The starting frequency is represented by  $f_0$  and is generated at time  $t_0$ . The slope of the waveform is given by  $\frac{\beta}{\Delta t}$ . The stepped angular frequency  $\omega(n)$  is given by

$$\omega(n) = \omega_0 + 2\pi n\Delta f \quad 0 \leq n \leq N \quad (5.7)$$

the unwrapped instantaneous phase angle  $\phi(t)$  of the waveform can be obtained integrating the previous equation

$$\phi(t) = \int \omega(t)dt = (\omega_0 + 2\pi n\Delta f)t + \theta_{tx}, \quad t_0 + n\Delta t \leq t \leq (n+1)\Delta t, \quad 0 \leq n \leq N \quad (5.8)$$

where  $\theta_{tx}$  is an arbitrary phase shift generated at the transmitter, the transmitted waveform  $s(t)$  can thus be written as

$$s_{tx}(t) = A_{tx}(\omega) \cdot \sum_{n=0}^N \cos(\phi(t)) \quad t_0 \leq t \leq t_1, 0 \leq n \leq N \quad (5.9)$$

$$s_{tx}(t) = A_{tx}(\omega) \cdot \sum_{n=0}^N \cos((\omega_0 + 2\pi n\Delta f)t + \theta_{tx}) \quad (5.10)$$

$A_{tx}(\omega)$  is the frequency dependent voltage amplitude of the transmit waveform. The transmit waveform propagates through space at the speed of light  $c$  and is backscattered by the UWB chipless transponder to the transceiver. The received waveform arrives to the transceiver with a specific time delay  $t_d$ , a modified amplitude and phase shift

$$s_{rx}(t) = A_{rx}(\omega) \cdot \sum_{n=0}^N \cos((\omega_0 + 2\pi n\Delta f)(t - t_d) + \theta_r) \quad (5.11)$$

The voltage amplitude of the received waveform  $A_{rx}(\omega)$  is determine by the target's RCS, pathloss and transceiver parameters (e.g.: antenna gain). At the receiver, the backscattered waveform frequency is shifted by multiplying or mixing it with a LO signal  $s_{LO}(t) = \cos(\omega_0 t + \theta_{LO})$ . Considering that the LO signal drives the mixer into saturation, the output amplitude of the mixer depends only of the product between its voltage conversion gain  $a_{min}$  and the amplitude of the received signal

$$\begin{aligned} s_{bb}(t) &= s_{LO}(t) \cdot s_{rx}(t) \\ &= a_{min} A_{rx}(\omega) \sum_{n=0}^N \cos((\omega_0 + 2\pi n\Delta f)(t - t_d) + \theta_{rx}) \cos(\omega_0 t + \theta_{LO}) \\ &= \frac{1}{2} a_{min} A_{rx}(\omega) \left[ \sum_{n=0}^N \cos(2\pi n\Delta f t - (\omega_0 + 2\pi n\Delta f)t_d + \theta_{rx} - \theta_{LO}) \right. \\ &\quad \left. + \sum_{n=0}^N \cos((2\omega_0 + 2\pi n\Delta f)t - (\omega_0 + 2\pi n\Delta f)t_d + \theta_{rx} + \theta_{LO}) \right] \quad (5.12) \end{aligned}$$



The baseband signal  $s_{bb}(t)$  contains two frequency components, a low frequency given by  $2\pi n\Delta f$  and a high frequency one with  $2\omega_0 + 2\pi n\Delta f$ . By selecting the proper low-pass filter  $F$  with cut-off frequency  $\omega_g$  and unity pass band gain, the higher frequency components is disregarded, and the resulting signal  $s_F(t)$  depends only on the frequency steps size and the phase term  $\theta_F$  from which the amplitude can be easily further processed.

$$s_F(t) = \frac{a_{min}A_{rx}(\omega)}{2} \sum_{n=0}^N \cos(2\pi n\Delta f t - (\omega_0 + 2\pi n\Delta f)t_d + \theta_{rx} - \theta_{Lo}) \quad (5.13)$$

### 5.2.2 Reader Architecture

A discrete SFM front-end using off-the-shelf high-performance components was built to evaluate the proposed UWB chipless RFID system architecture [65], coding technique, detection performance, and post-processing algorithms. The system was developed in the lower 3.8 – 5.7 GHz part of the UWB frequency band, to maximize the reading distance by avoiding higher frequencies path loss, guarantee the commercial availability of the components, and enough bandwidth to design the chipless RFID transponders.

The chosen UWB RFID reader architecture is shown in Fig. 5.5. The analog front-end sends a stepped frequency increasing signal to scan the environment and in case an UWB chipless RFID transponder is placed in its detection zone, it receives the backscattered signal and converts it to digital form for further processing.

A photograph of the realized transceiver is shown in Fig. 5.6, it consists of the above-mentioned frequency band transceiver module and a Genesys<sup>TM</sup> Virtex-5 field programmable gate array (FPGA) development board for control and interfacing with a host computer via joint test action group (JTAG) and universal serial bus (USB) interface.

For the transmission, the FPGA generates and increasing sequence of bits, that the 10 bits DAC model AD7533JNZ-ND from *Analog Devices* [66], translates into the input voltages to the *Hittite* VCO evaluation board 108648-HMC586LC4B [67]. The VCO forwards the specific frequency signal of up to 5 dBm to the *Pasternack* 10 dB coupler model PE2204-10 [68], and via the 20 dB attenuator to reduce the delivered power to the

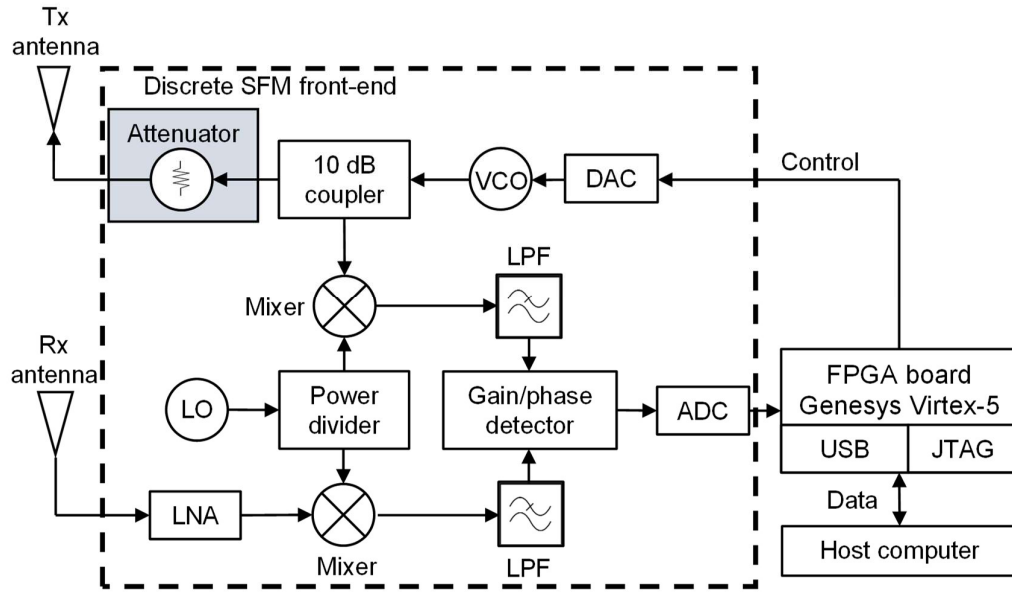


Fig. 5.5: Discrete UWB SFM RFID reader for chipless transponders system architecture

*Chengdu AINFO Inc.* horn antenna model LB-OH-159-10-C-SF with variable increasing gain between 7 dBm at 4GHz to 14 dBm at 8 GHz [69].

The receiver amplifies the signal received from the other horn antenna by means of the *MITEQ* LNA with variable gain of 40 dB at 4 GHz to 42 dB at 6 GHz and variable noise figure between 0.45 dB and 0.90 dB [70]. The LNA sends the amplified signal to one of the *Mini-Circuits* mixers model ZX05-153+, which performs the down conversion of the signal considering the local oscillator (LO) frequency, generated by another Hittite

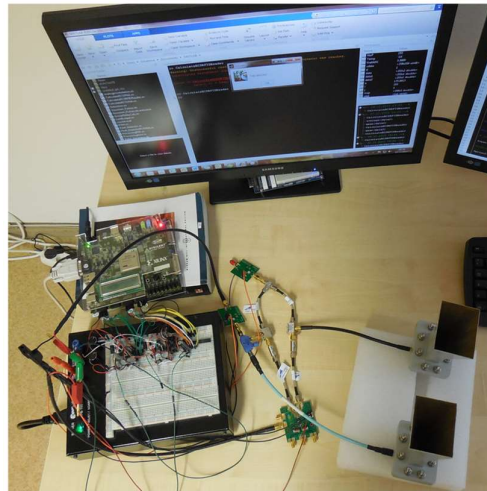


Fig. 5.6: Photograph of the discrete UWB SFM RFID reader for chipless transponders

VCO set to its starting frequency, and divided into two different paths to feed the two different Mini-Circuits low pass filter model VLF-2500 [71]. Both of which filter the signals with frequencies below 2.7 GHz and sends them to *Analog Devices* gain detector evaluation board model AD8302-EVALZ [72]. The gain detector makes a comparison between the two down-converted signals coming from 10 dB coupler and the LNA, and its output values converted to bits by the *Analog Devices* 8-bit analog to digital converter (ADC) AD7819 [73]. The main task of the digital back end is to control the hardware.

### 5.2.3 Test System Results

To verify the functionality of the frequency domain test system, an algorithm was developed to control the reader front-end, be able to transmit a stepped frequency train and record the received signal. The reader is placed on a table with the antennas pointing to the ceil as shown in Fig. 5.6. The reader is programmed to scan 371 different frequency points starting from 3.8256-GHz to 5.6971-GHz in average steps of around 5 MHz.

The fabricated UWB chipless RFID transponders based on dipoles, open conical resonators, concentric circles and octagons, are placed at different distances from the reader's antennas, hold by hand to emulated system normal working conditions, and their spectral signature is recorded for the above specified frequency bandwidth. The obtained results are compared to their VNA measured counterparts showing good agreement, the presence of the peaks and dips is verified and therefore the SFM UWB front-end reader is capable to retrieve their frequency response.

The eight fabricated UWB chipless transponders based on concentric rings are also measured individually when hold by hand at an approximated distance of 10 cm, Fig. 5.7 shows their normalized according to the procedure that will be described in subsection 6.2.2. Once again, the presence of peaks and dips can be verified and compared to their CST simulated or VNA measured counterparts shown in Fig. 4.26 and Fig. 4.28 respectively. In general, the obtained results with the UWB SFM reader are in good agreement with the expected shape for all UWB chipless RFID transponders. However, the second peak for the UWB chipless transponder with identification code 110 is completely missing, which in case of a detection technique based on the peaks' analysis, it would not be possible to decode this specific transponder. Nevertheless, by simple

visual inspection, it can be seen, that all identification codes have several differences when compared point-to-point along the whole frequency bandwidth, characteristic that will be exploited further at the time to implement the UWB chipless RFID transponders detector in chapter 6.

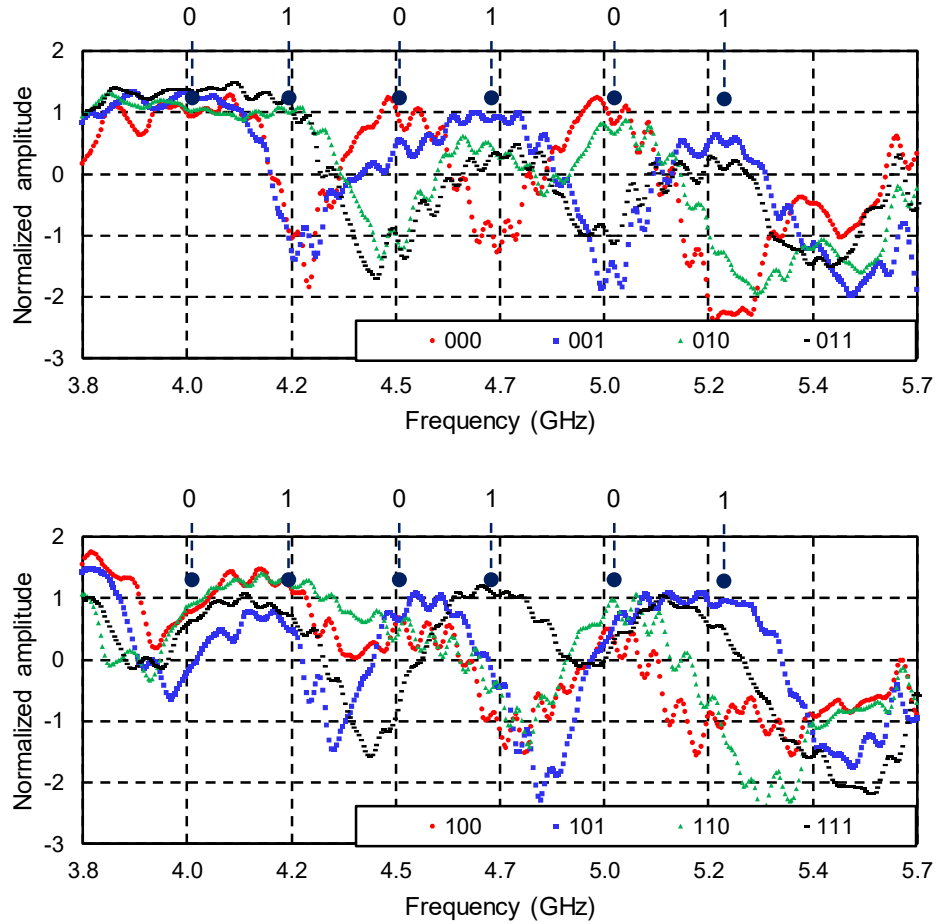


Fig. 5.7: UWB SFM reader front-end measurements of chipless RFID transponders based on concentric rings

To analyze further the obtained results, five different measurements of the UWB chipless RFID transponder with identification code 100 are taken with the UWB SFM reader, the results are shown in Fig. 5.8a. As can be seen, there are also slightly differences between different measurements of the same code under normal working conditions. They are coming from the imperfections of the UWB SFM reader (cable losses, variable power, path loss, etc.) and from the movement of the UWB chipless RFID transponder held by hand. Fig. 5.8b shows the standard deviation between same

frequency samples for this specific identification code. The detector should be able to identify the right code even though the backscattered frequency response has slightly differences for the same code, which should not be greater than the ones observed for different codes in Fig. 5.7.

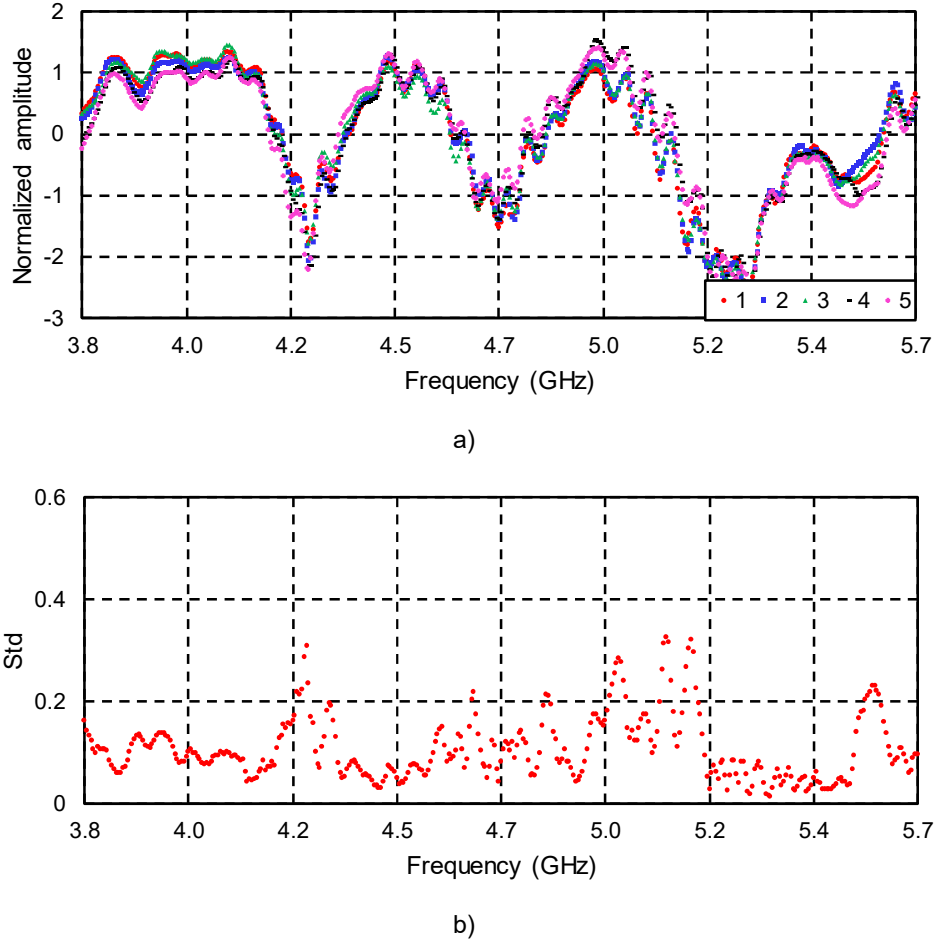


Fig. 5.8: UWB chipless RFID transponder with identification code 100: a) five different frequency response measurements with the UWB SFM reader, b) calculated standard deviation

### 5.3 Time Domain Reader

The working principle of the time domain reader to detect UWB chipless RFID transponders is depicted in Fig. 5.9. The IR UWB RFID reader transmits a short pulse  $s_{tx}(t)$ , which travel and is attenuated through the free space as explained in section 5.1, then is modified in its shape according to impulse response of the UWB chipless RFID

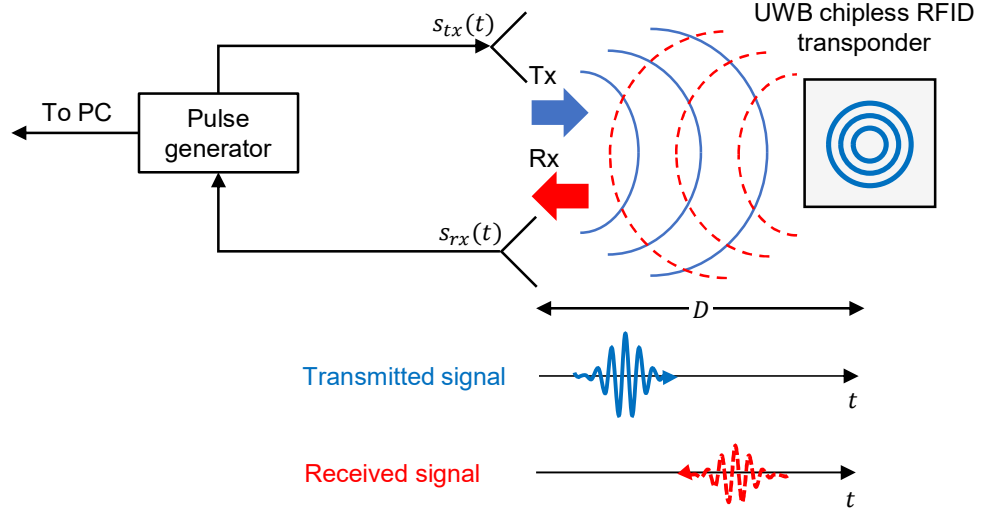


Fig. 5.9: Time domain reader working principle

transponder  $H_t(t)$  and backscattered to the reader again and is received with an amplitude attenuation  $A_{rx}$ , the receive signal  $s_{rx}(t)$  is given by

$$s_{rx}(t) = A_{rx}H_t(t) * s_{tx}(t) \quad (5.14)$$

### 5.3.1 Novelda Radar

The time domain UWB RFID reader is indeed based on the impulse radio commercially available Novelda development kit with reference NVA-R641 UWB radar, the used front-end model is shown in Fig. 5.10a. The Novelda radar based UWB reader for chipless RFID transponder consist of a pulse generator, transmit and receive antennas, sampler to discretize the received signal, and a processing section to perform further signal operations.

The development kit is based on the second generation of radar IC NVA6201 from Novelda, working in the frequency band from 4 to 9 GHz. The low power short microwave pulse with duration of less than one nanosecond shown in Fig. 5.10b is sent through the transmit antenna and is backscattered from the UWB chipless RFID transponder with the identification code embedded in it.

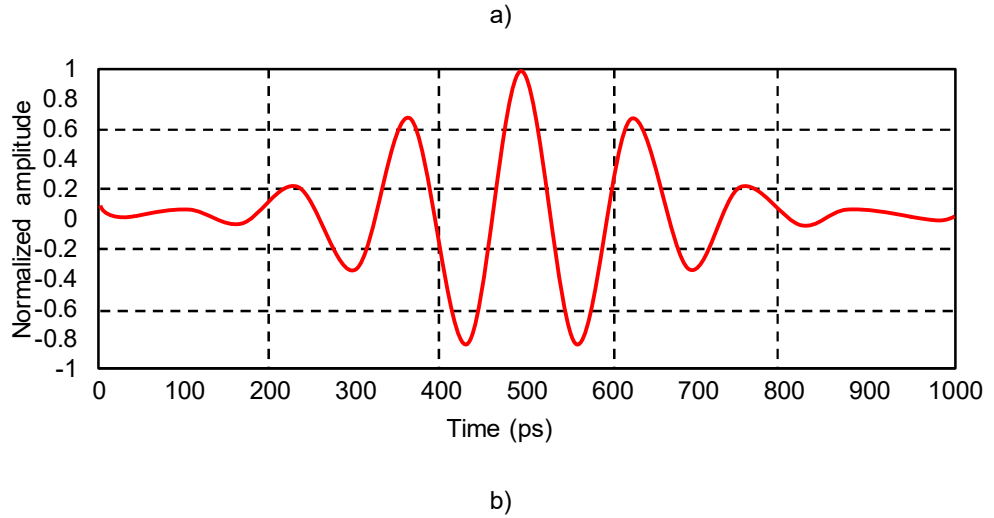
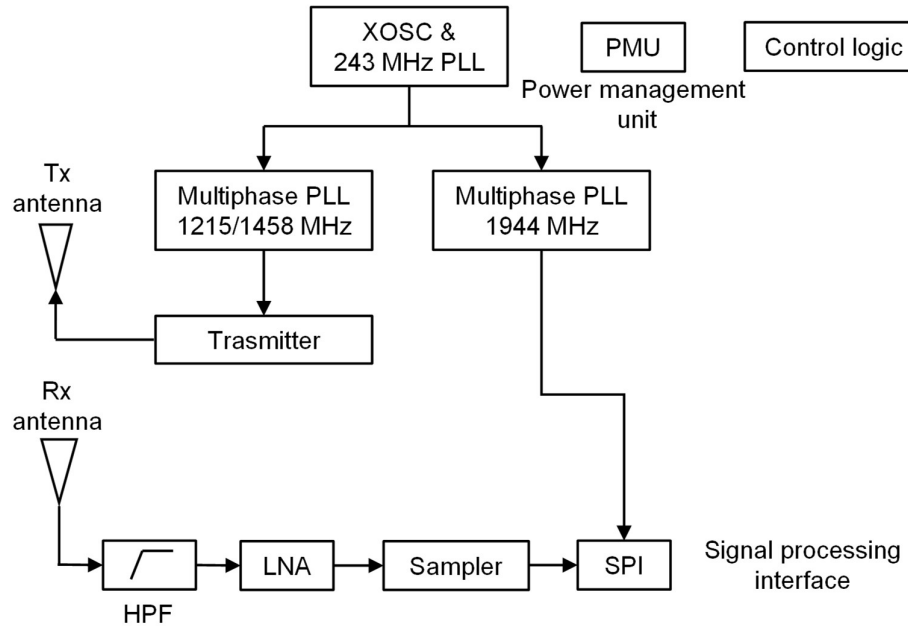


Fig. 5.10: Novelda radar: a) basic architecture [88], b) Gaussian pulse shape

### 5.3.2 Test System Results

To verify the functionality of the time domain test system, an algorithm was developed to control the reader front-end, be able to transmit a pulse and record the

received signal. The reader is placed on a table with the antennas pointing to the wall. The reader is programmed to average 100 pulses.

The fabricated COD2-UWB chipless RFID transponders are placed at different distances from the reader's antennas, hold by tripods as shown in Fig. A.4 of Appendix A, and their spectral signature is recorded. The obtained results are compared to their VNA measured counterparts showing good agreement as shown in Fig. 5.11, the presence of the peaks and dips is verified and therefore the IR UWB front-end reader is capable to retrieve their frequency response.

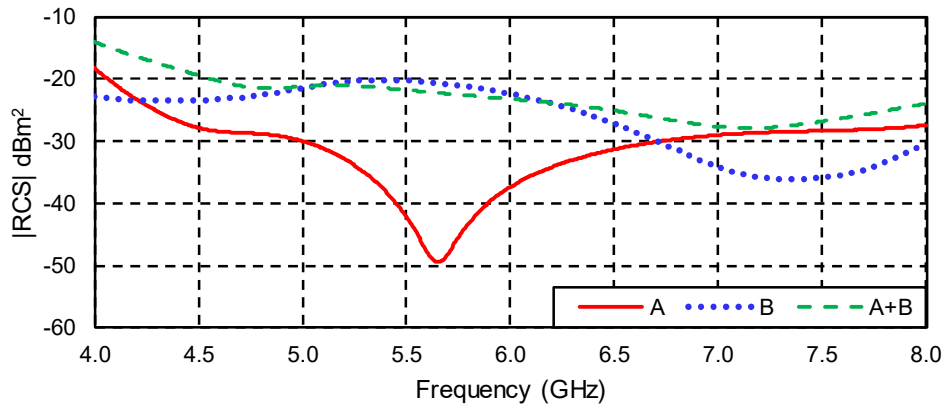


Fig. 5.11: COD2-UWB chipless RFID transponder calculated  $|RCS|$

## 5.4 Summary

In this chapter, the UWB RFID reader working principles have been discussed, two main UWB RFID readers based on SFM and IR radar were presented. The readers are used to interrogate the UWB chipless RFID transponders fabricated in this investigation work, store their response, and use them to perform the detection of the UWB chipless RFID transponders, which will be explained in the next chapter.



## 6 Detection of UWB Chipless RFID Transponders

This chapter introduces the detection methodology to automatically identify the UWB chipless RFID transponder's identification code designed in chapter 4, and which frequency response is obtained with the UWB RFID readers presented in chapter 5 under normal working conditions. Three different types of detectors based on conventional architectures are used to process the received signal and recognize the transmitted identification code.

### 6.1 Background

The UWB RFID system with chipless transponders shall guarantee the successful recognition of every identification code of the UWB chipless RFID transponders, when individually or simultaneously placed in its interrogation zone, and under its normal operational conditions. Researches are investigating different coding techniques to achieve this task and extract the information embedded in the chipless RFID transponders backscattered signal. Nevertheless, as mentioned in section 2.3, most of the by now proposed geometries are being decoded post-processing their time or frequency response by means of a calibration technique. Then, by simple human eye visual-inspection and based on arbitrary selection criteria, the identification codes are claimed to be recognizable, without in fact, a computer system performing this operation. Preradovic et. al. proposed an RFID system with chipless transponders in [27], based on a reader that transmits 15 dBm of power to interrogate the chipless transponders, and then proposes the use of a peak detector to identify different transponders, the experiment was conducted recognizing only two different identification codes. Vena et. al. in [34] detected the UWB chipless RFID transponders insensitive to polarization by analyzing its group delay response, the decoding takes place after its frequency response is post-processed with the calibration technique explained in Appendix A, to subtract the channel's effects. The same calibration technique is being used in other works to extract the UWB chipless RFID transponder's frequency response, and then perform the decoding by visual inspection [7], [32], [49]. Another approach proposed by Lu et. al.

considers the use of an adaptive direct path cancellation methodology, to detect the frequency encoded transponder [74], which allows extracting the backscattered chipless RFID transponder signal and then decode in the conventional way by analyzing the peaks and dips. However, these approaches still do not represent a real case detection scenario. Nevertheless, Kalansuriya et. al. proposed to recognize the UWB chipless RFID transponder identification codes based on a signal space representation by means of a minimum distance detector, and the chipless RFID transponders are measured connecting them directly to the ports of a VNA [75].

As explained in chapter 2, another important requirement of the UWB RFID system with chipless transponders, is the capability to simultaneously identify multiple chipless RFID transponders placed in its interrogation zone. That is, when several objects with different RFID chipless transponders attached to them are passing through the UWB RFID reader's interrogation zone. The different type of objects, as well as the amount of each one, should be recognized according to the UWB chipless RFID transponder stored identification code, and this information used for further processing.

The chipless RFID transponders are usually fabricated using metallic resonators, which produce a unique RF signature for each identification code, as presented in chapter 4. Adding extra resonance frequencies to implement any type of anti-collision protocol in UWB chipless RFID transponder, simply translates in a change in the chipless RFID transponder's overall frequency response, when seen from the used spectrum perspective, and it could finally mean that many different identification codes are generated to identify just one single object in a multiple transponder scenario [60]. On the other hand, if the decoding is to be conducted without implementing any anti-collision protocol at the UWB chipless RFID transponder side, the coding technique itself should provide enough robustness to help to overcome or detect the collision as explained in subsections 4.3.1.5 and 4.4.2 [60] [58] [76]. The reader, on the other hand, should increase its complexity and processing load to be able to perform the collision detection and successfully decode the type and amount of UWB chipless RFID transponders. Rezaiesarlak and Manteghi implemented in [77] and [78], a short-time matrix pencil method (STMPM) to decode multiple chipless RFID transponder for different reader's configurations. Azim and Karmakar used in [79], a linear frequency modulated (LFM) signal as an interrogation signal and a fractional Fourier transform (FrFT) is employed to

separate the responses from multiple transponders, and Anee et. al. proposed in [80], a collision detection method based on frequency-modulated continuous-wave (FMCW) radar.

Here, three different detectors are proposed to recognize under normal working conditions the UWB chipless RFID transponders developed in chapter 4, and which frequency response is obtained with the VNA considering the influence of communication channel, which will be described in detail further in the next section.

## **6.2 The Communication Channel**

The radio channel is the physical medium where the communication between the UWB RFID reader and the UWB chipless RFID transponder takes place, and the impairments effects it introduces to the UWB chipless RFID transponder's backscattered signal need to be investigated accordingly. The propagation effects have been previously discussed in subsection 5.1.1, and the normalization procedure used to overcome this, will be explained in this section. Additionally, the effect when the communication channel corrupts the received signal by adding white Gaussian noise is introduced, and the design of the optimum receivers to perform the detection and decoding of the frequency-coded UWB chipless RFID transponders. The UWB chipless RFID system shall guarantee the successful decoding of the different coded UWB chipless RFID transponders placed in the identification zone, and under its normal operational conditions. Therefore, the influence of the radio channel on the decoding and overall system reliability must be assessed. The noise is one of the major impairments being present in all communications channels [81]. A noisy signal could cause an UWB chipless RFID transponder identification code to be wrongly identified as other, compromising the reliability of the system. Therefore, the importance to study the noise influence over the UWB chipless RFID transponder received signal is evidenced. Furthermore, since the UWB RFID transponder is chipless, the implementation of a dynamic channel coding algorithm at its side, to help to cope with the signal impairments produced by the noisy channel is not possible. Thus, the UWB RFID reader must have the capability to overcome this problem, and the UWB chipless RFID transponder coding must be robust enough to guarantee the successful detection, and in this way, avoid confusion between

different codes when the received signal is influenced by a noisy channel [60] [58] [76] [82].

### 6.2.1 AWGN Channel Modeling and Detection

To achieve a successful implementation of the UWB chipless RFID system, a reliable decoding of each UWB chipless RFID transponder under normal radio channel conditions, namely the influence of its different effects, must be performed. The received signal from an UWB chipless RFID transponder may become practically undetectable to the human eye under the influence of a noisy. Consequently, the need to study the implementation of an algorithm capable to perform the successful decoding of different coded UWB chipless RFID transponders under these noisy conditions becomes imperative.

To reach this goal, first, the behavior of the channel must be understood and characterized, to be able to implement a statistical viable channel model. The simplest mathematical model for a noisy communication channel is the additive noise channel that can be mathematically described by [81]

$$s_{rx}(t) = s_{tx}^m(t) + n(t) \quad (6.1)$$

where  $s_{tx}^m(t)$  represents the  $m$ -th UWB chipless RFID transponder backscattered signal being corrupted by an additive random noise process  $n(t)$ , and  $s_{rx}(t)$  is the received signal at the detector. Assuming that the main source of noise comes from the electronic components and the amplifiers inside the receiver, it can be considered as thermal noise, which has a statistical characteristic of being Gaussian. Then, the channel can be modeled as an additive white Gaussian noise with zero-mean and a spectral density of  $\frac{N_0}{2}$ . The main goal of an optimal detector is to analyze the received signal  $s_{rx}(t)$ , and take the optimal decision of the UWB chipless RFID transponder's transmitted code  $s_{tx}^m(t)$  that minimizes the probability of detection error [81].

To proceed with further mathematical analysis and simplify the operations, the different waveforms in Eq. (6.1) are converted to vectors using any orthonormal basis.  $s_m(t)$  is represented by a vector  $\vec{s}_m \in \mathbb{R}^N$ , and in a similar way, the same operation can be applied to the remaining waveforms  $n(t)$ , and  $r(t)$ . The final vector additive noisy channel model is expressed by [81]

$$\vec{s}_{rx} = \vec{s}_{tx}^m + \vec{n} \quad (6.2)$$

The probability density function of the Gaussian noise vector  $\vec{n}$  is determinate by [81]

$$p(\vec{n}) = \left( \frac{1}{\sqrt{\pi N_0}} \right)^N e^{-\frac{\|\vec{n}\|^2}{N_0}} \quad (6.3)$$

Equation that serves as a based to develop the different detector's architectures discussed in the following subsections.

### 6.2.2 Free-Space Path Loss Modeling and Normalization

As explained in subsection 5.1.1, the received signal experiences propagation losses and these were expressed by the radar range equation in Eq. (5.4). Therefore, the noisy channel model of Eq. (6.1) can be extended to include these losses as follow

$$s_{rx}(t) = A_{rx} * s_{tx}^m(t) + n(t) \quad (6.4)$$

where  $A_{rx}$  represents the attenuation experienced by the transmitted signal, it varies according to the distance of the UWB chipless RFID transponder to the receiving antenna. To overcome this effect and make the signals comparable and independent of the distance, a simple normalization procedure is implemented, defined by [76]

$$s_{rx} = \frac{s_{rx} - \bar{\mu}}{\sigma} \quad (6.5)$$

where,

$\bar{\mu}$ : received signal's mean

$\sigma$ : received signal's standard deviation

To verify the implementation of the normalization procedure, the scattering parameters of the CR-UWB chipless RFID transponders are measured with the measurement setup described in Fig. A.3 of Appendix A. The VNA has been configured to measure the frequency spectrum located between 3.5 and 6.5 GHz, with a power control of 0 dB, an averaging factor of 20 sweeps per measurement and a total of 401 frequency samples. The measurement results for the CR-UWB chipless RFID transponder with identification code 00 placed at distances of 80 cm, 120 cm, and 180 cm are shown in Fig. 6.1a, and the normalized results in Fig. 6.1b. As can be seen, the normalization procedure helps to overcome the propagation losses and delivers to the

detector comparable signals, the detection procedure will be discussed in the next subsections.

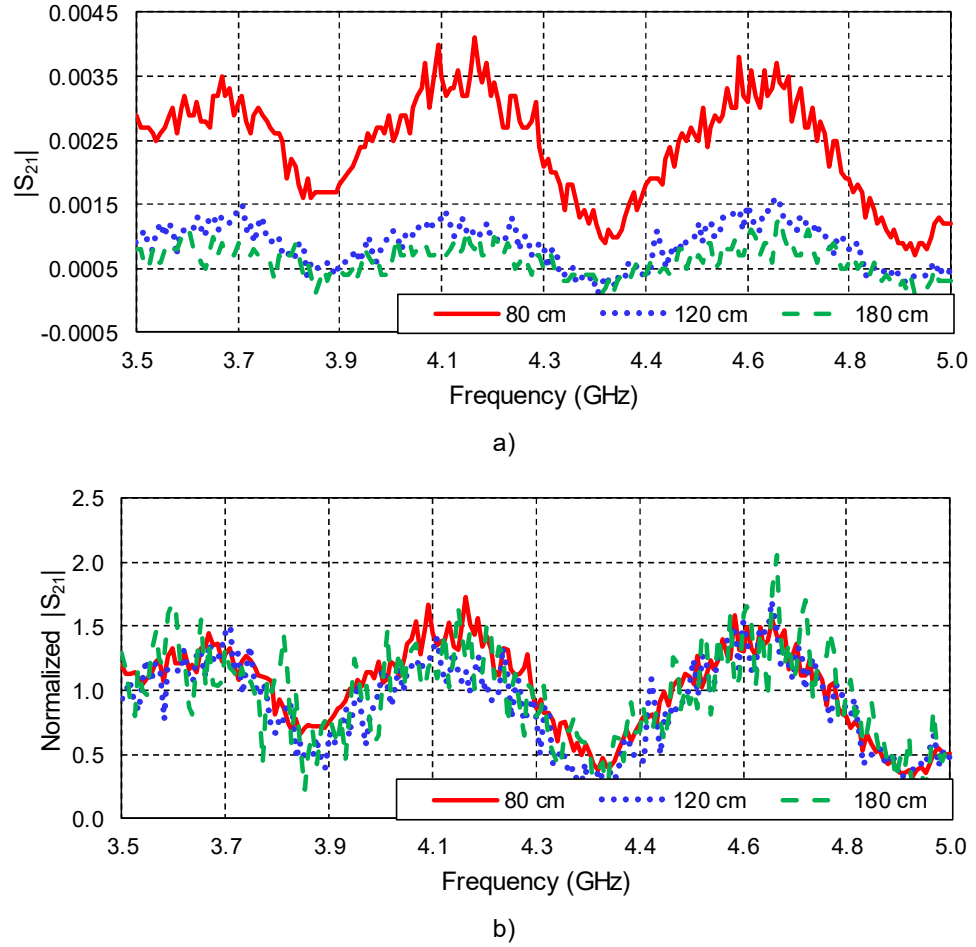


Fig. 6.1: CR-UWB chipless RFID identification code 00 measured at different distances of 80 cm, 120 cm, and 180 cm a) received  $|S_{21}|$ , b) normalized  $|S_{21}|$  according to Eq. (6.5)

### 6.3 Detection and Decoding of Chipless RFID Transponders

The optimal detection rule is the one that maximizes the conditional probability of  $\vec{s}_m$  being transmitted given that  $\vec{s}_{rx}$  is received  $P \left[ \frac{\vec{s}_{tx}}{\vec{s}_{rx}} \right]$ . It is described mathematically using the noise Gaussian probability density function by [81]

$$\hat{s}_{tx}^m = \underset{1 \leq m \leq M}{argmax} \left[ P_m \left( \frac{1}{\sqrt{\pi N_0}} \right)^N e^{-\frac{\|\vec{s}_{rx} - \vec{s}_{tx}^m\|^2}{N_0}} \right] \quad (6.6)$$

where  $\left( \frac{1}{\sqrt{\pi N_0}} \right)^N$  is a positive constant value that does not affect the calculation of the maximum and therefore can be dropped [81]

$$\hat{s}_{tx}^m = \underset{1 \leq m \leq M}{argmax} \left[ P_m e^{-\frac{\|\vec{s}_{rx} - \vec{s}_{tx}^m\|^2}{N_0}} \right] \quad (6.7)$$

An increasing logarithmic function can be applied to remove the exponential [81]

$$\hat{s}_{tx}^m = \underset{1 \leq m \leq M}{argmax} \left[ \ln P_m - \frac{\|\vec{s}_{rx} - \vec{s}_{tx}^m\|^2}{N_0} \right] \quad (6.8)$$

Multiplying by the positive constant  $\frac{N_0}{2}$  [81]

$$\hat{s}_{tx}^m = \underset{1 \leq m \leq M}{argmax} \left[ \frac{N_0}{2} \ln P_m - \frac{1}{2} \|\vec{s}_{rx} - \vec{s}_{tx}^m\|^2 \right] \quad (6.9)$$

is the  $m$ -th UWB chipless RFID transponder probability of occurrence, that is, the probability of the UWB chipless RFID transponder  $m$  being present in the interrogation zone. Assuming all UWB chipless RFID tags to be equiprobable, namely, each probability of occurrence is simply given by  $1/m$ . The variable  $P_m$  becomes a constant therefore it can be dropped from the Eq. (6.9), leaving only the  $m$  dependent terms, the decision rule becomes [81]

$$\hat{s}_{tx}^m = \underset{1 \leq m \leq M}{argmax} [-\|\vec{s}_{rx} - \vec{s}_{tx}^m\|^2] \quad (6.10)$$

### 6.3.1 Minimum Distance Detector

Using an intuitive reasoning for Eq. (6.10), it is known that maximizing the negative value of a term, it is equivalent to minimizing its positive. Minimizing the quadratic value of a term, it is equivalent to minimizing its square root. Then, Eq. (6.10) can be also represented by Eq. (6.11), and the whole operation becomes the magnitude calculation of a subtraction of the different UWB chipless RFID transponders backscattered signals from the corrupted noisy signal, and then selecting the minimum value among them [81]

$$\hat{s}_{tx}^m = \arg \min_{1 \leq m \leq M} [\|\vec{s}_{rx} - \vec{s}_{tx}^m\|] \quad (6.11)$$

Transforming back the vector signals to the time domain and then considering the signals sampling performed by the receiver. The minimum distance detection rule to be implemented is given by [81]

$$\hat{s}_{tx}^m = \arg \min_{1 \leq m \leq M} \sqrt{\sum_{i=0}^{\infty} [s_{rx}(i) - s_{tx}^m(i)]^2} \quad (6.12)$$

The minimum distance detector architecture is illustrated in Fig. 6.2, the detector receives the sampled signal and calculates the its Euclidean distance to the each of the previously stored templates. Finally, to estimate it chooses the smallest value, which represent the nearest neighbor or closest stored signal to received one.

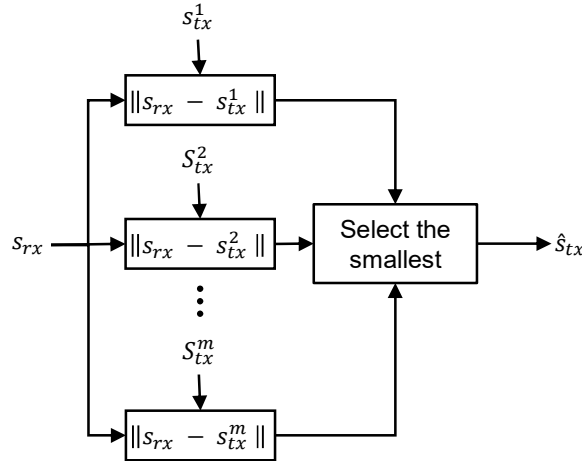


Fig. 6.2: Minimum distance detector architecture



### 6.3.2 Maximum Likelihood Detector

To derive the maximum likelihood ML detector, the optimal detection rule described in Eq. (6.12), is expanded solving the quadratic term [81]

$$\hat{s}_{tx}^m = \underset{1 \leq m \leq M}{\operatorname{argmax}} [- (\|\vec{s}_{rx}\|^2 + \|\vec{s}_{tx}^m\|^2 - 2\vec{s}_{rx} \cdot \vec{s}_{tx}^m)] \quad (6.13)$$

where  $\|\vec{s}_{rx}\|^2$  is the receive signal energy  $E_m$ ,  $\|\vec{s}_{rx}\|^2$  does not depends on  $m$  so it can be dropped. Therefore, the ML detection rule becomes [81]

$$\hat{s}_{tx}^m = \underset{1 \leq m \leq M}{\operatorname{argmax}} [2\vec{s}_{rx} \cdot \vec{s}_{tx}^m - E_m] \quad (6.14)$$

The ML detector architecture is shown in Fig. 6.3, the detector receives the sampled signal and calculates the its dot product to the each of the previously stored templates, substrates the respective energy. Finally, to estimate it chooses the largest value, which represent the most likely stored signal to received one.

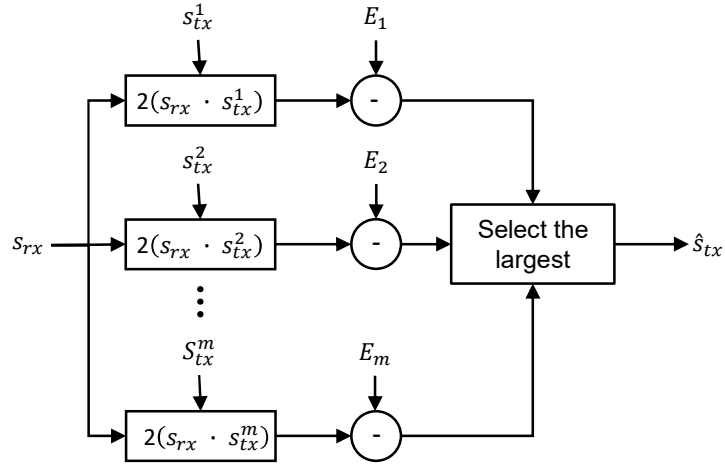


Fig. 6.3: Maximum likelihood detector architecture

### 6.3.3 Correlator Detector

Another type of detector that requires less operations than the optimal maximum likelihood rule, is the correlation detector given by [81]

$$\hat{s}_{tx}^m = \underset{1 \leq m \leq M}{\operatorname{argmax}} [\vec{s}_{rx} \cdot \vec{s}_{tx}^m] \quad (6.15)$$

The correlator detector architecture is shown in Fig. 6.4, like the ML detector, the correlator receives the sampled signal and calculates its dot product to the each of the previously stored templates and then estimates the sent code by choosing the largest value.

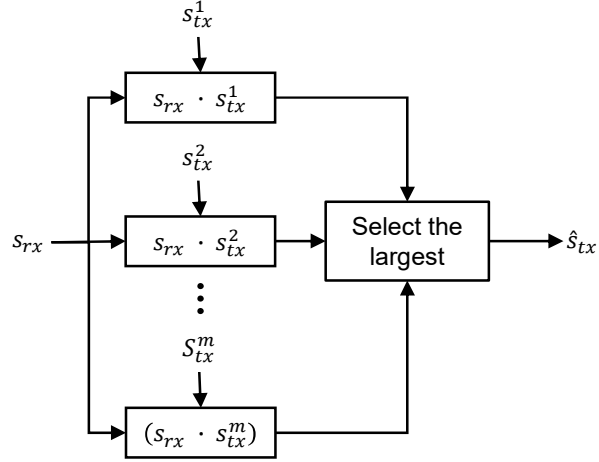


Fig. 6.4: Correlator detector architecture

### 6.3.4 Test Results

In this section, the decoding results of the UWB chipless RFID transponders using minimum distance and ML detectors are presented. The measurement setup is mounted in one of the offices at the Technische Universität Dresden. The VNA has been configured to measure the frequency spectrum located between 3.8 and 8.8 GHz, with a power control of 3 dB, an averaging factor of 20 sweeps per measurement, and the number of frequency points  $ns$  is set to different values. The DD-UWB chipless RFID transponders are measured at different separation distances  $x$  from the horn antennas. The UWB chipless RFID frequency response  $s_{tx}^m$ , used as a template to calculate the distance is obtained by simply removing the channel influence from the received signal at each distance  $x$ , as given by Eq. (A.9) of Appendix A.

The DD-UWB chipless RFID transponders received frequency response  $s_{rx}$  is given by the measured scattering parameter  $S_{21}$ . Fig. 6.5a shows the received  $s_{rx}$  for all four different codes and their counterpart  $s_{tx}^m$  calculated subtracting the channel influence in Fig. 6.5b. As can be noticed, in the case where no channel influence is removed, it is

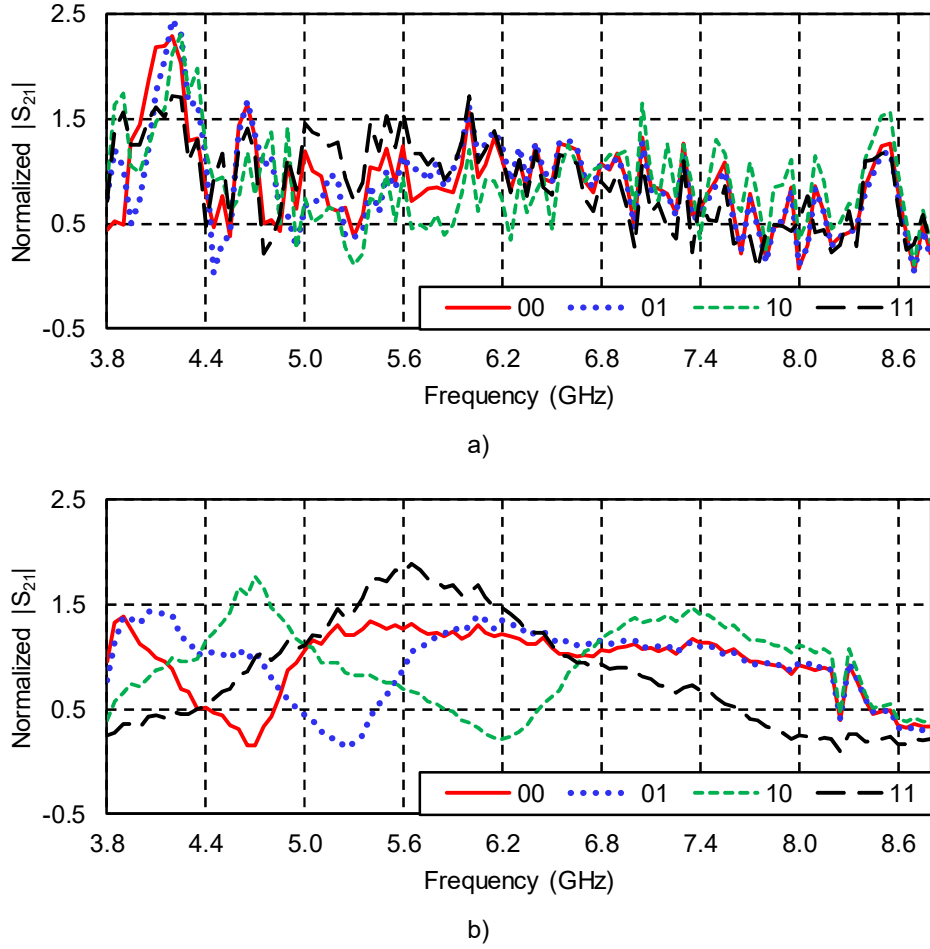


Fig. 6.5: UWB chipless RFID transponder measurements results: a) received  $S_{21}$  b) calculated  $s_{tx}^m$

not possible to distinguish between UWB chipless RFID transponders by simple visual inspection. Hence, the need to implement an algorithm and a proper coding to evaluate these signals and to obtain the correct response becomes more evident to improve the detection capabilities of the reader.

Table 6.1 presents the minimum distance detector results between the different DD-UWB chipless RFID transponders stored codes templates  $s_{tx}^m$ . These results serve to evaluate how distant are the UWB chipless RFID transponders codes, from the detectors perspective. They include the processing time to evaluate the performance of the detector and disregard unfounded high processing load claimed by other authors. The values show a consistent symmetric behavior, the distance between the received code 00 and stored code 01 is the same as the one between from received code 01 and stored code 00, and similar for other codes. It is important to point out, that although the coding technique is

based on the frequency shift principle, it is the whole frequency signature response that counts to perform the identification of the codes. Therefore, a higher frequency separation, as conventionally done, does not necessary means that the detector will obtain a higher performance, as can be noticed codes 00 and 11 have the higher frequency dip distance of 3.4 GHz but codes 00 and 10 have the higher distance of 9.3438, as measured by the detector.

Measurement parameters	Received Code $s_{tx}^m$	Stored code $s_{tx}^m$				Time (ms)
		00	01	10	11	
$x = 30$ cm $ns = 101$	00	<b>0.0000</b>	6.5287	9.3438	7.4702	0.578
	01	6.5287	<b>0.0000</b>	8.7176	9.1192	0.614
	10	9.3438	8.7176	<b>0.0000</b>	10.9716	1.555
	11	7.4702	9.1192	10.9716	<b>0.0000</b>	1.677

Table 6.1: Minimum distance detector results for different UWB chipless RFID transponders based on double-dipoles, according to Eq. (6.12)

Table 6.3 shows the minimum distance detector results, calculated for different distances  $x$  from the horn antennas and total number of frequency points  $ns$ . The minimum distance, which represents the detected DD-UWB chipless RFID transponder identification code, is represented by the numbers in bold for each scenario. The DD-UWB chipless RFID transponders were first located at a distance  $x$  of 30 cm away from the horn antennas. The total number of scans were varied between 101 and 1601 points. As can be seen, as the number of scanning points  $ns$  increases, the distance between DD-UWB chipless RFID transponders also increase. For instance, the distance between received signal  $s_{rx}^{00}$ , of DD-UWB chipless RFID transponder with identification code 00, and template  $s_{tx}^{11}$  of code 11 for  $x = 30$  cm and  $ns = 101$  is 9.7691, and for  $x = 30$  cm and  $ns = 1601$  is 38.3961, which represents a distance increase of more than 3 times. Furthermore, for  $ns = 101$ , the received signal  $s_{rx}^{10}$  of DD-UWB chipless RFID transponder with identification code 10 is wrongly identified as code 01, but after the number of total samples  $ns$  is increased, all DD-UWB chipless RFID transponders codes are successfully identified. Hence, the  $ns$  becomes a key factor of the UWB reader design to be considered along with the UWB chipless RFID transponders coding type to guarantee a successful identification under channel impairments. Further calculations are

Measurement parameters	Received Code $s_{rx}^m$	Stored code $s_{tx}^m$				Time (ms)
		00	01	10	11	
$x = 30$ cm $ns = 101$	00	<b>8.4985</b>	9.2880	13.0335	9.7691	0.850
	01	10.1520	<b>7.9034</b>	12.7409	10.7790	0.432
	10	10.9045	<b>9.6852</b>	9.9668	11.3221	1.116
	11	11.3482	11.3198	14.3293	<b>9.2225</b>	0.360
$x = 30$ cm $ns = 201$	00	<b>11.6590</b>	12.9470	17.4911	13.4878	4.573
	01	13.9654	<b>10.9228</b>	17.1259	15.0971	0.701
	10	15.6589	14.3251	<b>13.0013</b>	16.2443	0.637
	11	15.6344	15.9119	19.2953	<b>12.8700</b>	0.570
$x = 30$ cm $ns = 401$	00	<b>17.0566</b>	18.3831	24.7431	19.4902	4.549
	01	20.3854	<b>15.7730</b>	24.2113	21.3197	0.933
	10	22.6515	20.2479	<b>18.9059</b>	22.9407	0.694
	11	23.2029	22.7857	27.5037	<b>18.2015</b>	0.747
$x = 30$ cm $ns = 801$	00	<b>17.0566</b>	18.3831	24.7431	19.4902	4.661
	01	29.0284	<b>22.0783</b>	33.9736	29.4234	0.893
	10	32.2557	28.4394	<b>26.5324</b>	32.0400	0.761
	11	33.0979	31.8935	38.7269	<b>25.4109</b>	0.697
$x = 30$ cm $ns = 1601$	00	<b>33.7093</b>	37.1278	50.5398	38.3961	5.505
	01	39.9656	<b>31.4479</b>	48.2963	41.405	0.878
	10	45.7288	40.5135	<b>37.4894</b>	45.6467	0.850
	11	45.8048	45.3788	55.2679	<b>35.7914</b>	0.837
$x = 20$ cm $ns = 401$	00	<b>12.0272</b>	19.0540	22.6660	21.146	5.866
	01	17.6070	<b>11.8544</b>	20.0444	22.4532	0.675
	10	23.1515	21.7458	<b>11.8081</b>	26.3341	0.612
	11	19.0693	21.8613	24.2025	<b>15.8686</b>	0.622
$x = 10$ cm $ns = 401$	00	<b>7.5699</b>	15.9166	20.8790	17.8636	1.016
	01	18.3378	<b>6.6530</b>	18.4256	21.8406	0.601
	10	23.6268	19.7038	<b>7.2428</b>	23.6071	0.608
	11	19.7705	21.2238	21.8122	<b>9.3326</b>	0.592

Table 6.2: Minimum distance detector results for different UWB chipless RFID transponders based on double-dipoles and different measurement parameters, according to Eq. (6.12)

performed for  $ns$  of 401 and distances  $x$  of 20 cm and 10 cm, and all DD-UWB chipless RFID transponders codes are still successfully identified.

In a similar way, the UWB chipless RFID transponders based on concentric rings are measured. Table 6.3 presents the minimum distance detector results between the different CC-UWB chipless RFID transponders stored codes templates  $s_{tx}^m$ . The values show again a consistent symmetric behavior. As can be seen, with this type of frequency coding, similar distances as the ones obtained for the DD-UWB chipless transponders are

Measurement parameters	Received Code $s_{rx}^m$	Stored code $s_{rx}^m$								Time (ms)
		000	001	010	011	100	101	110	111	
$x = 30$ cm $ns = 101$	000	<b>0.0000</b>	6.8561	6.1325	8.0872	4.6346	7.2978	6.0479	7.7653	2.491
	001	6.8561	<b>0.0000</b>	7.8667	5.7752	7.4769	5.1772	8.7619	5.6207	2.091
	010	6.1325	7.8667	<b>0.0000</b>	4.873	6.4948	8.1473	6.2973	5.2659	1.889
	011	8.0872	5.7752	4.873	<b>0.0000</b>	7.5941	6.4477	7.9222	2.933	2.925
	100	4.6346	7.4769	6.4948	7.5941	<b>0.0000</b>	6.4683	4.1577	6.8767	5.003
	101	7.2978	5.1772	8.1473	6.4477	6.4683	<b>0.0000</b>	7.8607	5.7571	6.903
	110	6.0479	8.7619	6.2973	7.9222	4.1577	7.8607	<b>0.0000</b>	7.1045	2.627
	111	7.7653	5.6207	5.2659	2.933	6.8767	5.7571	7.1045	<b>0.0000</b>	2.976

Table 6.3: Minimum distance detector results for different UWB chipless RFID transponders based on concentric rings, according to Eq. (6.12)

obtained. The detector only sees the amount of points and not the fabrication type or frequency range of the UWB chipless RFID transponders that sends the signal. Nevertheless, from the UWB chipless RFID transponders perspective, a comparison is made between four double dipoles and eight concentric rings chipless RFID transponders measured within a 5 GHz and 2 GHz bandwidth respectively.

Following the same procedure, the CC-UWB chipless RFID transponders are located at a distance  $x$  of 30 cm away from the horn antennas, and the total number of scans were varying between 101 and 1601 points. Table 6.4 shows the minimum distance detector processing times and results, calculated for different total number of samples  $ns$ . The minimum distance is represented by the numbers in bold for each scenario. The results show that unlike the double dipoles based chipless RFID transponder, the concentric rings are successfully identified even for  $ns = 100$ , and in a similar way, as the number of samples increases, the distance between codes also does. There's a slightly increase in the processing times, as the detector must now compare four mores identification codes.

The next step is the validation of the ML detector with the COD1-UWB chipless RFID transponders, their frequency response was measured with the same VNA setup for a transponder distance  $x$  of 30 cm away from the horn antennas, and the total number of scans 401 points. As the detection takes place in the time domain, the inverse fast Fourier transform (IFFT) of the  $S_{21}$  is calculated and the results are plotted in Fig. 6.6, to visually recognized the difference among identification codes.

Measurement parameters	Received code $S_{rx}^m$	Stored code $S_{tx}^m$								Time (ms)
		000	001	010	011	100	101	110	111	
x= 30 cm ns = 101	000	<b>5.9342</b>	9.2324	8.6777	10.3314	7.6286	9.6098	8.1471	10.1966	0.473
	001	8.8407	<b>5.4435</b>	9.7386	8.1910	9.3909	7.6501	10.1625	8.2210	0.763
	010	8.4827	9.9291	<b>5.7945</b>	7.8094	8.7986	10.1934	8.2102	8.2249	0.654
	011	10.0005	8.1985	7.5395	<b>5.8498</b>	9.6169	8.7499	9.5076	6.7736	0.953
	100	7.6275	9.7567	8.9863	9.9737	<b>6.0458</b>	9.0117	6.8466	9.5535	2.743
	101	9.1289	7.5074	9.9105	8.6159	8.4754	<b>5.3359</b>	9.2829	8.2219	6.220
	110	8.9234	10.9965	9.1505	10.4565	7.8144	10.3248	<b>6.0311</b>	9.9801	0.558
	111	9.6917	8.0216	7.7470	6.4897	8.9807	8.1640	8.7398	<b>5.9562</b>	0.649
x= 30 cm ns = 201	000	<b>8.3638</b>	12.8843	11.9801	14.4011	10.6393	13.3099	11.6521	12.9588	1.071
	001	12.3393	<b>7.7171</b>	13.7507	11.6461	13.3755	10.7500	14.4027	11.3376	0.915
	010	11.7226	14.0276	<b>8.2516</b>	11.0327	12.1940	14.3224	11.4776	10.7482	0.433
	011	13.9371	11.6556	10.6372	<b>8.3345</b>	13.7905	12.3631	13.3609	10.1240	1.917
	100	10.8840	14.0389	12.6416	14.4377	<b>8.6941</b>	12.9069	9.8762	13.1428	1.270
	101	12.8164	10.7794	14.0743	12.3753	12.1825	<b>7.6453</b>	13.3634	11.5688	0.730
	110	12.7166	15.5573	12.7922	14.6954	10.9673	14.6290	<b>8.5690</b>	13.7464	1.178
	111	12.4565	11.4107	10.4037	10.1996	12.4353	11.6132	12.2710	<b>8.6167</b>	0.844
x= 30 cm ns = 401	000	<b>12.0549</b>	18.5837	17.0864	20.4582	15.6321	21.1604	16.5173	19.4455	0.700
	001	17.7398	<b>11.0007</b>	19.5214	16.1131	18.8281	16.2282	20.0798	16.3253	0.794
	010	16.7204	19.9829	<b>11.7671</b>	15.4714	17.6686	21.7662	16.9077	15.6366	0.850
	011	19.9801	16.4548	15.1771	<b>11.8834</b>	19.6754	18.1450	19.3752	14.0038	0.724
	100	15.5629	19.5768	17.9603	20.1314	<b>12.3454</b>	18.6558	14.0210	18.7811	2.357
	101	20.1030	15.7296	21.0209	17.3868	17.3980	<b>10.6952</b>	19.9517	17.3120	8.382
	110	17.8064	21.6665	18.4695	20.8608	15.6905	21.8696	<b>12.2358</b>	19.3951	1.195
	111	18.6441	16.3490	14.9662	13.5733	17.9715	17.8133	17.3637	<b>12.2380</b>	1.398
x= 30 cm ns = 801	000	<b>16.8254</b>	26.5320	24.3344	29.2742	21.4663	26.9309	23.1032	27.0377	1.223
	001	25.0709	<b>15.2476</b>	27.7760	22.9293	27.2559	21.5064	28.9529	22.9800	0.974
	010	23.8844	28.6979	<b>16.3822</b>	22.3999	25.2473	29.0930	23.1304	22.1628	0.84
	011	28.4271	23.4890	21.6582	<b>16.5134</b>	28.0828	24.9224	26.7445	20.3068	0.876
	100	21.4310	28.5597	25.6462	28.9414	<b>17.1694</b>	25.7452	19.1349	26.8836	0.964
	101	25.4798	21.4708	28.1674	24.3712	24.1962	<b>15.0640</b>	26.1174	23.0264	8.041
	110	25.3793	31.5981	25.7845	29.4272	22.0522	29.2003	<b>16.9798</b>	27.7178	1.388
	111	25.5685	23.0072	20.7487	19.6047	25.4038	23.0899	24.1353	<b>16.9832</b>	1.213
x= 30 cm ns = 1601	000	<b>23.2783</b>	36.5084	35.0232	41.0666	30.2241	39.9940	32.6261	38.4993	1.225
	001	34.4248	<b>21.2930</b>	38.7291	31.8697	36.7656	29.9960	39.6378	31.8251	2.668
	010	33.7212	39.4871	<b>22.5943</b>	29.9797	34.3842	40.8168	32.0049	30.0864	1.122
	011	39.6538	32.3425	29.3779	<b>22.9065</b>	38.7932	34.4523	38.0676	27.3413	1.017
	100	30.1560	38.6687	35.6253	40.2464	<b>23.9134</b>	36.6364	26.8190	37.3159	1.125
	101	37.7110	29.3423	39.6502	33.4369	34.0176	<b>20.8371</b>	37.8060	32.5568	6.552
	110	35.8490	43.5696	36.5112	42.0460	31.0124	42.4012	<b>24.3107</b>	39.0792	0.968
	111	36.4654	31.7981	28.8746	26.6654	35.1829	33.1504	33.9466	<b>23.5928</b>	0.898

Table 6.4: Minimum distance detector results for UWB chipless RFID transponders based on concentric rings and different measurement parameters, according to Eq. (6.12)

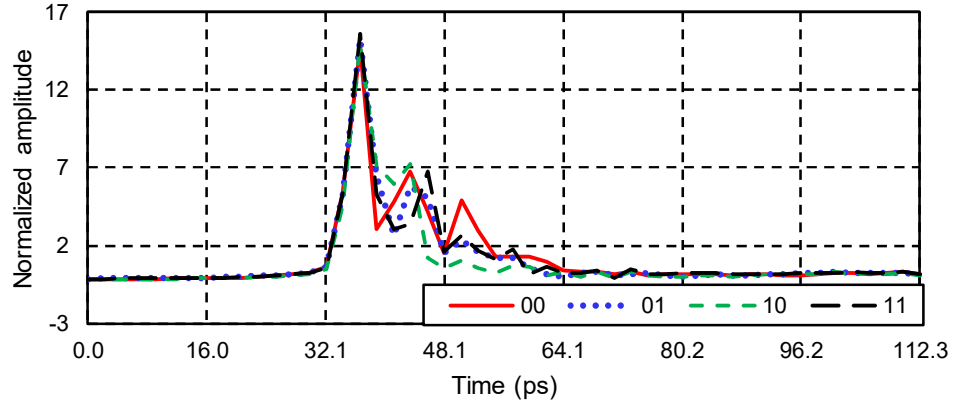


Fig. 6.6: Calculated time domain received  $S_{21}$  for the COD1-UWB chipless RFID transponder on PET substrate

The ML detector results are presented in Table 6.6 for the different substrates, as can be seen, all identification codes are detected successfully when selecting the maximum as marked in bold. In the case of the prototypes fabricated on PET, two different scenarios are calculated, the no noise scenario which is merely the ML between stored responses, subtracting the channel influence, basically between the different graphs shown Fig. 6.6, and the noise measurement or under normal conditions including the channel influence. For each substrate calculation their respective substrate signal template is used since, as discussed in subsection 4.4.1, the frequency responses differ considerable between same identification codes on different substrates, and one single template for each identification code for all different substrate was not possible to realized. Therefore, each set of COD1-UWB chipless RFID transponders printed on a specific substrate is considered as a complete new set of identification codes.

To verify the functionality of the last correlation detector, its implementation is considered using the Novelda Radar in a simultaneous detection of multiple chipless RFID transponders and will be discussed further in the next section.



Substrate	Measurement condition	Received code $s_{rx}$	Stored code $s_{tx}^m$				Time (ms)
			00	01	10	11	
PET	No noise	00	<b>371.14</b>	344.46	322.53	337.66	0.60
		01	344.46	<b>374.95</b>	343.33	363.03	0.50
		10	322.53	343.33	<b>379.77</b>	310.99	0.71
		11	337.66	363.03	320.99	<b>374.30</b>	0.64
	Noise	00	<b>352.80</b>	339.35	314.02	341.03	4.61
		01	335.89	<b>365.84</b>	334.28	362.32	0.61
		10	319.42	347.49	<b>371.32</b>	322.22	0.60
		11	310.43	341.17	284.43	<b>362.59</b>	0.54
Stadium	Noise	00	<b>334.15</b>	306.11	272.80	310.70	4.63
		01	278.88	<b>341.50</b>	264.17	269.53	0.58
		10	329.39	308.48	<b>360.87</b>	333.69	0.56
		11	325.30	333.93	299.62	<b>336.93</b>	0.58
Metro/cruise	Noise	00	<b>296.36</b>	286.85	269.47	271.97	4.55
		01	310.28	<b>328.10</b>	310.97	302.87	0.73
		10	302.28	320.08	<b>341.13</b>	291.65	1.03
		11	275.39	281.89	257.02	<b>308.49</b>	1.03
Airport	Noise	00	<b>378.49</b>	361.45	355.63	363.08	4.63
		01	361.45	<b>379.42</b>	353.83	368.08	0.69
		10	355.63	353.83	<b>383.69</b>	352.41	1.11
		11	363.08	368.08	352.41	<b>380.11</b>	0.56

Table 6.6: Maximum likelihood detector results for UWB chipless RFID transponders based on COD1 on different substrates, according to (6.14)

## 6.4 Simultaneous Detection of Multiple UWB Chipless Transponders

Before going into details of the simultaneous detection of multiple UWB chipless RFID transponders, the special case shown in Fig. 6.7 must be analyzed. It is meant to illustrate the signal responses of two different scenarios. Fig. 6.7a shows multiple UWB chipless RFID transponder with same identification codes separated a distance greater than the range resolution in a multipath free scenario. Fig. 6.7b considers one single UWB chipless RFID transponder placed in a multipath scenario. And Fig. 6.7c is showing the received signal considering the ToA of the second pulse is the same in both cases. That is, if the transponders are placed in a multipath scenario, the system could not be able to distinguish between two transponders or the multipath way of just one. Therefore, in this work, the multi-detection studies are conducted in a multipath free scenario due to the reader's limitations, as additional hardware and/or sensors are required to overcome the multipath channel effect in UWB chipless RFID transponders (e.g. rake receiver). Nevertheless, due to the short-range characteristics of the RFID systems with chipless transponders ( $< 50$  cm) achieving a multi-path free channel, represents no major inconvenience.

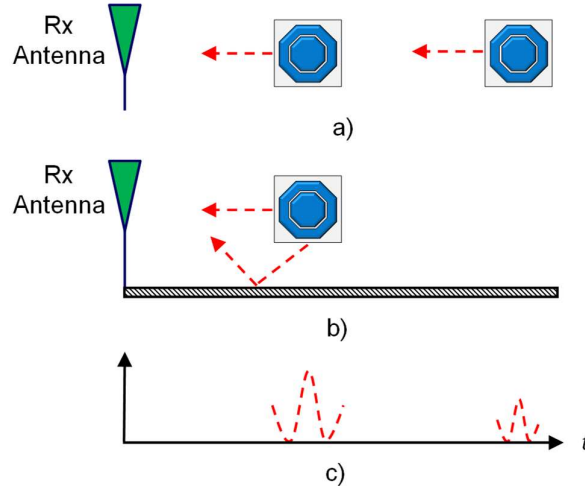


Fig. 6.7: UWB chipless RFID transponder with same identification code a) multi-detection scenario, b) multi-path channel scenario c) received signal

The LOS and multipath free scenarios for the simultaneous identification of the two chipless transponders are illustrated in Fig. 6.8. As explained in section 5.1.2, the radar's range resolution depends on the Novelda radar's one nanosecond pulse width and it

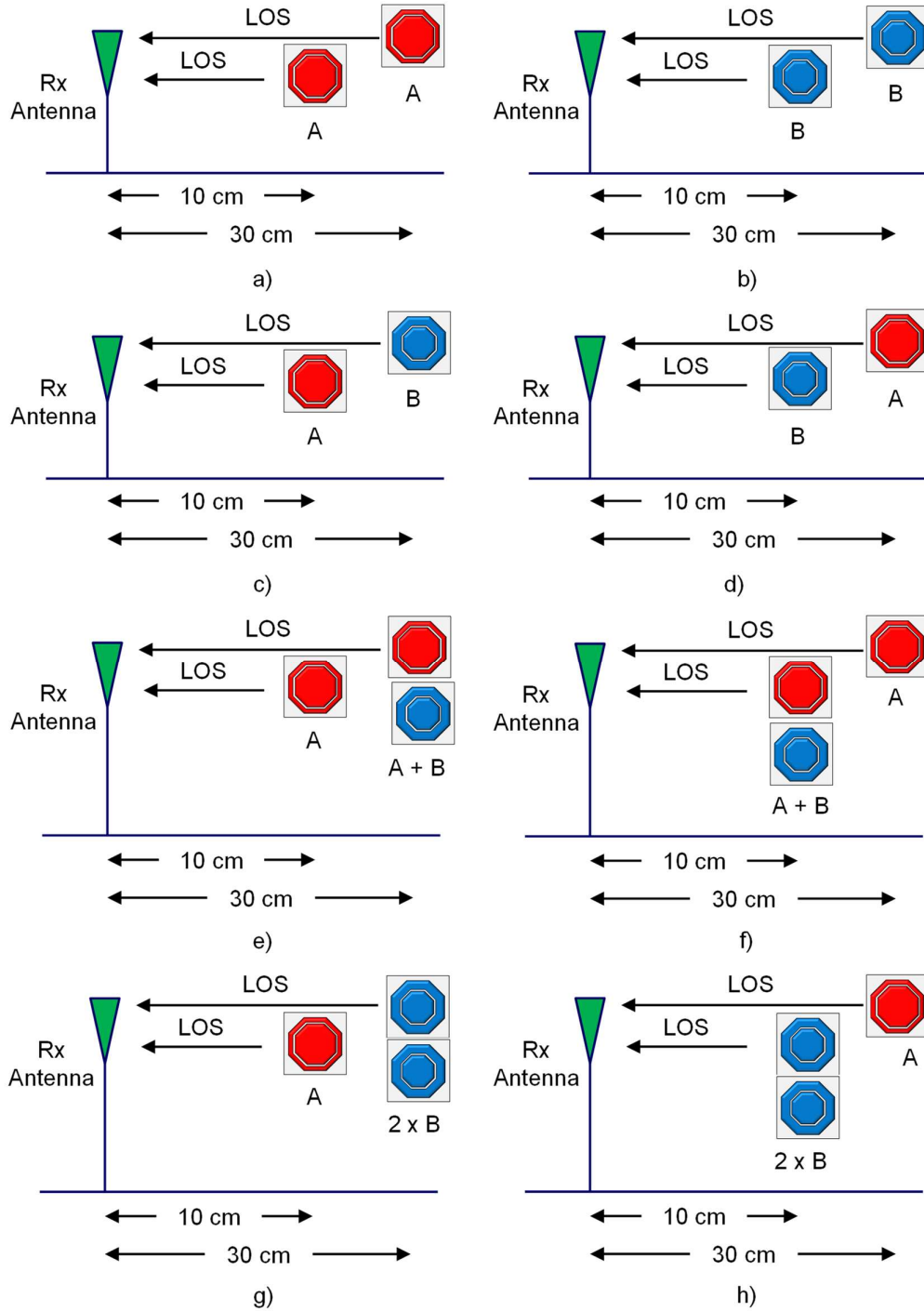


Fig. 6.8: Chipless RFID transponders simultaneous multi-detection scenarios: a)  $A - A$ , two type A located at 10 and 30 cm from the antennas, b)  $B - B$ , two type B located at 10 and 30 cm from the antennas, c)  $A - B$ , A located at 10 cm and B at 30 cm from the antennas, d)  $B - A$ , B located at 10 cm and A at the 30 cm from the antennas, e)  $A - A + B$ , A located at 10 cm and  $A + B$  at 30 cm from the antennas, f)  $A + B - A$ ,  $A + B$  located at 10 cm and B at 30 cm from the antennas, (g)  $A - 2B$ , A located at 10 cm and 2 B at 30 cm from the antennas, and (h)  $2B - A$ , 2 B located at 10 cm and A at 30 cm from the antennas [76].

are placed at 10 or 30 cm away from the antennas and guarantee enough time delay to distinguish between each received pulse. A direct LOS to the chipless RFID transponders is required to be able to backscatter the signal pulse directly back to the antennas. To avoid the influence of multipath components, the antennas are placed at a height of 80 cm, which is eight times the direct distance between the antennas and the chipless RFID transponder located at the closest position. Additionally, the distances from the antennas to the rest of the surrounding surfaces are in the order of several meters [76].

The UWB chipless RFID transponders are mounted on different tripods, as shown in Fig. A.4 of Appendix A, and placed with direct LOS at distances of either 10 or 30 cm from the horn antennas. One reference measurement of the backscattered pulse of every single transponder A, B and their generated code A + B placed at each distance is required to further serve as a comparison template signal in the decoding stage [76].

The obtained correlation results are shown in Table 6.7, as can be seen, despite the variations observed in the frequency domain, the correlation values clearly identify the correct UWB chipless RFID transponder from where the pulse is backscattered at each specific scenario. Furthermore, the calculations were also performed using only one reference pulse per chipless RFID transponder type at either 10 or 30 cm and the decoding were still successful [76].

Scenario	First pulse			Second pulse		
	A	B	A + B	A	B	A + B
A - A	<b>64.55</b>	49.4	29.96	<b>63.55</b>	48.64	36.77
A - B	<b>64.1</b>	46.84	34.11	37.08	<b>48.62</b>	28.41
B - A	52.12	<b>64.65</b>	33.46	<b>61.5</b>	35.59	48.2
B - B	34.22	<b>64.61</b>	52.89	33.78	<b>61.72</b>	52.29
AB – AB*	48.08	45.03	61.17	45.55	48.34	<b>63.77</b>

Table 6.7: Correlation detector results for different scenarios, \*partial results of scenarios A – AB and AB + A, according to Eq. (6.15) [76]

The received pulse energy calculations including the path loss are shown in Table 6.8, the values are calculated with the help of Eq. (6.16), and show a clear different between the case of two UWB chipless RFID transponders placed together to the case

when only one transponder is present. Therefore, by setting the proper energy thresholds, the right amount of transponders can be assessed [76].

$$\zeta_{rx} = \sum_{-\infty}^{+\infty} |s_{rx}(n)|^2 \quad (6.16)$$

Received pulse energy ( $\mu\text{J}$ )			
Amount	Transponder	10 cm	30 cm
1	A	0.81	0.69
2	A	2.59	2.01
1	B	1.50	1.44
2	B	3.61	2.82

Table 6.8: Calculated received pulse energy, according to Eq. (6.16) [76]

## 6.5 Summary

In this chapter, three different detectors used to recognize the identification codes embedded in four distinct UWB chipless RFID transponders geometries are introduced. A minimum distance detection rule was employed to decode four DD- and eight CR-UWB chipless RFID transponders in the frequency domain, and the importance of not only proposing a coding technique based on merely on human inspection but rather from a computing system point of view has been demonstrated. Highlighting that the detector sees the number of samples and not the frequency range of the UWB chipless RFID transponders. Therefore, the frequency response shape of the CR-UWB RFID transponders could be perfectly replicated in other frequency bands and use only one set of templates to recognized other bits placed in a different frequency band without significantly increasing the processing time.

In the same manner, the ML detector is implemented to recognized four COD1-UWB chipless RFID transponders in the time domain for prototypes printed on four different substrates. The detection and coding are performed considering each substrate fabrication as a unique set, due to the frequency responses differences obtained.

Finally, the simple correlator detector is implemented to study a simultaneous detection of multiple chipless RFID transponders having either the same or different

identification codes, place together or separated a distance greater than the range resolution. Again, the importance of choosing the configuration to realize a specific feature has been point out: either periodic structures to increase  $|RCS|$  and reading distance or a different single structure to enable the simultaneous detection by analyzing its received power. The implementation of the detectors in the readers and test in real case scenarios will be presented in next chapter.

## 7 System Implementation

The results of the implementation of two UWB chipless RFID systems with chipless transponders are presented in this chapter. The printed UWB chipless RFID transponders based on CR and COD1 designed in chapter 4, are interrogated by their respective SFM- and IR readers architectures described in chapter 5. For that purpose, the detection techniques presented in chapter 6 are realized by means of a detection algorithm.

The developed detection algorithms to control the UWB RFID readers are discussed in detail in the following sections, and to understand their functionality, the following system restrictions need to be considered:

1. The UWB chipless transponders must be interrogated with an incident waveform orthogonal to its surface, otherwise, frequency variations that may lead to wrong identification code detections might be experienced.
2. The interrogation zone is limited by the transmitted power and the radiation pattern of the antennas. This last one, is not homogenous, thus, the UWB chipless RFID transponders must be placed in between the two antennas, and avoid their near field zone, where the fields behave in a non-linear manner.
3. The UWB RFID reader has no tracking characteristics. Therefore, it cannot calculate whether an UWB chipless RFID transponder is entering or leaving its interrogation zone and follow its position throughout the whole detection process. Which means, the detection procedure must be carried out in a sequential way: one or two UWB chipless RFID transponders placed or removed at the same time, and once the last one has left the identification zone, a new one may be placed to continue with the detection procedure.
4. The detection process takes place in a real test-case scenario, considering people holding the UWB chipless transponders by hand. Therefore, the detection algorithm must consider, that the UWB chipless RFID

transponder has slightly movements while being place, remove or hold by hand until it reaches or remains in its rightful position between the antennas in the interrogation zone.

## 7.1 SFM-UWB RFID System with CR-Chipless Transponders

The implementation results of the UWB RFID system with chipless RFID transponders based on the SFM-reader and the CR-UWB RFID transponders are presented in this section. First, all the UWB chipless RFID transponders frequency responses measured with the SFM-Reader front-end together with an empty channel measurement are stored in the database. The channel measurement is meant to serve as a template for the no-transponder detection case, although a simple power detector could have been implemented also. To be able to interrogate, detect and recognized the different CR-UWB RFID transponders, the controlling and minimum distance detection algorithm shown in Fig. 7.1 has been developed. Together with the developed user interface, where the amount of detected transponder counting track is kept and different symbolic images representing the meaning of the detected identification code are displayed.

As mentioned previously, the RFID reader shall consider the handling of the UWB chipless RFID transponders and it has no tracking capabilities. Therefore, the reader must interrogate and recognize the UWB chipless RFID transponder a defined amount of times  $ts$  to have enough data, since the decision cannot be based solely in one frequency sweep, a counter  $sc$  is defined to keeps track of this requirement. Once a UWB chipless RFID transponder has been detected, a flag is raised, to lock the detection process and avoid unnecessary extra scanning, until the transponder leaves the interrogation zone, and a new detection process may be started.

The SFM-UWB reader sweeps the UWB chipless RFID transponder with a total number of  $ns$  frequencies and stores each received response. Then, the received frequency response is enhanced with a noise reduction technique and normalized to reduce the path-loss effects. The distance to each of the stored signal templates including the empty channel measurement is calculated ( $tc$ ), then the minimum is selected and given as the detected identification code. This process is repeated storing each result a total number of  $ts$ , then the mode of all the detection is calculated and this value represents the detected identification code. The flag is raised to let the algorithm known



that an UWB chipless RFID transponder has been placed and successfully detected in its interrogation zone, and that it should wait until it has left the interrogation zone to perform further detections. If this is the first time the transponder is detected (Flag = 0) then the

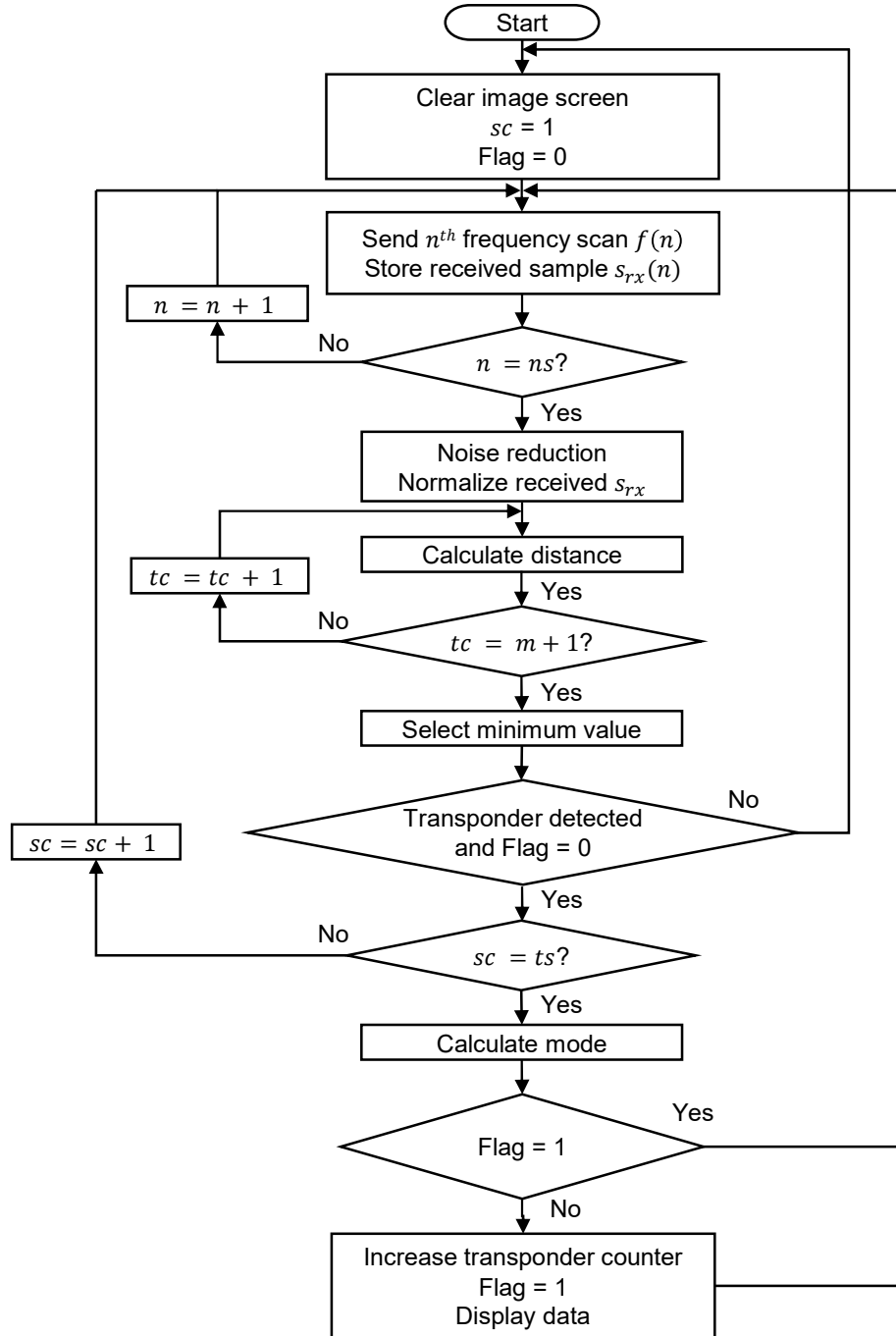


Fig. 7.1: UWB SFM-RFID reader detection algorithm

correspondent counter is increased, and the symbolic image displayed in the user interface, and the process starts all over again with a raised flag.

A specific number and a symbol image have been assigned to each identification code according to Table 7.1 to illustrated both types of possibilities, and are meant to be displayed in the interface, once the detection has taken place.

Code	Number	Image
000	6	Crew
001	7	Official
010	8	First responder
011	4	Pregnant woman
100	2	Child
101	1	Adult
110	5	Handicap
111	3	Baby

Table 7.1: Identification codes assigned numbers and images

The previous algorithm is implemented in the UWB SFM-RFID reader and the CR-UWB chipless RFID transponder are interrogated sequentially at approximately 10 cm from the horn antennas, as shown in Fig. 7.2. A total number of sweeps  $ts = 3$  per detection to keep the detection time as fast as possible (below 16 seconds). An illustrative video of this system is included within the DVD with this thesis.

The detectors results are shown in Table 7.2, the minimum values are marked in bold, as can be seen, all UWB chipless RFID transponders are correctly identified, when considering the mode of all the interrogation sweeps. However, identification codes 011, 100 and 110 are detected incorrectly for the first frequency sweep, due to the placement of the UWB chipless transponder. If the transponder is placed while the SFM-RFID is in the middle of the scanning sweep, wrong frequency samples are taken for the first half, influencing the detector results. The previous, reinforces the approach to consider several measurements to perform the detection based on the mode or simply discard the first one. A similar effect is experienced if the transponder is removed after the detection process has started and that is why an acoustic signal was programmed to let the user know when the transponder can be removed. Nevertheless, further studies must be conducted



Fig. 7.2: FD RFID system sequence of detection: a) No. 2 – child, b) No. 8 – first responder, c) No. 5 – handicap, d) No. 4 – pregnant woman, e) No. 6 – crew f) No. 1 – adult, g) No. 7 – official, h) No. 3 baby

considering more real-case scenarios, since each user places the UWB chipless transponders at his own pace, and one or more frequency sweeps might be affected in this process. For illustration purposes only 3 sweeps were considered as the author has already

Received code $s_{rx}$	Scan sequence	Stored code $s_{tx}^m$							
		000	001	010	011	100	101	110	111
000	1 <sup>st</sup>	<b>116.11</b>	582.57	422.07	620.32	340.18	488.91	418.64	607.14
	2 <sup>nd</sup>	<b>157.91</b>	398.19	214.57	450.22	256.43	369.84	207.29	317.47
	3 <sup>rd</sup>	<b>151.20</b>	361.70	156.01	390.26	216.67	399.17	183.64	297.28
001	1 <sup>st</sup>	430.87	<b>173.90</b>	364.22	314.55	406.26	341.63	484.46	291.66
	2 <sup>nd</sup>	450.66	<b>136.19</b>	475.93	414.41	488.82	435.78	537.06	324.14
	3 <sup>rd</sup>	476.73	<b>101.90</b>	379.48	279.10	313.00	454.43	460.23	341.44
010	1 <sup>st</sup>	421.02	476.56	<b>81.96</b>	197.65	221.25	508.60	262.81	306.36
	2 <sup>nd</sup>	513.02	405.80	<b>134.40</b>	259.58	307.10	379.95	268.27	211.82
	3 <sup>rd</sup>	430.59	359.86	<b>90.51</b>	206.58	224.95	373.40	206.48	212.09
011	1 <sup>st</sup>	1114.60	706.10	648.60	596.80	763.10	659.70	661.60	<b>386.30</b>
	2 <sup>nd</sup>	637.54	238.24	198.76	<b>136.14</b>	379.39	507.54	446.86	210.96
	3 <sup>rd</sup>	621.56	288.37	218.53	<b>156.38</b>	349.31	567.63	421.10	260.37
100	1 <sup>st</sup>	558.83	821.44	583.14	619.89	513.51	648.21	<b>492.06</b>	600.59
	2 <sup>nd</sup>	409.79	578.77	364.53	371.90	<b>220.47</b>	394.71	405.58	476.39
	3 <sup>rd</sup>	462.41	887.74	566.35	689.62	<b>411.88</b>	564.73	541.59	683.51
101	1 <sup>st</sup>	1016.5	778.3	1030	1067.7	1002.2	<b>586.4</b>	918.3	681.4
	2 <sup>nd</sup>	743.2	310.2	553.09	464.91	487.11	<b>98.4</b>	646.6	320.06
	3 <sup>rd</sup>	739.29	319.88	529.52	511.00	429.39	<b>170.57</b>	525.1	316.9
110	1 <sup>st</sup>	331.75	792.61	500.94	618.75	<b>233.95</b>	625.12	294.24	795.13
	2 <sup>nd</sup>	384.51	739.25	487.88	739.47	339.98	478.93	<b>200.69</b>	579.96
	3 <sup>rd</sup>	419.57	520.33	317.59	605.31	357.91	395.68	<b>213.91</b>	296.33
111	1 <sup>st</sup>	1115.70	820.40	945.50	991.70	1103.40	776.10	986.80	<b>587.80</b>
	2 <sup>nd</sup>	661.63	215.19	251.66	260.89	466.16	362.65	510.33	<b>63.01</b>
	3 <sup>rd</sup>	625.69	233.33	216.89	261.89	442.42	374.95	466.80	<b>49.10</b>

Table 7.2: SFM-UWB system detector results

experience with the system. Further test conducted for difference distances and the UWB chipless RFID transponders were successfully identify up to a 36 cm distance, as the  $|RCS|$  per transponder slightly varies, the distance is limited by the UWB chipless RFID transponder with less reading range. The detection period of the system including 3 sweep measurements rounds the 16 seconds, around 5.3 seconds per individual sweep. This time can be significantly decreased performing hardware optimization, developing an embedded system solution, and removing the computer-based user interface. To values near of the reported processing times in subsection 6.3, where the detectors were introduced.

Due to the bulky and relative long detection period of this system, it is not suitable to be implemented in a real evacuation scenario, therefore the system composed with the IR radar and the COD1-UWB chipless RFID transponder is chosen to conduct the field

test in the different venues premises, since with this IR-system, it takes less than 2 seconds to perform the detection.

## 7.2 IR-UWB RFID System with COD1-Chipless Transponders

The development of the controlling algorithm for the Novelda IR-radar bases system is based on the same consideration as for the SFM-reader and is shown in Fig. 7.3. However, as the pulse duration of the reader is in the order of nanoseconds, and the UWB

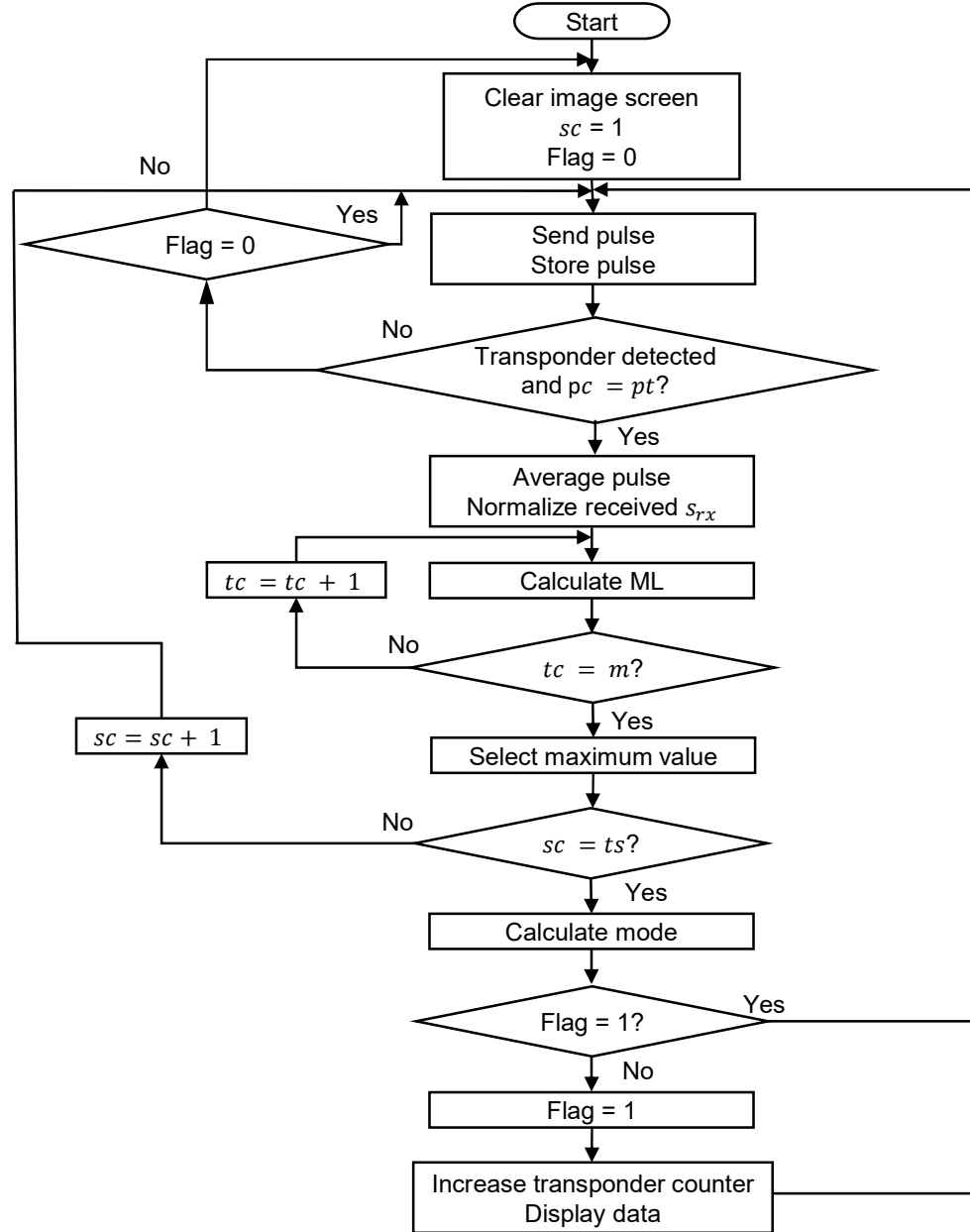


Fig. 7.3: UWB IR-RFID reader detection algorithm

chipless RFID transponder is interrogated at once by once single pulse, its placement becomes more critical to variations and more pulse samples need to be taken to guarantee successful detection. Therefore, a total number of  $pt$  pulses are taken (counted by  $pc$ ) and averaged to conduct one single interrogation scan of the UWB chipless RFID transponder. In this case, a peak detector determinate whether something has been placed on the interrogation zone or not. If yes, the pulses are averaged and then normalized, and then the identification code is estimated using a ML detection rule. The process is repeated a  $ts$  number of times (counted by  $sc$ ) and then the mode of the results is calculated, and its value given as the identification code placed on the interrogation zone.

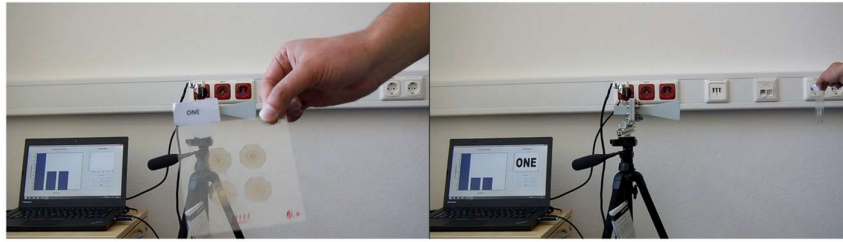
A specific number and a symbol image representing that number have been assigned to each identification code according to Table 7.3 are shall be displayed in the interface, once the detection has taken place.

Code	Number	Image
00	1	ONE
01	2	TWO
10	3	THREE
11	4	FOUR

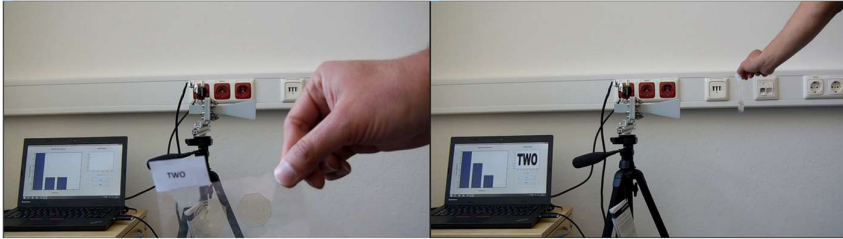
Table 7.3: Identification codes assigned numbers and images

The previous algorithm is implemented in the UWB IR-RFID reader and the COD1-UWB chipless RFID transponder are interrogated sequentially at different distances from the horn antennas, as shown in Fig. 7.4. Total number of sweeps of used pulses  $pt$  is set to 100 and the total number of samples to  $ts = 10$  per detection to keep the detection time as fast as possible (below 2 seconds). An illustrative video of this system is included in the DVD with this thesis.

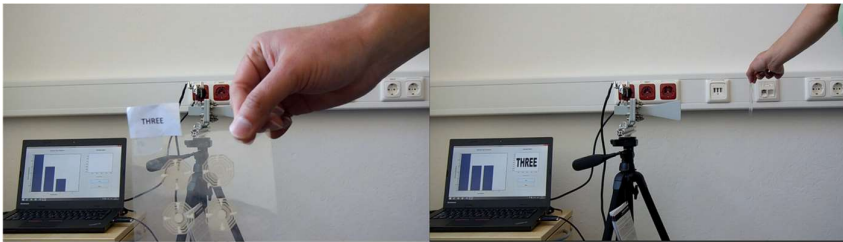
The detectors results taking using the measurement setup based on tripods at different distances, are shown in Table 7.4, the maximum values are marked in bold, as can be seen, all UWB chipless RFID transponders are correctly identified up to a 50 cm distance, when considering the mode of all the interrogation sweeps. The distance is limited by the internal configuration of the radar.



a)



b)



c)



d)



e)

Fig. 7.4: IR-UWB RFID system sequence of detection: a) ONE b) TWO c) THREE, d) FOUR and e) ONE and THREE



Measurement distance	Received code $s_{rx}$	Stored code $s_{tx}^m$			
		00	01	10	11
20 cm	00	<b>70.0</b>	33.9	44.4	36.2
	01	33.9	<b>70.0</b>	43.6	56.6
	10	44.4	43.6	<b>70.0</b>	57.1
	11	36.2	56.6	57.1	<b>70.0</b>
30 cm	00	<b>66.2</b>	28.3	39.9	30.8
	01	39.6	<b>59.8</b>	43.1	50.2
	10	50.3	45.8	<b>55.0</b>	53.9
	11	37.3	49.6	60.3	<b>60.4</b>
40 cm	00	<b>46.0</b>	33.8	44.5	31.3
	01	31.6	<b>63.1</b>	33.3	48.3
	10	48.2	50.5	<b>53.6</b>	50.1
	11	34.0	58.0	52.5	<b>64.0</b>
50 cm	00	<b>52.1</b>	34.0	46.6	40.1
	01	37.7	<b>63.5</b>	44.0	53.2
	10	44.4	44.8	<b>63.4</b>	49.9
	11	35.7	53.2	56.1	<b>64.4</b>

Table 7.4: IR-Reader detector results [82]

Similar tests were conducted using the COD1-UWB chipless RFID transponders printed on the different venues' substrates, illustrative videos showing these test can be found on the DVD.

The IR-UWB chipless RFID system is taken to each venue to perform real test-case scenarios, with volunteers holding the venue respective tickets and placing them in the interrogation zone of the reader, as illustrated in Fig. 7.5. As the system was not developed in a user-friendly way, and no individual training was allowed to manipulate the equipment, some user placed incorrectly the UWB chipless RFID transponders in front of the cavity of one antenna, as shown in Fig. 7.5a. Therefore, further developments are needed to present an optimal end-user friendly solution.

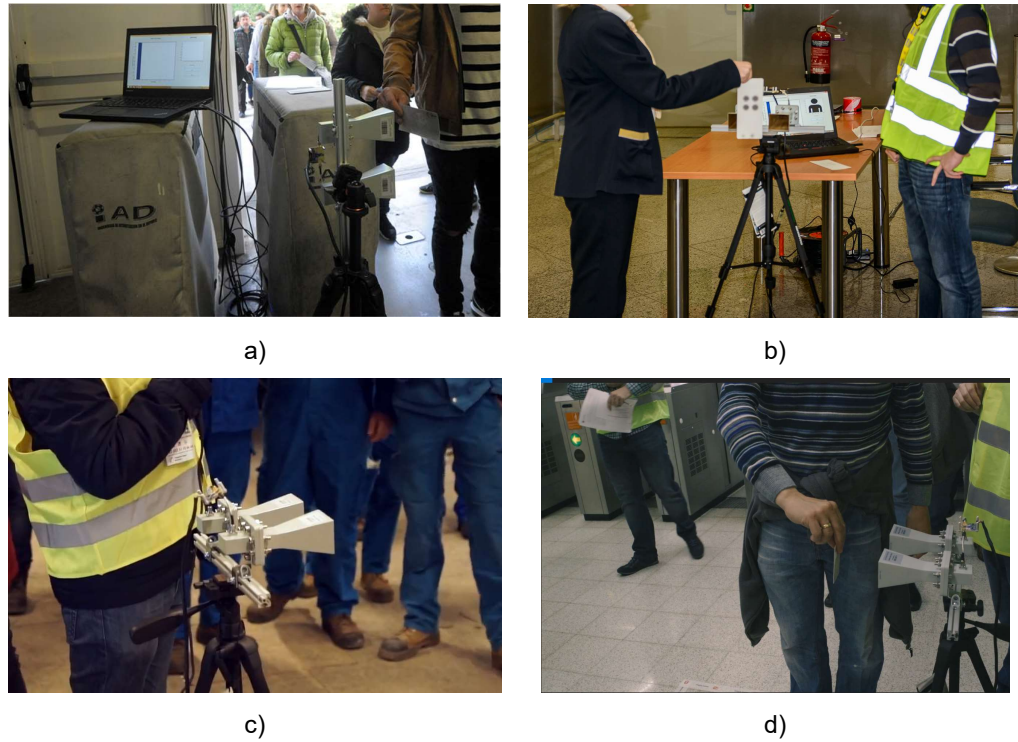


Fig. 7.5: IR-UWB chipless RFID system pilot demonstrations at: a) Anoeta soccer stadium [10], b) Athens international airport (photo courtesy of Vicente Serrulla), c) MSC Meraviglia cruise ship [10], d) Bilbao San Mamés metro station [10]

### 7.3 Summary

The final implementation of the UWB RFID systems with chipless transponders has been presented in this chapter, the different considerations to develop the algorithms and the algorithms themselves have been discussed. Both systems were validated through field test at the premises of the Technische Universität Dresden, verifying their functionality.

Now that the system has been tested and integrated, Table 7.5 presents their comparison with previously published works. As can be seen, several types of approaches can be found, using readers ranging from laboratory equipment to solutions fabricated on PCBs and different frequency bands. Nevertheless, until now, none of them constituting a full automatized RFID system, as most of the research has been focusing on the transponder design and fabrication, where capacity is merely assigned according to the number of achievable frequency peaks/dips. Using the readers just to measure the frequency response and giving for granted that the detection will occur if the human eye

Reference	Preradovic et. al. [25]	Preradovic et. al. [27]	Koswatta et. al. [83]	Lazaro et. al. [84]	Zheng et. al. [85]	This Work	
Working Principle	Frequency			Time		Frequency	Time
Frequency band (GHz)	2 – 2.5	5 – 10.7	4 – 8	5	3.1 – 10.6	3.8 – 5.8	4 - 9
Reader Type	VNA	Modular	PCB	Pulse generator/ high speed sampler	Pulse generator/ high speed oscilloscope	Modular	Commercial radar
Requires ref. measurement	Yes	No					
Coding type	Frequency shift			Pulse position		Differential	
Detection type	Amplitude & phase			Amplitude		Minimum distance	Maximum likelihood
Tx power (dBm)	-28	> 15	>10	$\pm 5$ V.	Not available	< 3	Not available
Transponder structure	Antennas + resonators			Antennas + transmission line		Scatterer	
Capacity bits (Theoretical)	35	23	9	1	8	3	2
Decoded transponders	2				1	8	4
Transponder substrate	Taconic TLX-0	Taconic TF-290	Taconic TLX-0	None	Rogers 4350	PET	PET/paper /plastic card
Size (mm <sup>2</sup> )	88 × 65	108 × 64	Not available			62 × 62	62 × 62
Reading range (cm)	40	15	1	200	0	36	50
Multi-detection	No						Up to 2
Reading time (s)	Not available					< 16	< 2
Measurement conditions	Anechoic Chamber		Normal		Connected to lab. equipment	Normal	

Table 7.5: RFID systems with chipless transponders comparison

is capable to identify it, disregarding the communication channel effects or normal working conditions (handling of transponders, movement, etc.), and the fact that a computer algorithm must indeed perform the detection.

The work presented by Preradovic et. al. in [25] considers the use of a VNA as a reader, measuring sequentially only two different chipless RFID transponders in an anechoic chamber, placing them at fixed positions from the antenna and then performing

the measurement. Removing the channel effects by the subtraction of a reference measurement, which allows to obtain a larger reading distance, up to 40 cm, and stating that the remaining identification codes should be identified using the same procedure of recognizing the frequency peaks. Later Preradovic et. al. presented in [27] a modular reader that didn't needed a reference measurement due to the fact that its transmission power is above 15 dBm, reaching a reading distance of 15 cm, also placing the chipless RFID transponders at a fixed position in an anechoic chamber and presenting the results for only two transponders. Basing the detection merely on a peak detection technique reduces the handling margin of the transponders in a real application scenario, as frequency shifts may occur during the interrogation procedure, and therefore fixed positions may be required for a successful detection.

Similar analysis can be done for the works of Koswatta et. al. [83], Lazaro et. al. [84], and Zheng et. al. [85], none of them performing automatic detection, nor providing detection times, and placing the chipless RFID transponders at fixed positions from the reader. This works on the other hand, presents for the first time two different systems programmed to perform the UWB chipless RFID transponders detections automatically when sequentially placed by hand at any distance under normal working conditions, as its purpose was to be implemented in real test-case scenarios. This is due to the implementation of a coding technique that together with detection algorithm enables the successful recognition of the identification codes by a computing system, when the UWB chipless transponders are placed in the interrogation zone, considering channel impairments like noise and path loss.

The chipless RFID transponders are manufactured by means of printed technology on flexible substrates like PET or paper, unlike other works, the whole claimed capacity is verified experimentally and automatically detected by the correspondent reader applying conventional detection techniques. The proposed chipless RFID transponders can be read by the lab equipment, when processed with a calibration technique at distances above the 1 m target, as established in section 1.2. Furthermore, the functionality of the UWB chipless RFID transponders was verified beyond the target lifetime period of three months.

The SFM-UWB RFID reader is capable to detect 8 different identification codes when placed sequentially under normal working conditions, up to a 36 cm distance with

a detection speed of 16s and Tx power less than 3 dBm. The IR-UWB RFID reader on other hand detects 4 different identification codes and simultaneous detection of two up to a 50 cm distance with a reading speed of less than 2 seconds. Furthermore, the UWB chipless RFID transponders are fabricated on cheaper substrates like PET or paper and in the specific case of IR system, it was tested in the different venues by volunteers holding the tickets/cards by hand and the system performing the scans automatically.

## 8 Conclusion and Outlook

This dissertation investigates extensively an innovative UWB RFID system with chipless transponders for short range applications ( $< 50$  cm), from chipless RFID transponders modeling, simulation and fabrication, to the study and implementation of different reader front-ends hardware with its respective decoding algorithms. A novel chipless RFID transponders frequency coding technique, that considers the communication channel effects and assigns a unique frequency response to each transponder is introduced, and which could be easily reproduced in other frequency bands to increase capacity, while keeping the same detection template.

Two novel fully automated prototypes of UWB RFID readers for chipless transponders working under normal conditions are presented, capable to automatically identify when a chipless RFID transponder is placed within their interrogation zones and proceed to the successful recognition of its embedded identification code. The UWB RFID readers are based on the SFM or IR radar principles, and the UWB chipless RFID transponders on the scattering properties of their geometries.

A novel chipless RFID transponder coding technique was derived to improve system robustness to imperfections caused by manufacturing, operation and channel influence. Relevant works investigate the implementation of peaks/dips detection techniques, mostly providing a proof of concept by decoding just one or two chipless transponders and focusing their analysis to small sections of their frequency response. This work focuses on exploiting the differences of the overall backscattered frequency signature of each chipless transponders for a specified frequency band and under normal working conditions (e.g. chipless transponders held by hand).

Several UWB chipless RFID transponders prototypes, fabricated using low-cost materials like aluminum or copper on bond paper substrate are presented and their frequency responses compared against their silver-ink printed electronics manufactured counterparts. The developed procedure could serve to produce prototypes in a very short period and evaluate the design performance at a very low cost.

The peak magnitude and frequency dip depth terms are introduced, to evaluate the performance and be able to compare between different UWB chipless RFID transponders frequency responses. The first one, as a measure of the reflectivity and the second one of the resonance capabilities.

The SFM RFID system prototype consists of a reader frond-end fabricated using high-performance off-the-shelf components, a personal computer with the decoding algorithms and eight different chipless transponders. The chipless RFID transponders are based on five concentric ring resonators, manufactured with silver-ink based printed electronics technology on PET, are differential-coded using changing the ring dimensions to obtain different frequency responses, and their identification codes successfully automatically retrieved when placed by hand sequentially at the stepped frequency reader's interrogation zone up to a 36 cm distance.

The pulse RFID system prototype is composed of a commercially available impulse radio radar, a personal computer with the pulse control and decoding algorithms and five different chipless transponders. The chipless transponder is based on concentric octagons, manufactured with silver-ink based printed electronics technology on PET, and differential-coded coded by short-circuiting their resonators to generate different frequency responses, and their identification codes successfully automatically retrieved when placed by hand sequentially at the impulse radio reader's interrogation zone up to a 50 cm distance.

The primary goal of this work was to introduce the functionality of an UWB RFID system with chipless transponders, cheap enough to replace the current barcode technology, capable of automatically detecting different chipless transponders when placed at its interrogation zone. UWB design specifications were employed to design or choose the readers architectures, and chipless RFID transponders based on scatter structures suitable for mass production techniques are used. The systems demonstrated that different UWB radar architectures can be used to detect and identify several chipless RFID transponders. Nevertheless, due to the multi-disciplinary nature of the RFID systems with chipless transponders, several further research opportunities can be identified:

Improvement in the mass production technology to fabricate UWB chipless RFID transponders with low-cost metals like aluminum or copper, either by printing technology or other alternatives, with enhanced RF performance.

Improve the detection performance, set the proper detection boundaries for the different identification codes, to reduce the probability of error detection by implementing conventional hypothesis testing criteria.

Development of more robust and structured coding techniques, to improve the detection performance of the system, as well as to overcome external effects like transponder tilting, human body, manufacturing imperfections. Furthermore, it is deemed necessary to establish the foundations to evaluate the performance of the different coding techniques implemented for chipless RFID transponders, to be able to compare between different geometries and coding approaches.

Design and fabrication of an UWB RFID reader fully integrated on a system on chip (SoC) solution, aimed to interrogate the UWB chipless RFID transponders, reducing in this way cable losses, current system inaccuracies and improving the link budget, including the necessary hardware architecture to implement features like multi-detection, multi-tracking and positioning of UWB chipless RFID transponders. And in this way, reduced the detection time to less than 1 second.





## References

- [1] J. Landt, "The History of RFID," *IEEE Potentials*, vol. 24, no. 4, pp. 8 - 11, 2005.
- [2] H. Stockman, "Communication by Means of Reflected Power," *Proceedings of the IRE*, vol. 36, no. 10, pp. 1196 - 1204, 1948.
- [3] R. Weinstein, "RFID: a Technical Overview and its Application to the Enterprise," *IT Professional*, vol. 7, no. 3, pp. 27 - 33, 2005.
- [4] A. C. Polycarpou, A. Dimitriou, A. Bletsas, P. C. Polycarpou, L. Papaloizou, G. Gregoriou and J. N. Sahalos, "On the Design, Installation, and Evaluation of a Radio-Frequency Identification System for Healthcare Applications," *IEEE Antennas and Propagation Magazine*, vol. 54, no. 4, pp. 255 - 271, 2012.
- [5] IDTechEx, "RFID Forecasts, Players and Opportunities 2017-2027: The complete analysis of the global RFID industry," [Online]. Available: <https://www.idtechex.com/research/reports/rfid-forecasts-players-and-opportunities-2017-2027-000546.asp>. [Accessed 29 05 2018].
- [6] A. de Panizza, S. Lindmark and P. Rotter, "RFID: Prospects for Europe: Item-level Tagging and Public Transportation," Publications Office of the European Union, Seville, 2010.
- [7] R. Nair, M. Barahona, D. Betancourt, G. Schmidt, M. Bellmann, D. Höft, D. Plettemeier, A. Hübler and F. Ellinger, "A Fully Printed Passive Chipless RFID Tag for Low-cost Mass Production," in *European Conference on Antennas and Propagation (EuCAP)*, The Hague, 2014.
- [8] Avery Denninson AD-236u7 UHF RFID, "Digi-Key Electronics," [Online]. Available: <https://www.digikey.com/product-detail/en/avery-denninson-rfid/600522/1543-1044-ND/5056150>. [Accessed 29 May 2018].
- [9] L. Roselli, *Green RFID Systems*, Cambridge: Cambridge University Press, 2014.
- [10] "eVACUATE A holistic scenario –independent, situation-awareness and guidance System for sustaining the Active Evacuation Route for large Crowds," [Online].

- Available: <http://www.evacuate.eu/publications/media-center/videos/>. [Accessed 29 11 2018].
- [11] K. Finkenzeller, *RFID Handbook: Fundamentals and Applications in Contacless Smart Cards and Identification*, Chichester: John Wiley & Sons Ltd, 2003.
  - [12] G. R. White, G. Gardiner, G. Prabhakar and A. A. Razak, "A Comparison of Barcoding and RFID Technologies in Practice," *Journal of Information, Information Technology, and Organizations*, vol. 2, pp. 119-132, 2007.
  - [13] J. Duda, P. Korus, . N. J. Gadgil, K. Tahboub and E. J. Delp, "Image-Like 2D Barcodes Using Generalizations of the Kuznetsov–Tsybakov Problem," *IEEE Transactions on Information Forensics and Security*, vol. 11, no. 4, pp. 691-703, 2016.
  - [14] S. Tiwari, "An Introduction To QR Code Technology," in *2016 International Conference on Information Technology*, Bhubaneswar, 2016.
  - [15] S. Son, H. So, K. Joondong, D. Choi and H.-J. Lee, "Energy-Efficient Adaptive Optical Character Recognition for Wearable Devices," *Electronics Letters*, vol. 53, no. 2, pp. 113 - 115, 2016.
  - [16] K. Sattlegger and U. Denk, "Texas Instruments: Navigating Your Way Through the RFID Jungle," 2014. [Online]. Available: <http://www.ti.com/lit/wp/slyy056/slyy056.pdf>. [Accessed 30 May 2018].
  - [17] R. S. Nair, "Contribution au Développement de Tags Chipless et des Capteurs à Codage dans le Domaine Temporel," Ph.D. Thesis. Université de Grenoble, 2013.
  - [18] R. M. White and F. W. Voltmer, "Direct Piezoelectric Coupling to Surface Elastic Waves," *Applied Physics Letters*, vol. 7, no. 12, pp. 314-316, 1965.
  - [19] V. P. Plessky and L. M. Reindl, "Review on SAW RFID Tags," *IEEE Transactions on Ultrasonics, Ferroelectrics, and Frequency Control*, vol. 57, no. 2, pp. 654-668, 2010.
  - [20] L. Zhang, S. Rodriguez, H. Tenhunen and L.-R. Zheng, "An Innovative Fully Printable RFID Technology Based on High Speed Time-Domain Reflections," in *Conference on High Density Microsystem Design and Packaging and Component Failure Analysis*,, Shanghai, 2006.

- [21] S. Hu, Y. Zhou, C. L. Law and W. Dou, "Study of a Uniplanar Monopole Antenna for Passive Chipless UWB-RFID Localization System," *IEEE Transactions on Antennas and Propagation*, vol. 58, no. 2, pp. 271 - 278, 2010.
- [22] S. Hu, C. L. Law and W. Dou, "A Balloon-Shaped Monopole Antenna for Passive UWB-RFID Tag Applications," *IEEE ANTENNAS AND WIRELESS PROPAGATION LETTERS*, vol. 7, pp. 366 - 368, 2008.
- [23] S. Gupta, B. Nikfal and C. Caloz, "Chipless RFID System Based on Group Delay Engineered Dispersive Delay Structures," *IEEE Antennas and Wireless Propagation Letters*, vol. 10, pp. 1366-1368, 2011.
- [24] R. A. Araújo Rodrigues, E. Candeia Gurjão, F. M. de Assis, S. Tedjini and E. Perret, "Group delay Analysis of Folded Multi-Layer C-Sections Used in Encoding of Chipless RFID Tag," in *2015 SBMO/IEEE MTT-S International Microwave and Optoelectronics Conference (IMOC)*, Porto de Galinhas, 2015.
- [25] S. Preradovic, I. Balbin, N. C. Karmakar and G. F. Swiegers, "Multiresonator-Based Chipless RFID System for Low-Cost Item Tracking," *IEEE Transactions on Microwave Theory and Techniques*, vol. 57, no. 5, pp. 1411-1419, 2009.
- [26] S. Preradovic, N. Karmakar and M. Zenere, "UWB Chipless Tag RFID Reader Design," in *IEEE International Conference on RFID-Technology and Applications*, Guangzhou, 2010.
- [27] S. Preradovic, S. M. Roy and N. . C. Karmakar, "RFID System Based on Fully Printable Chipless Tag for Paper-/Plastic-Item Tagging," *IEEE Antennas and Propagation Magazine*, vol. 53, no. 5, pp. 15 - 32, 2011.
- [28] C. M. Nijas, R. Dinesh, U. Deepak, A. Rasheed, S. Mridula, K. Vasudevan and P. Mohanan, "Chipless RFID Tag Using Multiple Microstrip Open Stub Resonators," *IEEE Transactions on Antennas and Propagation*, vol. 60, no. 9, pp. 4429 - 4432, 2012.
- [29] I. Jalaly and I. D. Robertson, "RF Barcodes using Multiple Frequency Bands," in *IEEE MTT-S International Microwave Symposium Digest*, 2005.
- [30] I. Jalaly and I. D. Robertson, "Capacitively-tuned split microstrip resonators for RFID barcodes," in *European Microwave Conference*, Paris, 2005.

- [31] A. Vena, E. Perret and S. Tedjini, "A Fully Printable Chipless RFID Tag with Detuning Correction Technique," *IEEE Microwave and Wireless Components Letters*, vol. 22, no. 4, pp. 209 - 211, 2012.
- [32] R. Nair, M. Barahona, D. Betancourt, G. Schmidt, M. Bellmann, D. Höft, D. Plettermeier, A. Hübler and F. Ellinger, "A Novel Fully Printed 28-bits Capacity Chipless RFID Tag Based on Open Conical Resonators," in *Progress In Electromagnetics Research Symposium (PIERS)*, Guangzhou, Aug. 25 - 28, 2014.
- [33] D. Betancourt, R. Nair, K. Haase, G. Schmidt, M. Bellmann, D. Höft, A. Hübler and F. Ellinger, "Square-Shape Fully Printed Chipless RFID Tag and its Applications in Evacuation Procedures," in *9th European Conference on Antennas and Propagation (EuCAP)*, Lisbon, 2015.
- [34] A. Vena, E. Perret and S. Tedjini, "High-Capacity Chipless RFID Tag Insensitive to the Polarization," *IEEE Transactions on Antennas and Propagation*, vol. 60, no. 10, pp. 4509 - 4515, 2012.
- [35] D. Betancourt, M. Barahona, K. Haase, G. Schmidt, A. Hübler and F. Ellinger, "Design of Printed Chipless-RFID Tags With QR-Code Appearance Based on Genetic Algorithm," *IEEE Transactions on Antennas and Propagation*, vol. 65, no. 5, pp. 2190 - 2195, 2017.
- [36] TEXAS INSTRUMENTS, "Semiconductor Manufacturing: How a Chip is Made," [Online]. Available: <http://www.ti.com/corp/docs/manufacturing/howchipmade.shtml>. [Accessed 5 May 2018].
- [37] G. Nisato, D. Lupo and S. Ganz, *Organic and Printed Electronics: Fundamentals and Applications*, Singapore: Pan Stanford Publishing Pte. Ltd., 2016.
- [38] Organic Electronics Association, "OE-A Roadmap for Organic and Printed Electronics," White Paper, 2009.
- [39] A. Kamysny and S. Magdassi, "Conductive Nanomaterials for Printed Electronics," *Small*, vol. 10, no. 17, pp. 3515 - 3535, 2014.
- [40] K. Rajan, I. Roppolo, A. Chiappone, S. Bocchini, D. Perrone and A. Chiolerio, "Silver nanoparticle ink technology: state of the art," *Nanotechnology Science and Applications*, no. 9, pp. 1 - 13, 2016.

- [41] B. Wiley, Y. Sun, B. Mayers and Y. Xia, "Shape-Controlled Synthesis of Metal Nanostructures: The Case of Silver," *Chemistry*, no. 11, pp. 454 - 463, 2004.
- [42] X. Shuang Shen, G. Zhong Wang, X. Hong and W. Zhu, "Nanospheres of Silver Nanoparticles: Agglomeration, Surface Morphology Control and Application as SERS Substrates," *Physical Chemistry Chemical Physics*, Vols. 7450 - 7454, no. 34, 2009.
- [43] ASYS GROUP, "X1 SL – Semi-Automatic Screen and Stencil Printer," [Online]. Available:  
[https://www.asys.de/files/machines/pdf/en/X1\\_SL\\_13\\_05\\_09\\_E.pdf?7=617fe3ad484e671b83594b0a2f61ff5e](https://www.asys.de/files/machines/pdf/en/X1_SL_13_05_09_E.pdf?7=617fe3ad484e671b83594b0a2f61ff5e). [Accessed 4 May 2018].
- [44] DUPONT, "DuPont 5028: Silver Conductor," [Online]. Available:  
<http://www.dupont.com/content/dam/dupont/products-and-services/electronic-and-electrical-materials/documents/prodlib/5028.pdf>. [Accessed 5 May 2018].
- [45] A. Vena, E. Perret and S. Tedjini, "Design of Chipless RFID Tags Printed on Paper by Flexography," *IEEE Transactions on Antennas and Propagation*, vol. 61, no. 12, pp. 5868 - 5877, 2013.
- [46] ERICHSEN, "FlexiProof 100 - Modell 630," [Online]. Available:  
<https://www.erichsen.de/oberflaechenpruefung/walzen-auftragsgeraete-fuer-druckfarben/flexiproof-100-630>. [Accessed 5 May 2018].
- [47] M. Barahona, D. Betancourt and F. Ellinger, "Comparison of UWB Chipless Tags on Flexible Substrates Fabricated Using either Aluminum, Copper or Silver," in *IEEE-APS Topical Conference on Antennas and Propagation in Wireless Communications (APWC)*, Cairns, 2016.
- [48] R. S. Khandpur, Printed Circuit Boards: Design, Fabrication, and Assembly, New Dehli, India: McGraw-Hill Electronic Engineering, 2006.
- [49] D. Betancourt, K. Haase, A. Hübler and F. Ellinger, "Bending and Folding Effect Study of Flexible Fully Printed and Late-Stage Codified Octagonal Chipless RFID Tags," *IEEE Transactions on Antennas and Propagation*, vol. 64, no. 7, pp. 2815 - 2823, 2016.
- [50] E. F. Knott, J. F. Schaeffer and M. T. Tuley, Radar Cross Section, Norwood: Artech House, Inc., 1993.

- [51] IEEE Aerospace and Electronic Systems Society, IEEE Standard Radar Definitions, New York: IEEE, 2008.
- [52] S. Narayan, B. Sangeetha and R. Mohan Jha, Frequency Selective Surfaces based High Performance Microstrip Antenna, Singapore: Springer, 2016.
- [53] R. A. Hill and A. B. Munk, "The Effect of Perturbating a Frequency Selective Surface and Its Relation to the Design of a Dual-Band Surface," *IEEE Transactions on Antennas and Propagation*, vol. 44, no. 3, pp. 368-374, 1996.
- [54] B. A. Munk, G. R. Kouyoumjian and L. Peters, "Reflection Properties of Periodic Surfaces of Loaded Dipoles," *IEEE Transactions on Antennas and Propagation*, Vols. AP-19, no. 5, pp. 612-617, 1971.
- [55] C.-C. Chen, "Scattering by a Two-Dimensional Periodic Array of Conducting Plates," *IEEE on Antennas and Propagation*, Vols. AP-18, no. 5, pp. 660-665, 1970.
- [56] J. Huang, T.-K. Wu and S.-W. Lee, "Tri-band frequency selective surface with circular ring elements," *IEEE Transactions on Antennas and Propagation*, vol. 42, no. 2, pp. 166 - 175, 1994.
- [57] B. A. Munk and R. J. Luebbers, "Reflection Properties of Two-Layer Dipole Arrays," *IEEE Transactions on Antennas and Propagation*, vol. 22, no. 6, pp. 766 - 773, 1974.
- [58] M. Barahona, D. Betancourt and F. Ellinger, "On the Decoding of Equiprobable UWB Chipless RFID Tags Using a Minimum Distance Detector," in *International Symposium on Antennas and Propagation (ISAP)*, Okinawa, 2016.
- [59] I. A. Md., Y. Yap, N. Karmakar and A. K. M. Azad, "Orientation Independent Compact Chipless RFID Tag," in *IEEE Conf. RFID – Technologies and Applications (RFID – TA)*, Nice, France, Nov. 5 – 7, 2012.
- [60] M. Barahona, D. Betancourt and F. Ellinger, "Decoding of Multiple Same-coded In-line Placed Chipless RFID Tags," in *IEEE Conference on Antenna Measurements & Applications (CAMA)*, Juan-les-Pins, 2014.
- [61] W. L. Melvin and J. A. Scheer, Principles of Modern Radar: Advance Techniques, Edison, NJ: SciTech Publishing, 2013.

- [62] M. A. Richards, J. A. Scheer and W. A. Holm, Principle of Modern Radar Vol. I: Basic Principles, Raileigh: SciTech Publishing, Inc., 2010.
- [63] ETSI, "Electromagnetic compatibility and Radio spectrum Matters (ERM); Short Range Devices (SRD); Technical characteristics for SRD equipment using Ultra Wide Band technology (UWB) Part 1: Communications applications," 2004. [Online]. Available: [http://www.etsi.org/deliver/etsi\\_tr/101900\\_101999/10199401/01.01.01\\_60/tr\\_10199401v010101p.pdf](http://www.etsi.org/deliver/etsi_tr/101900_101999/10199401/01.01.01_60/tr_10199401v010101p.pdf). [Accessed 2018 June 13].
- [64] ETSI, "Electromagnetic compatibility and Radio spectrum Matters (ERM); Short Range Devices (SRD) using Ultra Wide Band technology (UWB) for communications purposes; Harmonized EN covering the essential requirements of article 3.2 of the R&TTE Directive," 2010. [Online]. Available: [http://www.etsi.org/deliver/etsi\\_en/302000\\_302099/302065/01.02.01\\_30/en\\_302065v010201v.pdf](http://www.etsi.org/deliver/etsi_en/302000_302099/302065/01.02.01_30/en_302065v010201v.pdf). [Accessed 2018 June 13].
- [65] S. Preradovic , N. Karmakar and M. Zenere, "UWB Chipless Tag RFID Reader Design," in *IEEE International Conference on RFID-Technology and Applications*, Guangzhou, June 2010.
- [66] Analog Devices, "10-Bit Multiplying DAC," [Online]. Available: <http://www.analog.com/media/en/technical-documentation/data-sheets/AD7533.pdf>. [Accessed 28 May 2018].
- [67] Analog Devices, "Wideband MMIC VCO w/ Buffer Amplifier, 4 - 8 GHz," [Online]. Available: <http://www.analog.com/media/en/technical-documentation/data-sheets/hmc586.pdf>. [Accessed 28 May 2018].
- [68] Pasternack, "Directional 10 dB SMA Coupler From 4 GHz to 8 GHz Rated to 50 Watts," [Online]. Available: <https://www.pasternack.com/directional-10-db-sma-coupler-4-8-ghz-50-watts-pe2204-10-p.aspx>. [Accessed 28 May 2018].
- [69] A-INFO, "4.0 - 8.0 Octave Horn Antenna," [Online]. Available: [http://www.ainfoinc.com/en/pro\\_pdf/new\\_products/antenna/Standard%20Gain%20Horn%20Antenna/tr\\_LB-OH-159-10.pdf](http://www.ainfoinc.com/en/pro_pdf/new_products/antenna/Standard%20Gain%20Horn%20Antenna/tr_LB-OH-159-10.pdf). [Accessed 28 May 2018].
- [70] NARDA-MITEQ, "Model: AFS4-02000800-09-10P-4," [Online]. Available: [https://nardamiteq.com/docs/2-8\\_01.PDF](https://nardamiteq.com/docs/2-8_01.PDF). [Accessed 28 May 2018].



- [71] Mini-Circuits, "Low Pass Filter VLF-2500," [Online]. Available: <https://ww2.minicircuits.com/pdfs/VLF-2500.pdf>. [Accessed 28 May 2018].
- [72] Analog Devices, "RF/IF Gain and Phase Detector," [Online]. Available: <http://www.analog.com/media/en/technical-documentation/data-sheets/AD8302.pdf>. [Accessed 28 May 2018].
- [73] Analog Devices, "2.7 V to 5.5 V, 200 kSPS 8-Bit Sampling ADC," [Online]. Available: <http://www.analog.com/media/en/technical-documentation/data-sheets/AD7819.pdf>. [Accessed 28 May 2018].
- [74] Y. L. Lu, L. Y. Liu and W. Liu, "Chipless RFID Tag Design and Detection with Adaptive Direct Path Cancellation," in *Asia-Pacific Microwave Conference (APMC)*, Nanjing, China, 6-9 Dec., 2015.
- [75] P. Kalansuriya, N. Karmakar and E. Viterbo, "Signal Space Representation of Chipless RFID Tag Frequency Signatures," in *IEEE Global Telecommunications Conference - GLOBECOM 2011*, Kathmandu, Nepal, 5-9 Dec., 2011.
- [76] M. Barahona, D. Betancourt and F. Ellinger, "Using UWB IR Radar Technology to Decode Multiple Chipless RFID Tags," in *IEEE International Conference on Ubiquitous Wireless Broadband (ICUWB)*, Nanjing, 2016.
- [77] R. Rezaiesarlak and M. Manteghi, "A Space-Time-Frequency Anticollision Algorithm for Identifying Chipless RFID Tags," *IEEE Transactions on Antennas and Propagation*, vol. 62, no. 3, pp. 1425 - 1432, 2014.
- [78] R. Rezaiesarlak and M. Manteghi, "A New Anti-Collision Algorithm for Identifying Chipless RFID Tags," in *IEEE Antennas and Propagation Society International Symposium (APSURSI)*, Orlando, FL, USA, 7-13 Jul., 2013.
- [79] R.-E. Azim and N. Karmakar, "A Collision Avoidance Methodology for Chipless RFID Tags," in *Asia-Pacific Microwave Conference*, Melbourne, VIC, USA, 5-8 Dec., 2011.
- [80] R.-E.-A. Anee and N. . C. Karmakar, "Efficient Collision Detection Method in Chipless RFID Systems," in *International Conference on Electrical and Computer Engineering*, Dhaka, Bangladesh, 20-22 Dec., 2012.

- [81] J. G. Proakis and M. Salehi, *Digital Communications*, New York: McGraw-Hill Inc., 2008.
- [82] M. Barahona, D. Betancourt, F. Ellinger, K. Haase, G. C. Schmidt and A. C. Hübler, "Automatic IR UWB Chipless RFID System for Short Range Applications," in *IEEE-APS Topical Conference on Antennas and Propagation in Wireless Communications (APWC)*, Verona, Italy, 11-15 Sept., 2017.
- [83] R. V. Koswatta and N. C. Karmakar, "A Novel Reader Architecture Based on UWB Chirp Signal Interrogation for Multiresonator-Based Chipless RFID Tag Reading," *IEEE Transactions on Microwave Theory and Techniques*, vol. 60, no. 9, pp. 2925 - 2933, Sept. 2012.
- [84] A. Lazaro, A. Ramos, . D. Girbau and R. Villarino, "Chipless UWB RFID Tag Detection Using Continuous Wavelet Transform," *IEEE Antennas and Wireless Propagation Letters*, vol. 10, pp. 520 - 523, May 2011.
- [85] L. Zheng, S. Rodriguez, L. Zhang, B. Shao and L.-R. Zheng, "Design and Implementation of a Fully Reconfigurable Chipless RFID Tag Using Inkjet Printing Technology," in *IEEE International Symposium on Circuits and Systems*, Seattle, WA, USA, 18 - 21 May, 2008.
- [86] J. Guo, D. Kajifez and A. W. Glisson,, "Skin-effect Resistance of Rectangular Strips," *Electronic Letters*, vol. 33, no. 11, pp. 966 - 967, Apr. 1997.
- [87] Mini-Circuits, "Frequency Mixer ZX05-153+," [Online]. Available: <https://ww2.minicircuits.com/pdfs/ZX05-153+.pdf>. [Accessed 28 May 2018].
- [88] N. Andersen, K. Granhaug, J. A. Michaelsen, S. Bagga, H. A. Hjortland, M. R. Knutsen, T. S. Lande and D. T. Wisland, "A 118-mW Pulse-Based Radar SoC in 55-nm CMOS for Non-Contact Human Vital Signs Detection," *IEEE Journal of Solid-State Circuits*, vol. 52, no. 12, pp. 3421 - 3433, 2017.
- [89] "Design of Chipless RFID Tags Printed on Paper by Flexography," *IEEE Transactions on Antennas and Propagation*, vol. 61, no. 12, pp. 5868 - 5868, 2013.

## Publications

1. M. Barahona, D. Betancourt, F. Ellinger, K. Haase, G. Schmidt, and A. Hübler, "Automatic IR UWB Chipless RFID System for Short Range Applications," in Proc. IEEE-APS Topical Conference on Antennas and Propagation in Wireless Communications (IEEE - APWC), Sept. 11 - 15, 2017, pp. 274 - 279.
2. M. Barahona, D. Betancourt, and F. Ellinger, "On the Decoding of Equiprobable UWB Chipless RFID Tags Using a Minimum Distance Detector," in Proc. International Symposium on Antennas and Propagation (ISAP), Oct. 24 - 28, 2016, pp. 1006 - 1007.
3. M. Barahona, D. Betancourt, and F. Ellinger, "Using UWB IR Radar Technology to Decode Multiple Chipless RFID Tags," in Proc. IEEE International Conference on Ubiquitous Wireless Broadband (ICUWB), Oct. 16 - 19, 2016, pp. 1 - 6.
4. M. Barahona, D. Betancourt, and F. Ellinger, "Comparison of UWB Chipless RFID Tags on Flexible Substrates Fabricated Using Aluminum, Copper or Silver," in Proc. IEEE-APS Topical Conference on Antennas and Propagation in Wireless Communications (IEEE - APWC), Sept. 19 - 23, 2016, pp. 78 - 81.
5. M. Barahona, D. Betancourt, and F. Ellinger, "Decoding of Multiple Same-coded in-line Placed Chipless RFID tags," in Proc. IEEE Conference on Antenna Measurements & Applications (CAMA), Nov. 16 - 19, 2014, pp. 1 - 4.
6. P. Testa, C. Carta, M. Barahona, and F. Ellinger, "0.5-20 GHz UWB Distributed Combiners and Dividers for Multi-Antenna Transceivers," IEEE Transactions on Microwave Theory and Techniques, vol. PP, no. 99, pp. 1 - 12, Jul. 2017.
7. D. Betancourt, M. Barahona, K. Haase, G. Schmidt, A. Hübler, and F. Ellinger, "Design of Printed Chipless-RFID Tags with QR-code Appearance Based on Genetic Algorithm," IEEE Transactions on Antennas and Propagation, vol. 65, no. 5, pp. 2190 - 2195, May 2017.
8. P. Testa, C. Carta, M. Barahona, and F. Ellinger, "0.5 – 20 GHz UWB distributed combiners for multi-antenna receivers," in Proc. IEEE MTT-S Latin American Microwave Conference (LAMC), Dec. 12 – 14, 2016, pp. 1 - 4.

9. R. Nair, M. Barahona, D. Betancourt, G. Schmidt, M. Bellmann, D. Höft, D. Plettemeier, A. Hübner, and F. Ellinger, "A Novel Fully Printed 28-bits Capacity Chipless RFID Tag Based on Open Conical Resonators," in Proc. Progress in Electromagnetics Research Symposium (PIERS), Aug. 25 - 28, 2014, pp. 2219 - 2222.
10. R. Nair, M. Barahona, D. Betancourt, G. Schmidt, M. Bellmann, D. Höft, D. Plettemeier, A. Hübner, and F. Ellinger, "A Fully Printed Passive Chipless RFID Tag for Low-cost Mass Production," in Proc. 8th European Conf. on Antennas and Propagation (EuCAP), Apr. 6 - 11, 2014, pp. 3562 - 3566.

## Appendix A

### RCS Calculation

The RCS calculations are performed considering the calibration technique and equation described in [34]. The technique is derived here for further understanding of the process. First consider the radar range equation described in section 5.1.1 for a chipless RFID transponder located a distance  $r$  from the antennas and  $RCS_t$

$$\left[ \frac{P_{rx}}{P_{tx}} \right]_t = \frac{G_{tx} G_{rx} \lambda^2}{(4\pi)^3 r^4} RCS_t \quad (\text{A.1})$$

The objective is to calculate the chipless RFID transponder  $RCS_t$  in terms of the measured scattering parameters measured with the VNA. To do so, the transmit and received power is expressed first in terms of the signal transmitted and received voltages  $V_{tx}$  and  $V_{rx}$  respectively for the same impedance  $Z$

$$\left[ \frac{\frac{V_{rx}^2}{Z}}{\frac{V_{tx}^2}{Z}} \right]_t = \frac{G_{tx} G_{rx} \lambda^2}{(4\pi)^3 r^4} RCS_t \quad (\text{A.2})$$

cancelling the impedance terms gives

$$\left[ \frac{V_{rx}^2}{V_{tx}^2} \right]_t = \frac{G_{tx} G_{rx} \lambda^2}{(4\pi)^3 r^4} RCS_t \quad (\text{A.3})$$

using the transmission line equivalent circuit described in section 4.1.3, and setting  $V_2^- = V_{rx}$  and  $V_1^+ = V_{tx}$ , the relation  $\frac{V_{rx}}{V_{tx}}$  can be expressed in terms of the scattering parameter  $S_{21}$  by

$$[S_{21}^*]_t^2 = \frac{G_{tx} G_{rx} \lambda^2}{(4\pi)^3 r^4} RCS_t \quad (\text{A.4})$$

which means, by obtaining the  $S_{21}^*$  of a chipless transponder located a distance  $r$  from the antennas, and squaring its value, the power losses including the RCS can be calculated. However, the signal path loss and the gain of the antennas still need to be assessed to cancel them from the equation and be able to obtain the RCS. Thus, another

object which RCS is well known, like a metal plate, is used as a reference and placed at the same distance  $r$  from the antennas, to obtain its  $S_{21p}^*$ , and be able to experience the same path loss and antennas gain as the chipless RFID transponder. The reference plate's  $S_{21p}^*$  can also be expressed in terms of its  $RCS_r$  by

$$\left[S_{21p}^*\right]^2 = \frac{G_{tx}G_{rx}\lambda^2}{(4\pi)^3r^4}RCS_r \quad (\text{A.5})$$

Then, an expression independent of the pathloss and antenna gains can be obtained dividing the chipless RFID transponder  $\left[S_{21t}^*\right]^2$  by the reference plate  $\left[S_{21p}^*\right]^2$

$$\left[\frac{S_{21t}^*}{S_{21p}^*}\right]^2 = \frac{\frac{G_{tx}G_{rx}\lambda^2}{(4\pi)^3r^4}RCS_t}{\frac{G_{tx}G_{rx}\lambda^2}{(4\pi)^3r^4}RCS_p} \quad (\text{A.6})$$

the relation becomes

$$\left[\frac{S_{21t}^*}{S_{21p}^*}\right]^2 = \frac{RCS_t}{RCS_p} \quad (\text{A.7})$$

as the reference plate  $RCS_p$  is well known, the  $RCS_t$  can be simply calculated by

$$RCS_t = \left[\frac{S_{21t}^*}{S_{21p}^*}\right]^2 RCS_p \quad (\text{A.8})$$

nevertheless, as explained in chapter 6, the desired signal  $S_{21t}^*$  is influenced by the noisy channel  $S_{21n}$ , and they cannot be measured directly, the measured received signal  $S_{21t}$  by de VNA is indeed composed of the desired signal  $S_{21t}^*$  and the noisy channel contribution  $S_{21n}$

$$S_{21t} = S_{21t}^* + S_{21n} \quad (\text{A.9})$$

Therefore, to be able to calculate the  $RCS_t$ , three different measurements need to be conducted:

1. The received signal measurement of the chipless RFID transponder  $S_{21t}$
2. A measurement of the reference plate  $S_{21tp}$ , and

3. The noisy channel, which is measured by obtaining the response without any object

And finally, the  $RCS_t$  can be calculated by

$$RCS_t = \left[ \frac{S_{21_t} - S_{21_n}}{S_{21_r} - S_{21_n}} \right]^2 RCS_p \quad (\text{A.10})$$

## Measurement Setups

Fig. A.1 shows the measurement setup to obtain the UWB chipless RFID transponders frequency response. It is composed of the UWB chipless RFID transponders support, two Chengdu AINFO Inc. LB-OH-159-10-C-SF horn antennas designed to operate between 4 and 8 GHz, with an average gain of 10 dBi, and separated 4 cm from each other, and an Anritsu Vector Network Analyzer (VNA) model 37397D. The UWB chipless RFID transponders are placed on its support separated a distance  $x$  from the horn antennas.

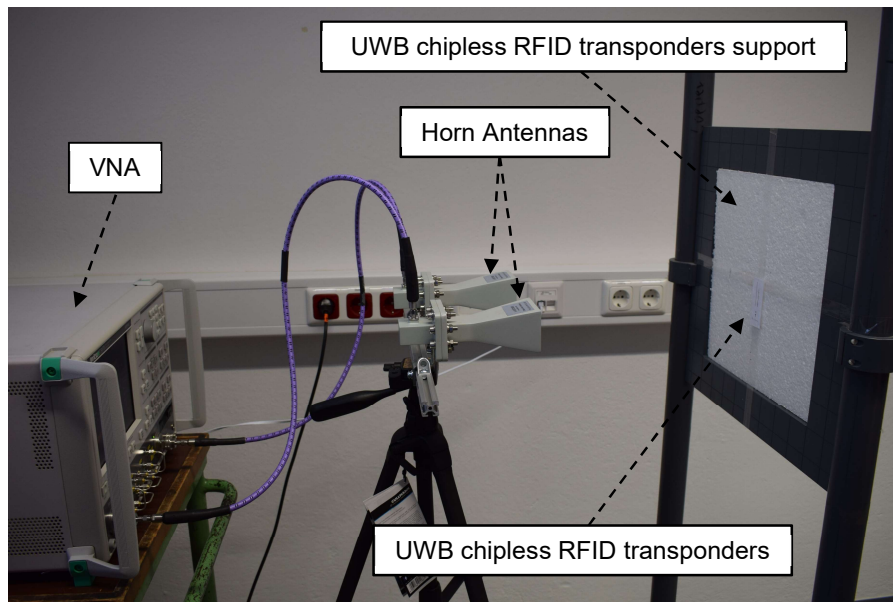


Fig. A.1: VNA 37397D with Chengdu antennas measurement setup

Fig. A.2 shows the measurement setup to obtain the UWB chipless RFID transponders frequency response. It is composed of the UWB chipless RFID tags support, two vertically polarized horn antennas (Rohde & Schwarz HF906) separated 40 cm from each other and capable to operate in the frequency range from 1 to 18 GHz with an average gain of 10 dBi, and an Anritsu Vector Network Analyzer (VNA) model MS46122A. The UWB chipless RFID transponders are placed on its support separated a distance  $D$  from the horn antennas.

Fig. A.3 shows the measurement setup to obtain the UWB chipless RFID transponders frequency response. It is composed of the UWB chipless RFID tags support, two vertically polarized horn antennas (Rohde & Schwarz HF906) separated 40 cm from



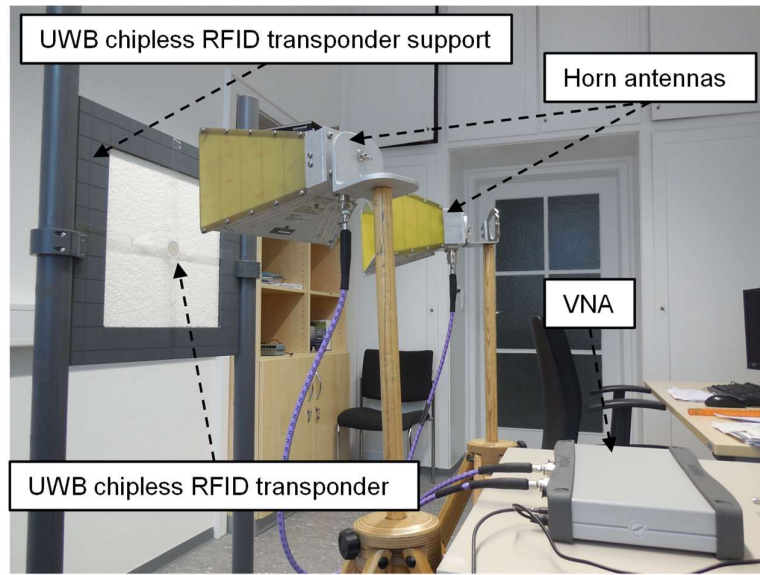


Fig. A.2: VNA MS46122A with Rohde & Schwarz antennas measurement setup each other and capable to operate in the frequency range from 1 to 18 GHz with an average gain of 10 dBi, and an Anritsu Vector Network Analyzer (VNA) model 37397D. The UWB chipless RFID transponders are placed on its support separated a distance  $x$  from the horn antennas.

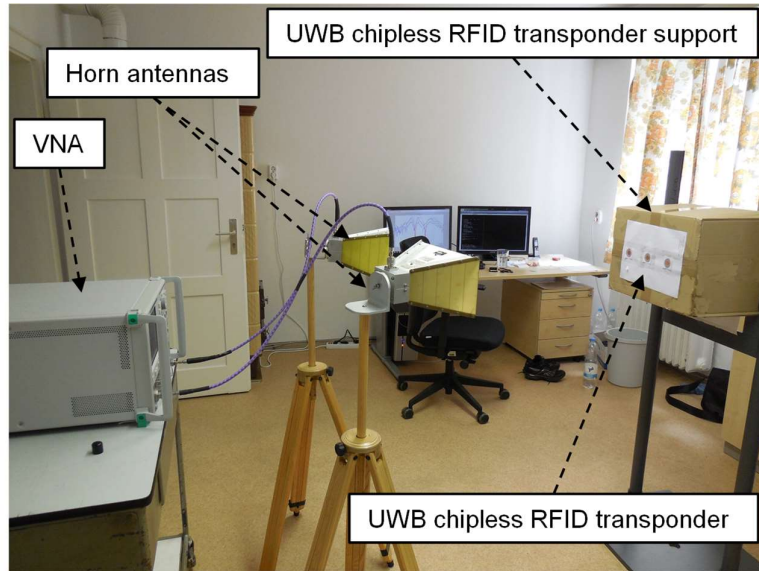


Fig. A.3: VNA 37397D with Rohde & Schwarz antennas measurement setup

Fig. A.4 shows the measurement setup to obtain the UWB chipless RFID transponders frequency response. It is composed of two tripods to support the UWB chipless RFID transponders, two Chengdu AINFO Inc. LB-OH-159-10-C-SF horn

antennas designed to operate between 4 and 8 GHz, with an average gain of 10 dBi, and the Novelda radar.

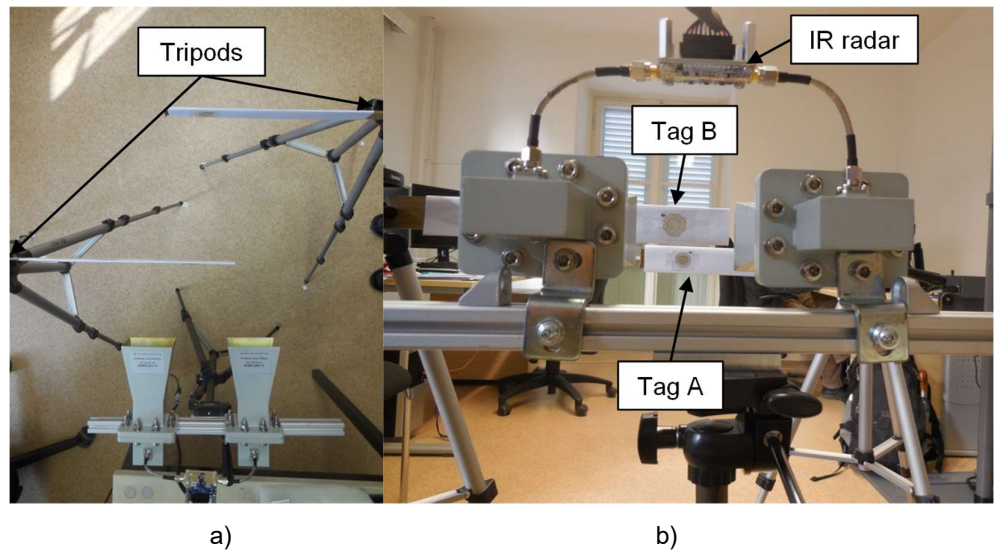


Fig. A.4: IR radar measurement setup: a) top view, b) rear view

## Appendix B

### Resistance and Skin Depth Calculation

To be able to understand the influence of the printing process in the RF performance of the chipless RFID transponders based on concentric circles, a methodology to estimate the resistance and conductivity values from the two-points measured direct-current (DC) resistance of each of its concentric rings is required and developed in this section.

Starting with the resistance definition of a rectangular strip of length  $l$ , width  $w$ , thickness  $T$ , and conductivity  $\kappa$ , provided that a DC current flows through it, is given by [86]

$$R_{DC} = \frac{l}{\kappa w T} \quad (\text{B.1})$$

The UWB chipless RFID tags have a ring like geometry with no starting or ending point, considering one ring with outer circumference of  $2\pi r$  and width  $w$ , an arbitrary pair of points need to be chosen to measure a DC resistance with a multimeter, and from there estimate the ring total resistance. For that purpose, taking into consideration the symmetry of a ring like structure, the resistance dependency on the length, as expressed by Eq. (B.1), and assuming that the printed metal strips are homogeneous throughout the whole ring structure. Two points separated at equal lengths ( $180^\circ$ ) from each other are picked to locate the multimeter's probes, as illustrated in Fig. B.1, at these points, the string ring is divided in two sections of equal lengths, outer circumferences of  $\pi r$  and therefore equal resistances. Furthermore, from the multimeter's perspective, to measure the DC resistance  $R_{\text{meas}}$  at these two points, will be equivalent to measure the resistance of two resistances in parallel, as also illustrated by the equivalent circuit in Fig. B.1a. Therefore, the measured resistance  $R_{\text{meas}}$  can be represented by

$$R_{\text{meas}} = \frac{R_1 R_2}{R_1 + R_2} \quad (\text{B.2})$$

where  $R_1 = R_2 = R$  are the resistances at both sides of the probes and then the  $R_{\text{meas}}$  can be expressed as

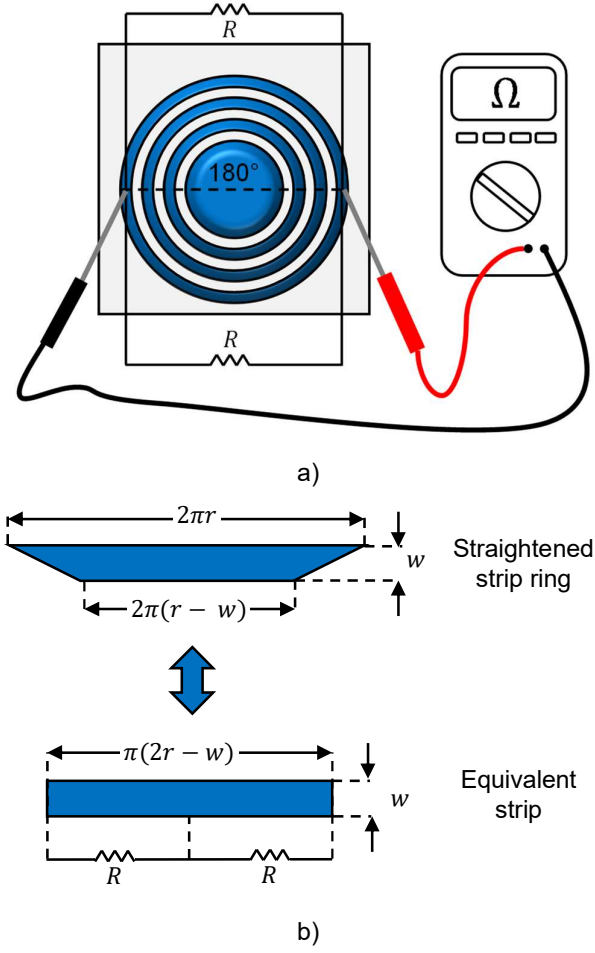


Fig. B.1: UWB chipless RFID transponder two-point resistance: a) measurement schematic, and equivalent circuit b) straightened strip ring, equivalent circuit

$$R_{\text{meas}} = \frac{R}{2} \quad (\text{B.3})$$

and each section resistance is given by

$$R = 2R_{\text{meas}} \quad (\text{B.4})$$

if the strip ring is straightened as shown in Fig. B.1b, the whole strip ring resistance  $R_{DC}$  is the result of its serial circuit equivalent, which means four times the multimeters measured DC resistance

$$R_{DC} = 2R = 4R_{\text{meas}} = \frac{l}{\kappa w T} \quad (\text{B.5})$$

Furthermore, straighten the ring will produce an isosceles trapezoid with parallel sides length of  $2\pi(r - w)$  and  $2\pi r$ , which has the same superficial area as a strip of length  $l = \pi(2r + w)$ . The conductivity  $\kappa$  can be then approximated by

$$\kappa = \frac{\pi(2r + w)}{4R_{\text{meas}}wT} \quad (\text{B.6})$$

The required skin depth to dissipate  $1/e$  of the power, is calculated by

$$\delta = \sqrt{\frac{1}{\kappa f \mu}} \quad (\text{B.7})$$

## **Appendix C**

### **List of Videos**

#### **Test Videos**

Videos elaborated by the author:

IR Radar - Anoeta Soccer Stadium Tickets

IR Radar - Anoeta Soccer Stadium Test Session PET

IR Radar - COD2

IR Radar - Dipole, Circular, Conical

IR Radar - Double Dipoles

IR Radar - Greece Airport Paper Tickets

IR Radar - Metro Bilbao Plastic Cards

SFM Reader - CR

#### **Consortium Videos**

Pilot videos elaborated by the eVACUATE consortium of the system demonstrations in which the author participated:

eVACUATE EU project trials at Athens International Airport

eVACUATE EU project trials at Metro Bilbao – RFID

eVACUATE EU project trials at Metro Bilbao

eVACUATE EU project trials at STX France

## Curriculum Vitae

### Professional experience

---

02/2018 – 12/2018	Ph.D. Thesis in RFID with chipless transponders
10/2017 – 01/2018	<b>Alfatraining Bildungszentrum GmbH, Dresden, Germany</b>
Position	<b>Professional qualification</b>
Duties	<ul style="list-style-type: none"><li>• Java SE 8, final grade: 100/100</li><li>• C++ / Microsoft C++ .NET, final grade: 95/100</li></ul>
06/2017 – 09/2017	Ph.D. Thesis in RFID with chipless transponders
07/2013 – 05/2017	<b>Technische Universität Dresden, Dresden, Germany</b>
Position	<b>Research Associate – Chair for Circuit Design and Network Theory</b>
Duties	<ul style="list-style-type: none"><li>• Research and development of an ultra-wideband (UWB) transceiver system with chipless transponders for the automatic, non-contact identification of objects and living beings with radio waves (RFID)</li><li>• Development of algorithms with MATLAB to be implemented on stepped frequency modulated (SFM) and pulse (IR) radar front ends for the detection and decoding of UWB chipless RFID transponders</li><li>• Assembly with standard components of a SFM UWB reader for chipless RFID transponders (4 - 6 GHz)</li><li>• Design and modelling of chipless RFID transponders with CST Microwave Studio (2 - 11 GHz)</li><li>• Measurement of the frequency response of chipless RFID transponders using vector network analyzers</li><li>• FPGA programming with Verilog and ISE Design Suite</li><li>• Record the research results and contribute to their publications</li><li>• Presentation of project results in meetings and conferences</li></ul>
12/2011 – 06/2013	Job seeking
09/2007 – 03/2009	<b>Telefónica Celular S. A., Tegucigalpa, Honduras</b>
Position	<b>Mobile network quality head</b>
Duties	<ul style="list-style-type: none"><li>• Manage department and overall expectations pertaining to setting accurate GSM/WCDMA network key performance indicators, costs and resources</li><li>• Directly supervise the network design and optimization team leaders, engineers and drive testers including the</li></ul>

preparation and delivery of staff performance evaluations and career

- Ensure delivery against the department goals and objectives, i.e. Meeting key performance indicators targets and coordinating overall network design and optimization tasks
- Implements ongoing quality improvement processes working with interdepartmental teams
- Develop and manage the department's metrics for performance improvement of all teams
- Establish and maintain policy for documentation of all processes
- Review documentation before sending it out to external customers

03/2006 – 08/2007

**Telefónica Celular S. A., Tegucigalpa, Honduras**

Position

**Mobile network senior optimization engineer**

Duties

- Coordinate all the Network optimization tasks to meet the key performance indicators goals
- Maintain the GSM radio network performance, such as: Accessibility, retainability, mobility and service integrity
- Analyze the key performance indicators to investigate and solve the network quality problems
- Plan and implement frequency reuse plans to achieve a high-quality network with minimum interference
- Plan and implement neighboring cells plans to achieve a high call retainability within the network
- Implement new radio access network features and database parameter tuning
- Audit and set the radio and core network parameters

09/2004 – 02/2006

**Telefónica Celular S. A., Tegucigalpa, Honduras**

Position

**Mobile network traffic planning and statistics engineer**

Duties

- Collect and analyze relevant information to build the demand model of the GSM network
- Develop optimization techniques for what-if analysis of network demand and topology
- Plan the GSM Network capacity expansion to meet the projected traffic growth
- Collaborate with other team members to identify, develop and implement base-lining and forecasting methods
- Solicit network nodes capacity expansions when needed, to maintain the target congestion levels
- Deliver overall network utilization reports for monitoring the traffic and efficiency of the network
- Provide network statistics as require



**Academic qualifications**

---

2009 – 2011	<b>Universität Kassel, Germany</b> M. Sc. Electrical Communication Engineering Final grade: 1.3 (very good)
1999 – 2006	<b>Universidad Nacional Autónoma de Honduras, Honduras</b> Ingeniero Eléctrico Industrial Final grade: 80% (good)

**Skills and competences**

---

Languages	German: Good English: Fluent Spanish: Mother tongue
Social skills and competences	Teamwork, willingness to help, tolerance, intercultural competence
IT-skills and competences	C++/ Microsoft Visual C++ .NET, Java SE 8, MATLAB, Verilog, Altium PCB Designer, CST Microwave Studio, Microsoft Office, Ericsson TEMS, Aircom Enterprise, Business Object
Equipment	Vector Network Analyzer, Spectrum Analyzer, Ambios Technology surface profilometer, SENTECH SENpro spectroscopic ellipsometer, Zygo NewView 5000 white light interferometer, TePla 200-G Plasma ashing, Oxford Plasmalab 80 PECVD, Pfeiffer PLS 500 depositio, Karl Süss MA4 mask aligner

**Awards**

---

Best student paper award	2016, IEEE International Conference on Ubiquitous Wireless Broadband (ICUWB)
--------------------------	--

Academic excellence award      2001, Universidad Nacional Autónoma de Honduras

Academic excellence award      2000, Universidad Nacional Autónoma de Honduras

Best student in integral calculus award      2000, Universidad Nacional Autónoma de Honduras